Structural Constraint and Flexibility in the Chemistry of Lewis-Acidic *p*-Block Atom-Based Molecules

Synthetic Chemistry of Calix[4]pyrrolato Complexes,
Quantum Chemical Studies, and Data-Driven Approaches

INAUGURAL DISSERTATION

to obtain the Academic Degree
Doctor Rerum Naturalium (Dr. rer. nat.)

of the Combined Faculty of Mathematics, Engineering,
and Natural Sciences of Heidelberg University

by
Lukas Maximilian Sigmund
born in Mosbach

2024

The experimental and computational work presented within this dissertation was carried out from March 2020 to December 2023 under the supervision of PROF. DR. LUTZ GREB at the *Institute of Inorganic Chemistry* at *Ruprecht-Karls-Universität Heidelberg* and at the *Department of Chemistry* at *Colorado State University*, hosted by PROF. ROBERT PATON. Some of the results described here were obtained by NICK RICHERT, ROUVEN MAIER, ELIANE ENGELS, and ANDREAS ALBERS as part of their research internships under my supervision. Also, some results were generated in direct collaboration with DR. CHRISTOPHER EHLERT and SHREE SOWNDARYA S. V.. Essential parts of this dissertation have already been published in scientific articles.

First referee and advisor	*Prof. Dr. Lutz Greb*
Second referee	*Prof. Dr. Dr. Hans-Jörg Himmel*
Date of disputation	*March 15, 2024*

List of Publications

12) L. M. Sigmund, S. Sowndarya S. V., A. Albers, P. Erdmann, R. S. Paton, L. Greb, "Predicting Lewis Acidity: Machine Learning the Fluoride Ion Affinity of *p*-Block Atom-based Molecules", *submitted*.

11) L. Kistner, L. M. Sigmund, F. F. Grieser, J. Krauß, S. Leingang, E. Kaifer, L. Greb, H.-J. Himmel, "Metal-Free B-B Dehydrocoupling Reaction of a Simple Borane Adduct: Convenient Access to a Nucleophilic Diborane(4)", *Angew. Chem. Int. Ed.* **2024**, *63*, e202317462.

10) L. M. Sigmund, E. Engels[+], N. Richert[+], L. Greb, "Calix[4]pyrrolato gallate: square planar-coordinated gallium(III) and its metal-ligand cooperative reactivity with CO_2 and alcohols", *Chem. Sci.* **2022**, *13*, 11215-11220. [+]: equal contributions.

9) L. M. Sigmund[+], F. Schön[+], F. Schneider, D. Hartmann, M. A. Wiebe, I. Manners, L. Greb, "Calix[4]pyrrolato Aluminate Catalyzes the Dehydrocoupling of Phenylphosphine Borane to High Molar Weight Polymers", *Angew. Chem. Int. Ed.* **2022**, *61*, e202202176. [+]: equal contributions.

8) L. M. Sigmund, C. Ehlert, G. Gryn'ova, L. Greb, "Stereoinversion of Tetrahedral *p*-Block Element Hydrides", *J. Chem. Phys.* **2022**, *156*, 194113.

7) L. M. Sigmund, R. Maier, L. Greb, "The inversion of tetrahedral *p*-block element compounds: general trends and the relation to the second-order Jahn-Teller effect", *Chem. Sci.* **2022**, *13*, 510-521.

6) L. M. Sigmund[+], H. Ruppert[+], L. Greb, "Calix[4]pyrroles as ligands: recent progress with a focus on the emerging *p*-block element chemistry", *Chem. Commun.* **2021**, *57*, 11751-11763. [+]: equal contributions.

5) L. M. Sigmund, C. Ehlert, M. Enders, J. Graf, G. Gryn'ova, L. Greb, "Dioxygen Activation and Pyrrole α-Cleavage with Calix[4]pyrrolato Aluminates: Enzyme Model by Structural Constraint", *Angew. Chem. Int. Ed.* **2021**, *60*, 15632-15640.

4) L. M. Sigmund, L. Greb, "Reversible OH-bond activation and amphoterism by metal-ligand cooperativity of calix[4]pyrrolato aluminate", *Chem. Sci.* **2020**, *11*, 9611-9616.

3) L. Greb, L. M. Sigmund[+], F. Ebner[+], Y. Ginzburg[+], "Element-Ligand Cooperativity with *p*-Block Elements", *Eur. J. Inorg. Chem.* **2020**, *2020*, 3030-3047. [+]: equal contributions.

2) F. Ebner, L. M. Sigmund, L. Greb, “Metal-Ligand Cooperativity of the Calix[4]pyrrolato Aluminate: Triggerable C-C Bond Formation and Rate Control in Catalysis”, *Angew. Chem. Int. Ed.* **2020**, *59*, 17118-17124.

1) L. M. Sigmund[+], F. Ebner[+], C. Jöst, J. Spengler, N. Gönnheimer, D. Hartmann, L. Greb, “An Air-Stable, Neutral Phenothiazinyl Radical with Substantial Radical Stabilization Energy”, *Chem. Eur. J.* **2020**, *26*, 3152-3156. [+]: equal contributions.

The rights to adapt the content of some of the above listed publications were obtained through RightsLink®.

To the three very best people in my life!

Do your best!

Abstract

Lewis acids are defined as electron pair acceptors, and the introduction of *structural strain* was shown a powerful lever to increase the Lewis acidity of *p*-block atom-based molecules. This dissertation presents *experimental*, *quantum chemical*, and *data scientific* contributions to the research area of *p*-block element-based Lewis acidity.

The reactivity of *calix[4]pyrrolato aluminates* (Cx[4]Al) was investigated experimentally. Cx[4]Al was found to heterolytically split the O-H bond of protic substrates (alcohols, carboxylic acids) in a reversible manner. With triplet dioxygen as substrate, Cx[4]Al forms an alkyl peroxido aluminate. A subsequent rearrangement reaction of the peroxido aluminates which yields α,β-unsaturated carboxylato aluminates was discovered and its reaction mechanism investigated. Furthermore, the reactivity of Cx[4]Al with nitrogen monoxide, nitrosobenzene, and phenyl isocyanate was studied. Characteristic for all reactions is an aluminum-ligand cooperative mechanism.

The chemistry of the calix[4]pyrrolato ligands was expanded to gallium, and *calix[4]pyrrolato gallates(III)* (Cx[4]Ga) were synthesized and fully characterized. They are the first examples for ideally square planar-coordinated Ga(III) atoms. Cx[4]Ga's reactivity with small molecules (*e.g.*, CO_2) as well as its redox chemistry were researched.

More than 250 small *p*-block atom-based molecules in square planar structural configuration were investigated with density functional theory and wavefunction-based quantum chemistry. Substituent effects on the planarization energies were discussed and related to the *second-order Jahn-Teller theorem*. Indeed, the square planar configurations can serve as transition states for the *stereochemical inversion* of the respective molecules. In addition to that, a new *stepwise mechanism for stereoinversion* was discovered.

Lastly, the *FIA49k dataset*, encompassing 48,986 fluoride ion affinities of molecules based on 13 different *p*-block elements, is presented herein. The data was generated with double-hybrid DFT calculations. It was used to train *FIA-GNN*, a graph neural network machine learning model that predicts FIA values. FIA-GNN's usefulness was demonstrated in four different case studies.

German Abstract

Lewis-Säuren werden als Elektronenpaarakzeptoren definiert, und die Einführung von *struktureller Spannung* erwies sich als wirksamer Hebel zur Erhöhung der Lewis-Azidität von Molekülen auf der Basis von *p*-Block-Atomen. Diese Dissertation präsentiert *experimentelle*, *quantenchemische* und *datenwissenschaftliche* Beiträge zum Forschungsgebiet der *p*-Block-Element-basierten Lewis-Azidität.

Die Reaktivität von *Calix[4]pyrrolato-Aluminaten* (Cx[4]Al) wurde experimentell untersucht. Es wurde festgestellt, dass Cx[4]Al die O-H-Bindung protischer Substrate (Alkohole, Carbonsäuren) auf reversible Weise heterolytisch spaltet. Mit Triplett-Disauerstoff als Substrat bildet Cx[4]Al ein Alkylperoxido-Aluminat. Eine anschließende Umlagerungsreaktion der Peroxido-Aluminate, die zu α,β-ungesättigten Carboxylato-Aluminaten führt, wurde entdeckt und ihr Reaktionsmechanismus untersucht. Darüber hinaus wurde die Reaktivität von Cx[4]Al mit Stickstoffmonoxid, Nitrosobenzol und Phenylisocyanat untersucht. Charakteristisch für alle Reaktionen ist ein Aluminium-Ligand-kooperativer Mechanismus.

Die Chemie der Calix[4]pyrrolato-Liganden wurde auf Gallium ausgeweitet; *Calix[4]pyrrolato-Gallate(III)* (Cx[4]Ga) wurden synthetisiert und vollständig charakterisiert. Sie sind die ersten Beispiele für ideal quadratisch planar koordinierte Ga(III)-Atome. Die Reaktivität von Cx[4]Ga mit kleinen Molekülen (z. B. CO_2) sowie seine Redoxchemie wurden untersucht.

Mehr als 250 kleine *p*-Block-Atom-basierte Moleküle in quadratisch-planarer Konfiguration wurden mit Dichtefunktionaltheorie und wellenfunktionsbasierter Quantenchemie untersucht. Substituenteneffekte auf die Planarisierungsenergien wurden diskutiert und mit dem *Jahn-Teller-Theorem zweiter Ordnung* in Zusammenhang gebracht. Tatsächlich können die quadratisch-planaren Konfigurationen als Übergangszustände für die *stereochemische Inversion* der jeweiligen Moleküle dienen. Darüber hinaus wurde ein neuer *schrittweiser Stereoinversionsmechanismus* entdeckt.

Abschließend wird der *FIA49k-Datensatz* vorgestellt, der 48.986 Fluoridion-Affinitäten (berechnet auf Doppelhybrid-DFT Niveau) von Molekülen basierend auf 13 verschiedenen *p*-Block-Elementen beinhaltet. Der Datensatz wurde verwendet um ein Graphneuronales-Netzwerk (*FIA-GNN*) zu trainieren, welches FIA-Werte vorhersagt. Der Nutzen von FIA-GNN wurde in vier verschiedenen Fallstudien demonstriert.

CONTENTS

1 INTRODUCTION

1.1 Preface

The periodic table organizes the atomic building blocks of the universe by grouping elements with similar chemical reactivity, and in fact with similar electronic structure, into the same column of its iconic raster pattern.[1-2] The so-called *p-block elements* are typically displayed at the right end of the periodic table (**Figure 1.1A**). Famous members are nonmetals like carbon, nitrogen, or oxygen, but also elements with (semi)metallic character such as aluminum or silicon. All atoms of the *p*-block's elements share the trademark of having either completely full or completely empty *d*-orbitals. At the same time, their partially filled *p*-orbitals (when excluding the noble gases) are the main ingredient for their reactivity with other atoms and are last but not least the group's namesake.[3]

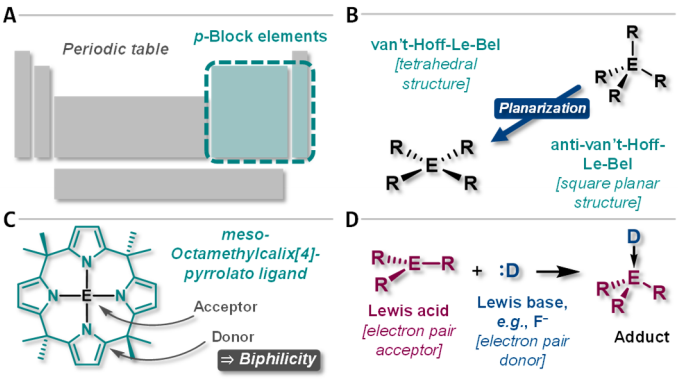

Figure 1.1: Conceptual building blocks of this dissertation. ***A)*** *Schematic representation of the periodic table.* ***B)*** *Molecular structures with tetrahedral and square planar configuration about the central atom.* ***C)*** *A meso-octamethylcalix[4]pyrrolato complex and its electronic features.* ***D)*** *Lewis acid / Lewis base adduct formation reaction.*

When participating in chemical reactions, the atoms of *p*-block elements strive for maintenance or attainment of eight electrons within their valence shell. This so-called *octet rule*[4] holds primarily for lighter *p*-block atoms as their heavier congeners more readily exceed or go below a valence electron count of eight. In either case, a complete valence electron octet typically dictates the *tetrahedral* arrangement of substituents around

tetrasubstituted *p*-block atoms (**Figure 1.1B**). The archetypical example is methane. Its equilibrium molecular structure is the ideal tetrahedron which is spanned by the four hydrogen atoms (corners) around the central carbon atom. Remarkably, this fundamental insight was already introduced in 1874 by VAN'T HOFF as he was describing *"[…] les affinités de l'atome de carbon dirigées vers les sommets d'un tetraèdre, dont cet atome lui-même occuperait le centre."*[5] LE BEL independently obtained similar results[6], giving rise to the today well-known *van't-Hoff-Le-Bel principle*.

The *anti-van't-Hoff-Le-Bel* configuration is obtained when the four substituents are arranged such that they represent a square with the central atom in its center (**Figure 1.1B**). The square planar configuration is for the vast majority of *p*-block atom-based compounds a non-equilibrium structure of high energy.[7] Only selected molecular frameworks are capable of forcing *p*-block atoms into square planarity by imposing *structural constraint*. In fact, this type of constraint and its various implications and consequences are at the heart of this dissertation.

One of the molecular structures that can force atoms in its center into an anti-van't-Hoff-Le-Bel configuration is the family of *calix[4]pyrrolato ligands* (**Figure 1.1C**). Their parent compound, *meso*-octamethylcalix[4]pyrrole, was synthesized for the first time in 1886 by VON BAEYER from pyrrole and acetone.[8] Dozens of derivatives were prepared thereafter, and the chemistry of calix[4]pyrroles is a rich and active field of research.[9-15]

One of the properties of molecules with square planar-coordinated *p*-block atoms is their ability to act as *Lewis acids*. In 1923, LEWIS introduced an acid-base theory which classifies acids as electron pair acceptors and bases as electron pair donors.[16] A Lewis-acid-Lewis-base adduct is formed when electron donation from the base to the acid occurs, ultimately resulting in a newly formed dative bond (**Figure 1.1D**). The quantitative scaling of Lewis acids with respect to their strength is not straightforward as it is always requires two components (Lewis acid and base) that make up the resulting adduct. Inevitably, a multidimensional problem arises. Numerous scales for Lewis acid strengths were introduced in the past[17], with the affinity toward a fluoride anion as reference Lewis base – the *fluoride ion affinity*[18] – being one of the most popular ones.

When both a Lewis acidic and Lewis basic center are present within a molecule without the ability for intra- or intermolecular adduct formation, biphilic reactivity patterns become possible. This means that the molecule can react simultaneously as Lewis acid and base given a suitable substrate is offered. When such an electronic structure is present in a metal complex, this reactivity pattern in its general form is termed *element-ligand*

cooperativity.[19-20] It typically relies on an electron-deficient central atom and an electron-rich ligand. These electronic conditions are found in calix[4]pyrrolato complexes of *p*-block elements (**Figure 1.1C**). Consequently, element-ligand cooperativity is the main reactivity pattern of this class of compounds.

In the following sections of this introductory chapter, the key concepts which are relevant for this dissertation are presented in more detail. These are:

- *Electronic structure of molecules with anti-van't-Hoff-Le-Bel configurated p-block atoms and their relation to stereochemical inversion* (**Chapter 1.2**)
- *The second-order Jahn-Teller theorem* (**Chapter 1.3**)
- *Lewis acidity and its quantitative scaling* (**Chapter 1.4**)
- *Element-ligand cooperativity* (**Chapter 1.5**)
- *Calix[4]pyrrole chemistry – especially with p-block elements* (**Chapter 1.6**)
- *Fundamentals of machine learning in chemistry with a focus on graph neural networks* (**Chapter 1.7**)

In the subsequent chapter, the motivations and objectives of this doctoral project are outlined (**Chapter 2**). The presentation of the results and their discussion (**Chapter 3**) can be grouped into four individual blocks:

- *Experimental chemistry of calix[4]pyrrolato aluminates and gallates* (**Chapters 3.1** *to* **3.6**)
- *Exploration of the electronic and molecular structure of small p-block atom-based molecules with quantum chemical methods – especially in regard of the stereochemical inversion of molecules with tetrasubstituted p-block atoms* (**Chapters 3.7** *and* **3.8**)
- *Compilation of a large dataset of fluoride ion affinities of p-block atom-based molecules and the construction of machine learning models for the prediction of fluoride ion affinities* (**Chapters 3.9** *to* **3.12**)
- *Quantum chemical simulations on dehydrogenation reactions of borane (BH_3) Lewis adducts with the hppH Lewis base* (**Chapters 3.13**)

1.2 Electronic Structure of Square Planar-Coordinated *p*-Block Atoms

When four points are positioned on a sphere such that the total distance between them is maximized, a tetrahedron is obtained after connecting every point with all the others. Assuming repulsion, it is therefore *per se* natural to assume a tetrahedral configuration of four independent substituents around a given central atom. While this is not true for every molecule with a tetravalent atom, this assumption holds indeed for the cases of tetrasubstituted *p*-block atoms with a complete valence octet (when excluding any sort of structural constraints or steric repulsions). Based on symmetry assumptions, molecular orbital theory (MO theory) allows a more elaborate approach to the problem at hand. In the following, the electronic structure of methane (CH_4) and silane (SiH_4) is presented using MO theory, and the electronic implications when forcing their tetrahedral ground state structure into square planarity are described.

The global minimum molecular equilibrium structures of both CH_4 and SiH_4 possess T_d symmetry. Four bonding ($1a_1$ and $1t_2$) and four anti-bonding ($2a_1$ and $2t_2$) molecular orbitals can be constructed by combining the central elements' valence *s*- and *p*-orbitals with the symmetry-adapted fragment orbitals of the four H substituents (**Figure 1.2A**).[21] The orbitals of the triply degenerate $1t_2$ representation are the highest occupied molecular orbitals (HOMO). The lowest unoccupied molecular orbital (LUMO) in the cases of CH_4 and SiH_4 is of a_1 symmetry ($2a_1$ representation). This can differ for central atoms other than carbon or silicon, and the $2t_2$ representation can become the lowest unoccupied level.[21] For CH_4 and SiH_4, the energetic separation between HOMO and LUMO is large (10.43 and 9.25 eV, respectively)[a].

The deformation into the square planar D_{4h} symmetric configuration occurs along the *E* harmonic vibration *via* intermediate D_{2d} symmetry (**Figure 1.2A**).[21-24] During planarization, the $1a_1$ orbital experiences slight stabilization owing to the increased overlap of the in-phase lobes of the substituent fragment orbital. The $1t_2$ set of the tetrahedral state splits up into the 1*e* and $1b_2$ representation. The 1*e* set becomes slightly stabilized (compared to the energetic level of $1t_2$) due to a more favorable interaction of the substituent and central atom orbitals. At the same time, the $1b_2$ orbital turns from bonding (as part of the $1t_2$ representation) to non-bonding and becomes considerably destabilized in the molecular orbital of a_{2u} symmetry in the resulting D_{4h} symmetric state. The unoccupied $2a_1$

[a] Calculated at the B97M-D3(BJ)/def2-QZVPP level of theory.

orbital is marginally stabilized after planarization for the same reason as the $1a_1$ orbital energy is lowered and results in the $2a_{1g}$ orbital in the square planar state. Finally, the $2t_2$ representation decomposes into a doubly degenerate set of e_u orbitals ($2e_u$) as well as into a b_{1g} symmetric orbital. The former are higher in energy compared to the initial $2t_2$ set, whereas the latter is significantly lower. In total, this MO theoretical perspective assigns the reason for the significant increase in electronic energy upon planarization to the energetic rise of one of the orbitals of the occupied $1t_2$ set of molecular orbitals. This is not compensated by the stabilization of the other occupied orbitals.

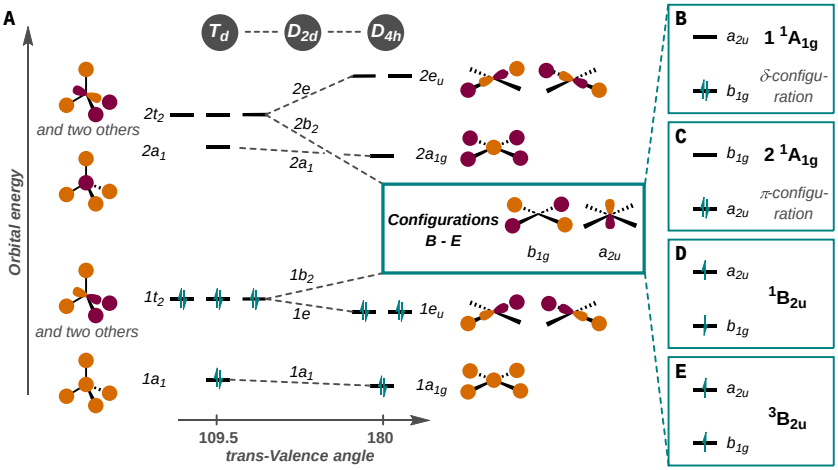

Figure 1.2: Electronic structure of molecules with a central tetravalent *p*-block atom with a complete valence electron octet and with four hydrogen substituents. ***A)*** *Schematic Walsh diagram for the distortion from the tetrahedral to the square planar configuration, for example, of CH_4 or SiH_4.* ***B-E)*** *Potential electronic configurations of the square planar state.*[25]

Candidates for the HOMO and LUMO of the D_{4h} symmetric configuration are the b_{1g} and a_{2u} molecular orbital (**Figure 1.2A**). The a_{2u} orbital, which is localized at the central atom, is generally described as being of π-type, whereas the b_{1g} orbital has δ-character and resides at the substituents.[26] Their energetic order is dependent on the electronegativity of the central element relative to the substituents. In the case of CH_4, which has a central atom that is more electronegative than its substituents, the carbon-centered a_{2u} orbital is occupied with electrons. For SiH_4, the central atom is less electronegative compared to hydrogen. Therefore, the b_{1g} orbital is the HOMO.[26-27] This means that the electronic structure of molecules with an anti-van't-Hoff-Le-Bel configurated *p*-block atom can vary drastically, even in a qualitative sense, depending on the involved central atom.

In either case, the HOMO-LUMO gap is significantly reduced in the square planar state (**Figure 1.2A**). It is 1.90 eV for CH_4 ($2\ ^1A_{1g}$) and 1.22 eV for SiH_4 ($1\ ^1A_{1g}$).[b] This predicts an increased reactivity of molecules with a square planar *p*-block atom, both in an electron accepting as well as donating manner, when engaging in chemical reactions.

The close approach of the HOMO and LUMO render possible several electronic configurations for the respective molecules: the closed-shell singlet δ-configuration ($1\ ^1A_{1g}$, doubly occupied b_{1g} MO, **Figure 1.2B**) and π-configuration ($2\ ^1A_{1g}$, doubly occupied a_{2u} MO, **Figure 1.2C**), the open-shell singlet, and the respective triplet configuration ($^1B_{2u}$ and $^3B_{2u}$, respectively, both singly occupied a_{2u} and b_{1g} MOs, **Figure 1.2D-E**). In **Chapter 3.8** of this dissertation, all these electronic configurations will be discussed in detail for 15 *p*-block element-hydrogen compounds.

The calculation of the harmonic vibrational frequencies of square planar SiH_4 ($1\ ^1A_{1g}$) results in a single imaginary frequency of b_{2u} symmetry. It relaxes the molecular structure in both directions on the potential energy surface to the tetrahedral ground state (**Figure 1.3A**). Indeed, it facilitates the stereochemical inversion of SiH_4 (*cf.* **Chapter 0**). The respective activation free energy is 358 kJ mol^{-1}.[b] This corresponds to an approximate half-life of more than 10^{40} years at 298 K. Thus, SiH_4 and in general all tetrasubstituted *p*-block atoms are considered stereo-configurationally stable.

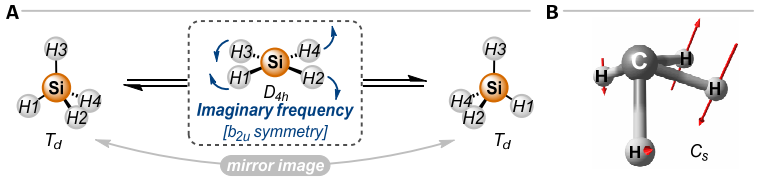

Figure 1.3: Stereochemical inversion of *p*-block element-hydrogen compounds. ***A)*** *Stereoinversion of SiH_4 via a square planar inversion transition structure.* ***B)*** *C_s symmetric inversion transition structure of CH_4 with the scaled displacement vectors of the single imaginary vibrational mode.*

The frequency analysis for square planar CH_4 gives four imaginary modes (b_{2u}, a_{2u}, e_u) and therefore the structure does not represent a stereoinversion transition state. Instead, it was found independently by GORDON and SCHMIDT[28] and by PEPPER *et al.*[29] that methane can undergo stereoinversion *via* a transition structure of C_s symmetry (**Figure 1.3B**). The corresponding activation free energy barrier (428 kJ mol^{-1})[b] is even higher as for SiH_4. In **Chapter 3.8**, the recalculation of this barrier as well as its interpretation with respect to

[b] Calculated at the B97M-D3(BJ)/def2-QZVPP level of theory.

methane's C-H bond strength is presented. Furthermore, the C_s inversion pathway is explored for central atoms other than C and is compared to the stereoinversion through the D_{4h} symmetric transition structure.

Experimental work on the unimolecular stereochemical inversion about a tetracoordinate *p*-block atom is rare (**Figure 1.4**). After several quantum chemical contributions[30-32], ARDUENGO III and coworkers reported on the barrier for inversion of germane **1**. It was determined to $\Delta H^{\ddagger} = 93 \pm 10$ kJ mol^{-1} using ^{1}H NMR spectroscopy.[33] Earlier, the stereoinversion barrier of silane **2** was estimated to 117 kJ mol^{-1}.[34]

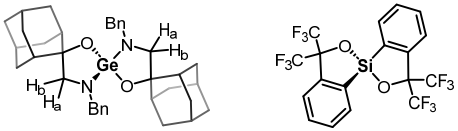

1 2

Figure 1.4: Experiments on the stereoinversion of four-coordinate *p*-block atoms. *The diastereotopic protons H_a and H_b in molecule 1 were used to determine the inversion barrier with the help of ^{1}H NMR spectroscopy. Bn stands for benzyl.*

As outlined in this chapter, the planarization of the coordination environment around a tetracoordinate *p*-block atom in its highest oxidation state is associated with a significant energy demand. There are several extensions to the MO considerations presented above to further rationalize this fact – one of which is the second-order Jahn-Teller theorem, which is presented in the following chapter. It was applied within this dissertation to the electronic structure of small *p*-block atom-based molecules with square planar structure.

1.3 The Second-Order Jahn-Teller Theorem

Symmetry considerations are deeply ingrained into the scientific descriptions of the universe, nature, and life. This is not surprising, as we are constantly surrounded by a plethora of objects that are considered symmetrical.[35] Not least, people are literally attracted by symmetry – an observation that is researched by hundreds of scientists all over the world within various different cultural areas and historical epochs.[36-41]

In 1937, JAHN and TELLER published a seminal paper on the "Stability of Polyatomic Molecules in Degenerate Electronic State".[42] Their findings are today generally known as the *Jahn-Teller effect* (JTE).[43] Following initial contributions from LANDAU in a discussion with TELLER[44], they were able to show that all non-linear nuclear configurations are unstable toward distortion in case they are in an orbitally degenerate electronic state (**Figure 1.5**).[42] The work relates the symmetry of molecules to their electronic structure which ultimately dictates the experimentally observable molecular structure. The JTE often leads to symmetry lowering within *a priori* highly symmetric molecules. Within the following sections, the theory, which is applicable to non-degenerate states, termed *second-order Jahn-Teller effect* (SOJTE, sometimes alternatively referred to as pseudo Jahn-Teller effect), is presented.[21, 43, 45] It was used within this dissertation project for the chemistry of *p*-block atoms within a square planar coordination environment.

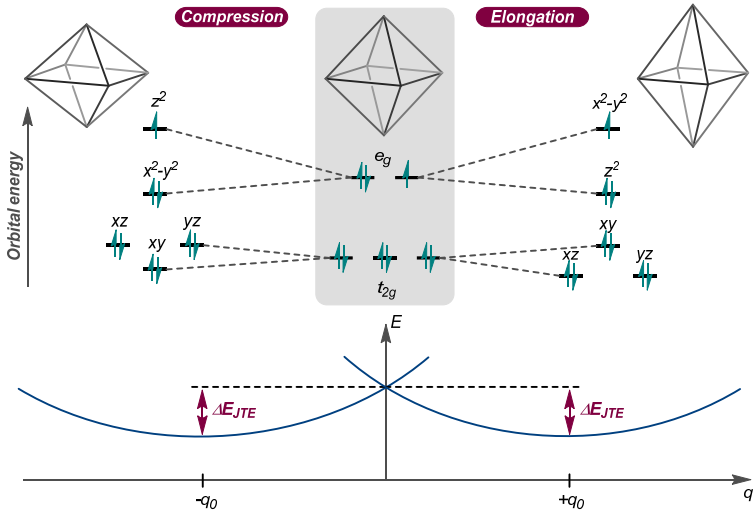

Figure 1.5: The Jahn-Teller effect (JTE). *Deformation of the ideal octahedral structure due to its double degenerate electronic state exemplified with a d^9 transition metal cation, e.g., $[Cu(OH_2)_6]^{2+}$.*

Within the Born-Oppenheimer approximation, the energy *E* of a system is dependent on its atomic positions, or, more precisely – derived from symmetry considerations – on its normal displacements *q*.

$$E = f(q) = \langle \Psi_0 | \mathrm{H} | \Psi_0 \rangle \tag{1.1}$$

Ψ_0 represents the ground state wavefunction and H is the Hamiltonian. The curvature *K* at the minimum point of the resulting potential energy surface (PES) along a given normal coordinate *q* is then obtained with

$$K = \left(\frac{\partial^2 E}{\partial q^2} \right)_0 . \tag{1.2}$$

The combination of **Equations 1.1** and **1.2** yields

$$K = \underbrace{\left\langle \Psi_0 \middle| \left(\frac{\partial^2 \mathrm{H}}{\partial q^2} \right)_0 \middle| \Psi_0 \right\rangle}_{K_0} + \underbrace{2 \left\langle \Psi_0 \middle| \left(\frac{\partial \mathrm{H}}{\partial q} \right)_0 \middle| \Psi_0{}' \right\rangle}_{K_v}, \Psi_0' = \left(\frac{\partial \Psi_0}{\partial q} \right)_0 . \tag{1.3}$$

The second summand, K_v, can be reformulated with the help of second-order perturbation theory as

$$K_v = -2 \sum_n \frac{\left| \left\langle \Psi_0 \middle| \left(\frac{\partial \mathrm{H}}{\partial q} \right)_0 \middle| \Psi_n \right\rangle \right|^2}{E_n - E_0}, \tag{1.4}$$

in which the excited state wavefunctions are denoted by Ψ_n, the respective state energies by E_n.[45]

In fact, it was proved that K_0 is always greater than zero for all highly symmetric atomic configurations.[45-47] Consequently, *K* can only get negative, and this is when stabilization occurs, if the absolute value of the second summand in **Equations 1.3**, K_v, is greater than K_0. Generally, K_v is termed the vibronic contribution to a potential state instability. It describes the mixing of excited states with the ground state given the structural displacement *q*. K_0 is the force constant associated with the distortion along *q*.[21, 45] To summarize the so far presented: "[...] any distortion of the high-symmetry configuration is due to and only to the mixing of its ground state with excited electronic states by the distortive nuclear displacements realized via the vibronic coupling [...].".[45] This is the second-order Jahn-Teller theorem, which is schematically illustrated in **Figure 1.6**.

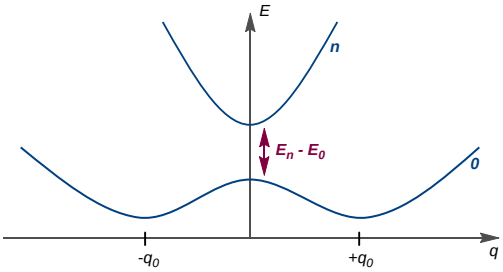

Figure 1.6: Schematic illustration of the second-order Jahn-Teller effect. *Depiction of the ground (0) and excited state (n) potential energy surface.*

K_v can only become operative if the numerators of its summands are non-zero (*cf.* **Equation 1.4**). This is the case if the direct product of the *irrep* of the ground ($\Gamma(\Psi_0)$) and the excited state ($\Gamma(\Psi_n)$) contains the *irrep* under which the distortion coordinate q, that is, its vibrational mode, transforms ($\Gamma(\Psi_0) \otimes \Gamma(\Psi_n) \in \Gamma(q)$). Also, K_v's contribution is scaled by the energy difference of the two considered states, which considerably reduces the influence of higher excited states.

The contribution to K of all relevant quantities (*cf.* **Equation 1.3**) is cumbersome to analyze.[48] However, focusing only on the most relevant portion, K_v, facilitates the evaluation. Moreover, as the state symmetry species $\Gamma(\Psi)$ are determined by the symmetry of the occupied molecular orbitals and because only the lowest-lying excited states can be expected to be of relevance, frontier molecular orbital considerations can be consulted. This means that K_v can be approximated to be proportional to the reciprocal of the HOMO-LUMO gap of the investigated configuration under a symmetry constrain (*vide supra*, numerator in **Equation 1.4**).

$$K_v \sim \frac{1}{E_{LUMO} - E_{HOMO}} \tag{1.5}$$

When utilized with awareness of the significant approximations induced, a tool which is straightforwardly applicable is obtained, and which is commonly even interpreted in quantitative sense, meaning that the extend of expectable stabilization is inversely proportional to the HOMO-LUMO gap.[49]

In this vein, the SOJTE was used to rationalize various experimental observations in *p*-block element chemistry. It was for example applied to multiply bonded higher main group atoms, which are the analogs of ethylene and acetylene.[49] Unlike their carbon congeners, they show a *trans*-bent molecular structure, which becomes apparent through the

SOJTE analysis of the frontier molecular orbitals. Furthermore, the trigonal inversion barrier of trivalent group 15-based molecules (*e.g.*, NH_3, PH_3) was studied (*cf.* **Figure 3.39B**).[50-54] It was shown that PH_3 has a much narrower HOMO-LUMO gap in the D_{3h} symmetric state as ammonia. This conforms with the larger barrier for stereoinversion found for PH_3 and phosphines in general.

Indeed, anti-van't-Hoff-Le-Bel-configurated *p*-block atoms, namely the element-hydrogen compounds, have been discussed in the context of the SOJTE.[55] By a detailed analysis based on **Equations 1.3**, it was shown that the vibronic coupling of ground and excited states as manifested in the SOJTE can be used to understand the instability of the D_{4h} symmetric structures. Formulated within the orbital picture: in the square planar state, the HOMO and LUMO are of a_{2u} and b_{1g} symmetry (*cf.* **Figure 1.2**). This means they are orthogonal to each other and cannot mix. The direct product of the symmetry species of the two FMOs transforms under the b_{2u} representation ($a_{2u} \otimes b_{1g} = b_{2u}$). Consequently, the vibronic interaction is facilitated by the B_{2u} vibrational coordinate, which is the deformation of the planar into the tetrahedral state (**Figure 1.3A**). It was therefore probed how the barrier for square planar stereoinversion of small *p*-block atom-based molecules correlates with the HOMO-LUMO gap values of the transition state (see **Chapter 3.7**).

Due to planarization, the electronic structure of respective molecules changes drastically (*cf.* **Figure 1.2**), the HOMO-LUMO gap is reduced, and the LUMO energy level in particular gets significantly lowered. Generally, this predicts increased chemical reactivity through an enhanced electron accepting character. Within the following chapter the concept of Lewis acids and bases, which is a theory of electron acceptance and donation is presented. Lewis acidity is the overarching reactivity principle of *p*-block atom-based molecules with anti-van't-Hoff-Le-Bel configuration.

1.4 Lewis Acidity and the Strength of a Lewis Acid

The *Compendium of Chemical Terminology*, published by the *International Union of Pure and Applied Chemistry* (IPUAC) defines a Lewis acid as "*a molecular entity (and the corresponding chemical species) that is an electron pair acceptor and therefore able to react with a Lewis base to form a Lewis adduct, by sharing the electron pair furnished by the Lewis base*."[56] Building up on that, Lewis acidity is described as "*the thermodynamic tendency of a substrate to act as a Lewis acid. Comparative measures of this property are provided by the equilibrium constants for Lewis adduct formation of a series of Lewis acids with a common reference Lewis base*."[56] As a prime example for a Lewis adduct formation, IUPAC gives the reaction of trimethylborane as Lewis acid with ammonia as Lewis base (**Figure 1.1D**).

The formation process of a Lewis adduct can conceptually be divided into a deformation and an association step (**Figure 1.7**).[57] The former comes with an energetic cost as the Lewis acid and base are deformed from their relaxed molecular structure into the respective conformation which they adopt in the adduct. The latter allows for the interaction of the reaction partners, which is dominated by the formation of the dative chemical bond. This step commonly results in a release of energy. If this release can overcompensate the energy demand for structural deformation (and the entropic penalty for adduct formation in terms of free energies), a Lewis adduct is formed. The deformation energy (DE) is thus a quantity with a large influence on the adduct formation energy and therefore on the strength of a Lewis acid.[57-59]

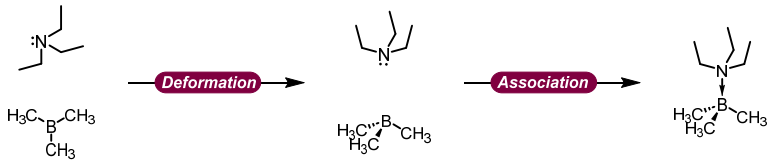

Figure 1.7: Formation of a Lewis adduct between trimethylborane and triethylamine dissected into a structural deformation and bond-forming association step.

There are numerous scales to quantify Lewis acid strength. Generally, Lewis acid scales can be described as being *intrinsic*, *effective*, or *global* in nature.[17]

Intrinsic scales are based exclusively on the Lewis acid itself, without any interaction with a base. Due to that, they do not include information on structural deformation required for adduct formation. The global electrophilicity index ω (GEI) is an example for an intrinsic Lewis acidity scale.[60-61] It is defined as

$$\omega = \frac{(E_{\mathrm{LUMO}} + E_{\mathrm{HOMO}})^2}{8(E_{\mathrm{LUMO}} - E_{\mathrm{HOMO}})} \tag{1.6}$$

and can be obtained after quantum chemically calculating the frontier molecular orbital energies E_{LUMO} and E_{HOMO}. Other examples for intrinsic scales are based on chemical shifts from nuclear magnetic resonance (NMR[62]) or electrochemical experiments.[63]

Effective scales[64] strive to quantify the effect of a Lewis acid on a given reference base. Prominent examples are the Gutmann-Beckett[65] and the Childs[66] experiment, relying on triethylphosphine oxide and *E*-crotonaldehyde, respectively, as probe Lewis bases for NMR spectroscopic measurements. Unlike intrinsic scales, effective datapoints also include information on the entire process of adduct formation and are therefore influenced, for example, by the chemical equilibrium of the adduct formation reaction (**Figure 1.7**).

Global scales are closely related to IUPAC's definition of Lewis acidity (*vide supra*). They use adduct formation reaction enthalpies with a chosen reference base as a quantitative measure for Lewis acidity. Like effective scales, they contain information on the Lewis adduct formation process and therefore also on deformation energy requirements. Global scales can be constructed based on experimentally obtained values or alternatively from quantum chemical data.

The affinity toward a fluoride anion (*fluoride ion affinity*, FIA), obtained with density functional theory (DFT) or wavefunction-based methods, is among the most popular global Lewis acidity scales.[18, 67-69] Because the experimental determination of absolute FIA values is a delicate task[18, 70-74], they are much more often computationally simulated. To avoid the explicit treatment of the naked fluoride anion within the simulations, the FIA is typically obtained with the help of an anchoring system, *e.g.*, the fluorotrimethylsilane system (**Figure 1.8**). This scheme was used within the research work presented in this dissertation to compile a large dataset of FIA values of *p*-block atom-based molecules (*cf.* **Chapter 3.9**).

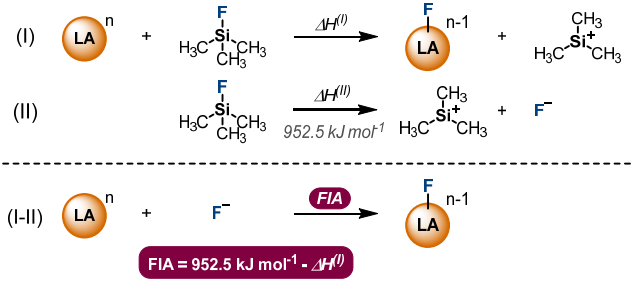

Figure 1.8: Fluorotrimethylsilane anchoring system for the calculation of the fluoride ion affinity (FIA) of a given Lewis acid (LA). *$\Delta H^{(II)}$ was calculated at the CCSD(T)/CBS level of theory.*[68]

Besides the outlined quantitative scales, there is the *theory of hard and soft Lewis acids and bases* (HSAB), which was introduced by PEARSON in 1963 and which is applied mainly in a qualitative sense.[75] HSAB is a binary classification scheme for both acids and bases, which categorizes them either as hard or soft. Hardness is associated with a low degree of electronic polarizability, whereas softness is related to high polarizability. Rather strong interactions can be expected between homo couples: "*hard acids bind strongly to hard bases and soft acids bind strongly to soft bases*." [75]

The *ECW model*, pioneered by DRAGO and coworkers, can be interpreted as a quantitative advancement of HSAB. It relates the Lewis adduct formation enthalpy ΔH_{AB} *via*

$$-\Delta H_{AB} = E_A E_B + C_A C_B + W \qquad (1.7)$$

to acid (A) and base-specific (B) electrostatic (E_A, E_B) and covalent (C_A, C_B) parameters. W combines interaction independent contributions to ΔH_{AB}.[76-85] Parameters were obtained after fitting **Equation 1.7** to a set of experimentally determined adduct formation enthalpies. As reference molecules, iodine (C_A = 2.0, E_A = 0.5), *N*,*N*-dimethylacetamide (E_B = 2.35), and diethyl sulfide (C_B = 3.92) were chosen.[85] W is usually equal to zero. The obtained set of E and C parameters allows for the prediction of Lewis adduct formation enthalpies, within the chosen training set.

1.5 Element-Ligand Cooperativity

In many transition metal-catalyzed reactions, the ligand(s) serve to adjust the electronic properties of the respective central metal atom. Alternatively, the steric influence of bulky substituents in the ligand is exploited, *e.g.*, to gain stereoselectivity. Sometimes, even ligand dissociation is a required event for the generation of the catalytically active species, which renders the dissociated ligand irrelevant for the actual catalytic process.

In contrast to the just described situation, one speaks of *metal-ligand cooperativity* (MLC), when both the central atom and the ligand synergistically form covalent bonds with the substrate molecule.[86] MLC is a widely applied concept in the chemistry of transition metal complexes but was also used for the explanation of enzymatic reactions. In recent years, MLC was further expanded to *p*-block atom-based molecules and is there, in a more general sense, termed *element-ligand cooperation* (ELC).[19] Often, the ligand acts as a nucleophile and the central metal atom as an electrophile. Therefore, ELC-active molecules of such kind possess ligand-centered HOMOs and rather central atom-centered LUMOs. Due to that, the concepts of ELC and ligand non-innocence (in a redox reactive sense) are closely related and must be distinguished for a given system based on its reactivity.[19]

There are two general reaction modes for ELC.[86] The first corresponds to the direct insertion of the substrate into the element-ligand bond. In the second, the element-ligand bond often stays intact, and the substrate forms a new bond with a ligand atom that is several bonds away from the central atom. The latter is often coupled with aromatization and dearomatization events in the ligand backbone with conservation of the redox state of the central atom (**Figure 1.9A**).[87-88] Especially the MILSTEIN group has vastly researched the metal-ligand cooperative reactivity of transition metal-based complexes using dearomatization/aromatization strategies. Aromatization/dearomatization-supported element-ligand cooperativity was also discovered in complexes of the calix[4]pyrrolato ligand with *p*-block elements.[89] Their chemistry is presented in the following chapter (**Chapter 1.6**). Before that, selected examples of element-ligand cooperativity with transition metal and *p*-block atom-based molecules are presented (**Figure 1.9**).

Ruthenium(II) PNN pincer complex **3** was shown to react with dihydrogen to form the ruthenium dihydride **4** (**Figure 1.9A**).[90] Due to that, it was possible to apply **3** as hydrogenation catalyst, *e.g.*, for ester, carbonate, or carbamate substrates.[90-91] Strikingly, **3** also catalyzes the photochemical splitting of water into its elements[92] as well as the direct

synthesis of amides from alcohols and amines under H_2 liberation.[93] The closely related ruthenium(II) PNP pincer complex **5** was found to reversibly add alcohol substrates (**Figure 1.9B**). In a subsequent reaction, the addition product **6** can eliminate H_2 resulting in the oxidation of the alcohol substrate to the aldehyde oxidation state.[94] The manganese(I) complex **7** undergoes 1,2-addition to the C-O double bond of carbon dioxide to yield **8** (**Figure 1.9C**), which facilitates the catalytic hydrogenation of CO_2.[95] Similar reactivity was also observed with closely related ruthenium[91], rhenium[96], and iridium[97] complexes. Lastly, platinum(IV) complex **9** was observed to bind dioxygen by MLC to form alkyl peroxide **10** (**Figure 1.9D**).[98-100]

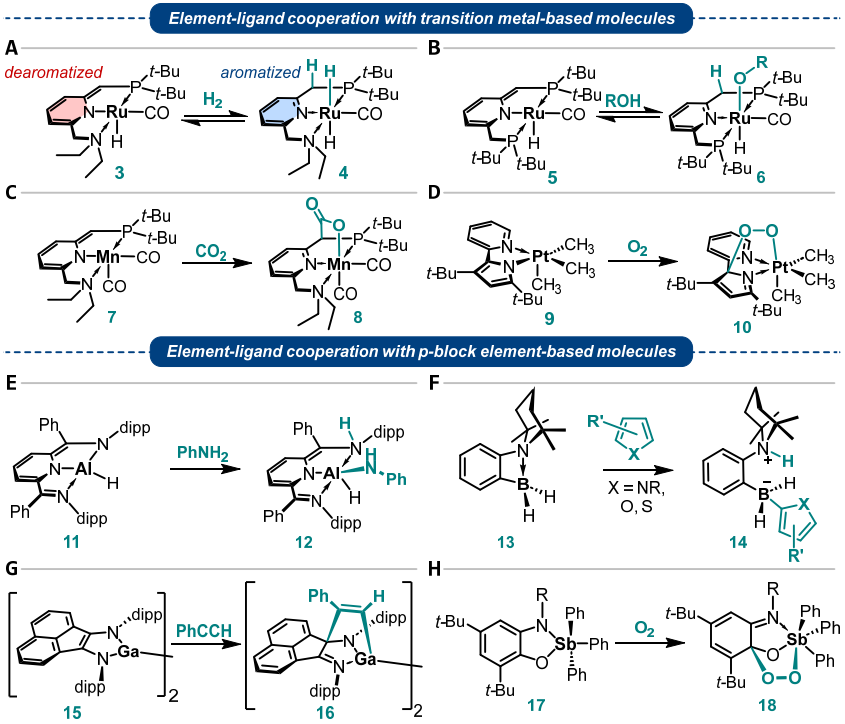

Figure 1.9: Element-ligand cooperativity (ELC). *Element-ligand cooperative reactivity of **A-D)** transition metal-based molecules and **E-H)** p-block atom-based molecules.*

The ELC chemistry of *p*-block atom-based molecules is probably the most developed for boron and aluminum compounds. It also is closely related to the chemistry of intramolecularly formed frustrated Lewis pairs (FLP), and the boundaries between the two fields can be blurred. Alane **11**, featuring a 2,6-bis(imino)pyridine ligand, activates the N-H bond of aniline to give addition product **12** (**Figure 1.9E**).[101] **11** also reacts with alcohols and carboxylic acids with a similar reaction mode (*cf.* **Figure 3.1**).[102] It further can function as a catalyst for the decomposition of formic acid into CO_2 and H_2.[103] In fact, when addition product **12** is exposed to elevated temperatures, it releases H_2. A prominent example for boron-ligand cooperativity is the C-H bond activation of heteroarenes with *ortho*-phenylene-linked aminoborane **13** (**Figure 1.9F**).[104] The addition product **14** can be treated with pinacolborane to yield the borylated arene and regenerate **13**. It was possible to combine the individual reaction steps to a catalytic cycle for the transition metal-free borylation of heteroarenes. Gallium-ligand cooperativity is much less investigated. FEDUSHKIN and coworkers observed that digallane **15** reversibly adds alkynes such as phenylacetylene, which they exploited for the catalytic hydroamination of the alkyne substrates to finally obtain imines (**Figure 1.9G**).[105-106] **15** also adds other unsaturated substrates like isocyanates or isothiocyanates.[107-108] O_2 addition, as it is possible with platinum complex **9**, is also feasible with an amidophenolato ligand at antimony(V) (**17**, **Figure 1.9H**).[109-110] The reaction is reversible and believed to proceed *via* single electron transfer steps to give alkyl peroxide **18**.

Within this dissertation, several additions to the field of aluminum- and gallium-ligand cooperativity are showcased (**Chapters 3.1** to **3.6**). They were achieved with the anionic calix[4]pyrrolato complexes of Al and Ga. The chemistry of calix[4]pyrroles, especially in combination with *p*-block elements, is now introduced in the following chapter.

1.6 Calix[4]pyrrole Chemistry

Meso-octamethylcalix[4]pyrrole (**19**) is a macrocyclic molecule featuring four pyrrole moieties which are linked by sp^3-hybridized carbon atoms (**Figure 1.10A**).[8, 10-11, 111-113] The substituents at these carbon atoms are defined to be in the *meso*-position, whereas the pyrrolic 3- and 4-positions are termed β-sites. **19** is closely related to porphin, the archetypical porphyrin, though, differs in the missing π-conjugation among the pyrrole rings. Due to a beaker-like conformation in the solid state when being cocrystallized with, *e.g.*, fluoride or chloride salts, the name calixpyrrole (lat. *calix* for chalice, beaker) was coined (**Figure 1.10B**).[10] Insertion of a number in brackets into the name allows for the specification of the amount of involved pyrrole moieties.

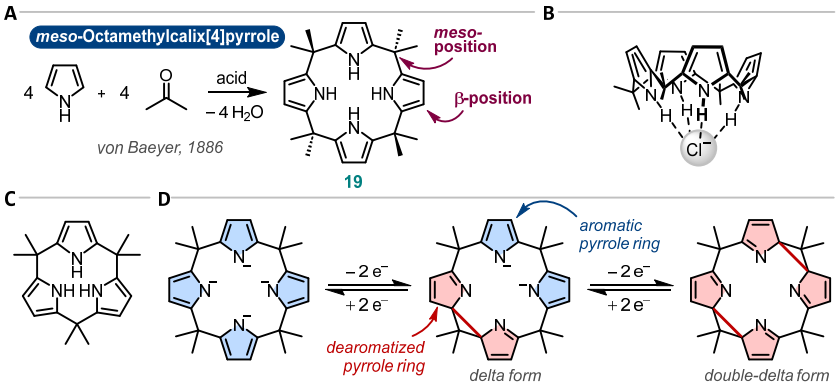

Figure 1.10: Calixpyrrole chemistry. ***A)*** *Synthesis of meso-octamethylcalix[4]pyrrole as it was discovered by* VON BAEYER *in 1886.* ***B)*** *Cone-like shape of meso-octamethylcalix[4]pyrrole when interacting with a chloride anion.* ***C)*** *Lewis structure of meso-hexamethylcalix[3]pyrrole.* ***D)*** *Redox reactivity of the meso-octamethylcalix[4]pyrrolato ligand.*

19 can easily be synthesized from pyrrole and acetone within one step *via* an acid-catalyzed condensation reaction (**Figure 1.10A**).[114-115] When different carbonyls are reacted with pyrrole, the *meso*-substituents can be modified readily.[12] However, calix[4]pyrroles with hydrogen atoms in the *meso*-positions are prone to oxidation yielding aromatic porphyrins. By use of 3,4-substituted pyrroles, the β-position can be varied.[116] Alternatively, the introduction of β-substituents after the calix[4]pyrrole synthesis is straightforward.[117] The chemistry of calix[4]pyrroles, is by far the most developed compared to that of the thermodynamically less favorable smaller and larger macrocycles. The synthesis of *meso*-hexamethylcalix[3]pyrrole (**Figure 1.10C**), for example, was only accomplished in 2021.[118-119]

Calix[4]pyrrolato ligands show redox activity.[120-123] Besides the fully reduced tetraanionic state, they can adopt the dianionic delta as well as the neutral double-delta form (**Figure 1.10D**). Each two-electron oxidation causes a C-C bond formation between two neighboring α-carbon atoms, leading to the formation of a cyclopropane ring and the dearomatization of the two pyrrol units. These redox processes were studied for a variety of calix[4]pyrrolato transition metal complexes, for example with iron or zinc as central atoms.[122-124]

Although, calix[4]pyrroles are discussed within the field of medicinal chemistry and drug development[113, 125-128], they were so far mainly applied either as binding agents for anions, ion pairs, or neutral substrates, or, in their deprotonated form, as ligands for transition metals[129-132], *f*-block elements[133-135], and only recently also for *p*-block elements (*vide infra*). The former research area is pioneered by the SESSLER group.[9, 11, 13, 136] They have, for example, designed various calix[4]pyrrole-based sensors for anions such as halides, phenolates, or phosphates. Their research activities mainly target environmental and biomedical questions. The chemistry of calix[4]pyrrolato ligands for transition metal complexes was expansively researched by FLORIANI and coworkers in the 1990s.[122, 137-138] Over the years, they have synthesized a brought assortment of complexes with a special focus on the modification of the calix[4]pyrrolato ligand framework.

After an early report on the aluminum(III) and tin(IV) complexes of the *meso*-octaethylcalix[4]pyrrolato ligand in *The Porphyrine Handbook*, which did not go beyond a brief mention[122], the *p*-block element chemistry of calix[4]pyrrolato ligands was initiated in 2018 in the GREB laboratory. Apart from the work presented herein, nine research papers[89, 139-146] on the *p*-block element chemistry of calix[4]pyrrolato ligands were published by this group by the time this chapter was written. Some of these papers were also recently summarized in a review article.[15] They are now briefly presented.

Tetraphenylphosphonium meso-octamethylcalix[4]pyrrolato aluminate ([PPh_4][**21**], **Figure 1.11A**) can be obtained by treating **19** with two equivalents of lithium aluminum hydride in 1,2-dimethoxyethane (DME).[140] This results in the formation of the lithium salt of the dianionic aluminum hydride ([$Li(dme)_2]_2$[**20**]). The exchange of the lithium against the tetraphenylphosphonium cation in CH_2Cl_2 causes the precipitation of LiCl and LiH and generates the free aluminate in good yield. The solid-state molecular structure of [**21**]$^-$ shows an essentially ideal square planar coordination of the central aluminum atom by its four N-substituents (**Figure 1.11B**). The N-Al-N angle is 179.7 °. The electronic structure of [**21**]$^-$ features an energetically low-lying p_z-type LUMO, almost exclusively located

at Al (**Figure 1.11C**). The HOMO is ligand-centered. This electronic structure impressively aligns with the statements made in **Chapter 1.2** of this dissertation. It thereby transports quantum chemical predictions made for the electronic structure of artificially planarized small *p*-block atom-based molecules, which certainly do not represent minima on the respective potential energy surfaces, to a molecule having a square planar-coordinated aluminum atom in its global minimum structure and which can be synthesized on multigram scale from commercially available starting materials within one week.[140]

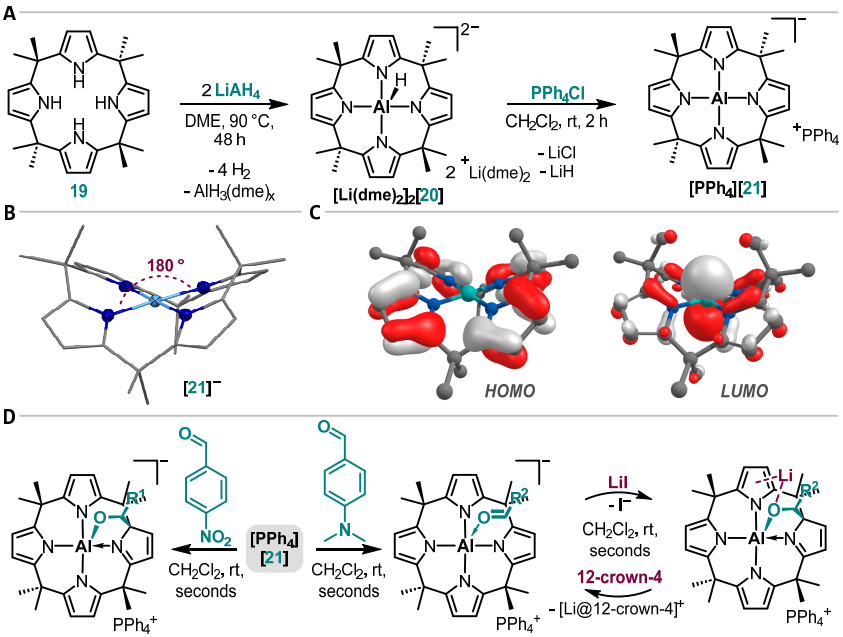

Figure 1.11: Synthesis, characterization, and reactivity of calix[4]pyrrolato aluminate. ***A)*** *Synthetic scheme for the preparation of tetraphenylphosphonium meso-octamethylcalix[4]pyrrolato aluminate ([PPh$_4$][21]).* ***B)*** *Molecular structure of the aluminate as determined by SCXRD analysis.* ***C)*** *Frontier Kohn-Sham molecular orbitals of [21]$^-$.* ***D)*** *Reactivity of [PPh$_4$][21] with carbonyl substrates.*

[**21**]$^-$ as well as its *meso*-octaethyl ([**34**]$^-$) and -cyclohexyl derivative[142] form adducts with tetrahydrofuran (THF) as donor of different stability. The disparities can be rationalized with differences in dispersive interactions and deformation energies.[142] Also, the fluoride adduct of [**21**]$^-$ was synthesized.[140] These reactivities document the tunable Lewis acidity of the calix[4]pyrrolato aluminates. They react as electron pair acceptors despite being negatively charged. Due to the presence of electron-rich pyrrole rings in close proximity to the Lewis acidic aluminum atom, they also engage in aluminum-ligand

cooperative reactivity with aldehyde and ketone substrates (*cf.* **Chapter 1.5**).[89] After activation of the carbonyl by the Lewis acidic aluminum center, a new C-C bond is formed between the 2-position of one of the ligand's pyrrole rings and the substrate (**Figure 1.11D**). This results in the dearomatization of the respective pyrrole moiety, which contrasts with, for example, the MILSTEIN systems. They undergo aromatization upon the metal-ligand cooperative reaction with a substrate. The addition reactions were found reversible in the sense of rapid substrate self-exchange reactions. They can be further tuned with the influence of the aluminate's counter cation to induce C-C bond formation or cleavage on-demand (**Figure 1.11D**). The switchable carbonyl binding modes were demonstrated to offer considerable rate control in hydroboration catalysis and actually allow for the faster conversion of *a priori* less reactive substrates.[89]

Calix[4]pyrrolato aluminates were also applied as *catalyst for the dehydropolymerization of phenylphosphine borane*.[145] Polymer molar masses of up to 43,000 Da were accessible. The reaction mechanism was studied experimentally and through quantum chemical simulations. A cooperative activation of the substrate's P-H bond by the aluminate was suggested. The discovered catalyst represents the first transition metal-free system for P-B dehydrocoupling.

Besides aluminum, also *silicon* was successfully incorporated into the calix[4]pyrrolato ligand.[139, 141] Starting out from the fully deprotonated ligand, hydridosilicate [**22**]$^-$ was synthesized using the *meso*-octamethyl ligand (**Figure 1.12A**).[139] As its tetraphenylphosphonium salt, [**22**]$^-$ was shown to be stable under ambient conditions, however, also reluctant against hydride abstraction to afford the free and neutral silane. The calculated hydride ion affinity is with 517 kJ mol^{-1} immense. Only by choosing the *meso*-octaethyl ligand, the free silane **24** became accessible.[141] The synthesis was accomplished *via* chloridosilicate [**23**]$^-$, from which chloride abstraction is possible with sodium tetrakis(pentafluorophenyl)borate (**Figure 1.12A**). Due to the square planar-coordinated silicon(IV) in **24**, the molecule shows remarkable features as for example agostic-type interactions between the ethyl groups and the central silicon atom, which are highly unusual for *p*-block atom-based molecules. It also undergoes silicon-ligand cooperative 1,2-addition of phenylacetylene (**Figure 1.12B**).[141]

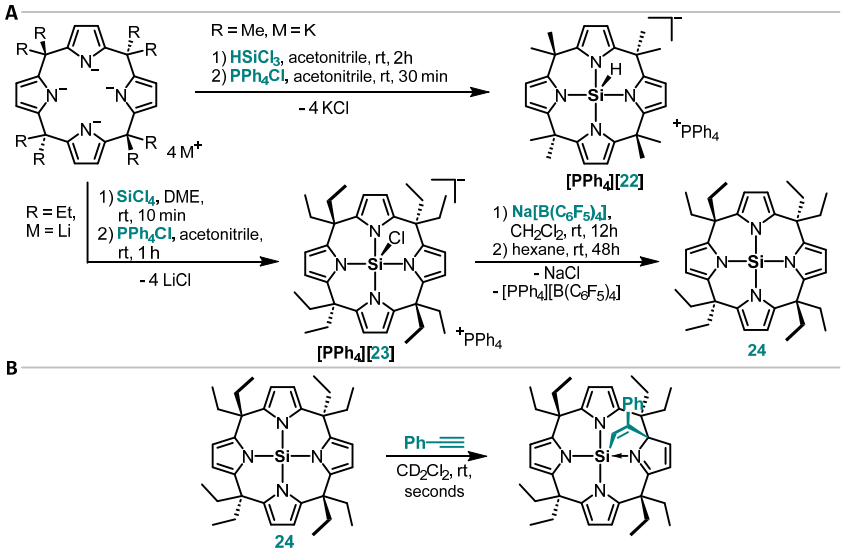

Figure 1.12: Synthesis and reactivity of calix[4]pyrrolato silane. ***A)*** *Synthetic scheme for the preparation of the corresponding meso-octamethylcalix[4]pyrrolato hydridosilicate and meso-octaethylcalix[4]pyrrolato silane.* ***B)*** *Silicon-ligand cooperative reactivity of the free silane with phenylacetylene.*

The *meso*-octaethylcalix[4]pyrrolato ligand was also combined with silicon's heavier homolog, *germanium*.[146] Bis-thf adduct **25** was synthesized from the tetra-potassium salt of the ligand and germanium(IV)iodide as Ge source (**Figure 1.13A**). Isolation of the thf-free germane was not possible, as both THF affinities were computed to be high (100 and 75 kJ mol^{-1}). Nonetheless, **25** was demonstrated to act as potent Lewis acid against donors such as chloride, fluoride, or hydride (**Figure 1.13B**). The experimentally observed fluoride abstraction from SbF_6^- was explained with a fluoride-coupled electron transfer mechanism to overcome the *per se* too low fluoride ion affinity compared to that of antimony pentafluoride (445 *versus* 495 kJ mol^{-1}). Like the calix[4]pyrrolato aluminate, **25** binds aldehydes in a metal-ligand cooperative manner (**Figure 1.13B**).[89, 146]

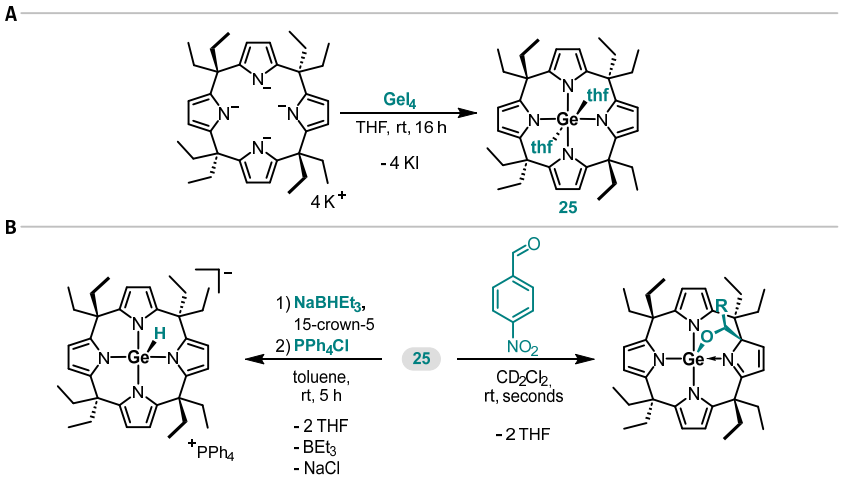

Figure 1.13: Synthesis and reactivity of a calix[4]pyrrolato germanium complex. *A)* *Synthetic scheme for the preparation of meso-octaethylcalix[4]pyrrolato germane as its bis-thf adduct.* ***B)*** *Reactivity with a hydride ion donor (left) and with 4-nitrobenzaldehyde (right).*

The chemistry of the *meso*-octaethylcalix[4]pyrrolato ligand of low-valent central atoms was developed so far for *tin(II)* and *antimony(III)*.[143-144] The dianionic calix[4]pyrrolato stannate(II) [**26**]$^{2-}$ can be synthesized from the fully deprotonated ligand and tin(II) chloride (**Figure 1.14A**).[143] The tin-centered lone electron pair was found to be a strong σ-donor. A Tolman electronic parameter (TEP) of 2032 cm^{-1} was calculated based on the Ni(CO)$_3$ complex of [**26**]$^{2-}$. For comparison, triphenylphosphine has a TEP value of 2069 cm^{-1}. Due to the strong σ-donor properties, [**26**]$^{2-}$ reacts with electrophiles such as benzyl chloride in nucleophilic substitution reactions to afford alkyl stannates (**Figure 1.14A**).[143]

The calix[4]pyrrolato antimonite(III) anion [**27**]$^{-}$ can be synthesized from the deprotonated ligand and antimony(III) chloride (**Figure 1.14B**).[144] It can be oxidized to the corresponding cationic stibenium(III) cation [**28**]$^{+}$ with ferrocenium hexafluorophosphate. As the central antimony atom remains in its +III oxidation state, the electrons for oxidation come from the ligand, which is transformed to its delta-form. [**28**]$^{+}$ was found to be stable against, *e.g.*, BF_4^-, and is therefore only a weak Lewis acid. Upon the addition of a Lewis base such as 4-dimethylaminopyridine, this stability rapidly vanishes, and decomposition reactions take place. This was explained with Lewis base-induced electromerism, which transfers two electrons from the central Sb(III) atom to the ligand restoring the initial calix[4]pyrrolato ligand by generating a Sb(V) center.[144]

Within the following chapters of this dissertation, the aluminum-ligand cooperative reactivity of calix[4]pyrrolato aluminates toward further substrates such as protic molecules[147], dioxygen[148], or nitrogen monoxide is presented. Also, the synthesis of calix[4]pyrrolato gallates and their reactivity is described.[149]

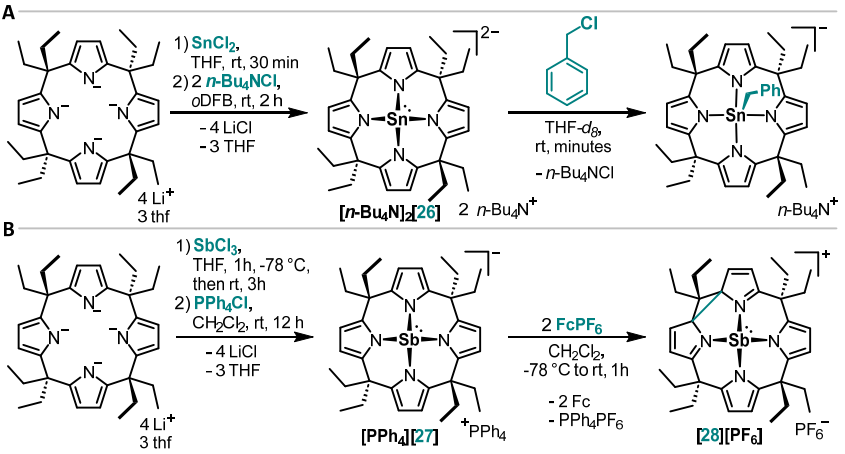

Figure 1.14: Synthesis and reactivity of tin and antimony calix[4]pyrrolato complexes. *Synthetic scheme for the preparation of* ***A)*** *meso-octaethylcalix[4]pyrrolato stannate(II) and its further reactivity with benzyl chloride and* ***B)*** *meso-octaethylcalix[4]pyrrolato antimonite(III) and its further reactivity with ferrocenium hexafluorophosphate.*

1.7 Machine Learning in Chemistry

Machine learning (ML) algorithms are a family of statistical models, that can be trained to perform dedicated tasks such as regression or classification. Of paramount importance for the success of ML is the underlying dataset, that is its size and quality. Depending on the availability of data, the task at hand, and the applied model architecture, dataset sizes of below 100 to up to billions of datapoints are employed.[150-151] Assessing the quality of the datapoints is a challenging task, which is impossible to accomplish in a fully comprehensive manner. In terms of chemistry-related datasets, uniform coverage of the chemical space, that is intended to be treated, is desirable. The coverage can be gauged by various methods, which, for example, rely on the distribution of occurring atoms, functional groups, structural characteristics, or of the target property, predicted by the ML algorithm. Deficiencies in dataset size or quality will bias resulting ML models, which must be analyzed carefully.

Generally, ML datasets for (small molecule) chemistry are often a collection of one or multiple molecular *features* characterizing the datapoint, *viz.* the molecule or material, and the target, which is typically denoted *label* (**Figure 1.15A**, left part). The label to be predicted can be of categorical (*e.g.*, active or inactive) or continuous (*e.g.*, an orbital energy) nature.

Regarding the features, there is a brought variety of molecular descriptors available. The cheminformatics software package *mordred*[152], for instance, provides the possibility to calculate more than 1,800 molecular descriptors. Examples are the acidic group count, the number of heavy atoms, or the hetero ring count (all obtainable from two-dimensional molecular representations) as well as the geometric radius or the partial negative surface area (obtainable from three-dimensional molecular representations). More elaborate features may come from quantum chemical simulations (orbital energies, partial atomic charges). Other features such as molecular fingerprints or graph representations are also available and are heavily used as inputs for statistical models.[153]

ML algorithms attempt to extract patters from the provided feature space such that the requested task can be carried out as accurately as possible. Models that predict concrete labels and which use those for training follow a *supervised learning* strategy (**Figure 1.15A**). This means that ML-generated target values can be compared to the true expected outcome, and the thereof obtained information is used to optimize the model during training. Architectures that are trained without labels operate in an unsupervised manner.

A typical example for *unsupervised learning* is clustering of the dataset into a certain number of groups (**Figure 1.15B**). Dimensionality reduction of feature spaces can also be done without supervision by provided ground truth labels.

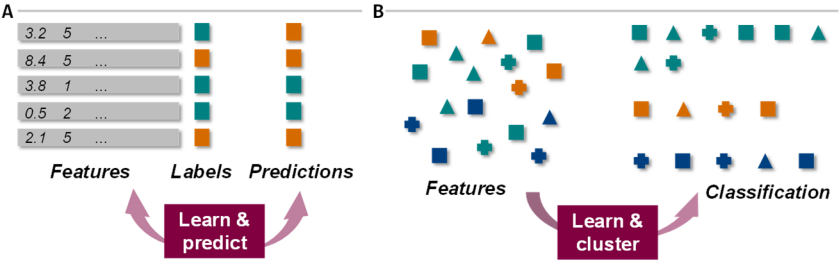

Figure 1.15: Machine learning paradigms. *Schematic illustration of **A)** supervised and **B)** unsupervised learning.*

There is a vast amount of different ML algorithms available and depending on dataset constitution as well as hardware and time availability, one must carefully decide which model is most suitable. It is possible to use a collection of models and combine the individual outputs to the final prediction. Also, there are many techniques that can assist in model selection as well as in the construction of data preprocessing pipelines.[154]

Examples for ML algorithms are the family of linear models (ordinary least squares linear regression and its regularized variations, Bayesian regression), kernel-based methods (kernel ridge regression, support vector machines) and decision tree-related architectures (random forests). Besides the mentioned examples, there is another category of ML models, which is generally referred to as *deep learning*. Deep learning algorithms are based on *artificial neural networks* (ANN). ANNs have a layered structure, and each layer is composed of neurons which serve to transform provided features in a typically non-linear fashion by making use of neuron connection-specific weights and a neuron-specific bias (**Figure 1.16**). By doing so, they learn features during training which are relevant for the task, and which are ultimately used for the predictions. The feature extraction and label prediction job are simultaneously optimized through back propagation. At first, data is passed forwardly through the ANN. Secondly, the weights and biases are updated such that an initially defined loss function, which compares obtained and expected outputs, is minimized.[154-155]

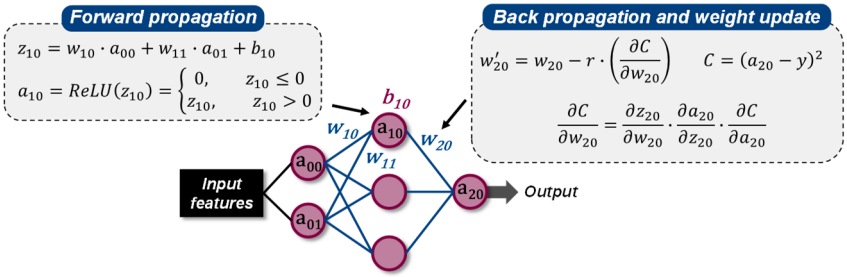

Figure 1.16: An artificial network of neurons. *Schematic structure of an artificial neural network and its functional operations (forward and back propagation and the update of weights and biases with help of the chain rule). z_{xy}: pre-activation of a given neuron, a_{xy}: output value (activation) of a given neuron, w_{xy}: weight value, b_{xy}: bias value, r: learning rate, C: cost (squared error in the chosen example), y: ground truth, ReLU (example for a neuron activation function): rectified linear unit; ReLU(z) = max(0, z).*[155]

Graph neural networks (GNN) are a special form of neural networks that accept feature input in graph data structure. Due to that, GNNs are ideally suited for applications in chemistry.[156] Molecules are perceived as graphs in which the atoms are the nodes and the bonds the edges of the graph.[153] Node and edge features allow to describe the graph in terms of chemical descriptors (**Figure 1.17**). Typical node features are atom type, hybridization, number of rings the atom is part of, or the chiral tag. Examples for edge features are the bond order, or whether it is part of a ring or not. It is also possible to use more elaborate feature, *e.g.*, from quantum chemical simulations (atomic partial charges, Wiberg bond orders, *etc.*). Importantly, GNNs can be constructed to make predictions on the node (for each atom), edge (for each bond), or graph (for the molecule as such) level.

GNNs and ML models in general are widely employed in chemical applications, and it is beyond this chapter to give a full survey of use cases.[157-167] A prominent research area to which statistical model are heavily applied is medicinal chemistry, in particular drug design.[168] GNNs can also serve as ML potentials for structural optimization and vibrational analyses of small molecules.[169-171] The PATON group developed GNNs to predict ^{1}H and ^{13}C NMR chemical shifts (node level predictions)[172] as well as models for bond dissociation energies[173-174] (edge level predictions). Estimators for MAYR's nucleophilicity parameter were built based on GNN architectures.[175] They were also used to predict reaction outcomes from the reactants, added reagents, and used solvents.[176] Considerable research effort is also invested into explaining the output of GNN models.[177]

Within the described work, GNNs were used to build FIA (*cf.* **Chapter 1.4**) regression models for *p*-block atom-based molecules with the help of the *nfp* Python package.[178] (*cf.* **Chapter 3.12**). Generally, GNNs function by learning the representation of atom and bond

states in order to perform, for example, the molecule-level regression task as accurately as possible.[156] Within the GNNs presented herein, initial atom and bond embeddings were obtained from tokenized node and edge features, respectively (**Figure 1.17**). This simply means to label a set of features with a categorical integer during preprocessing which then is passed to the GNN. Instead of tokenization, one-hot-encoding could also be used. The model expands the provided tokens into a higher dimensional vector. These vectors are continuously update in a so-called *message-passing* step based on atom connectivities.[156] Message-passing means that the embedding vectors of adjacent nodes or edges are mathematically combined with that of the currently treated node or edge to obtain an updated embedding vector. There are different options for the combination of multiple embedding vectors. One example is a weighted sum of the embedding of the currently treated position and all embeddings of the neighbors. The message-passing mechanism transmits information across the molecular graph allowing to obtain environment-aware representations. Typically, less than ten rounds of message-passing are carried out. At the end of each round, the individual embedding vectors are pooled to obtain a single graph embedding. Again, different pooling procedures have been developed. Ultimately, the graph embedding vector can be fed through a read-out network having a single neuron as its final building block. This neuron is performing the actual regression task.[178]

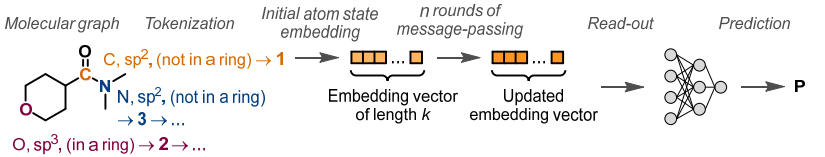

Figure 1.17: Message-passing graph neural networks for the prediction of molecular properties. *The assigned atom features are transformed into integer tokens (1, 2, and 3 in this example) which are used to obtain initial k-dimensional embedding vectors. These are updated during n rounds of message-passing, and the final graph embedding vector is fed to a read-out neural network which predicts the target property P. The same procedure can be executed for bonds, and the atom and bond embedding vectors can be combined to obtain the graph embedding.*

2 MOTIVATION AND OBJECTIVES

The main objective of the doctoral project described herein was to gain further knowledge on *p*-block atom-based molecules. One of the key concepts to describe the reactivity of this class of compounds is *Lewis acidity*. A Lewis acid is defined as an electron pair acceptor, and therefore, various conceptual handles have been developed to increase the electron acceptor propensity of respective molecules. Besides the installment of strongly electron withdrawing substituents, *structural constraint* arose as a powerful tool to render *p*-block atoms in their natural, that is, highest oxidation state increasingly Lewis acidic.

To shed light on the vast field of *p*-block element chemistry with respect to structural constraint and flexibility in an as rich as possible manner, the application of *experimental* and *applied quantum chemical* techniques was planned. In fact, later in the project, it was decided to expand this dual approach by another facet which is *data-driven chemistry* and *machine learning*. The obtained results of the three individual methodologies, all hosted under the unifying roof of Lewis acidity, are presented in the following chapter – beginning with the experimental work, followed by the quantum chemical simulations, and finally the contributions to chemical data sciences.

Prior to the start of this doctoral program, the macrocyclic tetradentate *calix[4]pyrrolato ligand* was used to incorporate an aluminum(III) atom in a structurally constrained, square planar coordination environment (**Figure 2.1A**).[140] The potential of the obtained aluminate to react by means of *aluminum-ligand cooperativity* due to the Lewis acidity of the central aluminum atom was discovered and initially investigated for carbonyl substrates.[89] The aim was to further expand the substrate range of the calix[4]pyrrolato aluminates, for example, to protic functional groups or to molecules with bonds between two heteroatoms (O-O, N-O). At the same time, it was desired to widen the scope of the calix[4]pyrrolato ligand to gallium, the heavier homolog of aluminum. After successful synthesis of calix[4]pyrrolato gallates, it was intended to study their properties and reactivity and compare the results to the findings made for the aluminates.

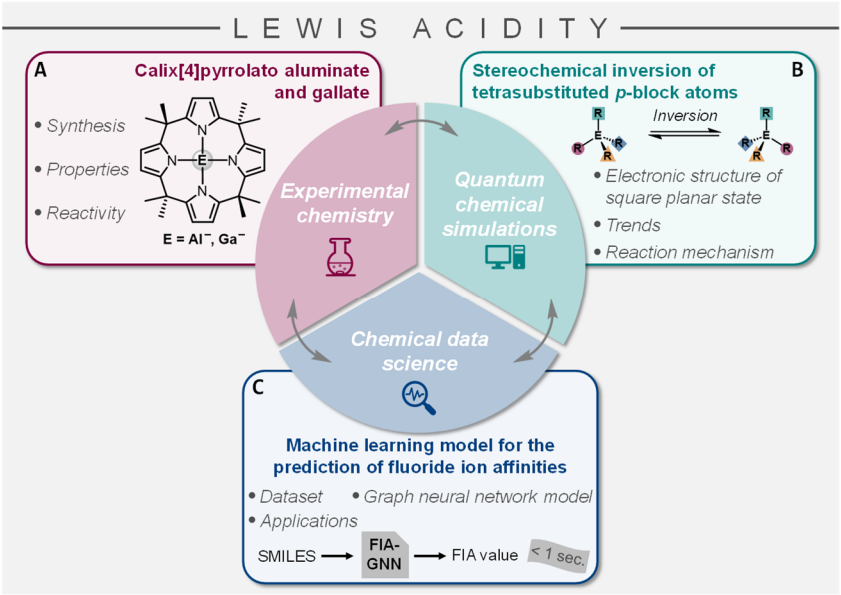

Figure 2.1: The objectives of this dissertation.

Paralleling the experimental work on square planar *p*-block atoms, it was aimed for a comprehensive understanding of the stereochemical inversion process of tetrasubstituted *p*-block atoms with the help of quantum chemical simulations (**Figure 2.1B**). The electronic structure in the square planar state, which is a possible transition structure for the stereoinversion process, should be examined in detail. Trends should be uncovered and alternative stereoinversion mechanisms were to be investigated.

Ultimately, the compilation of a large dataset of fluoride ion affinities of *p*-block atom-based molecules was sought (**Figure 2.1C**).[68] Computational routines for the complete automation of the data generation process should be devised and applied. It was planned to extract qualitative information on Lewis acidity in general from the data. Lastly, the development and application of machine learning models for the prediction of the affinity values, without the need for quantum chemical simulations, was pursued.

3 RESULTS AND DISCUSSION

3.1 Reactivity of Calix[4]pyrrolato Aluminate with Protic Substrates

The results presented within this chapter were previously published and can be found under: L. M. Sigmund and L. Greb, "Reversible OH-bond activation and amphoterism by metal-ligand cooperativity of calix[4]pyrrolato aluminate", Chem. Sci. ***2020****, 11, 9611-9616. This chapter was written based on the mentioned publication.*

Introduction and background

In advance to the research work of the herein presented doctoral project, the aluminum-ligand cooperative addition of alcohol substrates to *meso*-octamethylcalix[4]pyrrolato aluminate ([**21**]$^-$) was discovered.[179] It was focused on the oxidative transformation of the alcohols to carbonyl compounds in an acceptorless manner, that is, under the liberation of H_2. Indeed, oxidation to aldehydes and ketones was observed, though in a non-catalytic fashion. It was then focused on a detailed understanding of the reactivity of [**21**]$^-$ with protic substrates, especially on the reversibility of the observed addition reaction. The obtained results are presented in this chapter.

The element-ligand cooperative (ELC) addition of alcohols is a widely studied subject, both in transition metal and *p*-block element chemistry (**Figure 3.1**). In extension to the examples mentioned in the introduction (*cf.* **Chapter 1.5**), the MILSTEIN group found a 1,2-dihydrodiazaborolopyridine capable of adding benzoic acid through boron-ligand cooperativity.[180] BERBEN and coworkers observed aluminum-ligand cooperative addition of phenol, benzyl alcohols[102], water[181], and formic acid[103] to a bis(imino)pyridine-ligated aluminum hydride (**Figure 3.1A**).[182] Further examples of aluminum-based cooperative OH-addition reactions were provided by FEDUSHKIN[183] and ZHU.[184] The formal oxidative addition reaction of alcohols to a phosphorous(III) atom, likely assisted by ELC, was reported for structurally constrained systems by GOICOECHEA[185] and DOBROVETSKY.[186]

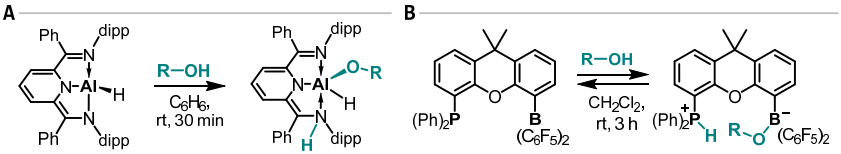

Figure 3.1: Examples for element-ligand cooperative addition of alcohol substrates.

The above listed examples all feature the irreversible addition of the O-H bond. Observations of reversible alcohol activation by ELC or closely related reaction modes are much less common. Examples are a xanthene-derived B/P frustrated Lewis pair published by VASKO *et al.* (**Figure 3.1B**)[187] and a structurally constrained tris(amido) phosphorous(III) system.[188]

Alcohol addition reaction and product characterization

The reaction of [PPh_4][**21**] with one equivalent of an alcohol substrate in CD_2Cl_2 at room temperature resulted in an immediate color change from colorless to yellow. A large variety of protic substrates was found suitable for the addition reaction including primary, secondary, and tertiary alkyl and benzyl alcohols, *para*-bromophenol, and interestingly also the more acidic benzoic acid (**Figure 3.2A**). Additional functional groups, such as a nitro or methoxy group, were tolerated. Remarkably, [**21**]$^-$ withstood a large excess of more than 50 equivalents of isopropanol and did not succumb to alcoholysis. The central aluminum atom remained within the calix[4]pyrrolato ligand, and the free and protonated ligand was not detectable by ^{1}H NMR spectroscopy.

To obtain information on the structure of the formed products, ^{1}H NMR spectroscopy was applied (**Figure 3.2C**). The formation of a new C_1 symmetric species with eight chemically inequivalent methyl groups, one dearomatized and three aromatic pyrrole rings, and one bound alkoxy substituent was detected. The observed splitting pattern in the ^{1}H NMR spectra and the cross-peaks in the ^{1}H,^{1}H COSY NMR spectra strongly suggest the transfer of the alcohol proton to the 2-position of one of the pyrrole rings. Unambiguous evidence for the aluminum-ligand cooperative reaction pattern was obtained from SCXRD measurements of the *para*-bromophenol addition product ([PPh_4][**29**], **Figure 3.2B**). In the solid-state structure, the aluminum atom resides in a significantly distorted square pyramidal coordination environment with the *para*-bromophenolato ligand in apical position. The Al-O bond length is 179.1(2) pm. The average bond length of the Al-N bonds that originate from the aromatic pyrrole rings in [**29**]$^-$ is 194.1(2) pm. By contrast, the nitrogen atom of the dearomatized pyrrole ring bearing the former alcohol proton is

separated from the central aluminum atom by 202.1(3) pm. Together with the C-C and C-N distances in this ring, the conceptual picture of dearomatization, as well as the switch in Al-N binding mode from a polar covalent bond to a rather dative interaction upon alcohol addition, is supported.

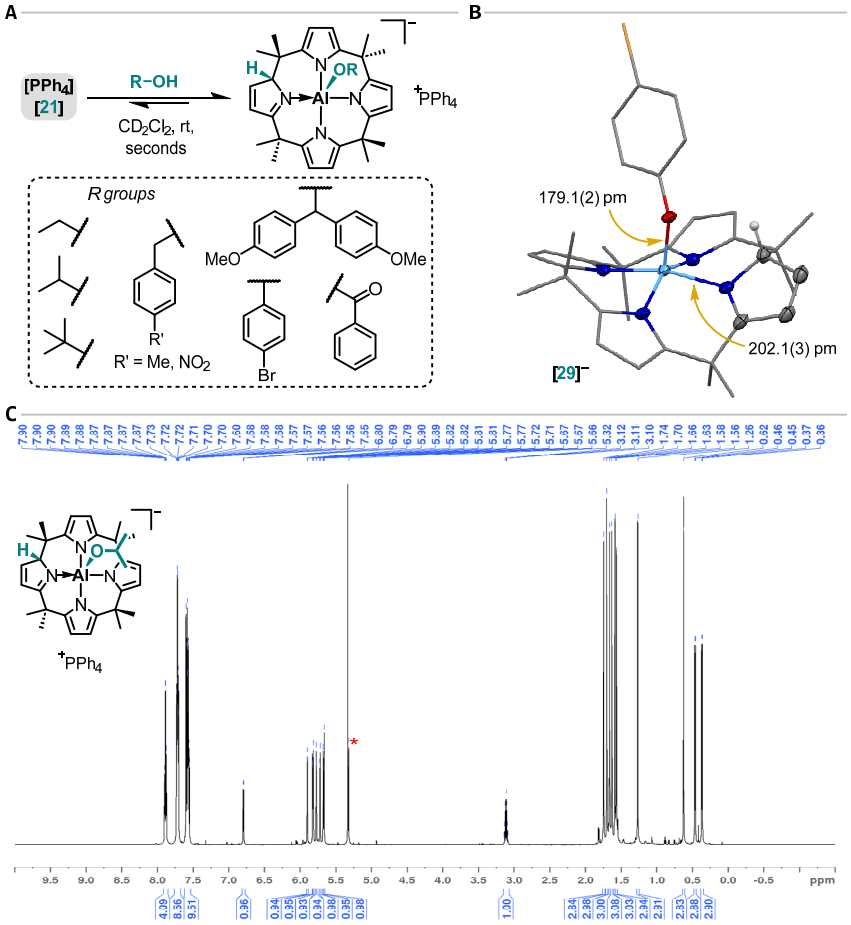

Figure 3.2: Reactivity of calix[4]pyrrolato aluminate with protic substrates. ***A)*** *Synthetic scheme and substrate scope.* ***B)*** *Solid-state molecular structure of the addition product of para-bromophenol as found by SCXRD analysis. The counter cation, cocrystallized solvent molecules, and the hydrogen atoms except for the one which was transferred to the ligand backbone are omitted. Thermal displacement ellipsoids are presented at a probability level of 50%. CSD identifier: YUXVEV.* ***C)*** *^{1}H NMR spectrum (600 MHz, CD_2Cl_2, 295 K) which was obtained when one equivalent of isopropanol was added to [PPh_4][21]. The signal of $CHDCl_2$ and of residual CH_2Cl_2 is marked with a red asterisk.*[147]

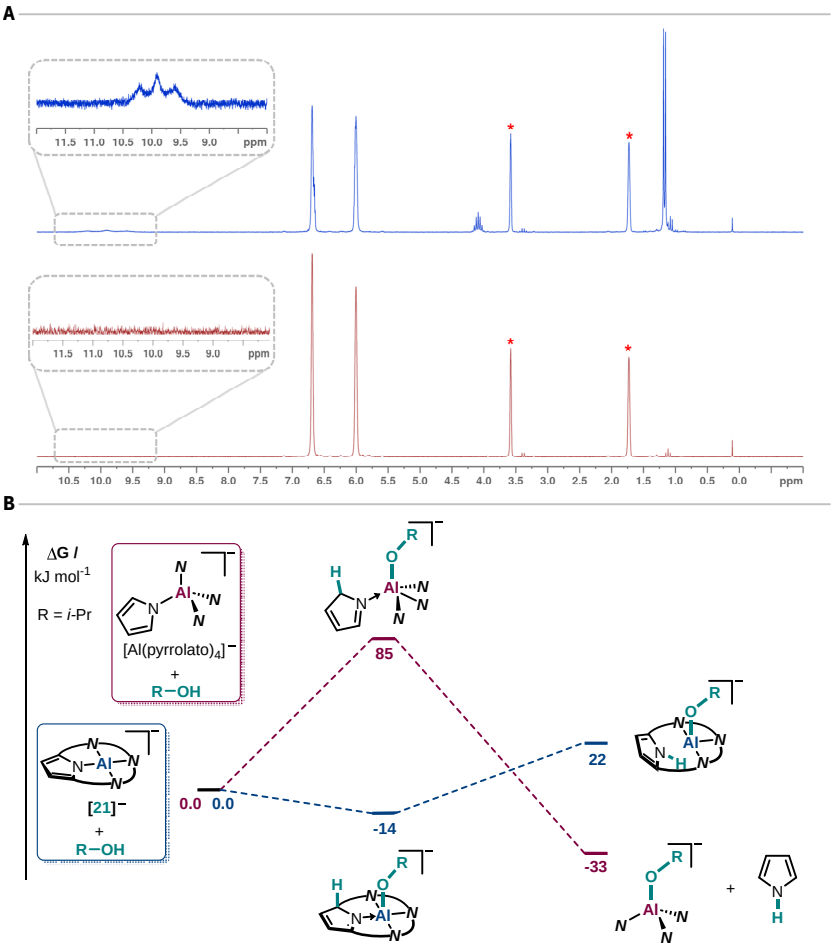

Figure 3.3: Reactivity of tetrapyrrolato aluminate with isopropanol. ***A)*** *^{1}H NMR spectrum (200 MHz, THF-d_8, 295 K) of [Li][Al(pyrrolato)$_4$] (bottom) and after addition of isopropanol (top). The signals of THF-d_7 are marked with red asterisks.* ***B)*** *Comparison of the reactivity of meso-octamethylcalix[4]pyrrolato aluminate and tetrapyrrolato aluminate with isopropanol using DFT (PW6B95-D3(BJ)/def2-QZVPP, COSMO-RS(CH$_2$Cl$_2$)//PBEh-3c).*[147]

To set the discovered alcohol additions into perspective, the reaction of tetrapyrrolato aluminate, which features four unconnected pyrrolato groups and therefore has an effective tetrahedral ground state structure, with isopropanol was examined. Tetrapyrrolato aluminate as its lithium salt was prepared by DR. FABIAN EBNER following a modified procedure taken from the patent of WHITNEY and KLEMANN.[189]

After isopropanol addition at room temperature using THF-d_8 as solvent, the instantaneous appearance of the characteristic NH-triplet signal of free pyrrole at around 10 ppm in the ^{1}H NMR spectrum was found (**Figure 3.3A**). There was no sign of cooperative proton transfer to the 2-position of a pyrrole ring. This difference compared to the reactivity of [PPh_4][**21**] with isopropanol is nicely mirrored by DFT calculations (PW6B95-D3(BJ), COSMO-RS(CH2Cl2)//PBEh-3c, was also used to get all below mentioned computational results). The cooperative addition of isopropanol to the tetrapyrrolato aluminate anion is endergonic by 85 kJ mol^{-1} (**Figure 3.3B**). However, the analogous addition to [**21**]$^-$ is exergonic by 14 kJ mol^{-1}. Consequently, tetrapyrrolato aluminate cannot bind isopropanol through aluminum-ligand cooperativity and instead undergoes pyrrole elimination which is overall exergonic (−33 kJ mol^{-1}). In contrast, the typically observed O-H-bond splitting across the aluminum-nitrogen bond within [**21**]$^-$ brings a thermodynamic disadvantage of more than 35 kJ mol^{-1} (relative to the observed species) and hence is not found experimentally.

Reversibility of the addition reaction

All alcohol substrates which were tested underwent quantitative and instantaneous addition to [**21**]$^-$ at room temperature, except for *tert*-butyl alcohol. A mixture of free and bound substrate, with the bound form being clearly favored, was obtained. It was possible to influence the equilibrium by temperature. Variable temperature ^{1}H NMR spectroscopy was used to determine the thermodynamic parameters by construction of a van't Hoff plot (**Figure 3.4**). The addition reaction is exothermic by −37 and exergonic by −16 kJ mol^{-1}. This is in reasonable agreement with the DFT-calculated values (ΔH_r = −48 kJ mol^{-1}, ΔG_r = 2 kJ mol^{-1}). In general, the O-H-bond additions to [**21**]$^-$ are calculated to be exergonic by −14 down to −50 kJ mol^{-1}.

Besides influencing the equilibrium of the *tert*-butyl alcohol addition by temperature, it was also possible to completely reverse the alcohol binding by vacuum application. The exposure of a mixture of [PPh_4][**21**] and *tert*-butyl alcohol in tetrachloroethane-d_2 to reduced pressure at room temperature for 90 min resulted in the disappearance of the ^{1}H NMR signals of the free substrate and the addition product. Instead, the free aluminate was regenerated, which demonstrates the full reversibility of the alcohol addition to [**21**]$^-$.

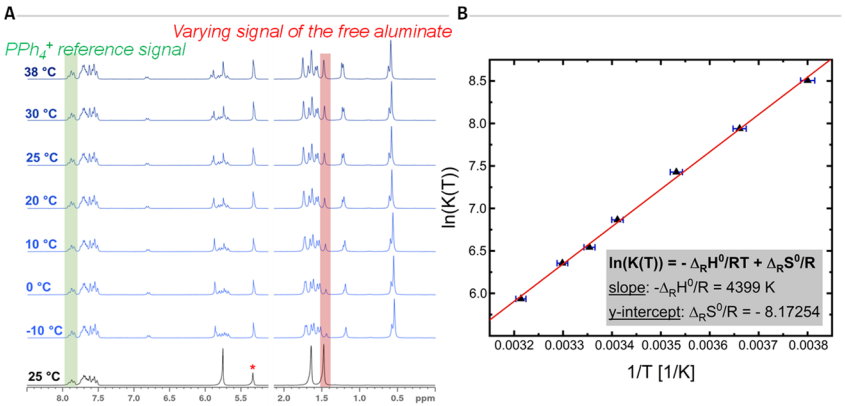

Figure 3.4: Analyzing the thermodynamics of the *tert*-butyl alcohol addition to calix[4]pyrrolato aluminate. ***A)*** *^{1}H NMR spectra acquired at variable temperatures (200 MHz, CD_2Cl_2). The signal of $CHDCl_2$ and that of residual CH_2Cl_2, which is contained in [PPh_4][21], is marked with a red asterisk. The spectrum shown in black at the bottom is that of free [PPh_4][21].* ***B)*** *Van't Hoff plot for the addition/elimination equilibrium derived from the NMR spectroscopic measurements.*[147]

EXSY NMR measurements

To further study the observed reversibility of the addition reaction of alcohols to the aluminate, [PPh_4][**21**] was examined in the presence of an excess of isopropanol through ^{1}H,^{1}H exchange NMR spectroscopy (^{1}H,^{1}H EXSY) in CD_2Cl_2 as solvent. Chemical exchange cross-peaks between bound and free isopropanol were found in the spectrum, thus proving the aluminum-ligand cooperative addition to be a dynamic, low-barrier process.

To investigate the mechanism of the self-exchange, samples with varying excesses of isopropanol were investigated with ^{1}H,^{1}H EXSY at room temperature. The obtained data strongly suggests a dissociative mechanism for the self-exchange of alcohols at [**21**]$^-$. The overall rate constant for the release of isopropanol from [**21**]$^-$ was found to be constant irrespective of the amount of excess isopropanol. It was determined to 0.122 s^{-1}. This corresponds to a Gibbs free activation energy for the elimination of isopropanol of 78 kJ mol^{-1}. The respective DFT-computed value is 63 kJ mol^{-1}, which is in acceptable agreement.

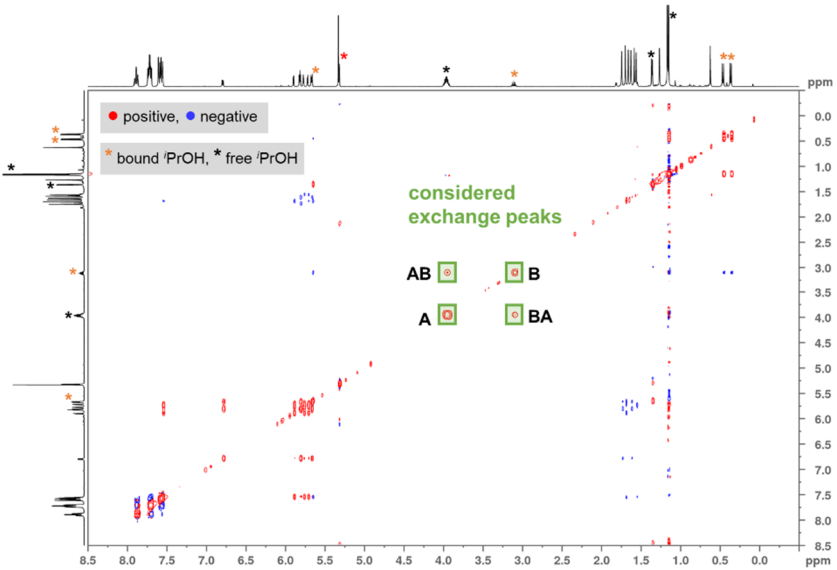

Figure 3.5: **^{1}H,^{1}H NMR EXSY to study the self-exchange of isopropanol at calix[4]pyrrolato aluminate.** *Exemplary ^{1}H,^{1}H NOESY NMR spectrum (400 MHz, CD_2Cl_2, 295 K, d1 = 20 s, d8 = 2 s) which was acquired for the NMR EXSY experiments. The signal of $CHDCl_2$ and that of residual CH_2Cl_2, which is contained in [PPh_4][21], is marked with a red asterisk.*[147]

Deuterium labeling experiments

Next, the alcohol addition process was elucidated with a deuterium-labeled substrate. For that, [PPh_4][**21**] was reacted with 1.7 equivalents of ethanol-*d*$_1$ (OD instead of OH group) in CD_2Cl_2 at room temperature. Immediately after the reaction was started, the mixture was analyzed by ^{1}H NMR spectroscopy. As expected, the obtained spectrum showed the characteristic signals of the known ethanol addition product; however, there was also a singlet resonance at 5.60 ppm, which is the exact chemical shift of the *proton* which was transferred to the 2-position of a pyrrole ring. The singlet signal grew over time (**Figure 3.6A**), along with the concomitant decrease of all pyrrolic β-proton signals. Hence, it is assumed that the β-positions serve as proton source. Indeed, the ^{2}H NMR spectrum of a sample of [PPh_4][**21**] and ethanol-*d*$_1$ in CH_2Cl_2 matches the ^{1}H NMR resonances of the aromatic region (β-protons) including the transferred proton in the α-position (**Figure 3.6B**). The addition of an excess amount (36 equivalents) of ethanol-*d*$_1$ to [PPh_4][**21**] allowed a degree of deuteration of up to 76% after 24 hours at room temperature. This was found by mass spectrometric investigations (**Figure 3.7**).

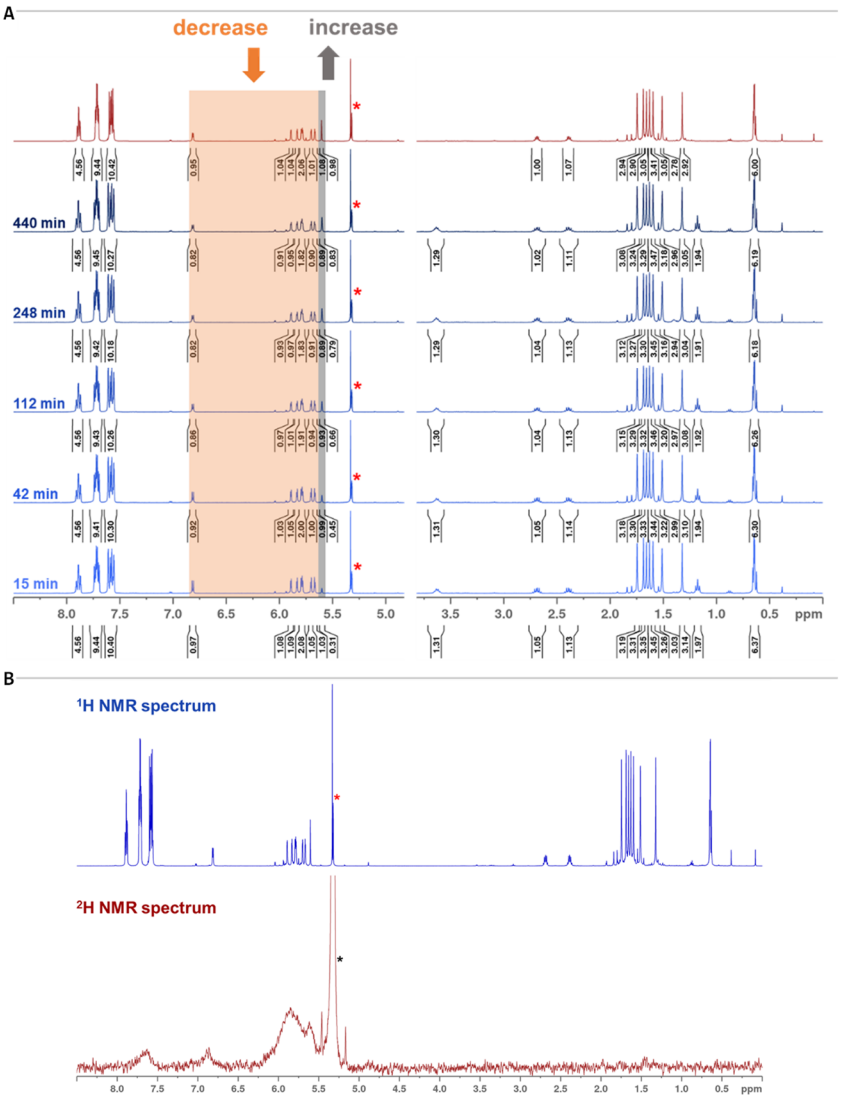

Figure 3.6: **Deuterium labeling within calix[4]pyrrolato aluminate investigated by NMR spectroscopy.** ***A)*** *^{1}H NMR spectra (400 MHz, CD_2Cl_2, 295 K) of a sample of $[PPh_4][21]$ treated with ethanol-d_1. The given times are the elapsed time after ethanol-d_1 addition. Red spectrum: ^{1}H NMR spectrum of the addition product of ethanol to $[21]^-$ for comparison. The signal of $CHDCl_2$ and that of residual CH_2Cl_2, which is contained in $[PPh_4][21]$, is marked with a red asterisk. This spectrum is also shown in the upper part of section B.* ***B)*** *^{2}H NMR spectrum (92 MHz, CH_2Cl_2, 295 K) of $[PPh_4][21]$ treated with a slight excess of ethanol-d_1 (bottom). To the sample was added 0.5 µL CD_2Cl_2 (black asterisk) as reference.*[147]

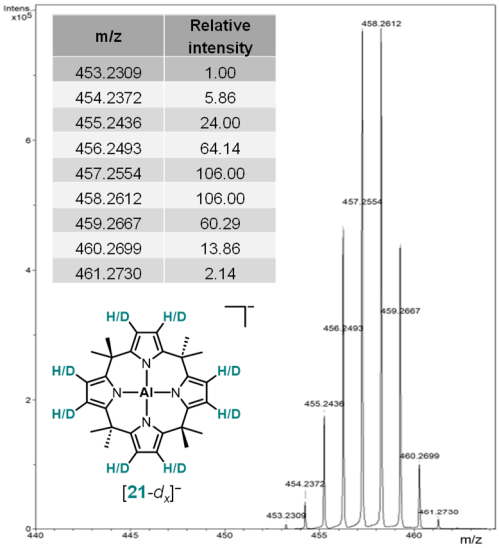

m/z	Relative intensity
453.2309	1.00
454.2372	5.86
455.2436	24.00
456.2493	64.14
457.2554	106.00
458.2612	106.00
459.2667	60.29
460.2699	13.86
461.2730	2.14

453.2309: 1.00 – 0 =							1.00
454.2372: 5.86	– **0.303** · 1.00 =						5.5570
455.2436: 24.00	– **0.303** · 5.5570	– **0.044** · 1.00 =					22.2722
456.2493: 64.14	– **0.303** · 22.2722	– **0.044** · 5.557	– **0.004** · 1.00 =				57.1430
257.2554: 106.00	– **0.303** · 57.1430	– **0.044** · 22.2722	– **0.004** · 5.5570 =				87.6835
458.2612: 106.00	– **0.303** · 87.6835	– **0.044** · 57.1430	– **0.004** · 22.2722 =				76.8285
459.2667: 60.29	– **0.303** · 76.8285	– **0.044** · 87.6835	– **0.004** · 57.1430 =				32.9243
460.2699: 13.86	– **0.303** · 32.9243	– **0.044** · 76.8285	– **0.004** · 87.6835 =				0.1527
461.2730: 2.14		– **0.044** · 32.9243	– **0.004** · 76.8285 =				0.3840
[21-d_0]⁻ :	[21-d_1]⁻ :	[21-d_2]⁻ :	[21-d_3]⁻ :	[21-d_4]⁻ :	[21-d_5]⁻ :	[21-d_6]⁻ :	[21-d_7]⁻ : [21-d_8]⁻
0.0 :	0.0 :	1.0 :	5.6 :	22.3 :	57.1 :	87.7 :	76.8 : 32.9
0.0% :	0.0% :	0.4% :	2.0% :	7.9% :	20.2% :	30.9% :	27.1% : 11.6%

Figure 3.7: Deuterium labeling within calix[4]pyrrolato aluminate investigated by mass spectrometry. *The grey box at the bottom shows how the monoisotopic contributions to the signals of the spectrum due to the isotope pattern of the 28 carbon atoms within [21]⁻ were calculated to obtain the relative ratios of the deuterated derivatives. For 28 carbon atoms, the isotope pattern scales with 1.000 : 0.303 : 0.044 : 0.004.*[147]

Further reactivity of the alcohol addition products

Lastly, an additional facet of the alcohol addition chemistry of [**21**]$^-$ was discovered which is presented with ethanol as example substrate (**Figure 3.8**). As the C_2H_5OH addition product ([PPh_4][**30**]) was prepared in 1 mL of CH_2Cl_2, and 5 mL of *n*-pentane were added, the expected addition product (*cf.* **Figure 3.2A**) precipitated as yellow solid, as determined by ^{1}H NMR spectroscopy. However, when the suspension was allowed to stand at ambient temperature for multiple days, the precipitate almost entirely redissolved, and orange crystals developed at the bottom of the reaction vessel. The obtained crystals were used to determine the atom connectivity by SCXRD analysis, identifying the crystalline material as the dianionic ethanolato complex of [**21**]$^-$ ([**32**]$^{2-}$, **Figure 3.8B**). The proton which had been transferred to the ligand backbone in the first reaction step is now absent. The Al(III) center is in a square pyramidal N_4O coordination environment.

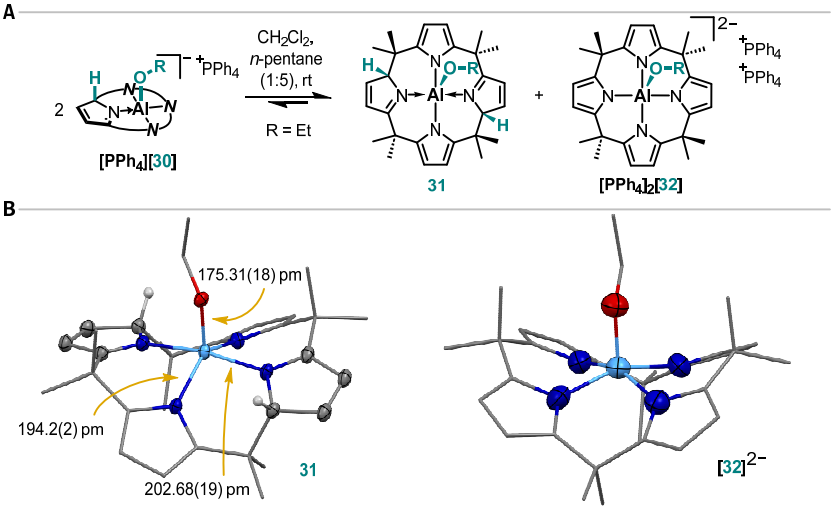

Figure 3.8: Amphoterism of calix[4]pyrrolato aluminate. ***A)*** *Autoprotolysis equilibrium of the ethanol addition product, enforced by a nonpolar solvent.* ***B)*** *Molecular structures as determined with SCXRD analysis of the autoprotolysis reaction products (left: neutral, right: dianionic). The counter cations, cocrystallized solvent molecules, and all hydrogen atoms except for the protons transferred to the ligand backbone are omitted. Thermal displacement ellipsoids are shown at the 50% probability level. CSD identifier: YUXVIZ. For the right structure, only atom connectivities were determined due to poor data quality.*[147]

The fate of the missing proton became clear from the SCXRD analysis of crystals grown from the supernatant of the exact same sample. The second species is the neutral, protonated ethanol addition product **31**. It is effectively C_2 symmetric, with two protonated, dearomatized pyrrole rings opposite to each other. This means the alcohol addition products to [**21**]$^-$ are the subject of a solvent polarity-dependent autoprotolysis process which demonstrates their amphoteric character.

Therefore, the acid/base chemistry of the alcohol adducts was considered (**Figure 3.9**). Successive addition of *para*-bromophenol to its calix[4]pyrrolato aluminate addition product ([**29**]$^-$) in CD_2Cl_2 at room temperature led to the increased formation of the neutral compound **33**. Even a weak Brønsted acid such as *para*-bromophenol is sufficiently acidic to protonate the initially formed species. In turn, it was expected that the addition of a Brønsted base to the initial alcohol activation products would induce deprotonation and the formation of the dianionic species. However, this was not observed. The treatment of the ethanol addition products in CD_2Cl_2 with an excess of pyridine at room temperature resulted in the quantitative substitution of the alcohols and the formation of the classic Lewis-acid-Lewis-base adduct, as observed by ^{1}H NMR spectroscopical measurements (**Figure 3.9**). An analogous replacement was possible with dimethyl sulfoxide as a substitution agent.

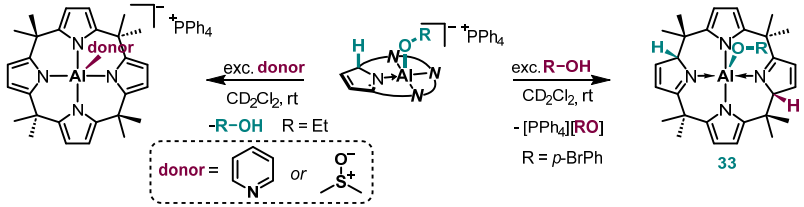

Figure 3.9: Reactivity of the alcohol addition products with weak Brønsted acids (right) and Lewis bases (left).

Conclusion

In summary, the reactivity of calix[4]pyrrolato aluminate toward protic substrates was investigated. The cooperation of the Lewis acidic square-planar Al(III) center with the electron-rich ligand backbone enables the rapid and reversible OH-bond addition. All Al-N bonds remain intact – even in the presence of a large excess of protons. The addition products undergo rapid self-exchange, and the equilibrium reaction of the alcohol binding can be influenced by the application of vacuum or elevated temperature as well as by the addition of Lewis bases. It is assumed that the reversible dearomatization/aromatization

of one of the ligand's pyrrole rings is important for an energetically balanced potential energy surface without deep sinks.

The findings demonstrate the evolution of an anti-van't-Hoff-Le-Bel species from a structural curiosity to a reagent with unique and well-defined reactivity. In addition to substrates with a carbonyl group (aldehydes, ketones, *cf.* **Figure 1.11D** in the Introduction), they introduce hydroxy groups as reagents for selective reactivity with calix[4]pyrrolato aluminate. In the following chapter, dioxygen as substrate is discussed.

3.2 Reactivity of Calix[4]pyrrolato Aluminates with Dioxygen

The results presented within this chapter were previously published and can be found under: L. M. Sigmund, C. Ehlert, M. Enders, J. Graf, G. Gryn'ova, L. Greb, "Dioxygen Activation and Pyrrole α-Cleavage with Calix[4]pyrrolato Aluminates: Enzyme Model by Structural Constraint", Angew. Chem. Int. Ed. ***2021****, 60, 15632-15640. This chapter was written based on the mentioned publication. The CASSCF and NEVPT2 calculations on the O_2 addition mechanism were conducted by DR. CHRISTOPHER EHLERT.*

Introduction and background

The selective activation of dioxygen, which has a triplet configuration in its electronic ground state, is literally vital to all processes of aerobic life on earth.[190-193] To accomplish selective reactivity, the spin barrier, which kinetically protects organic molecules from oxidation, is bypassed for example with flavin cofactors in flavoenzymes[194], with iron centers in intra- or extradiol dioxygenases[195-196], or with iron porphyrins in heme-based proteins[197-198] (**Figure 3.10**). A common black box of dioxygen activation within all the mentioned systems is the critical intersystem crossing (ISC) step which is inevitable to end up at closed-shell oxidation products. Various ISC mechanisms are debated in the literature such as the involvement of proton-coupled electron transfer (PCET) processes.[199-202] For iron-containing enzymes, ISC is proposed to involve the spin-mediating role of the open *d*-shell.[203]

Within this chapter, the reactivity of *meso*-octamethyl and *meso*-octaethylcalix[4]pyrrolato aluminate ([**21**]$^-$ and [**34**]$^-$) with $^3O_2$ is presented and interpreted against the background of naturally occurring dioxygen activation. The reactions proceed in an aluminum-ligand cooperative (AlLC) manner to form alkyl peroxido aluminates. Besides the herein presented examples, *p*-block element-ligand cooperative reactions with $^3O_2$ have been limited to antimony(V)-based complexes (*cf.* **Figure 1.9H** in the Introduction).[109-110, 204-206]

O_2 addition reaction and product characterization

When the tetraphenylphosphonium salts of *meso*-octamethyl and *meso*-octaethylcalix[4]pyrrolato aluminate ([PPh_4][**21**] and [PPh_4][**34**], respectively) were dissolved in CD_2Cl_2 and subjected to 1 bar of dioxygen gas at room temperature (**Figure 3.11A**), the appearance of the reaction solutions changed from colorless to orange within seconds.

The collected ^{1}H NMR spectra (**Figure 3.11B**) revealed complete consumption of the starting materials and the formation of new C_1 symmetric species. Indications for the dearomatization of one pyrrole ring was found (*cf.* the discussion on the NMR spectrum of the alcohol addition products to [**21**]$^-$ in the previous chapter). Therefore, an AlLC-type binding mode of $^3O_2$ to [**21**]$^-$ and [**34**]$^-$ to give alkyl peroxido aluminates ([PPh$_4$][**35**] and [PPh$_4$][**36**]) was assumed.

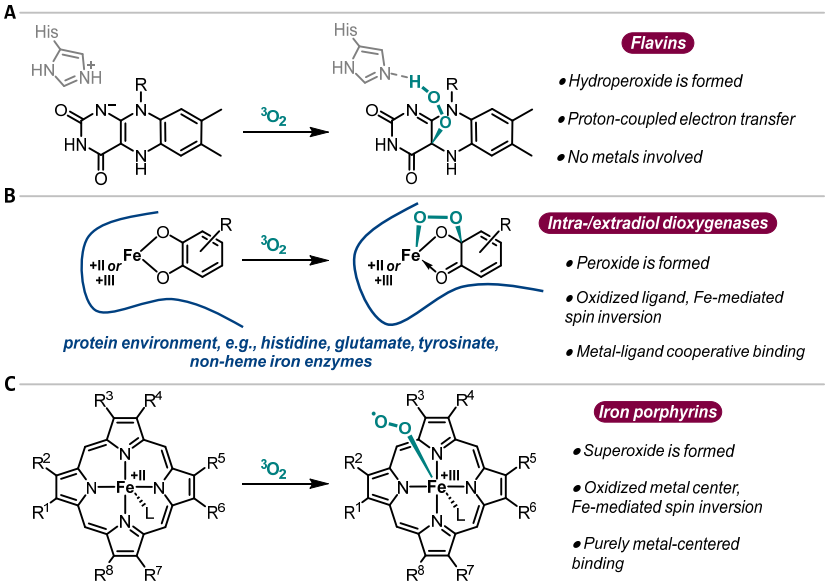

Figure 3.10: Dioxygen activation in nature. *Reactivity of triplet dioxygen with **A)** flavins occurring in flavoenzymes, **B)** intra- and extradiol dioxygenases, and **C)** iron porphyrins in heme proteins.*[148]

SCXRD analysis of crystalline [PPh$_4$][**35**] (crystals grown at −40 °C from a mixture of CH_2Cl_2 and *n*-pentane) confirmed this assumption (**Figure 3.11C**). In [**35**]$^-$, the dearomatized state of one pyrrole ring becomes clear from the average bond angle of 109.3(1)° around the now sp^3-hybridized carbon atom connected to the peroxido group. The C-N and C-C bond lengths of this ring support this interpretation. The C(sp^3)-O distance within the alkyl peroxido moiety is 143.11(19) pm. It is bound to the aluminum center *via* an Al-O bond of 183.11(12) pm. The interoxygen distance in [**35**]$^-$ experiences a significant elongation from 120.8 pm for $^3O_2$ in the gas phase[207] to 148.79(14) pm. This is consistent with the two-electron reduction of dioxygen to the oxidation state of a peroxide. Similar

distances (146-149 pm) were found for other alkyl peroxido complexes from transition metal-ligand cooperative binding of dioxygen.[100, 109, 208-209]

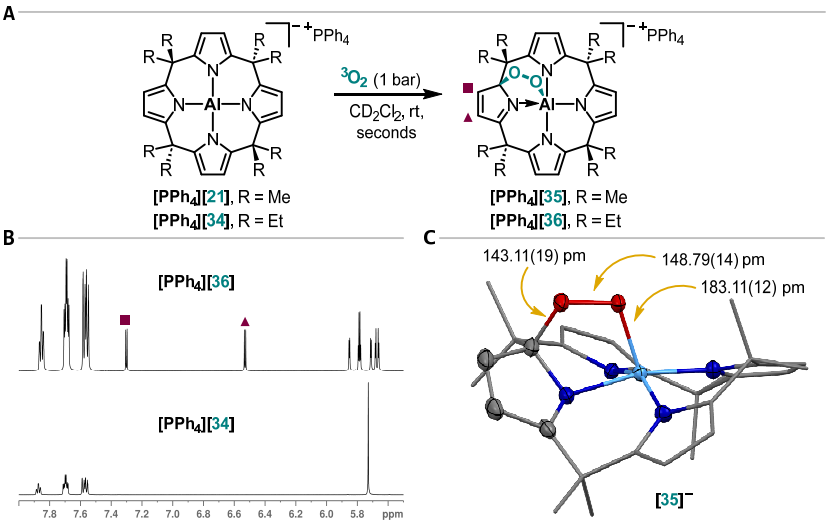

Figure 3.11: Reactivity of calix[4]pyrrolato aluminates with dioxygen. ***A)*** *Synthetic scheme.* ***B)*** *Aromatic section of the ^{1}H NMR spectrum (600 MHz, CD_2Cl_2, 295 K) of the free aluminate (bottom) and the addition product (top).* ***C)*** *Solid-state molecular structure of [35]$^-$ as found by SCXRD analysis. The counter cation, cocrystallized solvent molecules, and hydrogen atoms are omitted. Thermal displacement ellipsoids are presented at a probability level of 50%. CSD identifier: OVICAA.*[148]

The binding of O_2 to both aluminates was found to be irreversible and could not be undone by exposure to reduced pressure or elevated temperatures. The described reactions also took place when light was excluded from the systems. Notably, the reaction of dioxygen with the dianionic Co(II) complex of the ethyl-substituted calix[4]pyrrolato ligand did not result in the formation of an alkyl peroxide. Instead, the two-electron oxidation of the ligand framework was observed.[120] Other aluminum pyrrolato complexes with aluminum-alkyl groups engaged in the more common insertion of O_2 into the aluminum-carbon bond.[210]

The electronic structure of the O_2 addition products was further inspected by spectroscopy and computational simulations. The UV-Vis absorption spectra of [PPh_4][**35**] or [PPh_4][**36**] are similar to each other (**Figure 3.12A**), with broad bands at wavelengths of approximately 340 and 400 nm, reaching deep into the visible region. Time-dependent density functional theory calculations (TD-DFT, **Figure 3.12B/C**), carried out for [**35**]$^-$, identified the lowest energy electronic excitations as transitions from the three aromatic

pyrrole units to the dearomatized ring. The HOMO is primarily located on the aromatic pyrroles, while the dearomatized ring hosts the LUMO of [**35**]$^-$ (**Figure 3.12D**).

Commonly, metal alkyl peroxides are potent oxidants that can react through several pathways, such as O-O and M-O homolytic cleavage or through nucleophilic and electrophilic O-atom transfer.[211-214] In contrast, the peroxides [**35**]$^-$ and [**36**]$^-$ are stable to a notable extent. Even the markedly oxophilic triphenylphosphine did not react.

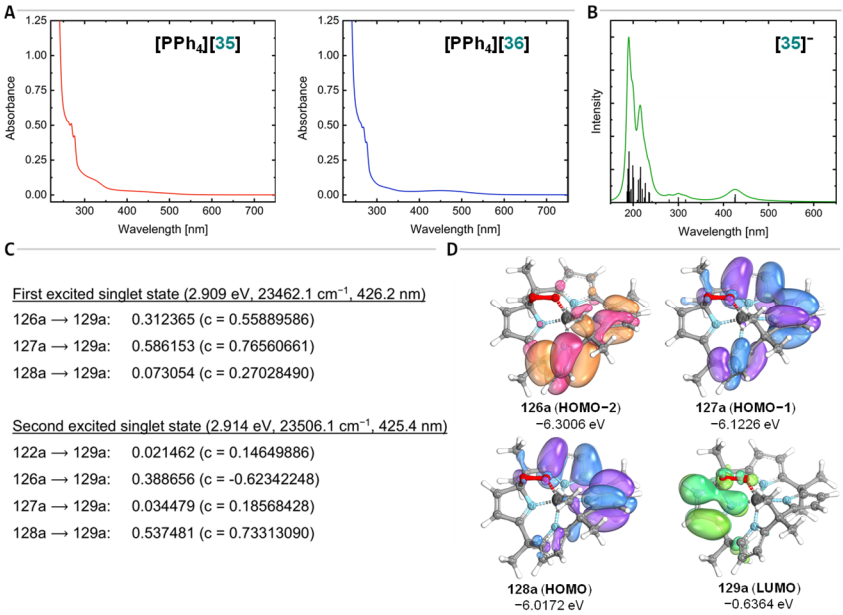

Figure 3.12: Optical properties of the O_2 addition products of calix[4]pyrrolato aluminates. ***A)*** *Solution phase UV-Vis absorption spectra. The data was obtained at room temperature with CH_2Cl_2 as solvent. The analyte concentration was approximately 1.5 · 10^{-4} mol L^{-1}.* ***B)*** *Computed vertical electronic singlet excitations and simulated UV-Vis absorption spectrum of [35]$^-$. The calculation was done at the TD-CAM-B3LYP/def2-TZVPP, CPCM(CH_2Cl_2) level of theory. The 30 energetically lowest singlet transitions were calculated. The continuous spectrum was obtained with the ORCA utility program `orca_mapspc` using a FWHM value of 2000 cm^{-1}.* ***C)*** *Contributions to the first and second singlet electronic excitation as obtained from the TD-DFT calculation.* ***D)*** *Kohn-Sham frontier molecular orbital representations of [35]$^-$ (CAM-B3LYP/def2-TZVPP, CPCM(CH_2Cl_2)) and associated orbital energies.*[148]

Quantum chemical simulations of the O_2 addition mechanism

Quantum chemical calculations were carried out to understand the mechanism of $^3O_2$ addition to the aluminates, which have a closed-shell singlet electronic ground state (**Figure 3.13**). For this purpose, the methyl-substituted system ([**21**]$^-$) was used, and the course of the reaction was evaluated with DFT at the B97M-D3(BJ)/def2-TZVPP, COSMO-RS(CH_2Cl_2) level of theory (**Figure 3.13A**). Dioxygen approaches the aluminate through a first transition state ([TS-**37**]$^-$), which is located on the triplet potential energy surface and comes with a Gibbs free energy barrier of 59 kJ mol^{-1}. In [TS-**37**]$^-$, the oxygen-aluminum distance is 237 pm, while the separation of the two oxygen atoms is 123 pm. The natural spin density (obtained at the PBE0/def2-TZVPP level of theory) is predominantly located on the dioxygen unit (90%, **Figure 3.13A**). The energies of the corresponding closed-shell (CSS) and open-shell singlet (OSS) state (addressed with the broken symmetry (BS) approach) are clearly higher in energy (81 kJ mol^{-1} for ^{CSS}[TS-**37**]$^-$ and 57 kJ mol^{-1} for ^{OSS}[TS-**37**]$^-$, relative to ^{trip}[TS-**37**]$^-$), ruling out a change in spin state before the association. The preference for the triplet state in [TS-**37**]$^-$ is rooted in the ferromagnetic spin coupling of the two unpaired electrons, which still mainly reside in the pseudo-orthogonal π*-orbitals at O_2.[215]

The subsequent local minimum structure [Int-**38**]$^-$ is essentially Gibbs isoenergetic to the starting materials (ΔG_r = −2 kJ mol^{-1}), though enthalpically favored by 44 kJ mol^{-1}, resulting in an unusually strong interaction of an anionic Lewis acid with the weak Lewis base O_2.

Compared to [TS-**37**]$^-$, the O-O bond length in [Int-**38**]$^-$ is increased to 134 pm while the Al-O distance decreases to 184 pm. Hence, the O_2 moiety is reduced to the superoxide redox state, and concomitantly, the calix[4]pyrrolato ligand gets oxidized by one electron. This reasoning is supported by the natural spin density within [Int-**38**]$^-$, which is now equally distributed between the dioxygen moiety and the ligand backbone (**Figure 3.13A**). Also, the total natural charge of the O_2 fragment changes from +0.07 in [TS-**37**]$^-$ to −0.75 in [Int-**38**]$^-$. The experimentally observed alkyl peroxido aluminate **35** is formed after the transition to the singlet potential energy surface and additional C-O single bond formation. The overall reaction is calculated to be exergonic by −79 kJ mol^{-1} (**Figure 3.13A**).

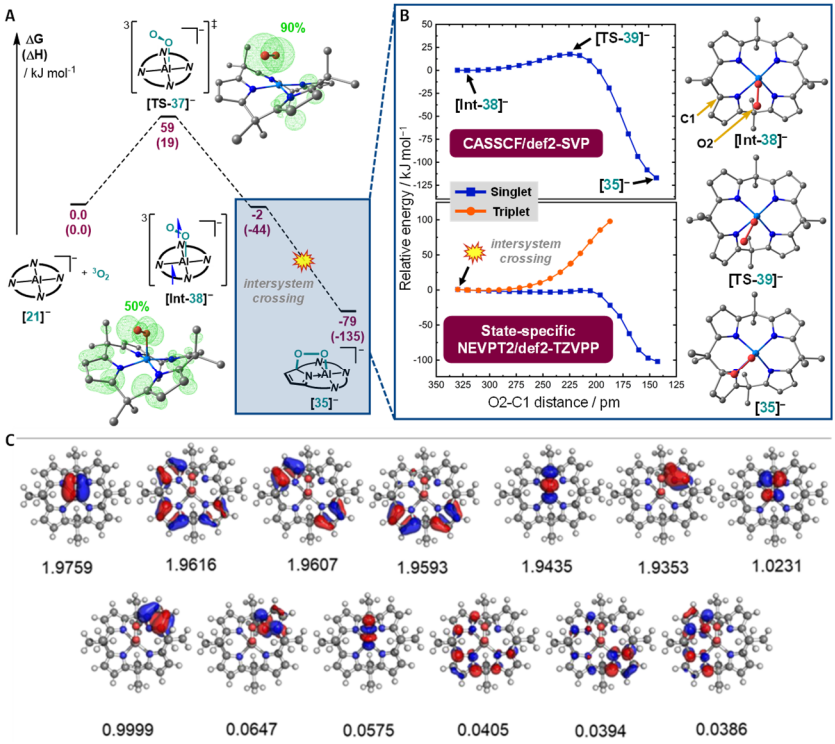

Figure 3.13: Quantum chemical investigation of the O_2 addition reaction to calix[4]pyrrolato aluminate. ***A)*** *Energy profile for the addition reaction of triplet dioxygen computed with DFT at the B97M-D3(BJ)/def2-TZVPP, COSMO-RS(CH_2Cl_2) level of theory. The natural spin density distributions (shown in light green) were obtained based on PBE0/def2-TZVPP single point calculations.* ***B)*** *Singlet CASSCF(14,13)/def2-SVP constrained potential energy surface scan to connect intermediate [Int-38]⁻ with [35]⁻ and state-specific NEVPT2(14,13)/def2-TZVPP triplet and singlet energies for each constrained minimum structure.* ***C)*** *Iso-density surface representations and respective natural orbital occupation numbers of the active molecular orbitals used for the multiconfigurational treatment of [Int-38]⁻. The data was obtained at the CASSCF(14, 13)/def2-TZVPP level of theory.*[148]

The spin-forbidden conversion from the triplet to the singlet potential energy surface was further studied with multiconfigurational and multireference calculations (**Figure 3.13B/C**). Electron correlation was treated within a CAS(14, 13), which covered the σ/σ* and π/ π*-orbitals at the O_2 fragment, the orbitals responsible for the formation of the Al-O and C-O bond, as well as several π/ π*-orbitals of the pyrrole rings. Analyzing [Int-**38**]⁻ within a singlet electronic configuration (CASSCF/def2-SVP level of theory) revealed an essentially identical molecular structure compared to the triplet analog (RMSD = 0.67 pm) as well as a minuscule singlet/triplet energy gap of 0.1 kJ mol^{-1}. The energetic barrier for

C-O bond formation to yield [**35**]$^-$ was approximated to 18 kJ mol^{-1} ([TS-**39**]$^-$), and the corresponding transition state has singlet diradical character. These findings explain the experimentally observed facile addition of O_2 to the aluminates: The entry of $^3O_2$ into the coordination sphere of the central aluminum atom ([TS-**37**]$^-$) is the rate-determining step of the overall reaction.

In detail discussion of the spin-inversion mechanism

In the following paragraphs, the ISC required for the transformation toward the alkyl peroxides is discussed in more detail and with respect to various backgrounds. The free superoxide radical anion ($O_2^{\bullet-}$) shows strong spin-orbit coupling (SOC) due to rotation of the degenerated π^*-orbitals. This SOC has been proposed as important for ISC in non-iron enzymes such as glucose oxidase or cofactor-free enzymes.[216-217] However, the uncoordinated superoxide molecule is not available in the case of the calix[4]pyrrolato aluminates. Instead, an inner-sphere electron transfer from the ligand to the substrate takes place while O_2 is coordinated to aluminum. This means that $O_2^{\bullet-}$ is not free but directionally bound to the Lewis acidic centers within [**21**]$^-$ and [**34**]$^-$. This also means that the symmetry of the system is broken, and the π^*-orbitals located on the superoxide fragment are not degenerate anymore (orbital energies of −7.9 and 0.9 eV on the CASSCF/def2-TZVPP level). Small absolute SOC matrix elements of less than 0.02 cm^{-1} were computed for [Int-**38**]$^-$. Consequently, SOC is not the driving force for the ISC occurring in the currently discussed systems.

Generally, ISC becomes likely if the energy and the molecular structure of both spin states are similar.[218-219] As discussed above, this is the case for the aluminates when interacting with $^3O_2$. Energetically degenerate spin-states are achieved if the relevant electrons are decoupled, for example, by spatial separation. In the present case, it is the calix[4]pyrrolato ligands' redox activity that produces the desired effect. The electron transfer from the ligand backbone to the dioxygen substrate reorganizes the spin density in non-interacting regions of the assembly. The driving force for the inversion from the triplet to the singlet manifold becomes obvious upon the inclusion of thermal corrections. Though the electronic energy of ^{trip}[Int-**38**]$^-$ and ^{sing}[Int-**38**]$^-$ is equal, the Gibbs free energy of the singlet state is 21 kJ mol^{-1} lower. This is due to the difference in zero-point vibrational energy (ZPVE). When applying the harmonic approximation, this is an outcome of a flatter potential energy surface in the singlet state. Overall, these characteristics can be interpreted to point to a spin-vibronic coupling of the two states.[220] Ultimately, irreversible C-O bond

formation, that is combination of the two unpaired electrons of opposite spin, drives the reaction to the experimentally observed alkyl peroxido aluminate products.

Relations to biological systems

In the previous sections, a detailed picture of the reaction between calix[4]pyrrolato aluminates and dioxygen was illustrated. For the final part of this chapter, this picture is related and compared to O_2 activation occurring in enzymes.

During the formation of [**35**]$^-$, the calix[4]pyrrolato ligand functions as the electron donor in an inner-sphere ligand-to-substrate (O_2) electron transfer, which is facilitated by the electrophilic activation of $^3O_2$ after coordination to the redox inactive, square planar-coordinated aluminum atom. Calix[4]pyrroles are closely related to porphyrins. Within iron porphyrins, dioxygen reduction to the superoxide state is found as well, but the electron originates from the ferrous iron center. It is proposed that *d*-electrons mediate the ISC in these cases.[203] This means that despite the close structural relationship between iron porphyrins and calix[4]pyrrolato aluminates, the differences with respect to central atom and ligand redox state result in completely different interactions with $^3O_2$.

In fact, the calix[4]pyrrolato aluminates lack any heavy atom; so do metal-free flavoenzymes such as pyranose 2-oxidase or the oxygenase component of *p*-hydroxyphenylacetate 3-hydroxylase. They also only comprise light main-group elements as their atomic building blocks. Therefore, their reactivity with dioxygen was compared to that of the aluminates. One can interpret the aluminum center as mimic of the histidinium proton side, while the calix[4]pyrrolato ligand takes the role of the flavin cofactor (*cf.* **Figure 3.10A**). Hence, this analogy suggests that flavoenzymes facilitate ISC by similar principles detailed in the preceding paragraph.

Conclusion

The tetraphenylphosphonium salts of calix[4]pyrrolato aluminates [PPh_4][**21**] and [PPh_4][**34**] react rapidly with triplet molecular oxygen to yield alkylperoxido aluminates ([PPh_4][**35**] and [PPh_4][**36**], respectively). The products and the reaction mechanism were characterized through experimental and computational tools. The reaction is initiated by O_2 coordinating end-on to [**21**]$^-$ and [**34**]$^-$, respectively. The attractive interaction is facilitated by the structural constraint-induced Lewis acidity of the square planar aluminates. An inner-sphere ligand-to-dioxygen electron transfer results in the ISC from the triplet to the singlet potential energy surface due to the energetic degeneracy of the two spin states at essentially identical structures. ISC is possible despite the absence of heavy

elements and negligible computed SOC matrix elements, possibly facilitated by spin-vibronic coupling.

The detailed mechanistic findings were related to dioxygen activation in nature, namely to the reactions of metal-free flavoenzymes and iron porphyrins with molecular oxygen.

The presented findings buttress the importance of constraint and cooperativity in natural dioxygen metabolism and offer a starting point to exploit air's redox potential with earth-abundant elements beyond iron or other transition metals. In fact, despite the absent reactivity with additional substrates, the alkyl peroxido aluminates were found to undergo a rearrangement at elevated temperatures, which was studied in detail. The collected insights are presented in the following chapter.

3.3 Reactivity of Dioxygen Addition Products of Calix[4]pyrrolato Aluminates

The results presented within this chapter were previously published and can be found under: L. M. Sigmund, C. Ehlert, M. Enders, J. Graf, G. Gryn'ova, L. Greb, "Dioxygen Activation and Pyrrole α-Cleavage with Calix[4]pyrrolato Aluminates: Enzyme Model by Structural Constraint", Angew. Chem. Int. Ed. ***2021****, 60, 15632-15640. This chapter was written based on the mentioned publication.*

Introduction and background

Meso-octamethyl- and *meso*-octaethylcalix[4]pyrrolato aluminate ([PPh_4][**21**] and [PPh_4][**34**], respectively) react rapidly with molecular oxygen and are selectively converted into the respective alkyl peroxido aluminates ([PPh_4][**35**] and [PPh_4][**36**], *cf.* **Figure 3.11**). Despite the rather week O-O single bond – as it is generally considered – the alkyl peroxido aluminates do not react with added substrates, *e.g.*, aldehydes, alkenes, strong donors such as pyridines, or even triphenylphosphine. Instead, when exposed to elevated temperatures, a rearrangement reaction occurs. This cleaves the O-O bond to yield an ester functional group. Concomitantly, the dearomatized pyrrole ring gets ruptured at the α-bond, that is, at its nitrogen-carbon bond.

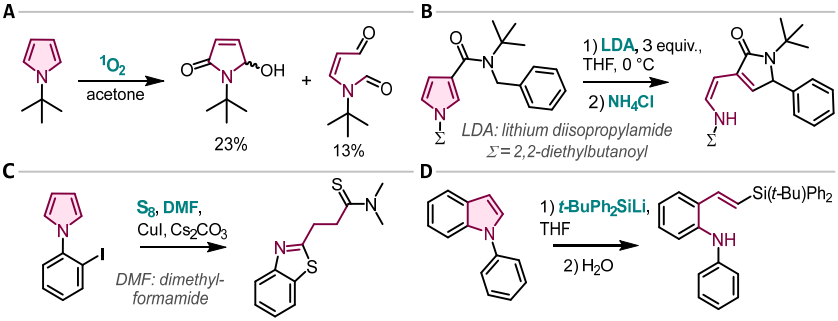

Figure 3.14: Examples for pyrrole ring cleavage reactions known to the literature.

The chemical modification of pyrrole rings is a widely studied field of chemical research. Most often, C-H or N-H functionalization as well as cycloaddition reactions are applied.[221] By contrast, ring-opening transformations of pyrroles are less researched. Examples are the oxidative cleavage of a *tert*-butyl-protected pyrrole by singlet dioxygen (**Figure 3.14A**)[222], an organolithium reagent-induced pyrrole α-cleavage (**Figure 3.14B**)[223], or a four-component ring opening of *N*-(2-iodophenyl)pyrroles using elemental sulfur

and formamide reagents (**Figure 3.14C**)[221]. Pyrrole ring openings within indoles are also well-known, including reactions that cleave the pyrrolic N-C bond (α-bond, **Figure 3.14D**).[224-225] Generally, however, the complete breaking of the C-C bond during pyrrole ring cleavage reactions is more common.[221]

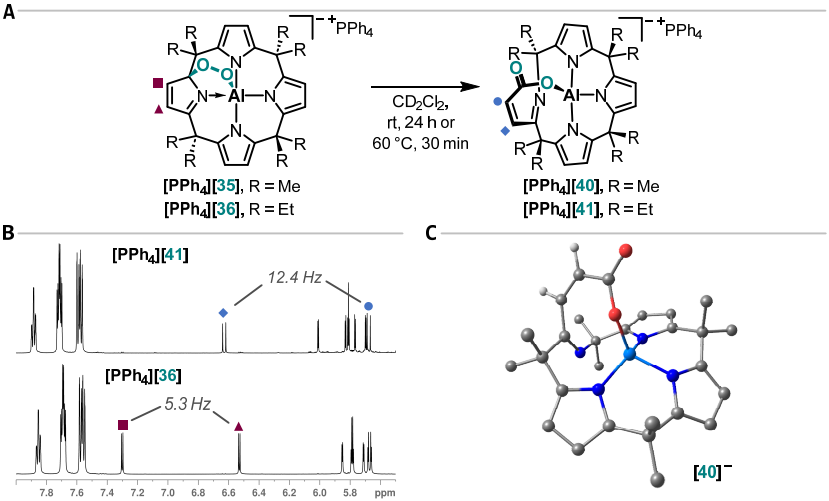

Figure 3.15: Reactivity of calix[4]pyrrolato peroxido aluminates. ***A)*** *Synthetic scheme.* ***B)*** *Aromatic section of the ^{1}H NMR spectrum (600 MHz, CD_2Cl_2, 295 K) of [PPh_4][36] (bottom) and [PPh_4][41] (top).* ***C)*** *Molecular structure of [40]$^-$, optimized at the B97M-D3(BJ)/def2-TZVPP level of theory. All hydrogen atoms except for the two attached to the C-C double bond which is α to the carboxylato group were omitted in the depiction.*[148]

Rearrangement reaction of calix[4]pyrrolato peroxido aluminates

When CD_2Cl_2 solutions of the alkyl peroxido aluminates [PPh_4][**35**] and [PPh_4][**36**] were stored at room temperature for 24 hours or alternatively at 60 °C for 30 min, transformations to new species [PPh_4][**40**] and [PPh_4][**41**], respectively, occurred (**Figure 3.15**). In general, no evidence was found that the reaction products differ depending on the *meso*-substituents (either methyl or ethyl). Despite significant efforts, it was not possible to grow single crystals of [PPh_4][**40**] or [PPh_4][**41**] suitable for SCXRD measurements. One reason for that is likely the fact that both anions as their tetraphenylphosphonium salts were found as either being extremely well or close to insoluble in the tested solvents and solvent mixtures, respectively. It was attempted to use the PNP cation instead of PPh_4^+. The transformations toward [**40**]$^-$ and [**41**]$^-$ were possible, however, the growth of single crystals remained unsuccessful. Nevertheless, in the following sections, extensive

evidence for the molecular constitution of [**40**]$^-$ and [**41**]$^-$, respectively, as it is shown in **Figure 3.15A/C**, is provided.

Experimental investigations on the rearrangement reaction

The electrospray-ionization (ESI, anion mode) high-resolution mass spectra of [**40**]$^-$ and [**41**]$^-$ show peaks at *m/z* ratios identical to those of [**35**]$^-$ and [**36**]$^-$, respectively. This points to a rearrangement process without the loss of the OO or potentially any other fragment. The IR spectra gave evidence for the presence of a carbon-oxygen double bond, as strong bands at 1662 cm^{-1} were detected, which are assigned to the C=O stretching vibrational mode (**Figure 3.16**). This is in line with bands observed for other metal carboxylato complexes, which possess the same RCOO-M binding mode.[226]

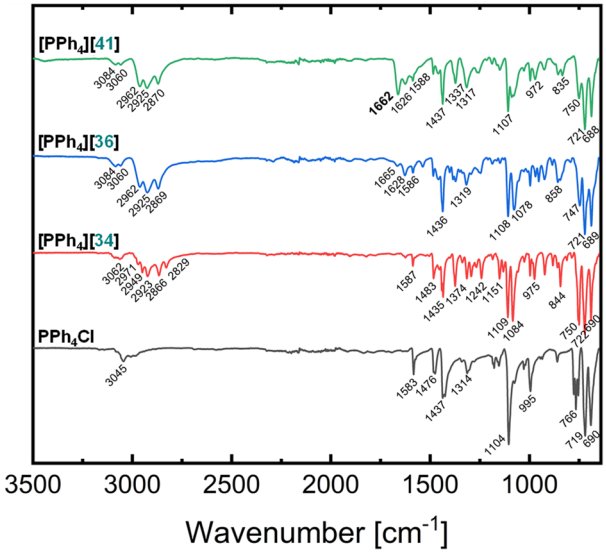

Figure 3.16: IR spectra of tetraphenylphosphonium salts of different calix[4]pyrrolato aluminates in comparison to PPh_4Cl. *The band at 1662 cm^{-1} in the top spectrum is an indication for the presence of a carbonyl group in the analyzed molecule.*[148]

Based on the molecular formula of [**40**]$^-$ and [**41**]$^-$, the structure elucidation was started from four distinct ^{13}C NMR signals of the ethyl-substituted derivative ([**41**]$^-$). These signals appear at 183.9, 165.3, 140.1, and 127.6 ppm. The first two are quaternary carbon atoms, which was easily seen from the DEPT-135 $^{13}C\{^1H\}$ NMR spectrum (**Figure 7.11** in the Appendix). The last two are part of a CH group, as observable in the $^1H,^{13}C$ HSQC spectrum (**Figure 7.12** in the Appendix). This is consistent with the following

connections for the respective CH groups; ^{13}C: 140.1 ppm is connected to ^{1}H: 6.70 ppm and ^{13}C: 127.6 ppm is connected to ^{1}H: 5.70 ppm. Noticeably, the two mentioned protons feature a mutual coupling constant of 12.4 Hz. Such a large $^{1}H,^{1}H$ coupling constant was not observed before for dearomatized pyrrole rings within the chemistry of the calix[4]pyrrolato aluminates. Typically, the coupling constant of the β-protons of a pyrrole ring that got dearomatized lies between 5 and 6 Hz.[89, 142]

The tetraphenylphosphonium salt of [**41**]$^-$ is superbly soluble in CH_2Cl_2. Therefore, it was possible to acquire a two-dimensional $^{13}C,^{13}C$ NMR INADEQUATE [227-229] spectrum using a sample containing 300 mg of [PPh_4][**41**] dissolved in 0.5 mL of CD_2Cl_2 (**Figure 7.17** in the Appendix). The obtained spectrum reveals the direct connection of the four discussed carbon atoms. It also shows that the C-atom at 165.3 ppm is attached to only one further carbon-atom, which is the one appearing at 127.6 ppm. The further connectivities are: C at 183.9 ppm: two neighboring C-atoms (140.1 and 56.7 ppm), C at 140.1 ppm: two neighboring C-atoms (183.9 and 127.6 ppm), C at 127.6 ppm: two neighboring C-atoms (165.3 and 140.1 ppm). The DEPT-135 $^{13}C\{^{1}H\}$ NMR spectrum shows that the resonance at 56.7 ppm originates from a quaternary C-atom (**Figure 7.11** in the Appendix). Furthermore, this C-atom is connected to two ethyl groups and an aromatic pyrrole ring.

The so far described observations can be combined into a substructure as shown in **Figure 3.17A**. The *cis*-configuration of the double bond is supported by the observed $^{1}H,^{1}H$ coupling constant of 12.4 Hz. Couplings arising from *trans*-configurations are typically slightly larger (around 16 Hz). Also, the $^{1}H,^{1}H$ NOESY NMR spectrum shows close spatial proximity of the two alkene protons, which further supports the proposed relative stereochemistry (**Figure 7.14** and **Figure 7.15** in the Appendix).

Another characteristic signal in the ^{13}C NMR spectrum of [**41**]$^-$ appears at 66.9 ppm, which is quaternary in nature, as seen in the DEPT-135 $^{13}C\{^{1}H\}$ NMR spectrum (**Figure 7.11** in the Appendix). In the $^{13}C,^{13}C$ INADEQUATE NMR spectrum, this signal shows direct connectivity to only three other C-nuclei, meaning that it bears one non-carbon substituent (**Figure 7.17** in the Appendix). Two of its neighbors can be assigned to methylene carbon atoms from the attached ethyl groups (38.0 and 29.6 ppm, respectively) and the remaining other one to a C_q of an aromatic pyrrole ring (139.9 ppm). Moreover, the chemical shift of 66.9 ppm is rather downfield-shifted for a quaternary C-atom connecting two pyrrole rings in the calix[4]pyrrolato ligand. Typically, those atom types appear between 45 and 30 ppm.[89, 142] Consequently, a second substructure can be formulated (**Figure 3.17B**).

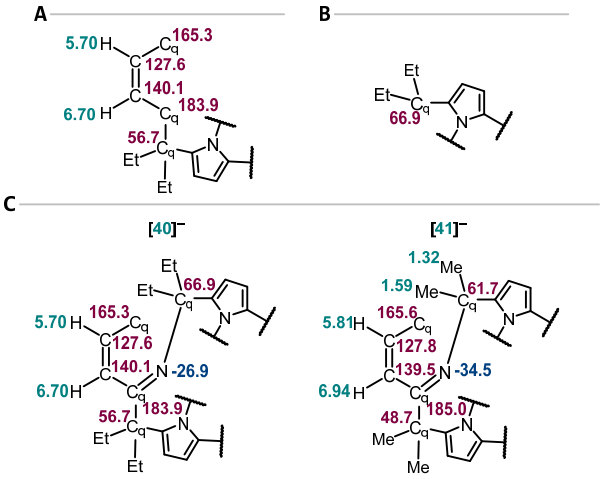

Figure 3.17: Deduced substructures of the rearrangement product of the calix[4]pyrrolato peroxido aluminates based on NMR spectroscopical measurements. *The two fragments shown in **A)** and **B)** were connected with each other in **C)** with an imine-nitrogen atom.*[148]

Generally, the methyl-substituted system allows a more straightforward interpretation of the NMR data, for example, regarding ^{1}H resonances. Therefore, the treatise from hereon is based on [**40**]$^{-}$. For that, its ^{1}H,^{15}N HMBC NMR spectrum is discussed (**Figure 7.8** in the Appendix). It shows nitrogen resonances at −34.5, −201.0, −202.9, and −206.6 ppm. The latter three are assigned to the three aromatic pyrrole rings. For comparison, the nitrogen atoms of the aromatic pyrrole rings in the alkyl peroxido aluminate [**35**]$^{-}$ resonate at similar chemical shifts (−184.4, −185.7, and −194.8 ppm). Contrastingly, the chemical shift of the nitrogen atom of the dearomatized pyrrole ring is −102.1 pm, which is markedly different to the −34.5 ppm resonance found for [**40**]$^{-}$. This suggests that the chemical environment of the respective nitrogen atom changes significantly once the reaction from [**35**]$^{-}$ to [**40**]$^{-}$ occurs.

In the ^{1}H,^{15}N HMBC NMR spectrum of [**40**]$^{-}$, the signal at −34.5 ppm shows three cross-peaks. Firstly, with the proton resonating at 6.94 ppm and secondly, with two methyl groups at 1.59 and 1.32 ppm. With the help of the ^{1}H,^{13}C HMBC NMR spectrum (**Figure 7.5** in the Appendix), these two methyl groups were identified to be connected to the quaternary carbon appearing at 61.7 ppm (The equivalent carbon atom in [**41**]$^{-}$ appears at 66.9 ppm; *vide supra*). This leads to the conclusion that the nitrogen atom at −34.5 ppm functions as the nexus between the two developed substructures (**Figure 3.17C**). This is

the only possibility to have it separated by three covalent bonds from the vinylic proton at 6.94 ppm and the protons of the methyl groups at 1.59 and 1.32 ppm.

The carbon atom appearing at 185.0 ppm is significantly downfield shifted (The equivalent carbon atom in [**41**]$^-$ appears at 183.9 ppm). Also, two free valences at this atom must be filled. This can be achieved by including a double bond, which connects the nitrogen at −34.5 ppm to the quaternary carbon atom at 185.0 ppm. Lastly, the nitrogen is connected to the C_q at 61.7 ppm with a single bond. This reasoning adds up to the extended substructures shown in **Figure 3.17C**. The discussed key correlations, found in the various NMR spectra, are summarized in **Figure 3.18**.

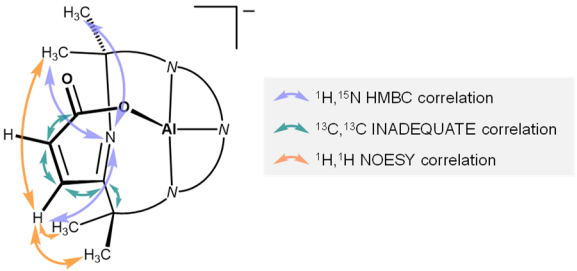

Figure 3.18: Extracted NMR spectroscopical correlations for the calix[4]pyrrolato carboxylato aluminates ([40]$^-$ and [41]$^-$).[148]

Importantly, the proton resonating at 5.81 ppm does not show any ^{1}H,^{15}N correlation (**Figure 7.8** in the Appendix). Such a correlation was extensively searched with various ^{1}H,^{15}N HMBC experiments. A cross peak could not be detected. Contrary to that, the two protons attached to the dearomatized pyrrole ring in [**35**]$^-$ show a cross peak with the ring's nitrogen atom as they are both separated from the nitrogen by three bonds. This is a clear hint at the absent covalent bond between the quaternary carbon atom resonating at 165.6 ppm and the nitrogen atom at −34.5 ppm. The four-bond distance between the proton at 5.81 ppm and the nitrogen at −34.5 ppm does not allow for a $^4J_{NH}$ spin-spin coupling detectable through ^{1}H,^{15}N HMBC NMR spectroscopy.

Next, the missing connectivities of the quaternary carbon resonating at 165.6 in the methyl and at 165.3 ppm in the ethyl case are addressed (*cf.* **Figure 3.17C**). Importantly, the two oxygen atoms need to be incorporated into the structure as well. Both aspects can be accounted for by introducing an ester moiety based on the said carbon atoms. The mesomerism of the resulting α,β-unsaturated ester also explains the relative chemical shifts of the CH-groups α and β to the ester. Both the ^{13}C and the ^{1}H nuclei at the β-position are

significantly more downfield-shifted compared to those at the α-position. Of note, in the peroxides [**35**]⁻ and [**36**]⁻, this situation is the exact opposite. There, the imine group is the "electronically" dominating factor making the β-CH group (β relative to the imine functional group) more downfield-shifted compared to the α-CH group.

Finally, the question about the atoms connected to aluminum is discussed. It should be reasonable to assume the preservation of the strong Al-O bond. Structure optimization at the DFT level (see the next section for further details) of the deduced structure revealed the detachment of the formed imine nitrogen atom from the aluminum center. The combination of all stated arguments yields the final molecular structure as it is presented in **Figure 3.19**.

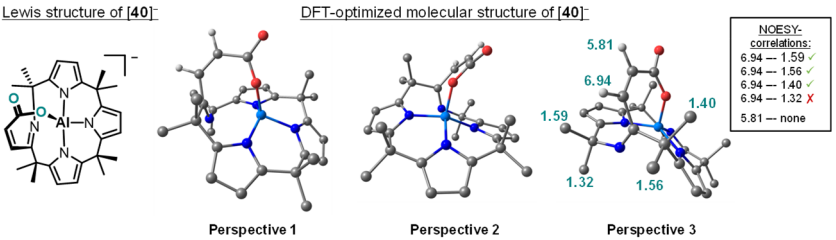

Figure 3.19: Deduced molecular structure of the rearrangement product of the calix[4]pyrrolato peroxido aluminates based on NMR spectroscopical measurements and DFT calculations. *The calculation was done at the B97M-D3(BJ)/def2-TZVPP level of theory.*[148]

To conclude this section and to further support the present structure suggestion, the ^{1}H,^{1}H NOESY NMR spectrum of [**40**]⁻ is discussed (**Figure 7.6** in the Appendix). It reveals spatial proximity of the proton in β-position relative to the ester grouping (appearing at 6.94 ppm) to three methyl groups, which appear at 1.59, 1.56, and 1.40 ppm. These were identified to frame the imine group (see perspective 3 in **Figure 3.19**). Also taking into account that the α-proton is not showing these correlations (it is further away), this is another supporting argument for the concluded structure. Moreover, the molecular structure as shown in **Figure 3.19** agrees with the fact that the fourth framing methyl group (chemical shift of 1.32 ppm) is not indicated by the acquired NOESY NMR spectrum to be in close spatial proximity to the proton in β-position.

The discussed spectroscopic findings provide strong evidence for the deduced molecular constitution of [**40**]⁻ and [**41**]⁻, respectively. In the following section, the results of quantum chemical simulations are presented which further support the statements made. This was done by comparing the experimentally determined ^{1}H, ^{13}C, and ^{15}N chemical

shifts with gauge-independent atomic orbital DFT calculations (GIAO-DFT) as well as with the simulation of the reaction mechanism.

Quantum chemical investigations on the rearrangement reaction

For all quantum chemical calculations, the methyl-substituted system was considered. At first, the conformational space of [**40**]$^-$ was investigated (**Figure 3.20A**). Four individual conformers were obtained, which are relatively close in energy (range of 21 kJ mol^{-1} on ΔG scale). The lowest energy conformer was used for all further calculations.

In **Figure 3.19**, [**40**]$^-$ is shown with the imine group in *E*-configuration, which is supported by the experimental findings. Computationally, the *Z*-configuration was investigated as well and was found to be 26 kJ mol^{-1} higher in Gibbs free energy. It was also possible to locate the transition state for the *E*/*Z*-isomerization. It comes with a Gibbs free activation energy of 87 kJ mol^{-1} (relative to the *E*-isomer of [**40**]$^-$).

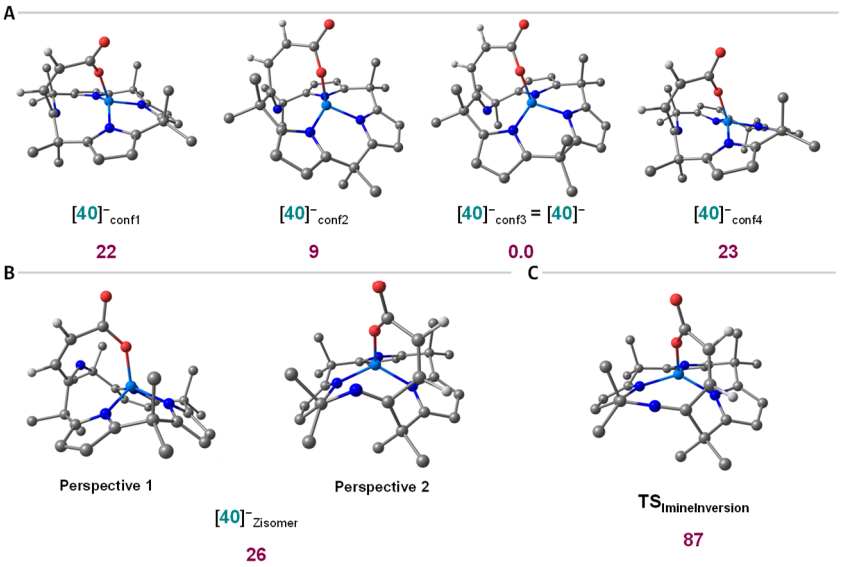

Figure 3.20: **Quantum chemical calculations on the structure of calix[4]pyrrolato carboxylato aluminate.** *All given numbers are Gibbs free energies in kJ mol^{-1}, calculated at the B97M-D3(BJ)/def2-TZVPP level of theory. The data is COSMO-RS(CH_2Cl_2)-corrected. All hydrogen atoms, except for the two of the α,β-unsaturated ester were omitted for clarity.* ***A)*** *Considered conformational space.* ***B)*** *Stereoisomer of [40]$^-$ with a Z-configurated imine group.* ***C)*** *Transition structure for the E/Z isomerization at the imine group.*[148]

Following the structural investigations, the NMR chemical shifts of [**35**]$^-$ and [**40**]$^-$ were simulated using the PBE0/IGLO-II computational method (**Figure 3.21** and **Figure**

3.22). The absolute isotropic chemical shielding data, as obtained from the calculations, were converted to values comparable with experimental numbers by referencing to the standard anchor molecules (tetramethylsilane for ^{1}H and ^{13}C, nitrobenzene for ^{15}N).

The computations were found to be in good agreement with the experimental values. For [**40**]$^{-}$, the mean absolute difference for the proton shifts is 0.09 ± 0.06 ppm. For the ^{13}C shifts, it is 4.2 ± 2.3 ppm, and for the ^{15}N nuclei, 13 ± 15 ppm. The larger deviation for the nitrogen atoms, is due to the poor reproduction of the chemical shift of the imine nitrogen atom. The deviation is 36 ppm. A possible explanation for that is the conformational flexibility of [**40**]$^{-}$ that might influence the respective nitrogen atom particularly strongly.

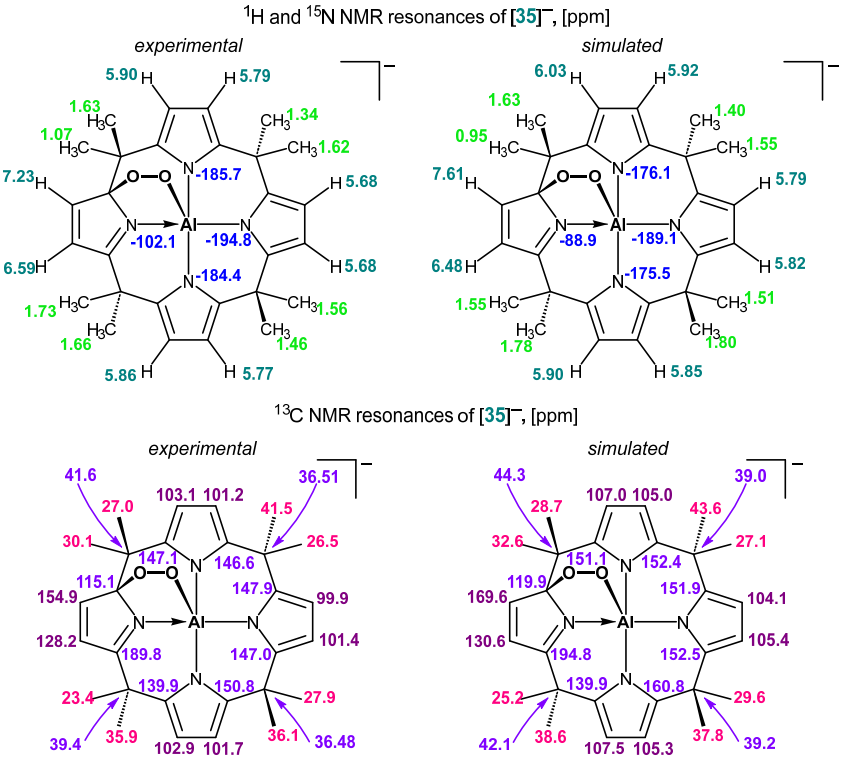

Figure 3.21: Quantum chemical simulation of the NMR chemical shifts of calix[4]pyrrolato peroxido aluminate and comparison to the data obtained from experiment. *The calculations were done at the PBE0/IGLO-II//B97M-D3(BJ)/def2-TZVPP level of theory.*[148]

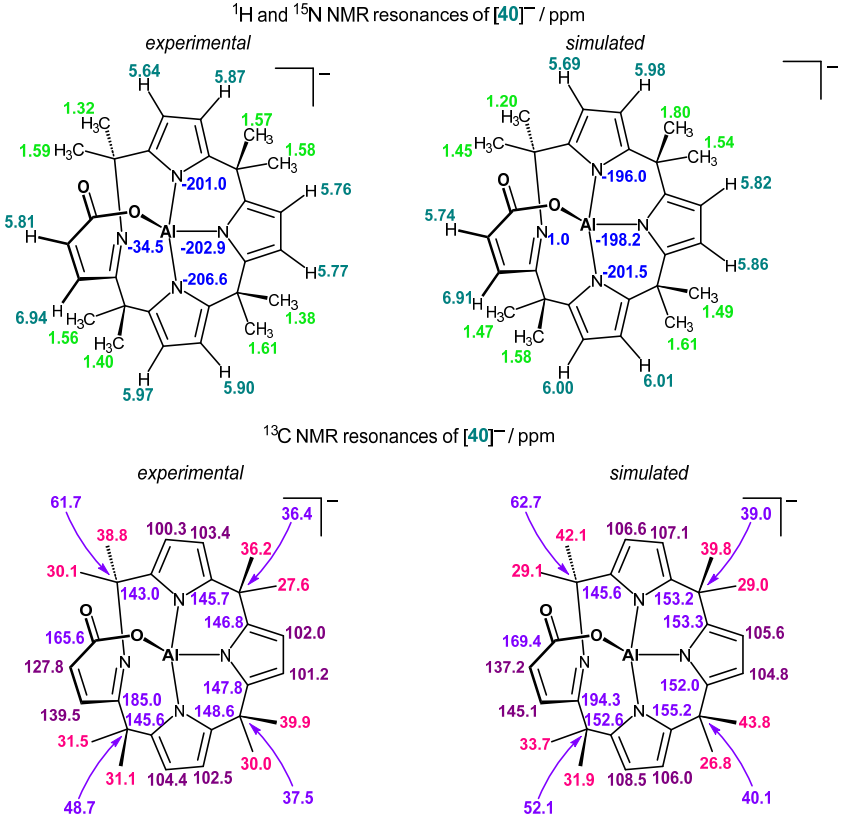

Figure 3.22: Quantum chemical simulation of the NMR chemical shifts of calix[4]pyrrolato carboxylato aluminate and comparison to the data obtained from experiment. *The calculations were done at the PBE0/IGLO-II//B97M-D3(BJ)/def2-TZVPP level of theory.*[148]

The $^{1}H,^{1}H$ spin-spin coupling constants were also simulated at the same level of theory as the chemical shifts, including the diamagnetic, paramagnetic, Fermi-contact, spin-dipolar, and the spin-dipolar/Fermi-contact cross term contributions (**Figure 3.23**).

Characteristic for peroxide [**35**]$^{-}$ is the coupling constant of the two protons of the dearomatized pyrrole ring. This value was experimentally determined to 5.3 Hz, which is larger than the values for the aromatic pyrrole rings (3.0 Hz). In [**40**]$^{-}$, a pair of protons is coupled to the extent of 12.4 Hz. The computational simulations excellently reproduced this significantly larger coupling constant (12.4 *versus* 12.7 Hz). Generally, the quantum theoretical model systematically overestimated the $^{3}J_{HH}$ spin-spin coupling constants with a mean absolute deviation of 0.22 Hz.

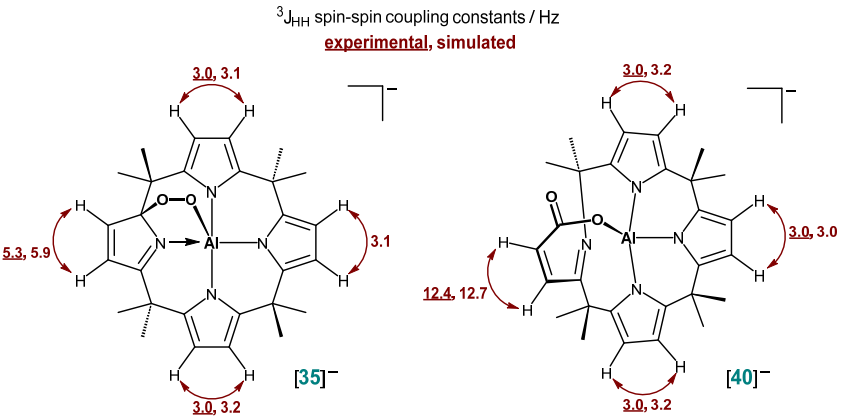

Figure 3.23: Quantum chemical simulation of spin-spin coupling constants of calix[4]pyrrolato peroxido and carboxylato aluminate and comparison to the data obtained from experiment. *The calculations were done at the PBE0/IGLO-II//B97M-D3(BJ)/def2-TZVPP level of theory. It was not possible to extract the coupling constant of the two protons of the aromatic pyrrole ring opposite to the dearomatized ring in [35]⁻ from the ^{1}H NMR spectrum as they have an extremely similar chemical shift.*[148]

Ultimately, the reaction mechanism for the rearrangement from the peroxido to the carboxylato aluminates was investigated computationally – again using the methyl-substituted ligand as the system to be studied. The B97M-D3(BJ)/def2-TZVPP, COSMO-RS(CH_2Cl_2) computational level was applied (**Figure 3.24**).

Initially, the cleavage of the O-O single bond was investigated. It was possible to optimize the structure of the potentially resulting intermediate with a broken O-O bond ([Int-**42**]⁻) on the triplet potential energy surface. It is 85 kJ mol^{-1} higher in electronic energy than [**35**]⁻. The OSS and the CSS energies are even higher (90 and 163 kJ mol^{-1}). This means that the rupture of the O-O bond in [**35**]⁻ and [**36**]⁻ is most likely not the initial step of the observed reaction (**Figure 3.24B**).

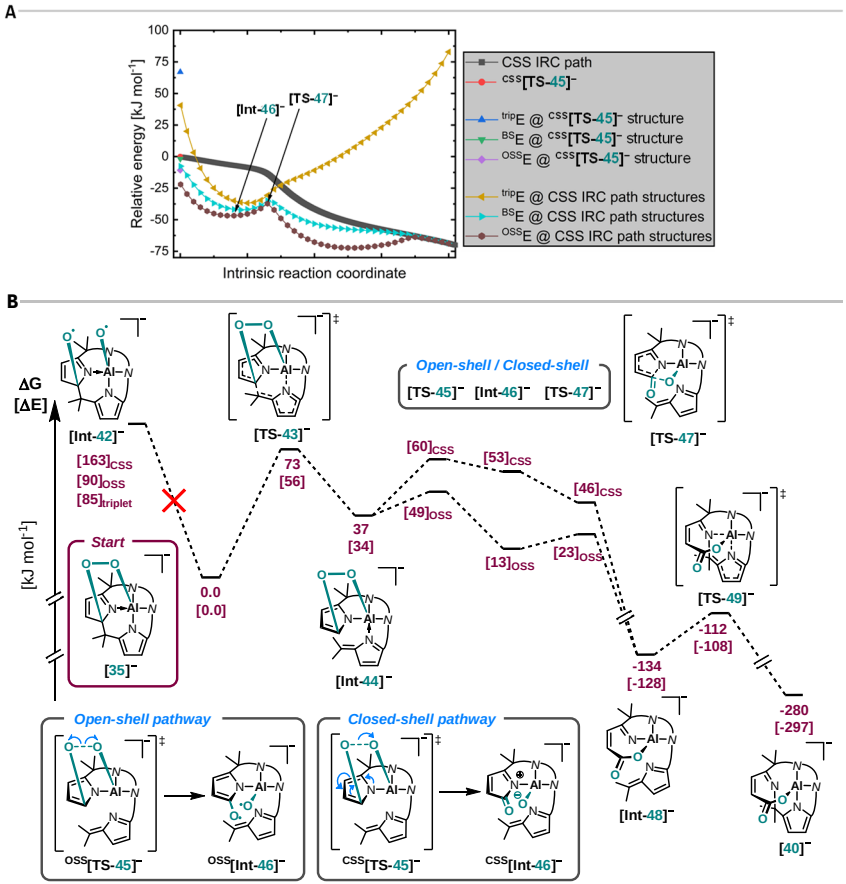

Figure 3.24: Quantum chemical calculations on the rearrangement reaction of calix[4]pyrrolato peroxido aluminate. *All computations were carried out at the B97M-D3(BJ)/def2-TZVPP level of theory. The given Gibbs free energies include COSMO-RS(CH_2Cl_2) solvation correction. Open-shell singlet energies were estimated with the help of Yamaguchi's equation (cf. Chapter 5.2).* ***A)*** *Forward closed-shell singlet IRC path starting at [TS-45]⁻ and respective triplet, broken-symmetry, and open-shell singlet energies of selected IRC structures.* ***B)*** *Proposed mechanistic pathway and calculated energy profile for the rearrangement of the peroxido to the carboxylato aluminate.*[148]

Instead, the C-C bond α to the alkyl peroxido moiety is cleaved with a Gibbs free activation energy of 73 kJ mol^{-1}. This induces the dearomatization of the adjacent pyrrole ring and the rearomatization of the peroxo-containing ring in the resulting intermediate ([Int-**44**]$^-$). From there, the reaction proceeds by detachment of the dearomatized pyrrole ring from the aluminum center and subsequent O-O bond cleavage. A respective transition state ([TS-**45**]$^-$) was located on the CSS potential energy surface. Following the

intrinsic reaction coordinate (IRC) in the productive direction revealed the located transition state to not only induce O-O bond cleavage but also C-O bond formation and C-N bond cleavage to yield [Int-**48**]$^-$ (**Figure 3.24A**). For selected molecular structures along the IRC path, the OSS energies were calculated and were found to be lower than the CSS energies. This means, that this section of the reaction mechanism most likely has singlet diradical character. The extrema along the obtained OSS energy curve were interpreted as approximate intermediate ([Int-**46**]$^-$) and transition structure ([TS-**47**]$^-$).

The experimentally observed product is formed from [Int-**48**]$^-$ after nucleophilic attack of the imine nitrogen on the exocyclic double bond ([TS-**49**]$^-$, **Figure 3.24B**). This step closes the cyclic structure of the ligand again, rearomatizes the initially dearomatized pyrrole ring, and also reattaches this ring to the aluminum center. The overall reaction is calculated to be strongly exergonic by -280 kJ mol^{-1}, and the obtained relative Gibbs free energies agree with the feasibility of the reaction at room temperature.

Conclusion

In **Chapter 3.2**, the addition reaction of triplet dioxygen to the tetraphenylphosphonium salts of *meso*-octamethyl and *meso*-octaethylcalix[4]pyrrolato aluminate was presented. The formed peroxido aluminates undergo a rearrangement reaction toward α,β-unsaturated carboxylato aluminates within 24 h at room temperature or 30 min at 60 °C. The structure of the reaction products was elucidated with NMR spectroscopical investigations supported by quantum chemical simulations.

As suggested by DFT, the rearrangement does not start out with the cleavage of the O-O bond in the peroxides but rather with the rupture of a C-C bond within the ligand backbone und subsequent detachment of one of the pyrrole rings from the aluminum center. After that, O-O bond cleavage occurs. This indicates the potential importance of the hemilability of a ligand coordination side for the reaction to occur. Likewise, the occurring aromatization/dearomatization steps are believed to be important for the reaction. Overall, the presented reactions demonstrate that aluminum-ligand cooperativity due to structural-constraint-induced Lewis acidity allows the oxidative incorporation of $^3O_2$ into a pyrrole ring, concomitant with its ring cleavage.

3.4 Further Reactivities of Calix[4]pyrrolato Aluminates

Introduction and background

As it was showcased in **Chapter 1.5** in the Introduction, metal-ligand – or more generally element-ligand cooperativity is a powerful *modus operandi* in transition metal chemistry[86] but also gets increasing attention in the context of *p*-block atom-based molecules.[19] Within this chapter, the aluminum-ligand cooperative reactivities of calix[4]pyrrolato aluminates with phenyl isocyanate, nitrogen monoxide, and nitrosobenzene is presented.

Isocyanates can formally be perceived as the imines of carbon dioxide obtained through condensation of CO_2 and a respective primary amine. As such, they were studied as substrates for various element-ligand cooperative reactions. Examples are the addition of *tert*-butyl isocyanate to pyrazolylborane **50** *via* the substrate's C=O bond to give the bora-heterocycle **51** (**Figure 3.25A**).[230] The geminal boron/phosphorus FLP **52** adds phenyl isocyanate through the N=C double bond (**53**, **Figure 3.25B**).[231] One example from transition metal chemistry within this context is the rhodium(I) complex **54** which also reacts with phenyl isocyanate under preservation of the C=O double bond (**55**, **Figure 3.25C**).[232] Examples for gallium-ligand cooperative binding of isocyanates are also known.[108]

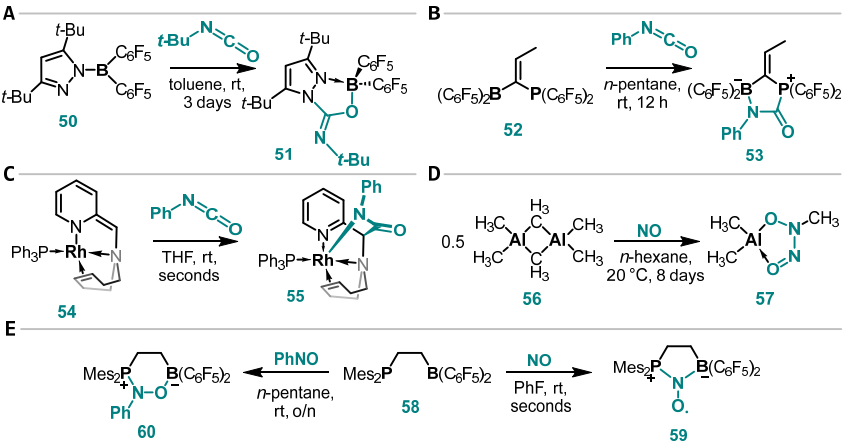

Figure 3.25: Element-ligand cooperative reactions with isocyanates, nitrogen monoxide, and nitrosobenzene as substrate.

Nitric oxide plays important roles in atmospheric as well as physiological processes.[233-236] Because of that, its chemistry, also with respect to its dimerization, was heavily studied.[237-247] Within small molecule *p*-block element chemistry, various reaction patterns of NO were discovered. For example, trimethylaluminum (**56**) inserts a ONNO dimer into one of its Al-C bonds (**57**, **Figure 3.25D**).[248-250] The formed ONNO entity is called nitrosohydroxylaminato or diazeniumdiolate group. The ammonium salt of the *N*-nitroso-*N*-phenylhydroxylamine anion and more generally its complexes with metal ions are denoted cupferron(s). Especially the ERKER group has extensively studied the reactions of nitrogen monoxide with intramolecular FLPs, *e.g.*, **58**. They trap NO in a 1,1-addition reaction to form persistent *N*-oxyl radicals (**59**, **Figure 3.25E**).[251-256] Interestingly, the reaction of **58** with nitrosobenzene was also investigated, and the 1,2-addition across the N=O double bond to form a six-membered ring in the product **60** was discovered (**Figure 3.25E**).[257] Generally, nitroso compounds are much less commonly applied in studies on element-ligand cooperativity.

Reaction of the calix[4]pyrrolato aluminate with phenyl isocyanate

meso-Octamethylcalix[4]pyrrolato aluminate ([PPh_4][**21**]) was treated with phenyl isocyanate in CD_2Cl_2 at room temperature (**Figure 3.26A**). An immediate color change of the reaction mixture from colorless to yellow was observed, which indicates the dearomatization of one of the ligand's pyrrole rings (*cf.* the previous chapters). The collected ^{1}H NMR spectrum of the reaction product proved this assumption and revealed the quantitative conversion to a single new species. Distinctive are the two mutually coupled doublets of the dearomatized ring's protons at 7.85 and 6.66 ppm, the six doublets of the unaffected pyrrole rings, as well as eight individual signals for the methyl groups of the ligand. The ^{1}H NMR resonances of the phenyl ring of the substrate are shifted upfield compared to free phenyl isocyanate.

It was possible to grow single crystals of the reaction product at room temperature from a mixture of CH_2Cl_2 and toluene which were used for SCXRD measurements (**Figure 3.26B**). The addition reaction takes place across the C=O double bond and the *N*-phenyl imidato aluminate [**61**]$^-$ is formed as its tetraphenylphosphonium salt. The imine group is *Z*-configurated in the solid state with a C=N bond length of 128.15(15) pm which is longer compared to the one in **51** (125.0 pm, *cf.* **Figure 3.25A**).[230] The newly formed Al-O bond has a length of 184.72(9) pm (*cf.* 184.8(3) pm for the Al-O bond in the addition product of CO_2 to the aluminate).[89]

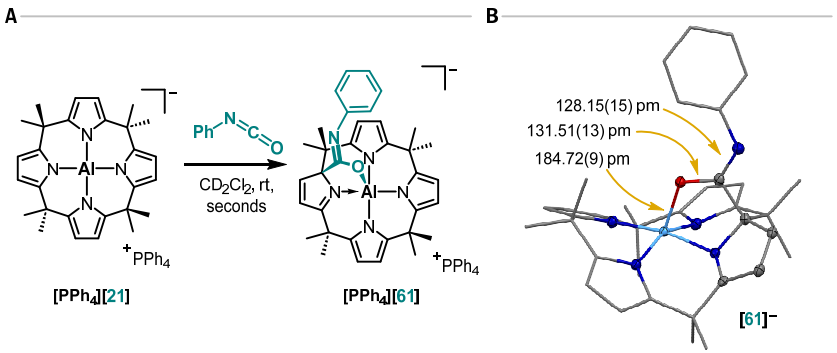

Figure 3.26: Reactivity of calix[4]pyrrolato aluminate with phenyl isocyanate. ***A)*** *Synthetic scheme.* ***B)*** *Solid-state molecular structure of the addition product as found by SCXRD analysis. The counter cation, a cocrystallized toluene molecule, and the hydrogen atoms are omitted. Thermal displacement ellipsoids are presented at a probability level of 50%.*

The reaction of calix[4]pyrrolato aluminate with phenyl isothiocyanate was tested as well under the identical reaction conditions as applied for the reaction with phenyl isocyanate. According to ^{1}H NMR spectroscopy, the dearomatization of a pyrrole ring is occurring within 24 h at 60 °C. Additional signals (rather weak in intensity) were observed indicating occurring side reactions.

Reaction of the calix[4]pyrrolato aluminate with nitrogen monoxide

Meso-octaethylcalix[4]pyrrolato aluminate ([PPh$_4$][**34**]) was reacted at room temperature with nitrogen monoxide gas (1 bar) using CD_2Cl_2 as solvent (**Figure 3.27A**). Immediately after exposure, the reaction mixture turned dark red. The acquired ^{1}H NMR spectrum showed the transformation of the starting material toward a new C_1 symmetric, diamagnetic product featuring a dearomatized pyrrole ring. Characteristic splitting patterns as just described for the phenyl isocyanate addition product were found.

The analysis of the reaction mixture with ESI(−) mass spectrometry pointed to a reaction product with an *m/z* ratio of 593.3804, which fits the expectations for the addition of one NO molecule to the aluminate. The expected *m/z* ratio with two nitrogen monoxide moieties is 623.3660. However, mono addition would result in an open-shell species of doublet multiplicity due to the uneven number of electrons introduced to the system by NO. This is inconsistent with the observed ^{1}H NMR spectrum, which clearly ascribes diamagnetism to the reaction product.

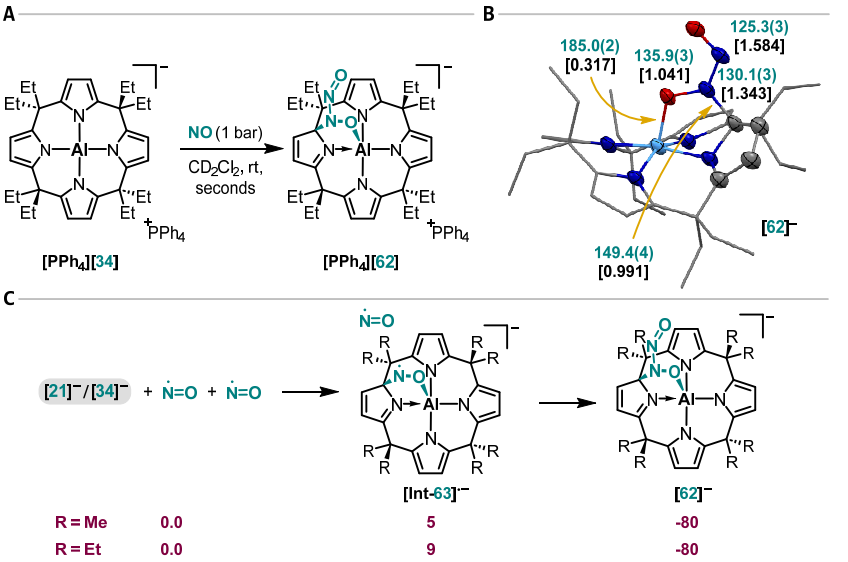

Figure 3.27: Reactivity of calix[4]pyrrolato aluminates with nitrogen monoxide. ***A)*** *Synthetic scheme.* ***B)*** *Solid-state molecular structure of the addition product as found by SCXRD analysis. The counter cation, a cocrystallized diethyl ether molecule, and the hydrogen atoms are omitted. Thermal displacement ellipsoids are presented at a probability level of 50%. The numbers in green (top) are bond lengths in pm, the values in black and brackets (bottom) are Wiberg bond indices (calculated for the methyl substituted ligand) obtained at the PBE0/def2-TZVPP computational level.* ***C)*** *Gibbs free reaction energies (kJ mol^{-1}) for the addition reaction, calculated at the RI-DSD-PBEB95-D3(BJ)/def2-QZVPP, COSMO-RS(CH2Cl2)//PBEh-3c level of theory. Values with insignificant deviation were obtained with other methods.*

SCXRD measurements caried out with single crystals obtained from a THF/diethyl ether solution resolved the contradiction and revealed the formation of *N*-nitrosohydroxylaminato aluminate [**62**]$^-$ due to aluminum-ligand cooperativity-induced dimerization of NO (**Figure 3.27B**). The Al-O bond length in the reaction product is 185.0(2) pm. In its solid-state low-temperature structure, the NO-dimer shows a NO bond length of 112(2) pm.[258-260] Within [**62**]$^-$, the analogous distance in the terminal N=O cap is with 125.3(3) pm significantly larger. The *N*-nitrosohydroxylaminato group adopts a coplanar *s*-cis structure with an O-N-N-O dihedral angle of 1.8(4)°. The N-N distance (130.1(3) pm) is significantly shortened compared to the *cis*-NO dimer (218(6) pm)[258-260], but it is larger than that of a typical N=N double bond (approximately 124 pm).[261]

To gain further understanding of the reaction, it was studied with quantum chemical calculations at the RI-DSD-PBEB95-D3(BJ)/def2-QZVPP, COSMO-RS(CH_2Cl_2)//PBEh-3c level of theory (**Figure 3.27C**). The initial step toward the observed product is assumed to

be the aluminum-ligand cooperative addition of one NO molecule to give [Int-**63**]$^{\bullet-}$. This is slightly endergonic by 5 and 9 kJ mol^{-1} for the methyl and ethyl-substituted version of the ligand. Only upon the formation of the *N*-nitrosohydroxylaminato group the reaction becomes exergonic ($\Delta G_r = -80$ kJ mol^{-1} for both ligands). The binding of the first NO equivalent to the aluminates primes the systems to form stable N-N bonds with bond dissociation enthalpies of around 140 kJ mol^{-1}. The Wiberg bond index of the N-N bond was calculated to 1.343, which indicates N-N double bond character.

Reaction of the calix[4]pyrrolato aluminate with nitrosobenzene

The putatively formed intermediate [Int-**63**]$^{\bullet-}$ in the reaction of calix[4]pyrrolato aluminate with nitrogen monoxide bears a highly reactive center due to the unpaired electron. It was therefore tested how an analogous substrate with a closed valence electron shell would react, for which nitrosobenzene was considered.

The reaction between nitrosobenzene and *meso*-octamethylcalix[4]pyrrolato aluminate ([PPh_4][**21**]) in CD_2Cl_2 at room temperature yielded a yellow solution, which was analyzed with ^{1}H NMR spectroscopy. The quantitative conversion to a new species was observed, astonishingly though, with higher symmetry as expected. The ^{1}H NMR spectrum showed four signals for the ligand's methyl groups, one set of resonances for the substrate's phenyl ring, three aromatic pyrrole rings (around 5.5 ppm, three signals), and one pyrrole ring significantly different from the others at 6.62 and 7.58 ppm. Overall, these findings indicate the presence of a mirror plane within the product's effective molecular structure on ^{1}H NMR time scale and unambiguously rule out the formation of a [Int-**63**]$^{\bullet-}$-type molecule (*cf.* **Figure 3.27C**).

Fortunately, the reaction product ([PPh_4][**64**]) readily crystalized from a CH_2Cl_2/toluene/*n*-pentane solution. The SCXRD analysis uncovered a ligand rearrangement reaction. The reacted pyrrole ring is indeed dearomatized, however, not due to the common reactivity pattern (*cf.* **Figure 3.2**, **Figure 3.11**, **Figure 3.26**, **Figure 3.27**) but because of the dual inclusion of its 5-position within the macrocyclic ligand structure. A planar [3.3.0]bicyclic substructure containing the central aluminum atom is formed, which also defines the above-mentioned mirror plane. The Al(III) atom is in almost ideal trigonal pyramidal N_4O-coordination environment. The Al-O distance amounts to 188.40(7), the N-O distance to 140.47(10) pm (*cf.* 135.9(3) pm in [**62**]$^-$, see **Figure 3.27B**). The compound is stable at room temperature when being dissolved in CD_2Cl_2.

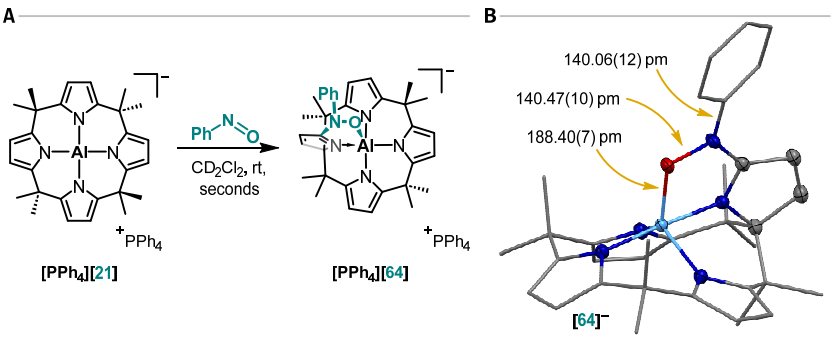

Figure 3.28: Reactivity calix[4]pyrrolato aluminate with nitrosobenzene. ***A)*** *Synthetic scheme.* ***B)*** *Solid-state molecular structure of the addition product as found by SCXRD analysis. The counter cation and the hydrogen atoms are omitted. Thermal displacement ellipsoids are presented at a probability level of 50%.*

To understand the rearrangement reaction mechanism, quantum chemical simulations using the RI-DSD-PBEB95-D3(BJ)/def2-QZVPP, COSMO-RS(CH_2Cl_2)//PBEh-3c computational method were carried out (**Figure 3.29**). The initial addition reaction to the *a priori* expected reaction product [Int-**65**]$^-$ is with −60 kJ mol^{-1} strongly exergonic. From there, the reaction is suggested to proceed by cleavage of one of the extra-pyrrolic C-C bonds. This leads to the rearomatization of the initially dearomatized pyrrole ring while one of its neighboring rings loses aromaticity. This is in analogy to the proposed reactivity of the O_2 addition product of the aluminate (*cf.* **Figure 3.24**) and of the ligand-protonated calix[4]pyrrolato gallate, which is presented in **Chapter 3.6** (*cf.* **Figure 3.36**). After that, the experimentally observed product is formed by restoration of the macrocyclic structure through C-C bond formation. This second step is the rate-determining one with a Gibbs free activation barrier of 88 kJ mol^{-1} relative to the proposed intermediate [Int-**65**]$^-$. This agrees with the observation of the reaction at room temperature. Overall, the reaction can be perceived as C-C bond metathesis. It is exergonic by 14 kJ mol^{-1}.

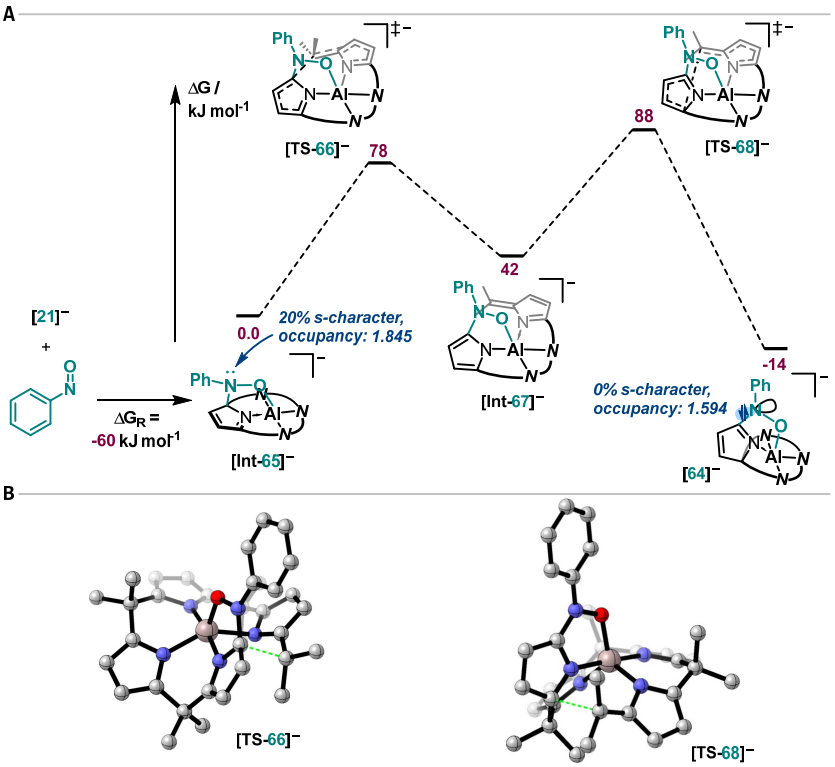

Figure 3.29: Mechanistic studies on the addition reaction of nitrosobenzene to calix[4]pyrrolato aluminate. ***A)*** *Computed reaction profile for the rearrangement reaction, obtained at the RI-DSD-PBEB95-D3(BJ)/def2-QZVPP, COSMO-RS(CH_2Cl_2)//PBEh-3c level of theory. The NBO calculation was done with PBE0/def2-TZVPP.* ***B)*** *Transition structures. All hydrogen atoms were omitted in the depictions.*

In [Int-**65**]$^-$, the nitrogen atom of the added nitrosobenzene is trigonal pyramidal. Accordingly, its lone-pair has 20% *s*-character and a natural population of 1.845 (PBE0/def2-TZVPP). This is markedly different in the product. There, the said nitrogen atom is within a trigonal planar environment, and its lone-pair is of pure *p*-character with an occupancy of 1.594. This means the driving for of the rearrangement is the extension of π-conjugation to the nitrogen's lone-pair which stabilizes the system. In case of the nitrogen monoxide addition product [**62**]$^-$ (*cf.* **Figure 3.27**), the respective lone pair is already delocalized within the *N*-nitrosohydroxylaminato group (coplanar ONNO unit). Therefore, the analogous rearrangement of [**62**]$^-$ (as it was observed for nitrosobenzene as substrate) is endergonic by 23 kJ mol^{-1} and does not take place.

Conclusion

The aluminum-ligand cooperative reactivity of *meso*-octamethylcalix[4]pyrrolato aluminate toward phenyl isocyanate, nitrogen monoxide, and nitrosobenzene was investigated. All reaction products were crystallographically characterized. They go along with the dearomatization of one of the pyrrole rings. Notably, especially the reactions with phenyl isocyanate and nitrosobenzene proceed with very high selectivity and exclusively form a single product.

For phenyl isocyanate, 1,2-addition of the C=O rather than the C=N bond was observed. A conceivable further reaction of the formed *N*-phenyl imidato aluminate, or more generally, of the imidato aluminates, is the reduction of the exposed C=N double bond, *e.g.*, through hydroboration. The chemoselective hydroboration of isocyanates is a current field of study – primarily worked on with transition metal catalysts.[262-264]

With nitrogen monoxide as reagent, the aluminum-ligand cooperativity-induced dimerization of the substrate was found to give a *N*-nitrosohydroxylaminato group. This functional group is a potent entity for complexation of transition metals, which could be explored in further studies.[265-266] Likewise, iron-based flavoproteins are known to catalyze the reduction of nitrogen monoxide. They potentially bind 2 NO molecules as *N*-nitrosohydroxylaminato group. Studying the similarities and differences of the two systems (calix[4]pyrrolato aluminate *versus* enzyme) certainly would be worthwhile.[267]

Nitrosobenzene induces a C-C bond metathesis within the calix[4]pyrrolato ligand which was rationalized with DFT calculations. Further experimental investigations could be carried out to underpin the theoretical findings on the rearrangement, *e.g.*, low-temperature NMR measurements to potentially detect the putative intermediate.

The herein presented results widened the scope of aluminum-ligand cooperative reactivity of calix[4]pyrrolato aluminates. They should serve as starting point for further investigations. Within the next two chapters, the chemistry of the calix[4]pyrrolato ligands is expanded to gallium.

3.5 Synthesis and Characterization of Calix[4]pyrrolato Gallates

The results presented within this chapter were previously published and can be found under: L. M. Sigmund, E. Engels, N. Richert, and L. Greb, "Calix[4]pyrrolato gallate: square planar-coordinated gallium(III) and its metal-ligand cooperative reactivity with CO_2 and alcohols", Chem. Sci. ***2022****, 13, 11215-11220. This chapter was written based on the mentioned publication. Some of the results shown below were generated in collaboration with* ELIANE ENGELS *and* NICK RICHERT*.*

Introduction and background

In advance of the work presented herein, the calix[4]pyrrolato ligands were already combined with aluminum[140, 142], silicon[139, 141], germanium[146], tin[143], antimony[144], and various transition metals.[15, 123-124, 137-138, 268] Hence, it was desired to expand the scope of the ligand family to gallium, the heavier homolog of aluminum, as group 13 elements are the archetypical building blocks for Lewis acids.

The synthesis of calix[4]pyrrolato aluminates is accomplished with the free and protonated ligand and with lithium aluminum hydride, which combines the base for ligand deprotonation and the source of aluminum in one reagent (*cf.* **Figure 1.11A** in the Introduction). The analogous lithium gallium hydride is commercially not available. Therefore, an alternative route was chosen, which comprises first ligand deprotonation, and second gallium installation.

Synthesis and isolation of calix[4]pyrrolato gallium complexes

Meso-octamethyl- and *meso*-octaethylcalix[4]pyrrole were chosen as ligand system and were prepared as described in the literature.[114, 148-149] Initially, the ligands were deprotonated with *n*-butyllithium to obtain their lithiated versions, which were treated with gallium trichloride. This resulted in the successful installation of gallium in the ligand, but only incomplete precipitation of lithium chloride was observed. Also, it was not possible to quantitatively exchange the lithium counter cation of the formed gallates against the non-coordinating tetraphenylphosphonium. Quantitative salt metathesis was not achieved as proved by the continuous observation of resonances in the ^{7}Li NMR spectrum of the materials.

Therefore, sodium bis(trimethylsilyl)amide (NaHMDS) was chosen as base for ligand deprotonation.[129] The sodium salts $Na_4(thf)_4$[**69**] and $Na_4(thf)_4$[**70**] were obtained by

dissolving the ligands in THF followed by treatment with NaHMDS at room temperature. In the case of the methyl ligand, the product precipitated and was separated from the liquid phase by filtration. It was purified by washing with THF. In the case of the ethyl ligand, no precipitation was observed. Therefore, the solvent was removed under reduced pressure after the reaction was complete, and the obtained solid was washed with *n*-hexane. Redissolving in THF and precipitation with *n*-pentane gave the desired deprotonated ethyl ligand.

As gallium(III) source, tetraphenylphosphonium tetrachloridogallate ($[PPh_4][GaCl_4]$) was selected, which was prepared according to the literature.[269] This allowed the complete avoidance of lithium in the system. The reactions of the tetrasodium salt of the respective ligand with $[PPh_4][GaCl_4]$ in DME at room temperature over 3 h resulted in colorless precipitates (**Figure 3.30A**). The solids were separated from the solutions by filtration, were washed with DME and *n*-pentane, and were subsequently suspended in CH_2Cl_2. It was again filtered, and the extraction of the solid phases with CH_2Cl_2 allowed the isolation of $[PPh_4]$[**71**] and $[PPh_4]$[**72**] as pale rose solids in fair yields (69 and 57%, here and in the following, the data for the methyl version is given first).

Characterizations

The ^{1}H NMR spectra of the obtained substances showed a singlet at around 5.7 ppm and two sets of aliphatic resonances from the methyl and ethyl groups, respectively (**Figure 3.30C**). These characteristics indicate effective D_{2d} molecular symmetry in solution, which is consistent with a square planar environment around the gallium atoms. Single crystals obtained from CH_2Cl_2/*n*-pentane mixtures at −40 °C suitable for SCXRD analyses proved the NMR spectroscopical data and unveiled the square planar arrangement of the N-donor sites enclosing the gallium(III) atoms (**Figure 3.30A**). The mean distances between the four nitrogen donors and gallium are 193.8(1) and 195.0(1) pm. This is larger compared to the analogous aluminum compounds (189.3(2) and 188.3(1) pm).[140, 142] The average *trans*- and *cis*-N-Ga-N angles are 178.7(1) and 178.7(1)° and 90.0(1) and 90.0(1)°, respectively. The τ_4 value[270] for both gallates was calculated to 0.02, which indicates perfect square planarity in the solid state. $[PPh_4]$[**71**] and $[PPh_4]$[**72**] were also characterized by $^{13}C\{^1H\}$ and $^{31}P\{^1H\}$ NMR spectroscopy, elemental analysis, mass spectrometry, and infrared spectroscopy.

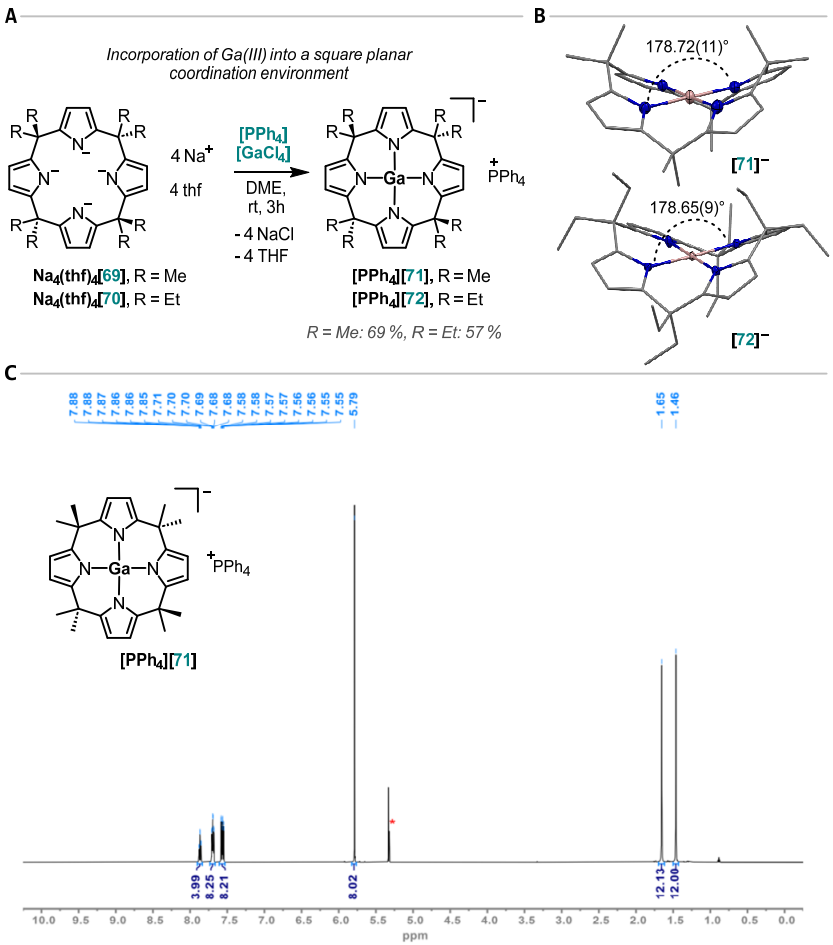

Figure 3.30: **Gallium(III) in square planar coordination environment.** ***A)*** *Synthetic scheme for the preparation of meso-octamethyl- and meso-octaethylcalix[4]pyrrolato gallate as their tetraphenylphosphonium salts.* ***B)*** *Solid-state molecular structures of the gallates as found by SCXRD analysis. The counter cations, cocrystallized solvent molecules, and the hydrogen atoms are omitted. Thermal displacement ellipsoids are presented at a probability level of 50%. CSD identifier: NEMDUI, NEMDOC.* ***C)*** *^{1}H NMR spectrum (600 MHz, CD_2Cl_2, 295 K) of [PPh_4][71]. The signal of $CHDCl_2$ and of residual CH_2Cl_2 is marked with a red asterisk.*[149]

The peculiar square planar structural arrangement was analyzed by quantum chemical techniques. Structure optimization of [**71**]$^-$ with DFT (r^2-SCAN-3c) confirmed the square planar structure as the energetic global minimum. Constrained structural optimization of [**71**]$^-$ with the valence angles around gallium set to 109.5° gave a conformer which is 581 kJ mol^{-1} higher in electronic energy as the fully relaxed structure (**Figure**

3.31C). By contrast, constraining the non-cyclic tetrapyrrolato gallate, which has an effectively tetrahedral structure in its ground state, to square planarity costs 166 kJ mol^{-1} (**Figure 3.31B**). This illustrates the strong support of the macrocyclic calix[4]pyrrolato ligand and its electronic properties (σ-accepting, π-donating)[271] as crucial for the experimental realization of the square planar configuration.

[**71**]$^-$ features an energetically low-lying LUMO (1.48 eV, r^{2}SCAN-3c, **Figure 3.31A**), having its largest coefficient (0.754 within a natural atomic orbital basis) for the *4p$_z$* orbital of the central gallium atom. By contrast, the HOMO is entirely located in the ligand backbone. This spatial separation of the frontier molecular orbitals should impart the isolated gallates with biphilic character. This is discussed in the following chapter.

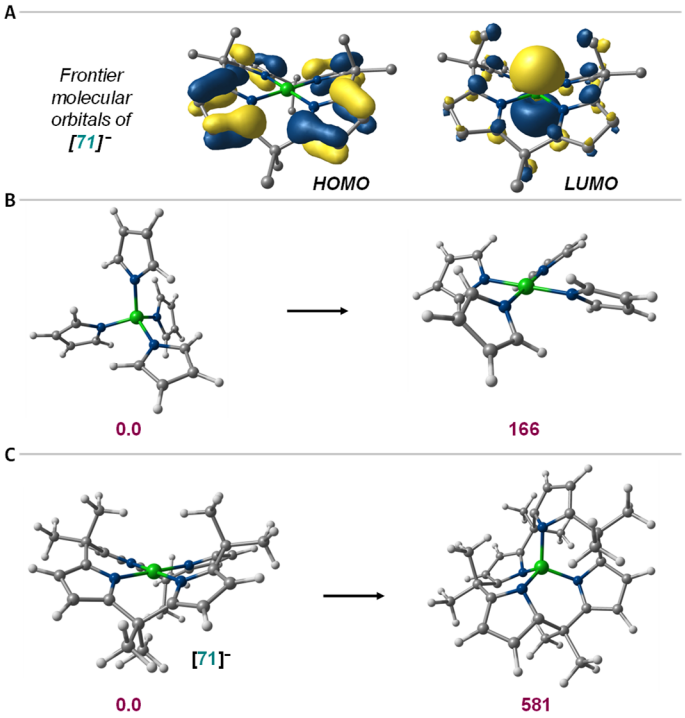

Figure 3.31: Calix[4]pyrrolato gallate investigated by quantum chemical calculations. ***A)*** *Kohn-Sham frontier molecular orbital representations of meso-octamethylcalix[4]pyrrolato gallate (r^{2}SCAN-3c). Hydrogen atoms are omitted. Structural deformation of* ***B)*** *tetrapyrrolato gallate into square planarity and* ***C)*** *of [71]$^-$ into a tetrahedral conformation around gallium. The given numbers are electronic energies in kJ mol^{-1} calculated at the RI-DSD-PBEP86/2013-D3(BJ)/def2-QZVPP//r^{2}SCAN-3c level of theory.*[149]

To probe the global Lewis acidity of the gallates, their FIA_{solv} values (CH_2Cl_2) were computed as described in **Chapter 1.4** and in the literature.[68] Values of 149 kJ mol^{-1} and 132 kJ mol^{-1} were obtained (RI-DSD-PBEP86/2013-D3(BJ)/def2-QZVPP//r^{2}SCAN-3c, COSMO-RS(CH_2Cl_2)). These are slightly reduced compared to the analogous *meso*-octamethylcalix[4]pyrrolato aluminate (196 kJ mol^{-1}), still substantial though, given the anionic charge state of [**71**]$^-$ and [**72**]$^-$. For comparison, the FIA_{solv} value of the tetrahedral tetrapyrrolato gallate is 58 kJ mol^{-1}. This corresponds to an increase in Ga-F bond strength of 90 kJ mol^{-1} mainly based on geometric effects due to square planarity around gallium.

Conclusion

Meso-octamethyl- and *meso*-octaethylcalix[4]pyrrolato gallate ([**71**]$^-$ and [**72**]$^-$) were successfully synthesized, isolated, and characterized as their tetraphenylphosphonium salts. Their square planar structure around the central gallium atoms was proved in solution and in the solid state, and it was thoroughly investigated with quantum chemical calculations. The calix[4]pyrrolato gallates represent the first examples for gallium(III) (in anionic form) with ideal square planar, anti-van't-Hoff-Le-Bel configuration. In the following chapter, the reactivity of the two gallates is presented.

3.6 Reactivity of Calix[4]pyrrolato Gallates

Some of the results presented within this chapter were previously published and can be found under: L. M. Sigmund, E. Engels, N. Richert, and L. Greb, "Calix[4]pyrrolato gallate: square planar-coordinated gallium(III) and its metal-ligand cooperative reactivity with CO_2 and alcohols", Chem. Sci. ***2022****, 13, 11215-11220. This chapter was written based on the mentioned publication. Some of the results shown below were generated in collaboration with* ELIANE ENGELS *and* NICK RICHERT.

Introduction and background

In the previous chapter, the synthesis, isolation, and characterization of two calix[4]pyrrolato gallates(III) was presented. In the here following section, their reactivity as Lewis acids and in a metal-ligand cooperative manner is discussed.

Compared to other *p*-block elements, gallium-ligand cooperativity (GaLC) is less explored.[19] Examples come from dinuclear Ga(II) species, which cooperatively bind alkynes,[105-106] isocyanates,[108] and others substrates[19, 107, 272-274]. GaLC of mononuclear complexes with amidophenolato[275] or deprotonated β-diketiminato[276] ligands is also known (**Figure 3.32**). Calix[4]pyrrolato gallate expands this series of examples.

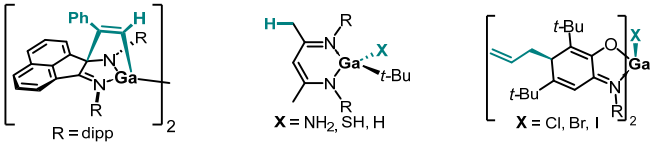

Figure 3.32: Examples for gallium-ligand cooperativity.[149]

At the end of the chapter, an oxidation reaction of the gallate is presented as well. As alluded to in the introduction, the calix[4]pyrrolato ligand can be oxidized either by two or four electrons, concomitant with the formation of one or two cyclopropane rings within the ligand backbone (*cf.* **Figure 1.10D** in the Introduction). Compared to research on the redox activity of transition metal calix[4]pyrrolato complexes, *p*-block atom calix[4]pyrrolato complexes are much less investigated in this regard. One example is the oxidation of the calix[4]pyrrolato antimonite(III) anion to yield the respective cationic stibenium(III) cation (*cf.* **Figure 1.14B** in the Introduction).[144]

Lewis acidity of calix[4]pyrrolato gallates

At first, the Lewis acidic reactivity of the gallates was probed. Quantum chemical calculations showed that the FIA_{solv} of the gallates is substantial (see **Chapter 3.5**). Therefore, [PPh_4][**71**] was reacted with one equivalent of the fluoride ion donor tetrabutylammonium difluorotriphenylsilicate (TBAT) in acetonitrile at room temperature (**Figure 3.33**, right reaction). This resulted in a pale-orange solution to which diethyl ether was added. Further addition of *n*-pentane resulted in the formation of an orange oil which was separated by centrifugation. Washing with *n*-pentane and drying at reduced pressure gave the final product in 80% yield ([PPh_4][*n*-Bu_4N][**73**]). The corresponding ^{1}H NMR spectrum showed two doublets for the pyrrolic β-protons and four signals for the methyl groups. Interestingly, the signal of the *endo*-methyl groups next to the fluoride is split into a doublet (coupling constant: 3.1 Hz). This indicates through-space fluorine-proton spin-spin coupling. The doublet splitting was also found for the signal of the carbon atom of the respective methyl groups (coupling constant: 18.3 Hz). The ^{19}F NMR spectrum showed a resonance at −146 ppm, significantly broadened due to the discussed coupling.[140] In total, this is consistent with the formation of the dianionic fluoride adduct of [**71**]$^-$. Mass spectrometry confirmed this conclusion. The results also agree with the calculated lower FIA_{solv} of fluorotriphenylsilane (85 kJ mol^{-1}) in comparison to the value of [**71**]$^-$ and further with the overall negative solution-phase Gibbs free reaction energy of −65 kJ mol^{-1} for the fluoride transfer from difluorotriphenylsilicate to [**71**]$^-$ in acetonitrile.

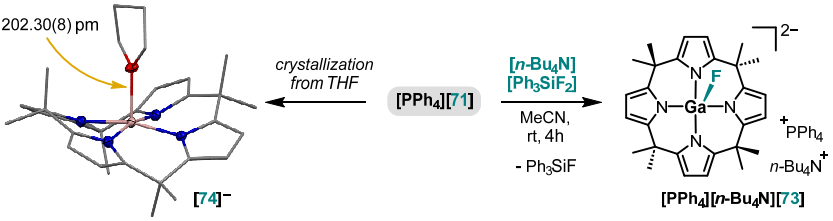

Figure 3.33: **Reactivity of calix[4]pyrrolato gallate as Lewis acid.** *Reaction scheme for the reaction with TBAT to form the fluoride adduct of the gallate (right) and solid-state molecular structure as found by SCXRD analysis of [PPh_4][71] crystallized from a THF solution (left). Thermal displacement ellipsoids are presented at a probability level of 50%. The counter cation and the hydrogen atoms are omitted. CSD identifier: NEMFAQ.*[149]

Additional experimental proof for the Lewis acidic behavior of the gallate was obtained when [PPh_4][**71**] was crystallized from THF as solvent (**Figure 3.33**, left reaction). A THF molecule coordinating to the gallium atom was observed in the solid-state structure obtained though SCXRD with a Ga-O distance of 202.30(8) pm ([PPh_4][**74**]). The computed

solution-phase affinity toward THF as Lewis base is low for both gallates ([**71**]$^-$: 0, [**72**]$^-$: −4 kJ mol^{-1}). This explains why the quantitative removal of THF during the isolation of the gallates was possible (*cf.* **Chapter 3.5**).

Reactivity of calix[4]pyrrolato gallates with carbon dioxide

After the Lewis acidity of the gallates was established, it was tested if their properties that arise from the square planar-coordinated Ga(III) atoms can serve to facilitate reactions with other substrate molecules. The calix[4]pyrrolato aluminates showed manifold reactivity with carbonyl-containing compounds in an aluminum-ligand cooperative manner.[89] Therefore, both gallates were dissolved in CD_2Cl_2 and reacted with carbon dioxide (CO_2, **Figure 3.34A**). In general, binding of CO_2 by ELC is a widely studied reaction with various transition metal[95-97, 232, 277-279] and *p*-block atom-based molecules[230, 280-287] and was also investigated in small molecule contexts other than ELC.[276, 288-294]

After the exposure to CO_2 (5 bar) at room temperature for 10 hours, the reaction mixtures turned intensively yellow within several hours. Such a color change indicates the dearomatization of one pyrrole moiety and was already previously observed with the calix[4]pyrrolato aluminates. The collected ^{1}H NMR spectra showed the clean emergence of new C_1 symmetric molecular species (**Figure 3.34B**). Together with mass spectrometric investigations, the reaction products were unambiguously identified as the gallium-ligand cooperative addition products of CO_2 to the gallates ([**75**]$^-$ and [**76**]$^-$), respectively.

The starting material conversion to [**75**]$^-$ (methyl ligand) was found almost quantitative (96%), whereas a 2:1 ratio of free gallate to addition product was observed for the ethyl case under the applied reaction conditions. The Gibbs free activation energy for the addition of CO_2 to the free gallate [**71**]$^-$ was calculated to 90 kJ mol^{-1}, and the overall Gibbs free reaction energy to 6 kJ mol^{-1} (RI-DSD-PBEP86/2013-D3(BJ)/def2-QZVPP//r^{2}SCAN-3c). This is in line with the experimental observations. Further, the computational simulations also reproduced the decreased binding strength of CO_2 to [**72**]$^-$ (ΔG_r = 18 kJ mol^{-1}). This can be rationalized by the slightly decreased Lewis acidity on the FIA_{solv} scale of the gallium atom in [**72**]$^-$. Moreover, a larger stabilization of [**75**]$^-$ in CH_2Cl_2 solution is suggested by COSMO-RS calculations (−220 for the methyl *versus* −200 kJ mol^{-1} for the ethyl gallate).

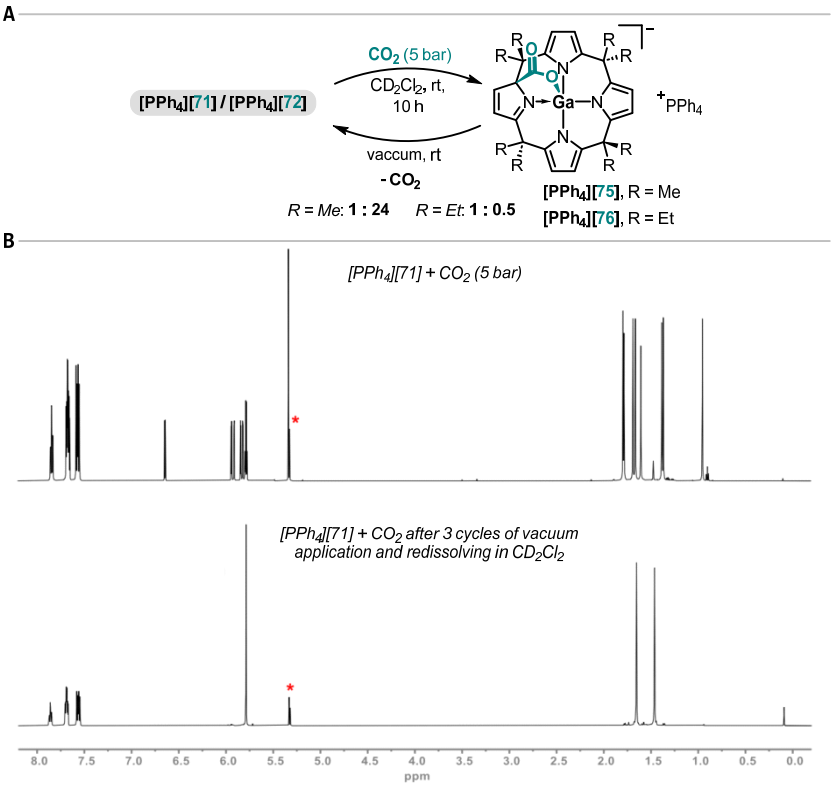

Figure 3.34: Reactivity of calix[4]pyrrolato gallates with CO_2. ***A)*** *Reaction scheme for the addition and elimination of CO_2 to/from the gallates. The given ratios were obtained in the presences of 5 bar of CO_2 (addition reaction). The elimination proceeds quantitatively when the excess CO_2 is removed.* ***B)*** *^1H NMR spectrum (600 MHz, CD_2Cl_2, 295 K) of [PPh_4][71] in the presence of CO_2 (5 bar, top) and after three cycles of vacuum application (bottom). The signal of $CHDCl_2$ and of residual CH_2Cl_2 is marked with a red asterisk.*[149]

Inspired by the computational results, the removal of CO_2 from the gallates was attempted. The application of multiple cycles of reduced pressure to solutions of [PPh_4][**75**] and [PPh_4][**76**] over several hours at room temperature resulted in the quantitative removal of CO_2 from both systems and in the selective reformation of [PPh_4][**71**] and [PPh_4][**72**] (**Figure 3.34B**). The described reaction represents the first example for reversible CO_2 fixation by a Ga(III) platform. This is achieved by the balanced energetics due to dearomatization/rearomatization of one of the pyrrole rings of the calix[4]pyrrolato ligands.

Reactivity of calix[4]pyrrolato gallates with protic substrates and Brønsted acids

Next, protic substrates, namely alcohols, came into focus as their activation by *meso*-octamethylcalix[4]pyrrolato aluminate ([PPh_4][**21**]) was already noticed. It is described in detail in **Chapter 3.1**. Upon mixing one equivalent of isopropanol with [PPh_4][**71**] and [PPh_4][**72**], respectively, in CD_2Cl_2 no reaction occurred as found by ^{1}H NMR spectroscopy (*cf.* **Figure 3.37**, left reaction), contrasting the behavior of the corresponding aluminates. This means that the gallates cannot activate and bind alcohols strong enough for an overall macroscopic binding to be detectable by NMR spectroscopy. It was reasoned that protonation of the ligand backbone might significantly increase the reactivity of the gallates by second sphere reactivity modulation. Such tactics are well-known in an alternative scenario[295], for example, applied by the COREY group in enantioselective catalysis of Diels-Alder reactions.[296-298]

To probe this hypothesis, the α-pyrrole-protonated, neutral **77** was optimized by DFT, and its electronic structure was examined (**Figure 3.35**). The α-position is the most basic site in [**71**]$^-$. The HOMO is now located almost exclusively in the pyrrole unit opposite to the protonated pyrrole ring, which itself is hosting the LUMO. The LUMO+1 resembles the former LUMO and is dominated by the contribution of the $4p_z$ orbital of the gallium atom. The calculated FIA_{solv} (CH_2Cl_2) of **77** is 191 kJ mol^{-1}. This value is more than 40 kJ mol^{-1} higher as the one for the parent, anionic gallate, hence pointing to an augmentation of Lewis acidity within the system.

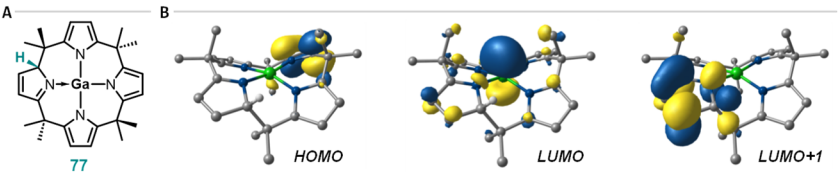

Figure 3.35: Electronic structure of protonated calix[4]pyrrolato gallate. ***A)*** *Lewis structure of the α-pyrrole-protonated, neutral derivative of the anionic gallate [71]*$^-$*.* ***B)*** *Kohn-Sham frontier molecular orbital representations of 77 calculated at the r*^{2}*SCAN-3c level of theory.*[149]

Based on the computational results, [PPh_4][**71**] and [PPh_4][**72**] were treated with bis(trifluoromethyl)sulfonimide ($HNTf_2$), which is a strong Brønsted acid, in CD_2Cl_2 as solvent at room temperature. The subsequently collected ^{1}H NMR spectra of the two reaction mixtures showed unselective reaction outcomes. The observed decomposition was further investigated with quantum chemical simulations (**Figure 3.36**). An energetically low-lying (67 kJ mol^{-1} relative to [**71**]$^-$) and at room temperature well-accessibly transition state

(TS-**78**), which accounts for the cleavage of the exopyrrolic C-C bond originating from the proton-bearing carbon atom, was found. The subsequently obtained molecule Int-**79** is essentially Gibbs free isoenergetic with **77**. Starting from Int-**79**, in which the macrocyclic ligand is ruptured, further decomposition may take place.

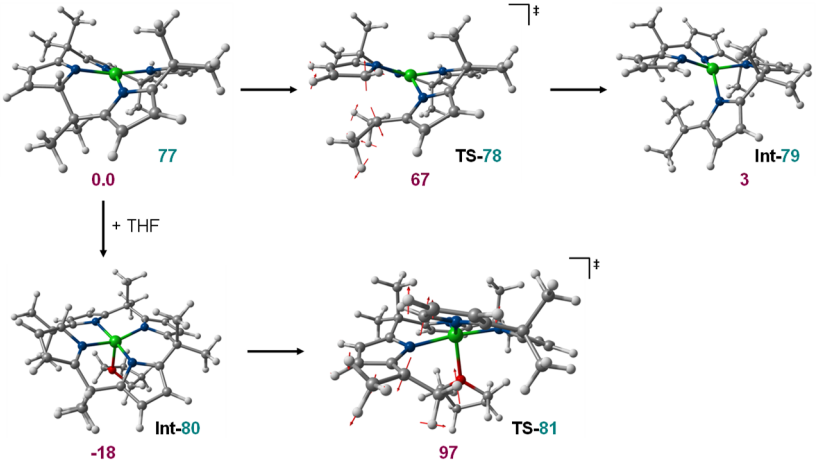

Figure 3.36: **Computational investigation of the reactivity of protonated calix[4]pyrrolato gallate.** *All given numbers are Gibbs free energies in kJ mol^{-1} and were calculated at the RI-DSD-PBEP86/2013-D3(BJ)/def2-QZVPP, COSMO-RS(CH_2Cl_2)//r^{2}SCAN-3c level of theory. The isomer of Int-80 with the thf donor syn to the additional proton was calculated to have a Gibbs free energy of –34 kJ mol^{-1} relative to 77. This gives rise to the overall activation barrier of 131 kJ mol^{-1} mentioned in the main text. The depicted arrows are the scaled displacement vectors of the single imaginary mode.*[149]

By contrast, a selective transformation took place when [PPh_4][**71**] was treated with $HNTf_2$ in THF-d_8. The collected ^{1}H NMR data revealed the dearomatization of one of the pyrrole rings, besides an additional singlet resonance at 5.02 ppm, which is assigned to the new proton in the α-position of the dearomatized pyrrole ring. This is explained with the Lewis basic properties of THF which suppress the undesired decomposition pathway. Indeed, when the C-C bond cleavage transition state was remodeled in the presence of an explicit THF molecule coordinating to the gallium center in Int-**80**, a significant increase in Gibbs free activation energy to 131 kJ mol^{-1} was obtained (**Figure 3.36**). When the reaction of [PPh_4][**71**] with $HNTf_2$ was repeated in a mixture of CD_2Cl_2 and diethyl ether (2:1 %vol), the same ^{1}H NMR characteristics as detected for the reaction in THF-d_8 were found. This supports the Lewis base stabilization rationale.

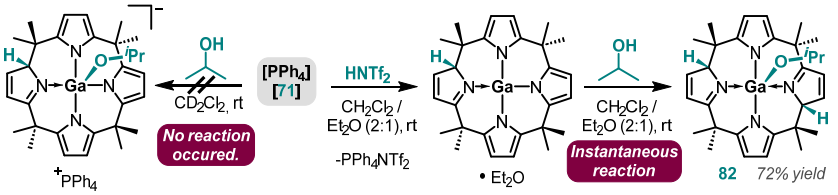

Figure 3.37: Reactivity of calix[4]pyrrolato gallate with isopropanol.[149]

Having the protonation of the calix[4]pyrrolato ligand backbone under control, the reaction with isopropanol was repeated with the *in situ* generated **77** in the CH_2Cl_2/diethyl ether mixture (**Figure 3.37**, right reaction). After stirring the reaction mixture at room temperature for 1 min, the solvents were removed. Extraction with *n*-pentane/diethyl ether (4:1 %vol), gave a pale-yellow solid in 72% yield. The compound's ^{1}H NMR spectrum showed the formation of a symmetric species having two dearomatized pyrrole rings due to protonation at their respective 2-positions. Also, the resonances of an *iso*-propyl group with shifted signals compared to the free substrate were contained. These observations unequivocally point to the formation of the neutral O-H bond addition product **82** by a gallium-ligand cooperative mechanism. Whereas the anionic parent gallate [**71**]$^-$ on its own is not able to split the O-H bond through gallium-ligand cooperativity, the protonated, neutral **77** (Lewis base-stabilized) instantaneously adds isopropanol. This confirms the hypothesis that the reactivity of calix[4]pyrrolato gallates, and molecules including a calix[4]pyrrolato ligand in general, can be enhanced by protonation of the ligand backbone. These insights can be used in future research efforts to further develop the concept of Lewis acidity enhancement through ligand backbone protonation.

Oxidation of the calix[4]pyrrolato gallate

To close this chapter, the reactivity of *meso*-octamethylcalix[4]pyrrolato gallate with an oxidant, *viz.*, ferrocenium hexafluorophosphate ($FcPF_6$) is presented (**Figure 3.38A**). The reaction was carried out in THF-d_8 as solvent at room temperature. A dark brown reaction solution was immediately obtained, which was analyzed with ^{1}H NMR spectroscopy. A selective transformation was observed. For the protons of the pyrrole rings, a set of four doublets was found which all had the same integration value. They appeared at 8.44, 7.46, 6.17, and 6.15 ppm, which indicates the dearomatization of two of the four pyrrole units. For the methyl groups, six singlet resonances were found.

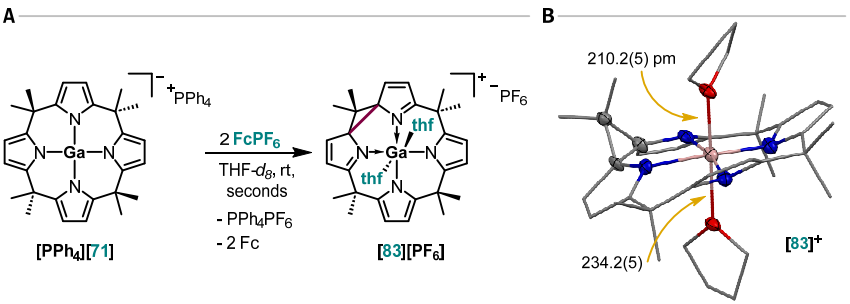

Figure 3.38: Reactivity of calix[4]pyrrolato gallate with ferrocenium hexafluorophosphate. ***A)*** *Synthetic scheme.* ***B)*** *Solid-state molecular structure of the reaction product as found by SCXRD analysis. The counter anion, a cocrystallized THF molecule, and the hydrogen atoms are omitted. Thermal displacement ellipsoids are presented at a probability level of 50%.*

It was possible to grow single crystals suitable for SCXRD measurements from a THF/diethyl ether solution at −40 °C (**Figure 3.38B**). They identified the reaction product as the hexafluorophosphate salt of the delta-calix[4]pyrrolato gallium cation in form of its bis-thf-adduct ([**83**][PF_6]). The central gallium atom is in a distorted octahedral coordination environment. The oxygen-gallium distances measure 210.2(5) and 234.2(5) pm with the thf donor *syn* to the cyclopropane ring is more closely bound. The mean Ga-N distances are 205.0(6) for the two dearomatized pyrrole rings and 192.1(6) pm for the aromatic pyrrole moieties. The newly formed C-C bond (cyclopropane ring) has a bond length of 154.7(9) pm.

The obtained results show the significant increase in Lewis acidity upon oxidation of the ligand. While the anionic calix[4]pyrrolato aluminate only loosely interacts with one equivalent of THF as Lewis base as described above, the cationic species captured two THF donors. This is underlined by the computed FIA_{solv} value (CH_2Cl_2, *cf.* **Figure 1.8** in the Introduction) of the free cation which is 243 kJ mol^{-1}, corresponding to an increase of 94 kJ mol^{-1} with respect to the parent gallate (149 kJ mol^{-1}). Compared with backbone protonation, ligand oxidation appears as a more powerful handle for Lewis acidity enhancement based on the FIA_{solv} scale (*vide supra*).

Conclusion

The reactivity of calix[4]pyrrolato gallates was researched. It emerges from the Lewis acidic central Ga(III) atom. The Lewis adducts of the gallate with the fluoride anion and THF were synthesized. Carbon dioxide was found to reversibly bind to both studied gallates, and the equilibrium constant is dependent on the substituents in the *meso*-position.

The addition of CO_2 can be fully reversed to regenerate the free gallates. This contrasts the reactivity of the analogous aluminates for which CO_2 elimination from the respective addition product was only possible after the addition of more strongly binding substrates.[89] The protonation of the ligand backbone was discovered as a lever to increase the Lewis acidity and thereby the reactivity of calix[4]pyrrolato gallates, though it also introduces instability to the ligand backbone. In fact, the cleavage of one of the exopyrrolic C-C bonds is also part of the rearrangement reaction mechanisms presented in **Chapters 3.3** and **3.4**. Generally, the propensity of the calix[4]pyrrolato ligand system to undergo reactions initialized by the cleavage of the said C-C bond substantiates. Ultimately, the redox chemistry of the calix[4]pyrrolato gallate was initially studied. Similar to ligand protonation, ligand oxidation also transpires to increase the Lewis acidity of the gallate. This lays the basis for furth explorations in this direction.

p-Block atoms in their highest oxidation state and within a square planar coordination environment are definitely the exception compared to the much more common tetrahedral arrangement of the substituents around the central atom. If accessible with the help of structurally constraining ligand frameworks, unique reactivity patterns can be explored as it was demonstrated in the preceding six chapters. The following two chapters aim to provide an in detail understanding of the electronic structure of "square planar *p*-block atoms" on the basis of quantum chemical simulations which is essential for the further development and application of anti-van't-Hoff-Le-Bel species.

3.7 Tetrasubstituted *p*-Block Atoms in Square Planar Structure

The results presented within this chapter were previously published and can be found under: L. M. Sigmund, R. Maier, and L. Greb, "The inversion of tetrahedral p-block element compounds: general trends and the relation to the second-order Jahn–Teller effect", Chem. Sci. ***2022****, 13, 510-521. This chapter was written based on the mentioned publication. Some of the results shown below were generated in collaboration with* ROUVEN MAIER.

Introduction and background

The tetrahedron dominates the structural chemistry of the *p*-block's elements, *e.g.*, that of carbon, aluminate anions, silanes, or ammonium cations. It constitutes the fundamental building block for the molecular architecture of our bio- and geosphere. For species with eight valence electrons and four substituents, the tetrahedral preference is well-founded by molecular orbital theory, as it was showcased with full details in **Chapter 1.2** in the Introduction.[21, 299] Within this chapter, the investigations on the square planar state of small *p*-block atom-based molecules encompassing six elements and ten different substituents are presented (**Figure 3.39A**).

Generally, the square planar structures have been perceived to correspond to high-energy states of only theoretical interest. However, in recent years, several "anti-van't-Hoff-Le-Bel" species (*i.e.*, isolated square planar states), such as planar aluminates, silicon compounds, or phosphonium ions, were realized experimentally.[140, 147, 182, 300-311] Hence, the knowledge on square planar *p*-block atoms is transforming from fundamental to applied interest. This is why it was decided to incorporate quantum chemical simulations on square planar and related structural states into this dissertation project.

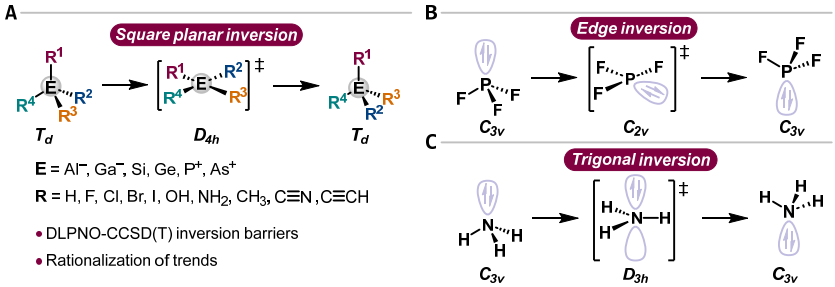

Figure 3.39: Stereoinversion in *p*-block atom-based molecules.[7]

In fact, the square planar states can serve as transition structures for stereochemical inversion of respective molecules, and they were previously discussed in this context (*cf.* **Chapter 3.8**).[26] Also, for SiF_4 and PF_4^+, analogies with the edge inversion mechanism applicable to trigonal group 15 compounds with electronegative substituents were found (*e.g.*, PF_3, **Figure 3.39B**).[30-31] Less electronegative groups attached to trivalent group 15 centers typically lead to the trigonal inversion pathway (**Figure 3.39C**), which was heavily studied in the past.[312-314] Different approaches to the inversion of $\mathbf{ER_3}$ molecules, like perturbational molecular orbital theory,[21, 50, 315-316] the second-order Jahn-Teller effect (SOJTE),[51-54] or recoupled pair bonding[317] were pursued, which widened our understanding of chemical bonding in main-group element chemistry.[318-319]

Applied computational methods

The data which is shown in the following was obtained at the DLPNO-CCSD(T)/cc-pVQZ//B97M-D3(BJ)/cc-pVTZ theoretical level.[320] If not stated otherwise, the numbers are given as relative electronic energies. 270 of the 276 attempted transition state calculations were successful. This was confirmed by numerical Hessian evaluations and IRC computations. The applied DLPNO-CCSD(T) method was benchmarked against CCSD(T)/CBS data, and a MAE of 1.3 kJ mol^{-1} was found. The influence of diffuse basis functions was investigated as well (aug-cc-pVQZ) and was found minor. On average, inversion energies were 2.2 kJ mol^{-1} lower as with cc-pVQZ. For a selected number of molecules, the HOMO-LUMO gap of the inversion transition state (as the key value of the study) was compared to the respective vertical excitation energy to the lowest energy excited singlet state obtained by time-dependent DFT (TD-DFT). Good correlations were obtained justifying the use of the HOMO-LUMO gap. The references to used software, methods, and basis sets are given in **Chapter 5.2**.

Trends and effects due to mono-substitution

The comparison of the inversion barriers of mono-substituted $\mathbf{EH_3R^n}$ molecules with the value of $\mathbf{EH_4^n}$ allowed to assess the influence of the respective substituent **R** (**Figure 3.40**). The stabilization energies range from around 10 (methyl) to 180 kJ mol^{-1} (amino) with respect to the barriers of the unsubstituted $\mathbf{EH_4^n}$. For the group 13 halide anions $\mathbf{EH_3R^-}$ (R = F, Cl, Br, I), the transition state energy gets increasingly lowered for the heavier halides. For the neutral group 14 molecules and the group 15 cations, fluoride, and iodide

substituents[c] stabilize more efficiently than chloride and bromide. The stabilizing effect of the hydroxy group is larger than that of the halogen ligands in groups 14 and 15. In general, the amino group has the most powerful impact of all considered substituents (up to 180 kJ mol^{-1} in $PH_3(NH_2)^+$ *versus* PH_4^+). The ligands without the electronic ability for π-donation (methyl, nitrile, and ethynyl) stabilize less effectively but still substantially (up to 40 kJ mol^{-1}).

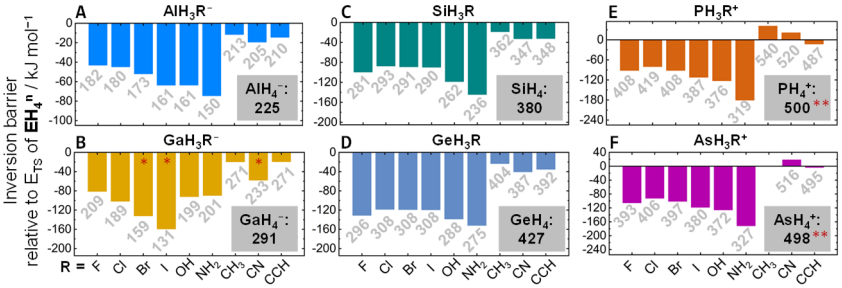

Figure 3.40: **Mono-substitution effects on inversion barrier heights.** *The inversion barriers (deformation energy toward the square planar state) were calculated at the DLPNO-CCSD(T)/cc-pVQZ//B97M-D3(BJ)/cc-pVTZ level of theory. The label on each bar gives the respective absolute inversion barrier of EH_3R^n. No inversion transition state was found for $AsH_3(CH_3)^+$.* The transition structure optimization converged to a dissociative structure (GaH_3 and R^-). ** The inversion barriers were obtained with NEVPT2/cc-pVQZ//CASSCF(8,8)/cc-pVTZ (see Chapter 3.8 for more details).*[7]

The effect of substitution is more pronounced for groups 14 and 15 than for group 13. Also, it has more influence on third period-based compounds compared to the fourth period analogs (**Figure 3.40**). Regarding the central element, the inversion barriers increase significantly when going from left to right in the periodic table (Al<Si<P and Ga<Ge<As), with the group 15 element cations showing the largest stereoinversion barriers. When comparing the third- and fourth-period elements within one group, the trend of the inversion barrier is Al < Ga, Si < Ge but P > As. As expected, the difference between the periods 3 and 4 is less pronounced than that between the individual groups, and it is often outmatched by additive substitution effects.

[c] The terms "ligand" and "substituent" are used interchangeably within this chapter.

Additive substituent effects

The consecutive replacement of the hydrogen substituents against R groups revealed additive ligand effects on the inversion barrier heights. For the series of the halogens and the amino group, **$EH_{4-y}R_y^n$** (R = F, Cl, Br, I, NH_2), the largest stabilization is reached with two substituents in *trans*-arrangement, as shown for the silicon halides in **Figure 3.41A**. The stereoisomeric *cis*-**$EH_2R_2^n$** transition states are roughly 50 kJ mol^{-1} higher in electronic energy than the *trans*-versions. The trend along the transition **$EH_2R_2^n$** ⟶ **EHR_3^n** ⟶ **ER_4^n** depends on the central element. For the period three elements (E = Al, Si, and P), the barriers rise, ultimately reaching energies like found for the monosubstituted **EH_3R^n** (**Figure 3.41A**). This means that counter-stabilizing effects occur upon addition of more than two R groups. For the fourth-period cases, the trend is different: the barriers remain invariant along two, three, and four substituents, *i.e.*, the stabilizing and destabilizing effect cancel (**Figure 3.41B**).

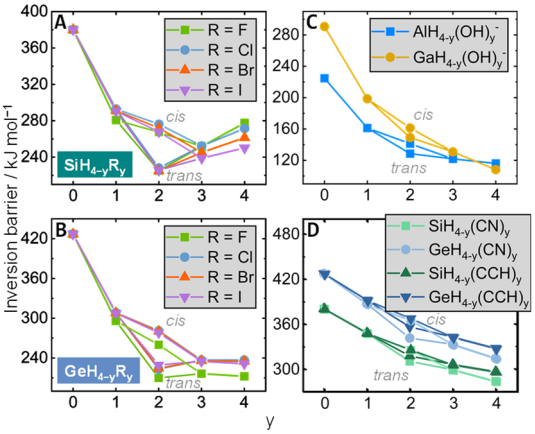

Figure 3.41: Additive substituent effects. *Stereoinversion barrier heights of* ***A)*** *$SiH_{4-y}R_y$, and* ***B)*** *$GeH_{4-y}R_y$, with R = F, Cl, Br, and I, of* ***C)*** *$AlH_{4-y}(OH)_y^-$ and $GaH_{4-y}(OH)_y^-$, and of* ***D)*** *$EH_{4-y}R_y$, with E = Si, Ge and R = CN, CCH. The inversion barriers (deformation energy toward the square planar state) were calculated at the DLPNO-CCSD(T)/cc-pVQZ//B97M-D3(BJ)/cc-pVTZ level of theory.*[7]

Interestingly, the molecules with hydroxy groups show no saturation effect; exceptions are silicon and phosphorus, which show minor saturation. For the other cases, the four-fold substituted **$E(OH)_4^n$** have the lowest energy transition states (E = Al, Ga, Ge, As, **Figure 3.41C**). This deviation may be explained by hydrogen bonding, which is especially efficient in the transition structures (**Figure 3.42**). A comparison of different transition

state conformers of the **EH(OH)$_3^n$** class of molecules allowed to estimate the transition state stabilization for the individual elements to approximately 5 (E = Al), 10 (E = Ga), 12 (E = Si), 15 (E = Ge), and 21 (E = P, As) kJ mol^{-1} per hydrogen bond. When, TS1-**EH(OH)$_3^n$** was compared with TS2-**EH(OH)$_3^n$** and TS3-**EH(OH)$_3^n$** with TS4-**EH(OH)$_3^n$** (*cf.* **Figure 3.42**), it was found that the two energy differences are of comparable size, and the mean values were taken as the approximate stabilization influence.

The absence of a saturation effect with increasing degree of substitution was also found for the nitrile and ethynyl ligands (**Figure 3.41D**). The inversion barrier heights steadily drop with each additional substitution. They find a minimum for the four-fold substituted derivatives **ER$_4^n$** (R = CN, CCH).

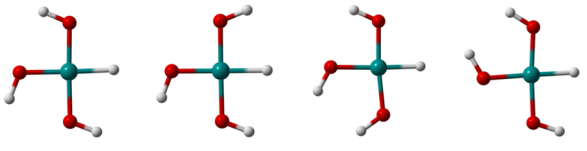

Figure 3.42: Conformational space of GaH(OH)$_3^-$ in square planar configuration.[7]

Low activation barriers for stereochemical inversion

Some molecules possess barriers for stereoinversion that are exceedable at ambient conditions. One example are the di-substituted group 13 anions (**EH$_2$R$_2^-$**). They show unexpectedly low inversion barriers; *e.g.*, *trans*-AlH$_2$(NH$_2$)$_2^-$, with a value of 103 kJ mol^{-1}. This corresponds to a configurational stability half-live at 298.15 K of less than two hours calculated from the corresponding Gibbs free activation energy for stereoinversion which is 106 kJ mol^{-1}. Likewise, the experimentally accessible Al(NH$_2$)$_4^-$ has a barrier for stereochemical inversion of $\Delta G^{\ddagger}$ = 122 kJ mol^{-1}. Most remarkably, the stereoinversion of Al(OH)$_4^-$ has a Gibbs free activation energy of 130 kJ mol^{-1}. Tetrahydroxo aluminate is a well-known anion which is formed during worldwide aluminum production (BAYER process).[321] Process temperatures of around 200 °C correspond to a tetrahedron inversion half-life for Al(OH)$_4^-$ of approximately 15 seconds. Thought-provokingly, a tetrahedral inversion process is most likely happening since more than 130 years at gigatonne scale. The hydroxide ion affinity (on ΔG scale) of Al(OH)$_3$ was calculated to 394 kJ mol^{-1} in the gas phase and 173 kJ mol^{-1} in aqueous solution, which is significantly larger than the stereoinversion activation energy.

MO considerations

In the following, the intrinsic reaction coordinate (IRC) which is connecting the T_d symmetric ground state with the inversion transition state (D_{4h} symmetry) is analyzed for SiH_4, SiF_4, and $Si(CN)_4$ (**Figure 3.43**). The comparative analysis among those three compounds illustrates the effects of π-donor or σ-acceptor substituents on the orbital energies. For the D_{4h} symmetric states of the element hydrides $\mathbf{EH_4^n}$ (E = Al^-, Si, Ga^-, Ge), the Kohn-Sham molecular orbitals agree with the qualitative MO-picture given in **Figure 1.2** in the introduction: a HOMO of b_{1g} and LUMO a_{2u} symmetry. This situation is quantitatively illustrated for SiH_4 in **Figure 3.43A**. In fact, SiH_4 possesses a rather small frontier molecular orbital (FMO) gap of 1.1 eV in its square planar state. Contrastingly, for molecules with σ-acceptor/π-donor substituents, *e.g.*, SiF_4 (Fig. 5B), the energetic spacing between the FMOs (6.7 eV in the case of SiF_4) is much wider in the D_{4h} state than it is for the hydride analog. This difference is the consequence of the following points.

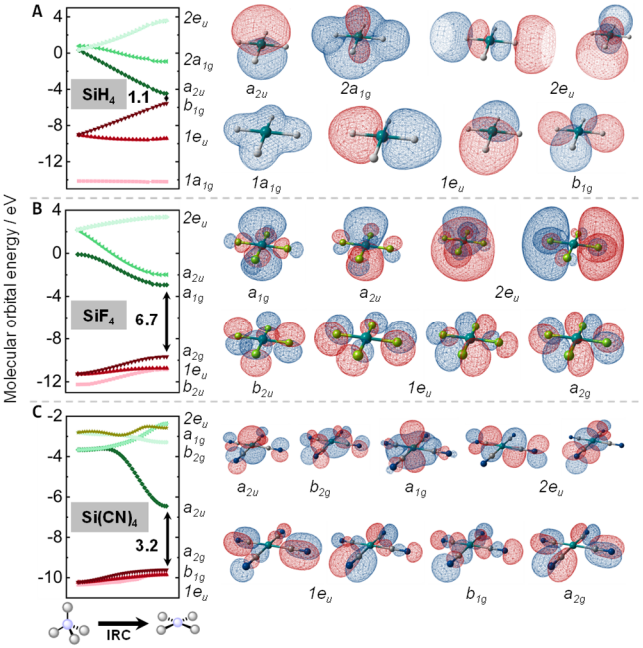

Figure 3.43: Molecular orbital energies during stereoinversion. *Kohn-Sham frontier molecular orbital energies along the inversion reaction coordinate and the corresponding isodensity plots of the square planar inversion transition state shown for* ***A)*** *SiH_4,* ***B)*** *SiF_4, and* ***C)*** *$Si(CN)_4$. The data was obtained at the B97M-D3(BJ)/cc-pVTZ level of theory.*[7]

The a_{2u} orbital in square planar SiH_4 is non-bonding, whereas its counterpart in the tetrahedral ground state ($2t_2$) is fully anti-bonding. Therefore, it drops considerably by 5.3 eV due to planarization. For SiF_4, this drop is reduced to 4.1 eV, as the a_{2u} orbital remains slightly anti-bonding in the D_{4h} state because of the π-donor interaction of the central silicon with its fluoride substituents (π-donor effect). All the highest occupied molecular orbitals of the square planar states are ligand-based. Hence, they are substantially lower in energy in case of SiF_4 (electronegative fluoride substituents) than for SiH_4 (σ-acceptor effect).

The described effects increase the FMO gap in the D_{4h} symmetric state and influence the energetic ordering of the orbitals as well. The diminished energy drop of the empty a_{2u} orbital in SiF_4 during approaching square planarity causes the LUMO to be of a_{1g} symmetry. The a_{2u} molecular orbital is the LUMO+1 (**Figure 3.43B**).

The MO-situation for $Si(CN)_4$ can be regarded as a mixture of the hydride and fluoride case (**Figure 3.43C**). As it was found for SiH_4, the a_{2u} orbital drops substantially, though the occupied orbitals remain little affected, resembling the situation of SiF_4. These characteristics reflect the σ-acceptor character of the nitrile group but the inability for π-donation, which would prevent the a_{2u} orbital from getting lowered in energy (as is the case for SiF_4).

Analysis with respect to the second-order Jahn Teller effect

As alluded to in the introduction of this dissertation (*cf.* **Chapter 1.3**), the SOJTE applies to the rationalization of the instability of the square planar states in case of the element-hydrogen compounds.[55] So, it was probed how the SOJTE's approximate FMO interpretation (*cf.* **Equation 1.5**) relates to the planarization energies – also for substituents other than hydrogen.

For the element hydrides, $\mathbf{EH_4^n}$, a perfect linear correlation is obtained when the electronic inversion barrier is plotted against the HOMO-LUMO gap of the square planar state (**Figure 3.44A**). The smaller the FMO gap, the larger the inversion activation barrier. PH_4^+ and AsH_4^+ were excluded from the analysis as their electronic structure in the D_{4h} symmetric state differs significantly from that of the group 13 and 14-based molecules, which is discussed in **Chapter 3.8** (*vide infra*).

As shown in **Figure 3.44I** and J, also systems with σ-acceptor substituents (nitrile and ethynyl) show this excellent correlation, indicating that these molecules also obey the SOJTE-model. It even holds well for the entire set of $\mathbf{EH_{4-y}R_y^n}$ (R = CN, CCH, see **Figure 7.18** in the Appendix). The combination of the data for the hydrogen, nitrile, and ethynyl

substituents in one graph gives an offset between the two groups (see **Figure 7.19** in the Appendix). This is most likely because of differences in the further contributions to the overall SOJTE (*cf.* **Equations 1.3**) which are not captured by the simplified FMO approach. Interestingly, the ethynyl and nitrile data align well – both ligands bind through *sp*-hybridized carbon atoms to the central atoms (see **Figure 7.19** in the Appendix).

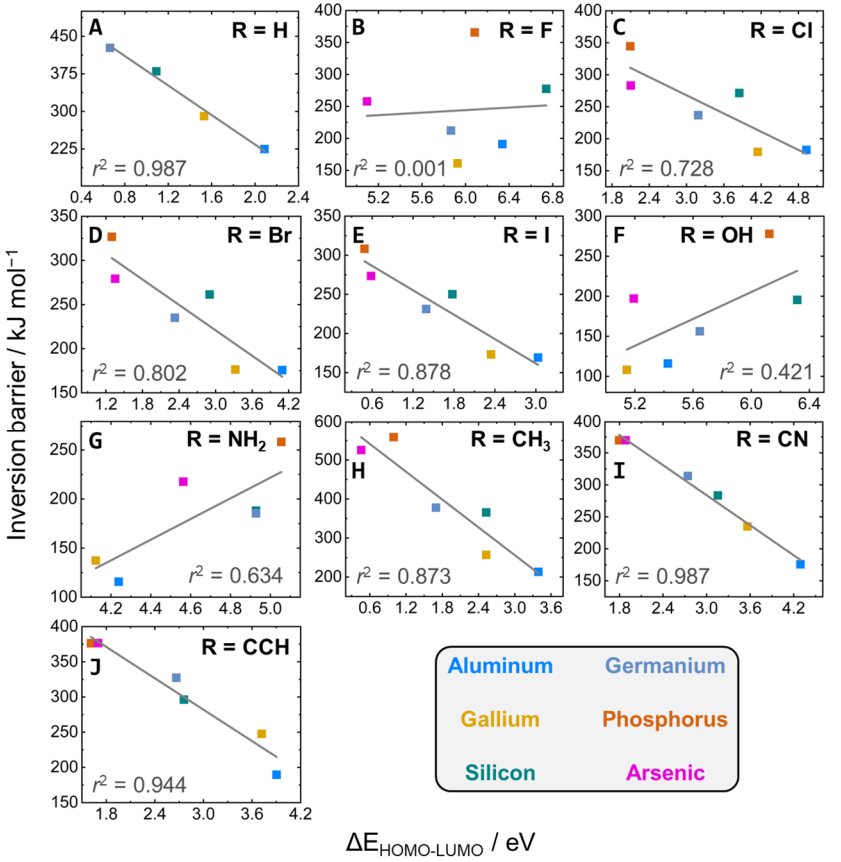

Figure 3.44: The frontier molecular orbital approximation of the second-order Jahn-Teller effect applied to square planar *p*-block atom-based molecules. *The inversion barriers (deformation energy toward the square planar state) were calculated at the DLPNO-CCSD(T)/cc-pVQZ//B97M-D3(BJ)/cc-pVTZ level of theory and orbital energies were extracted from the B97M calculations. The HOMO-LUMO gap of the square planar states ($\Delta E_{HOMO\text{-}LUMO}$) is plotted for the molecules of constitution ER_4^n ($n = -1$ for E = Al, Ga, $n = 0$ for E = Si, Ge, $n = +1$ for E = P, As).*[7]

Overall, these findings can be contextualized as follows. The LUMO (a_{2u} symmetry) is localized at the central atom whose electronegativity largely influences its orbital energy.[21] A high electronegativity causes a lower a_{2u} orbital energy which leads to a smaller HOMO-LUMO gap. Consequently, the inversion barrier increases with the electronegativity of the central atom. On the other hand, the HOMO (b_{1g} symmetry) is located at the substituents. Thus, its energy is heavily influenced by the substituents' (group) electronegativity. An increasing ligand electronegativity lowers the HOMO energy and, therefore, the energy gap between HOMO and LUMO. Consequently, the inversion barrier decreases with the electronegativity of the substituents.

Indeed, the electronegativity increases from left to right in the periodic table, as does the planarization energy (Al<Si<P, Ga<Ge<As). Likewise, the electronegativity increases from period three to period four, which also is in line with the observed trend of inversion barriers between the periods (Al<Ga, Si<Ge, P≈As). If the HOMO-LUMO gap becomes too small in the D_{4h} symmetric state, as for the most electronegative central atoms P and As, multiconfigurational approaches are needed for an accurate description (see the following chapter).

Next, the difference of (group) electronegativities of central atom and substituents as a descriptor for the inversion barrier was probed. For the non-π-donor ligands (H, CH_3, CN, CCH), proper linear correlations were found (**Figure 3.45**). Again, an offset occurs between the different sets of ligands. Interestingly, the group electronegativities of the nitrile (3.3) and ethynyl (3.3) group are identical.[322] Accordingly, their data aligns very well in the plot in **Figure 3.45**, and their effect on the inversion barriers is almost the same (*cf.* **Figure 3.40** and **Figure 3.41**).

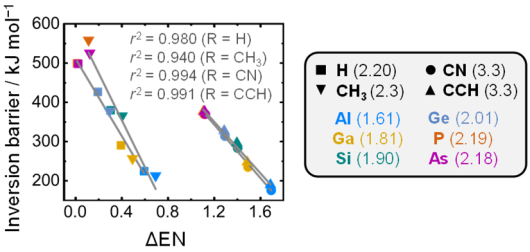

Figure 3.45: The relationship of the barrier for stereoinversion to electronegativity differences between substituents and central atom. *The inversion barriers (deformation energy toward the square planar state) were calculated at the DLPNO-CCSD(T)/cc-pVQZ//B97M-D3(BJ)/cc-pVTZ level of theory. Molecules of constitution ER_4^n ($n = -1$ for E = Al, Ga, $n = 0$ for E = Si, Ge, $n = +1$ for E = P, As) were investigated. Pauling (group) electronegativities are given in parenthesis in the legend.*[7]

Lastly, the approximate SOJT model was applied to π-donor cases. For the fluoride substituted derivatives, **EF_4^n**, the SOJT-correlation breaks down entirely (**Figure 3.44B**). There is no linear relation between the planarization energies and the FMO gap in the square planar state. Within the FMO-SOJT model this can be explained with the absence of the b_{1g} symmetric occupied MO among the highest occupied ones (*cf.* **Figure 3.43B**). For D_{4h} symmetric SiF_4, the b_{1g} orbital is the HOMO−6 which is separated from the a_{2u} (LUMO+1) orbital by 10.0 eV – a massive energetic gap. For GeF_4, the b_{1g}-a_{2u} separation is 8.0, for AlF_4^- 8.7, for GaF_4^- 7.5, for PF_4^+ 9.3, and for AsF_4^+ 7.5 eV. These values are all significantly larger as they are for cases in which a SOJT correlation was observed (FMO gaps below 5 eV). The model recaptures its validity along the series Cl<Br<I with a steady increase in the correlation coefficient (**Figure 3.44C** to **E**). Here, the energetic separation between occupied and unoccupied MOs is considerably lower. For example, the HOMO-LUMO gap in square planar SiI_4 is 1.8 eV, and the b_{1g}-a_{2u} separation is 3.2 eV. Interestingly, the data is clearly separated with respect to the row of the periodic table in which the central atom is located, and the separation diminishes along Cl, Br, I.

For the OH and NH_2 substituted cases the expected correlation was not found (**Figure 3.44F** and **G**). Instead, the inversion barrier even tends to increase with increasing HOMO-LUMO gap, though only with very poor linear dependency. Again, it was found that the energetic separation between the b_{1g} and a_{2u} FMO, which are the basis for the approximate SOJT model, is larger – for $Si(NH_2)_4$ it is 9.1 eV. In the case of the OH ligands, the influence of the hydrogen bond stabilization in the square planar state as an additional factor might contribute to the absence of the SOJT correlation.

In summary, for π-donor substituted systems, additional factors cause deviations from the SOJTE-FMO model and simple HOMO-LUMO gap investigations are not sufficient. Additional lone electron pairs introduced by the substituents disturb the basic FMO picture with the b_{1g} and a_{2u} MO as the HOMO and LUMO, respectively, thereby increasing their energetic separation. Somewhat comparable observations have been made for the trigonal inversion of group 15 pyramids with halogen substituents.[51]

Conclusion

The stereoinversion of **ER_3** molecules through a planar trigonal or T-shaped inversion structure is a well-studied process, and the obtained knowledge has been used in various applied contexts (*e.g.*, phosphines can serve as chiral ligands whereas amines *cet. par.* cannot). In contrast, the inversion of **ER_4** species and their configurational stability is

much less explored. Within this chapter, accurate barrier heights for *p*-block tetrahedron inversions through square planar transition states were presented. Barriers increase for molecules from group 13 to group 15 (of the periodic table) and decrease with π-donor/σ-acceptor substituents.[26] The increasing introduction of substitution was studied, and substituent dependent trends were found. Remarkably low inversion barriers were uncovered for a subgroup of the considered dataset, *e.g.*, for disubstituted aluminates or $Al(OH)_4^-$. Given the obtained results, the stereochemical inversion of *p*-block atom-based tetrahedrons as it was studied is an indeed happening process.

A HOMO-LUMO gap approximation to the full second-order Jahn-Teller theorem (*cf.* **Chapter 1.3**) was applied to the calculated planarization energies. Correlations well-following the theory were obtained for hydrogen and σ-acceptor substituted systems. The fluoride, hydroxide, and amine cases are exceptions to the FMO-SOJT model. The other molecules with halogen ligands follow the model again, though with a separation of the data due to the grouping of the central atoms in two different rows of the periodic table.

The following mnemonics substantiate for the conceptual cogitation on *p*-block atom planarization and tetrahedron inversion (**Figure 3.46**): electronegative central atoms lower the LUMO energy; the inversion barrier increases. For more electronegative substituents, the HOMO energy is lowered – the inversion barrier decreases (σ-acceptor effect). π-Donor substituents increase the LUMO energy – the inversion barrier decreases (π-donor effect).[26] The findings should be applied with awareness of the significant approximations induced.

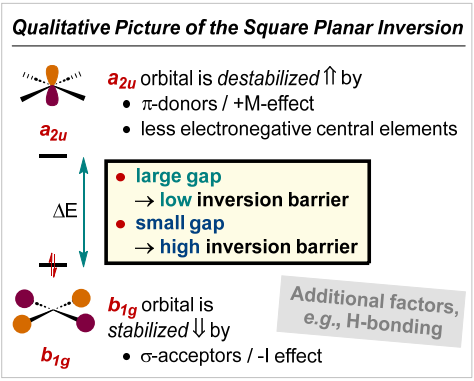

Figure 3.46: Simplified presentation of the factors that determine the barrier height for stereoinversion *via* a square planar transition structure of tetrahedral *p*-block atom-based molecules.[7]

3.8 Stereochemical Inversion of Tetrahedral *p*-Block Element Hydrides

The results presented within this chapter were previously published and can be found under: L. M. Sigmund, C. Ehlert, G. Gryn'ova, and L. Greb, "Stereoinversion of tetrahedral p-block element hydrides", Chem. Phys. ***2022****, 156, 194113. This chapter was written based on the mentioned publication. The CASSCF and MRCI+Q calculations for the square planar structures and the mHEAT+ calculations were conducted by* DR. CHRISTOPHER EHLERT.

Introduction and background

The previous chapter addressed the square planar state of 270 small *p*-block atom-based molecules. They were identified as transition structures for the square planar stereoinversion mechanism (*cf.* **Figure 3.39** and **Chapter 3.7**). During these studies, it was recognized that the hydrogen-substituted *p*-block atoms (element hydrides) have a more intricate electronic structure in the square planar and other, lower-symmetrical states. Therefore, they were investigated separately with both, *ab initio* and DFT quantum chemical simulations, which is presented in the following.

Tetracoordinate carbon atoms are configurationally stable; a paradigm that is at the heart of (bio)organic chemistry; *e.g.*, it allows for the construction of enzymes with precise structure-activity relationships with the *homochiral* feedstock of the naturally occurring amino acids. The prototypical carbon atom with four substituents, methane, was intensively studied concerning its stereochemical inversion.[24, 323-330] It was shown that stereoinversion might occur *via* a C_s symmetric transition state with a high inversion barrier (*cf.* **Chapter 1.2** in the Introduction).[28-29] Importantly, the planarization of methane is energetically even more demanding than the distortion to the C_s symmetric transition structure. Furthermore, the D_{4h} state is a higher-order saddle point on the potential energy surface (PES), ruling out the stereoinversion of methane *via* a square planar transition structure. Generally though, the C-H bond dissociation enthalpy (439.3 ± 0.4 kJ mol^{-1})[331-332] is considered prohibitive for CH_4 inversion by approximately 20 to 30 kJ mol^{-1}.[28-29]

The obtained results are portioned into two sections. The first one discusses the square planar states of the element hydrides, $\mathbf{EH_4^n}$, of the second through the sixth period of the periodic table based on calculations at the CASSCF and MRCI+Q level (**Figure 3.47**). The electronic configuration of the lowest energy structures is identified (*cf.* **Figure 1.2** in **Chapter 1.2**). Also, their harmonic vibrations and their relevance as inversion transition states is discussed. In the second part, non-planar structures of all element-hydrogen

compounds and their potential role in alternative inversion mechanisms are inspected. In particular, the C_s inversion found for methane is probed for the other molecules. All possible inversion mechanisms are weighed against each other and competing reactions, for example, **E-H** bond dissociation or the elimination of H_2.

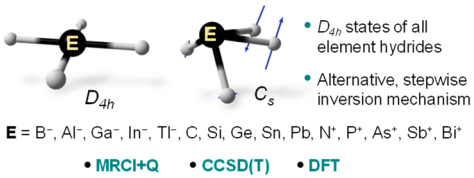

Figure 3.47: Stereoinversion of *p*-block element-hydrogen compounds. *Square planar (D_{4h}) and distorted square pyramidal (C_s) structure. The scaled displacement vectors of the imaginary mode (stereoinversion of CH_4) are shown in blue.*[25]

Applied computational methods

To cover all electronic configurations of the square planar structures (D_{4h} symmetry), a state-specific multiconfigurational level was applied. Structure optimizations and frequency calculations were carried out with the complete active space self-consistent field method (CASSCF). The active space was defined to include the entire valence space (CAS(8*e*,8*o*)). The aug-cc-pwCVQZ basis set was employed for B, C, N, Al, Si, and P atoms. For hydrogen atoms, aug-cc-pVQZ was used. For all heavier elements, Stuttgart-Köln MCDHF RSC effective core potentials (ECPs) were applied with the respective ECP-based aug-cc-pwCVQZ-PP basis set. Final single point electronic energies were obtained from multireference configuration interaction calculations, including the Davidson correction for unlinked quadruples (MRCI+Q). The same basis sets and ECPs as for the CASSCF calculations (which were also used as multiconfigurational reference) were deployed.

Coupled cluster calculations including singles and doubles with perturbative triples corrections (CCSD(T)) were used to investigate lower symmetric inversion mechanisms, competing side reactions, and other structures on the respective PESes. The same basis set and ECP settings as for the MRCI+Q calculations were employed. Only the structure optimizations and the computations of harmonic frequencies were done with the respective triple-ζ basis sets (aug-cc-pwCVTZ(-PP)). The obtained numbers were compared to experimentally determined values, and good agreement was found (MAE of 4.4 kJ mol^{-1}, *cf.* **Table 7.1** in the Appendix).

The correct nature of located transition structures was verified by the presence of a single imaginary mode of desired symmetry and by applying IRC calculations. Relative

energies are given as enthalpies at 298.15 K and in kJ mol^{-1}, if not stated differently. FMO considerations were carried out based on data obtained with the B97M-D3(BJ)/def2-QZVPP computational level. The references to applied software, methods, and basis sets are given in **Chapter 5.2**.

Evaluation of D_{4h} symmetric structures

The structures of the square planar *p*-block element-hydrogen compounds were optimized with a D_{4h} symmetry constraint in four considered electronic configurations (*cf.* **Figure 1.2** in the Introduction). **Table 3.1** lists the results, and the lowest energy states are highlighted in green. The following discussion is done based on electronic energies, as some structures are higher-order saddle points on the respective PES. Also, in some cases, root-flipping occurred for the displaced structures during the numerical calculation of vibrational frequencies with the CASSCF method, that could not be suppressed. The results of these calculations are not given (np for "not possible" in **Table 3.1**). Fortunately, this issue did not occur for the lowest energy states.

For square planar BH_4^-, the triplet state (476 kJ mol^{-1}) is more favorable, though it is only slightly below the open-shell singlet configuration (477 kJ mol^{-1}). They possess two and three imaginary frequencies, respectively. Owing to the enormous energetic demands to achieve square planar BH_4^- and the absence of a single imaginary mode of B_{2u} symmetry for both lowest energy electronic configurations, the stereoinversion of the tetrahydridoborate anion through a square planar transition structure can be ruled out.

For methane, the results of GORDON and SCHMIDT[28] were qualitatively reproduced. CH_4 preferentially occupies the 2 $^1A_{1g}$ electronic configuration in the square planar state, which is characterized by four imaginary vibrational modes. However, with the MRCI+Q/aug-cc-pwCVQZ//CASSCF(8*e*,8*o*)/aug-cc-pwCVQZ computational procedure, which is more elaborate, significantly lower planarization energies were obtained compared to the previous ones (*e.g.*, 571 *vs.* 663 kJ mol^{-1} at the SOCI/6-31G(*d*,*p*) computational level for the 2 $^1A_{1g}$ state).

For the ammonium cation, it is also concluded that square planar inversion is not possible. As in the case of CH_4, the lowest energy singlet state (485 kJ mol^{-1}) represents a higher-order saddle point on the PES. The same is true for the triplet state (three imaginary modes). Additionally, it is associated with an exorbitant increase in electronic energy (923 kJ mol^{-1}).

Table 3.1: Square planar element hydrides and their electronic configurations. *Energies, enthalpies, and bond lengths of the four different square planar states relative to the tetrahedral ground state (GS) calculated at the MRCI+Q/aug-cc-pwCVQZ(-PP)//CASSCF(8e,8o)/aug-cc-pwCVQZ(-PP) computational level. If only one number is given, the electronic energy is meant. For certain configurations, the reliable calculation of numerical frequencies was not possible (np).*[25]

	State	Energy | enthalpy / kJ mol^{-1}	Bond length / pm	Imag. modes
BH_4^-	GS	0.0	126	0
	1 $^1A_{1g}$ (δ)	534.9	140	np
	2 $^1A_{1g}$ (π)	532.3	121	np
	$^1B_{2u}$	477.3	133	3; B_{2u}, E_u
	$^3B_{2u}$	**475.5**	**131**	**2; E_u**
AlH_4^-	GS	0.0	167	0
	1 $^1A_{1g}$ (δ)	**222.3 | 215.4**	**172**	**1; B_{2u}**
	2 $^1A_{1g}$ (π)	---	---	---
	$^1B_{2u}$	417.6	170	np
	$^3B_{2u}$	421.1	169	3; E_u, A_{2u}
GaH_4^-	GS	0.0	166	0
	1 $^1A_{1g}$ (δ)	**279.7 | 268.0**	**175**	**1; B_{2u}**
	2 $^1A_{1g}$ (π)	359.9	161	np
	$^1B_{2u}$	397.8	169	np
	$^3B_{2u}$	404.1	168	3; E_u, A_{2u}
InH_4^-	GS	0.0	184	0
	1 $^1A_{1g}$ (δ)	**235.0 | 225.5**	**193**	**1; B_{2u}**
	2 $^1A_{1g}$ (π)	310.9	177	np
	$^1B_{2u}$	359.0	186	np
	$^3B_{2u}$	365.8	185	3; A_{2u}, E_u
TlH_4^-	GS	0.0	185	0
	1 $^1A_{1g}$ (δ)	**246.8 | 233.7**	**199**	**1; B_{2u}**
	2 $^1A_{1g}$ (π)	---	---	---
	$^1B_{2u}$	324.7	186	np
	$^3B_{2u}$	330.4	185	4; A_{2u}, E_u, B_{1g}
CH_4	GS	0.0	110	0
	1 $^1A_{1g}$ (δ)	727.2	128	np
	2 $^1A_{1g}$ (π)	**571.4**	**110**	**4; B_{2u}, A_{2u}, E_u**
	$^1B_{2u}$	674.6	120	2; B_{2u}, B_{1g}
	$^3B_{2u}$	680.0	119	1; B_{1g}
SiH_4	GS	0.0	150	0
	1 $^1A_{1g}$ (δ)	**376.6 | 369.5**	**155**	**1; B_{2u}**
	2 $^1A_{1g}$ (π)	384.1	155	np
	$^1B_{2u}$	482.6	156	np
	$^3B_{2u}$	482.2	155	3; A_{2u}, E_u

GeH_4	GS	0.0	155	0
	1 $^1A_{1g}$ (δ)	**419.1 | 407.3**	**164**	**1; B_{2u}**
	2 $^1A_{1g}$ (π)	456.5	157	np
	$^1B_{2u}$	463.3	161	np
	$^3B_{2u}$	468.5	161	3; A_{2u}, E_u
SnH_4	GS	0.0	173	0
	1 $^1A_{1g}$ (δ)	**333.5 | 323.9**	**182**	**1; B_{2u}**
	2 $^1A_{1g}$ (π)	466.5	175	np
	$^1B_{2u}$	409.1	179	np
	$^3B_{2u}$	416.7	178	3; A_{2u}, E_u
PbH_4	GS	0.0	178	0
	1 $^1A_{1g}$ (δ)	**326.6 | 313.6**	**192**	**1; B_{2u}**
	2 $^1A_{1g}$ (π)	---	---	---
	$^1B_{2u}$	381.7	183	np
	$^3B_{2u}$	387.5	183	3; A_{2u}, E_u
NH_4^+	GS	0.0	103	0
	1 $^1A_{1g}$ (δ)	---	---	---
	2 $^1A_{1g}$ (π)	**485.4**	**105**	**4; B_{2u}, A_{2u}, E_u**
	$^1B_{2u}$	906.8	117	np
	$^3B_{2u}$	923.0	116	3; B_{1g}, E_u
PH_4^+	GS	0.0	141	0
	1 $^1A_{1g}$ (δ)	604.9	146	np
	2 $^1A_{1g}$ (π)	611.4	148	np
	$^1B_{2u}$	**518.5 | 481.0**	**148**	**1; B_{2u}**
	$^3B_{2u}$	519.7	148	3; A_{2u}, E_u
AsH_4^+	GS	0.0	150	0
	1 $^1A_{1g}$ (δ)	598.6	160	np
	2 $^1A_{1g}$ (π)	611.2	156	np
	$^1B_{2u}$	**493.5**	**158**	**3; B_{2u}, E_u**
	$^3B_{2u}$	501.1	158	3; A_{2u}, E_u
SbH_4^+	GS	0.0	168	0
	1 $^1A_{1g}$ (δ)	454.8	178	np
	2 $^1A_{1g}$ (π)	472.2	174	np
	$^1B_{2u}$	**426.0**	**176**	**4; B_{2u}, E_u, A_{2u}**
	$^3B_{2u}$	435.9	176	3; A_{2u}, E_u
BiH_4^+	GS	0.0	175	0
	1 $^1A_{1g}$ (δ)	423.9	191	np
	2 $^1A_{1g}$ (π)	452.1	179	np
	$^1B_{2u}$	**401.4**	**183**	**4; B_{2u}, E_u, A_{2u}**
	$^3B_{2u}$	409.5	183	3; A_{2u}, E_u

To summarize the so far discussed results, distortion of the second-period element hydrides to D_{4h} symmetry comes with massive energy demands and does not provide a feasible pathway for stereochemical inversion of the respective molecules.

This significantly changes for the heavier homologs of groups 13 and 14 (**EH_4^n** with **E^n** = Al^-, Ga^-, In^-, Tl^-, Si, Ge, Sn, and Pb). All of them are characterized by a lowest energy $1\,^1A_{1g}$ electronic configuration; the other configurations are clearly higher in energy. Furthermore, they all feature a single imaginary mode of B_{2u} symmetry. Therefore, the square planar structures correspond to inversion transition states, which was indicated previously for some of the herein investigated molecules.[7, 24, 30] Group 14 atom-based molecules invert at higher enthalpies as the group 13 cases do. Within a given group, the inversion energy barriers are highest for the fourth-period central atoms (GaH_4^-, GeH_4).

The lowest energy configurations for the square planar states of the heavier element hydrides with group 15 central atoms (**EH_4^n** with **E^n** = P^+, As^+, Sb^+, and Bi^+) were identified as open-shell singlets, slightly below the triplet states. The respective planarization energies are very high, surpassing those observed for group 13 and 14 atom-based compounds. Frequency analyses revealed a single imaginary mode of B_{2u} symmetry for PH_4^+ and thus a proper inversion transition state with an activation enthalpy of 481 kJ mol^{-1}. Importantly though, for all **EH_4^n** except AlH_4^-, the square planar structures do not correspond to the lowest energy transition states (*vide infra*).

Evaluation of inversion processes along lower symmetry pathways and a comparison with competing reactions

The investigations of the square planar structures on the multiconfigurational level identified inversion transition states for nine of the 15 considered element hydrides. To probe if the processes *via* the square planar transition structure ("*D_{4h}-inversion*") indeed are the lowest energy possibility, structures of lower symmetry were considered next. Also, the identification of the energetically most favorable pathways for stereoinversion for the remaining species was targeted. To allow for general statements on the feasibility of stereoinversion, reaction and activation enthalpies of dissociative processes were evaluated as well (**Figure 3.48**).[26] The entirety of the obtained data is given in the Appendix in **Table 7.1**. The most critical results are discussed in the following.

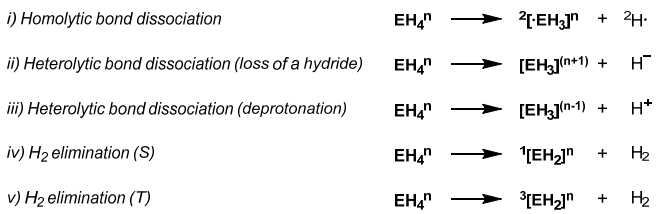

Figure 3.48: Competition reactions for stereoinversion processes of the *p*-block element-hydrogen compounds. *n: charge of the species.*[25]

A transition state of C_s symmetry was obtained for BH_4^- (**Table 3.2**). Its structure features two markedly different pairs of hydrogen atoms and can therefore be interpreted as a complex of the dihydroboryl anion with side-on coordinating H_2. The analysis of the harmonic frequencies and IRC calculation confirmed that the structure corresponds to an inversion transition state with $\Delta H^{\ddagger} = 361$ kJ mol^{-1}. However, the low hydride affinity of BH_3 in the gas phase (calculated to 307 kJ mol^{-1}, experimental value: 310 ± 12 kJ mol^{-1})[333-334] rules out stereoinversion of BH_4^-. Consequently, a non-dissociative stereoinversion of the tetrahydridoborate anion in the gas phase is unlikely.

For the NH_4^+ cation, the transition structure optimization converged to a square pyramidal structure (C_{4v} symmetry, **Table 3.2**). IRC computations as well as the calculation of the harmonic frequencies validated the inversion transition structure. It exhibits a high activation enthalpy of 405 kJ mol^{-1}. Nevertheless, it is significantly lower in energy than *all* potentially competing reactions (*cf.* **Figure 3.48**, the homolytic bond cleavage has the lowest reaction enthalpy; 520 kJ mol^{-1}). Consequently, the intramolecular stereoinversion of the ammonium cation is enthalpically feasible. Interestingly, the C_{4v} symmetry of the inversion transition structure of the ammonium cation was already briefly mentioned by PEPPER *et al.* in their seminal work on methane, but got never further elaborated.[29]

Subsequently, the inversion barrier of methane *via* the C_s symmetric transition state was investigated. GORDON and SCHMIDT as well as PEPPER *et al.* concluded from their computations that the stereoinversion of CH_4 is impossible because of the homolytic C-H bond dissociation enthalpy (439.3 ± 0.4 kJ mol^{-1})[331-332]. They found it to be lower than the barrier for inversion. Herein, an activation energy of 436 kJ mol^{-1} was obtained from the CCSD(T)/aug-cc-pwCVQZ//CCSD(T)/aug-cc-pwCVTZ computational method which is already below the C-H bond dissociation enthalpy. However, as this value is still within the error range of the bond dissociation (given the accuracy of the applied computational procedure), an even more precise barrier height for the stereochemical inversion of CH_4

was determined. This was done with the modified high-accuracy extrapolated *ab initio* thermochemistry protocol (mHEAT+).[335-339] An activation enthalpy of 434.2 kJ mol^{-1} was obtained – 5.1 kJ mol^{-1} (1.22 kcal mol^{-1}) below the experimentally determined C-H bond dissociation enthalpy. Based on these results, the intramolecular stereoinversion of CH_4 *via* the C_s symmetric transition state appears enthalpically feasible. It is not prohibited by the strength of the C-H bond. Importantly, the mHEAT+ procedure predicts the C-H bond dissociation enthalpy to 439.4 kJ mol^{-1}.

Table 3.2: Stereochemical inversion of BH_4^-, CH_4, and NH_4^+. *Inversion transition structures with scaled displacement vectors of the single imaginary vibrational mode, their energy and enthalpy relative to the tetrahedral ground states, and selected structural parameters. Energies (given in kJ mol^{-1}) were obtained at the CCSD(T)/aug-cc-pwCVQZ//CCSD(T)/aug-cc-pwCVTZ computational level. "Lowest energy competition reaction" means the lowest energy reaction among those given in Figure 3.48, and "D_{4h} minimum" the lowest energy of a square planar structure along with its electronic configuration (cf. Figure 1.2 in the Introduction).*[25]

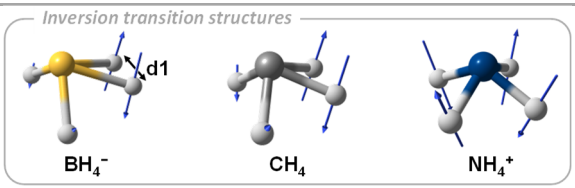

	BH_4^-	CH_4	NH_4^+
Inversion barrier ($\Delta E^{\ddagger}$/ $\Delta H^{\ddagger}$)	368.3 / 361.1	457.9 / 436.0	439.1 / 404.8
Lowest energy competition reaction ($\Delta E/\Delta H$)	320.0 / 307.1 (loss of H^-)	469.4 / 436.4 (loss of $H^{\bullet}$)	558.1 / 519.9 (loss of $H^{\bullet}$)
D_{4h} minimum ($\Delta E^{\ddagger}$)	475.5 ($^3B_{2u}$)	571.4 (2 $^1A_{1g}$)	485.4 (2 $^1A_{1g}$)
Molecular point group	C_s	C_s	C_{4v}
Ground state bond length / pm	123.6	108.8	102.2
Transition state bond lengths / pm	122.8 / 145.3	111.3 / 121.1	106.9
d1 / pm	80.4	91.6	134.9
trans-valence angle / °	105.4	110.1	126.4

Next, the C_s symmetric inversion transition structures were probed for the heavier homologs (**Table 3.3**). Except for GaH_4^-, structures of C_s symmetry were located for all heavier *p*-block element hydrides. The IRCs were followed in both directions along the imaginary mode (*A''* symmetry). Without exception, the IRC calculations did not converge to the tetrahedral ground states, as it was expected and found for CH_4, but instead to a new structure (Int-**A**, **Table 3.3**), also of C_s symmetry. These minimum structures, which

were verified by minimum structure optimizations, can be viewed as σ-complexes of molecular hydrogen coordinating to the $\mathbf{EH_2^n}$ fragments. Indeed, structures of Int-**A**-type of the group 14 atom-based molecules were debated as intermediates in the context of reductive elimination of H_2 from the tetrahedral $\mathbf{EH_4}$ or as pre-complexes during the oxidative addition of dihydrogen to $\mathbf{EH_2}$.[340-351] MERINO *et al.* compared the calculated scaled harmonic vibrations they obtained (B3LYP/LANL2DZ+dp) of the Int-**A** structure of SiH_4 and GeH_4 with previously unassigned bands in IR spectra from matrix isolation experiments and found remarkable agreements.[345] The calculations presented herein now suggest such intermediates, also for the isoelectronic group 13 and group 15 compounds, and for the first time as intermediates during stereoinversion (*vide infra*). In order to reach Int-**A** from the tetrahedral ground states, the reductive elimination transition states, TS-**A**, need to be traversed. It was possible to optimize the respective transition structures for all considered cases (**Table 3.3**).

The combination of the three stationary points (TS-**A**, Int-**A**, and TS-**B**) leads to a new mechanism for the stereoinversion of tetrasubstituted *p*-block elements, which is called *stepwise C_s-inversion*. The mechanism begins at the tetrahedral ground state, which engages in the rate-determining reductive semi-elimination of H_2 (TS-**A**) to give Int-**A**, in which H_2 remains bound. The following rotation of the H_2 fragment in the coordination sphere of $\mathbf{EH_2^n}$ (TS-**B**) proceeds *via* a low activation barrier. The final oxidative-addition-type step (TS-**A**) furnishes the inverted molecule.

The barrier height for the rate-determining H_2 semi-elimination decreases within a given group of the periodic table with increasing atomic number (*cf.* **Table 3.3**, entry 1). Following the Bell-Evans-Polanyi principle,[352-354] this agrees with the increasing stability of the lower oxidation state for the heavier elements. The lowest activation enthalpies were calculated for the group 15 atom-based molecules (211 – 134 kJ mol^{-1}), followed by the group 13 species (227 – 160 kJ mol^{-1}), and compounds with central atoms from group 14 (236 – 157 kJ mol^{-1}). The numbers agree well with those of Merino *et al.* obtained for the group 14 element hydrides.[345]

Table 3.3: A stepwise mechanism for stereoinversion. *All given energies and enthalpies are relative to the respective tetrahedral ground states (GS). Entry 4 gives the barrier heights for the oxidative addition of the H_2 fragment, entry 5 the dissociation energy and enthalpy of the Int structures into H_2 and the EH_2^n fragment, and entry 6 the energy and enthalpy of the lowest D_{4h} symmetric structures. If not mentioned otherwise, all numbers were obtained at the CCSD(T)/aug-cc-pwCVQZ(-PP)//CCSD(T)/aug-cc-pwCVTZ(-PP) computational level and are given in kJ mol^{-1}.*[25]

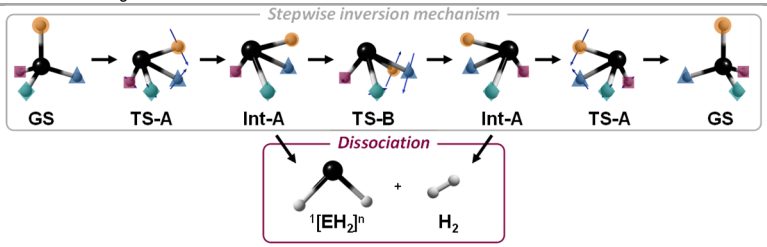

	State	AlH_4^-	GaH_4^-	InH_4^-	TlH_4^-
1	**TS-A** ($\Delta E^‡$ | $\Delta H^‡$)	234.7 | 227.4	211.7 | 203.1	200.9 | 193.2	168.3 | 159.9
2	**Int-A** (ΔE | ΔH)	196.4 | 196.8	152.2 | 149.4	91.6 | 89.8[a]	11.8 | 9.1[a]
3	**TS-B** ($\Delta E^‡$ | $\Delta H^‡$)	200.7 | 196.5	*not found*	93.4 | 91.3	13.2 | 10.4
4	**Int-A** ⟶ **TS-A** ($\Delta E^‡$ | $\Delta H^‡$)	38.3 | 30.6	59.5 | 53.7	109.3 | 103.4	156.5 | 150.8
5	**Int-A** ⟶ H_2 + ^{1}**[EH_2^n]** (ΔE | ΔH)	10.1 | 3.2	10.2 | 4.3	7.6 | 5.2	7.6 | 5.4
6	D_{4h} minimum ($\Delta E^‡$ | $\Delta H^‡$)	222.4 | 215.3 ($1\,^1A_{1g}$)	280.5 | 268.2 ($1\,^1A_{1g}$)	235.9 | 225.5 ($1\,^1A_{1g}$)	248.7 / 234.4 ($1\,^1A_{1g}$)
	State	**SiH_4**	**GeH_4**	**SnH_4**	**PbH_4**
1	**TS-A** ($\Delta E^‡$ | $\Delta H^‡$)	248.1 | 235.8	218.6 | 206.3	207.2 | 196.8	167.6 | 157.1
2	**Int-A** (ΔE | ΔH)	222.7 | 217.4	155.0 | 148.7	81.8 | 79.2	−22.4 | −24.0
3	**TS-B** ($\Delta E^‡$ | $\Delta H^‡$)	236.0 | 226.2	160.6 | 150.5	84.1 | 78.5	−21.2 | −25.5
4	**Int-A** ⟶ **TS-A** ($\Delta E^‡$ | $\Delta H^‡$)	25.4 | 18.4	63.6 | 57.6	125.4 | 117.6	190.0 | 181.1
5	**Int-A** ⟶ H_2 + ^{1}**[EH_2^n]** (ΔE | ΔH)	33.6 | 21.6	22.7 | 13.3	14.9 | 8.0	13.1 | 7.1
6	D_{4h} minimum ($\Delta E^‡$ | $\Delta H^‡$)	378.6 | 371.0 ($1\,^1A_{1g}$)	421.3 | 408.6 ($1\,^1A_{1g}$)	335.7 | 325.2 ($1\,^1A_{1g}$)	329.5 | 315.2 ($1\,^1A_{1g}$)
	State	**PH_4^+**	**AsH_4^+**	**SbH_4^+**	**BiH_4^+**
1	**TS-A** ($\Delta E^‡$ | $\Delta H^‡$)	226.1 | 210.7	196.2 | 181.7	189.4 | 177.1	146.7 | 133.9
2	**Int-A** (ΔE | ΔH)	217.5 | 208.9	145.1 | 138.7	68.3 | 65.8	−42.6 | −43.3
3	**TS-B** ($\Delta E^‡$ | $\Delta H^‡$)	239.2 | 227.9	154.7 | 145.0	72.4 | 66.9	−40.7 | −44.1
4	**Int-A** ⟶ **TS-A** ($\Delta E^‡$ | $\Delta H^‡$)	8.6 | 1.8	51.1 | 43.0	121.1 | 111.3	189.3 | 177.2
5	**Int-A** ⟶ H_2 + ^{1}**[EH_2^n]** (ΔE | ΔH)	133.5 | 119.2	94.3 | 82.0	59.1 | 49.8	47.8 | 39.9
6	D_{4h} minimum (ΔE)	518.5[b] ($^1B_{2u}$)	493.5[b] ($^1B_{2u}$)	426.0[b] ($^1B_{2u}$)	401.4[b] ($^1B_{2u}$)

(a) Structure has a single imaginary frequency. (b) Calculated at the MRCI+Q/aug-cc-pwCVQZ(-PP)//CASSCF(8e,8o)/aug-cc-pwCVQZ(-PP) level of theory.

Interestingly, the comparison of *D_{4h}-inversion* pathway (**Table 3.3**, entry 6) with the reductive semi-elimination/H_2-rotation/oxidative addition process (*stepwise C_s-inversion*) renders the latter as the favored pathway for stereoinversion for most of the element hydrides. The planarization enthalpies, either toward the 1 $^1A_{1g}$ (**EH_4**, **E** = Al^-, Ga^-, In^-, Tl^-, Si, Ge, Sn, Pb) or $^1B_{2u}$ (**EH_4**, **E** = P^+) electronic configuration, are considerably larger as the barrier heights of the stepwise C_s-inversion (*e.g.*, for SiH_4 the enthalpy difference is 135 kJ mol^{-1}, for PH_4^+ it is 270 kJ mol^{-1}). They increase when going from left to right in the periodic table, contrasting the findings for the square planar stereoinversion. Consequently, only for AlH_4^- the D_{4h}-inversion outcompetes the stepwise C_s-inversion by 12 kJ mol^{-1}. Notably, the D_{4h}-inversion of AlH_4^- is also preferred over all considered competing reactions (*cf.* **Figure 3.48**), including H^- expulsion (315 kJ mol^{-1}) or the elimination of dihydrogen (activation enthalpy of 227 kJ mol^{-1}). Thus, it can be concluded that tetrahydrido aluminate can undergo stereochemical inversion *via* transition state of D_{4h} symmetry with an activation enthalpy of 215 kJ mol^{-1}.

Having established the stepwise C_s-inversion, it was further compared to the inversion pathway *via* the square planar transition structure. This was done with TS-**A** and the D_{4h} symmetric transition structure (**TS_{D4h}**) of SiH_4 and AlH_4^-. The IRC paths were followed toward the tetrahedral ground state, and orbital energies were calculated for selected IRC structures on the B97M-D3(BJ)/def2-QZVPP level of theory (**Figure 3.49**). In both cases, the deformation toward the transition structure increases the energy of one of the MOs of the triply degenerate fully occupied t_2 representation. For the aluminate (**Figure 3.49A**), this increase is slightly stronger for the C_s path (2.61 *vs.* 2.15 eV) but is counterbalanced by the stabilization of the three other valence MOs (−4.16 eV in total). In the square planar **TS_{D4h}** of AlH_4^-, this stabilizing effect is less pronounced (−0.45 eV). Overall, both paths are energetically very similar, with the square planar inversion being marginally favored. For the silane (**Figure 3.49A**), the transformation toward the C_s symmetric TS-**A** leads to a diminished increase of the occupied orbital energies compared to the path to D_{4h} symmetry (2.68 *vs.* 3.44 eV). Concomitantly, the stabilization of the other orbitals remains substantial (−2.47 eV) which further supports TS-**A**. The stabilizing contribution found for **TS_{D4h}** is only −0.93 eV. This explains that the semi-elimination of H_2 from SiH_4 is energetically more favorable than the ascent of the square planar inversion transition state by 131 kJ mol^{-1} in electronic energy ($\Delta\Delta H^‡$ = 135 kJ mol^{-1}). Similar findings were made for the other investigated element hydrides.

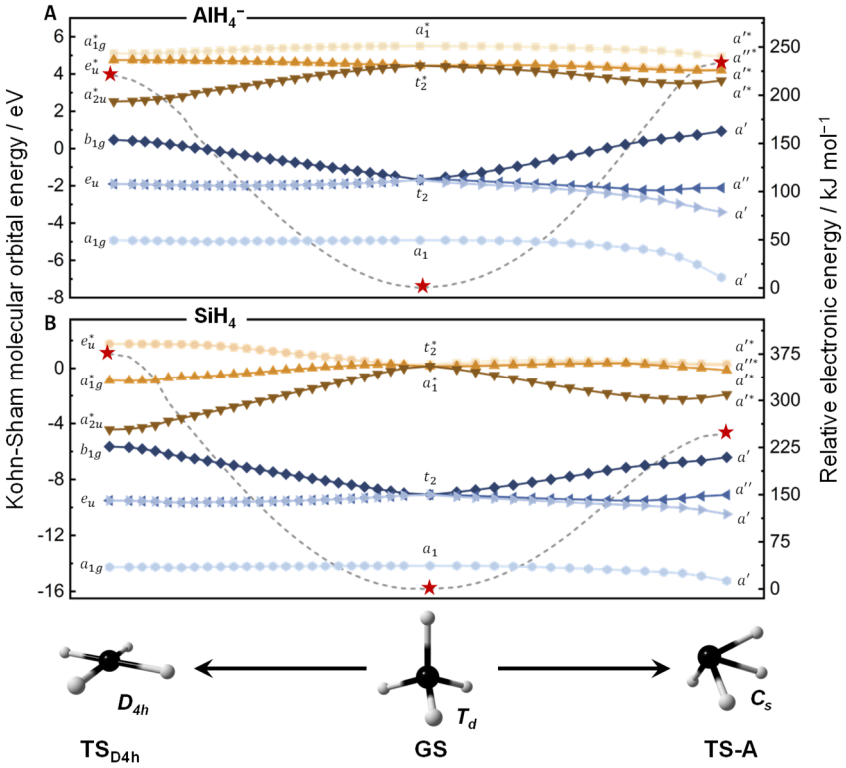

Figure 3.49: The stepwise and square planar inversion mechanism in comparison. *Kohn-Sham frontier molecular orbital energies of individual IRC structures of the transformation of the tetrahedral ground state to the D_{4h} (TS_{D4h}) or C_s symmetric (TS-A) transition state for **A**) AlH_4^- and **B**) SiH_4. The relative electronic energy is shown as dashed line. Stationary points are marked with red stars. The IRC structures were obtained with CCSD(T)/aug-cc-pwCVTZ, molecular orbital energies were calculated at the B97M-D3(BJ)/def2-QZVPP computational level.*[25]

After the comparison of the C_s and D_{4h} pathway, it was investigated if the stepwise C_s-inversion can compete with the alternative reactions given in **Figure 3.48**. In all cases the elimination of H_2 from $\mathbf{EH_4^n}$ to yield singlet $\mathbf{EH_2^n}$ is the enthalpically most favorable competition reaction for the third to sixth-period element hydrides (*cf.* **Table 7.1**). If the H_2 fragment in Int-**A** leaves the coordination sphere of $\mathbf{EH_2^n}$ or rotates and undergoes oxidative (re)addition depends on whether these two reaction steps (H_2 rotation and oxidative addition) are enthalpically more favorable than the dissociation of Int-**A** into $^1[\mathbf{EH_2^n}]$ and H_2 (**Int** ⟶ $\mathbf{EH_2^n}$ + H_2). The comparison (**Table 3.3**, entry 4 *vs.* entry 5) shows that the stepwise C_s-inversion is likely for PH_4^+ and AsH_4^+. The differences between dissociation

enthalpy and oxidative addition activation enthalpy are large and favor the reformation of the tetrahedron over the dissociation. For SiH_4, the two enthalpies are similar (18 *versus* 22 kJ mol^{-1}), though slightly in favor of the inversion. For the rest of the considered element-hydrogen compounds, the elimination of dihydrogen is more favorable than the oxidative addition by at least 40 kJ mol^{-1}. Based on the presented results, it can be stated that the tetrahedral hydrides of Ga, Ge, In, Sn, Sb, Tl, Pb, and Bi cannot undergo intramolecular stereochemical inversion.

Evaluation of further structures

As an exhaustive understanding of the PESes of the considered *p*-block element-hydrogen compounds was sought, the pyramidal and the sawhorse structural motive was surveyed in the end (**Table 3.4**). These structural arrangements are of relevance for reactivity enhancement of *p*-block atom-based molecules by structural constraints (*vide infra*).[89, 188, 307, 355-359]

Generally, the pyramids with a triplet electronic configuration are higher in energy than their singlet counterparts, with differences ranging from 29 kJ mol^{-1} for AlH_4^- to up to 197 kJ mol^{-1} for BiH_4^+. The second-row atom-based triplet pyramids are not stable, and the respective structural optimization resulted in planarization. The pyramidal structures with singlet electronic configuration are between 469 and 155 kJ mol^{-1} higher in electronic energy than the tetrahedral ground states. The pyramidalization energy decreases along a given group and from left to right within the periodic table. Compared to the D_{4h} symmetric structures, the group 13 pyramids are higher in energy, whereas for groups 14 (except for CH_4) and 15, the pyramidalization of the square planar structure results in energy lowering. This is in agreement with previous results for methane, silane, and germane on the Hartree-Fock and DFT computational level.[24] The harmonic frequencies of the singlet pyramids were computed. Except for the ammonium cation, which has only one imaginary vibration (*cf.* **Table 3.2**), either two or three imaginary modes were obtained.

The sawhorse (**SH**) configurations demand much less energy than the pyramidal arrangements and are only between 246 and 117 kJ mol^{-1} higher in electronic energy than the tetrahedral ground states. They do not represent stationary points on the respective PESes. The non-linear *trans*-valence angles are around 100°. As it was found for the pyramidal configurations, the energy demand for the deformation to the **SH** structure declines from top to bottom and left to right within the *p*-block of the periodic table. Of

note, the **SH** configurations have lower electronic energies in comparison to the lowest energy square planar states.

Table 3.4: The deformation of *p*-block atom hydrides toward the sawhorse and pyramidal structure. *Molecular structures and electronic energies of the sawhorse and the pyramidal configuration. All numbers (kJ mol^{-1}) are relative to the respective tetrahedral ground states and were obtained at the CCSD(T)/aug-cc-pwCVQZ(-PP)//CCSD(T)/aug-cc-pwCVTZ(-PP) computational level.*[25]

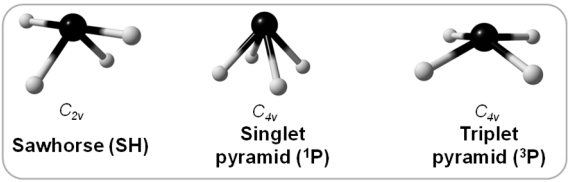

	BH_4^-	AlH_4^-	GaH_4^-	InH_4^-	TlH_4^-
SH	194.3	172.8	167.5	145.1	116.8
^{1}P	426.1	360.0	326.3	301.2	228.1
^{3}P	*planarization*	388.9	375.4	335.3	301.5
	CH_4	**SiH_4**	**GeH_4**	**SnH_4**	**PbH_4**
SH	233.0	211.2	196.2	169.2	144.2
^{1}P	468.7	351.2	303.1	277.4	188.2
^{3}P	*planarization*	451.8	432.9	374.0	332.2
	NH_4^+	**PH_4^+**	**AsH_4^+**	**SbH_4^+**	**BiH_4^+**
SH	245.9	223.1	204.8	179.0	154.7
^{1}P	439.1	318.1	267.5	246.1	154.5
^{3}P	*planarization*	506.7	476.9	399.0	351.9

To investigate whether the structural deformation toward the **SH** structure might enable likewise beneficial electronic effects (in terms of reactivity enhancement, *cf.* **Chapter 1**) as planarization does, the orbital energies of the **SH** configurations were investigated. The blue bars in **Figure 3.50A** present the LUMO lowering that occurs when the structure is deformed from the tetrahedral ground state to the **SH** configuration ($\Delta LUMO_{GS\rightarrow SH}$) relative to the change that occurs when going from the ground to the square planar state ($\Delta LUMO_{GS\rightarrow planar}$). The orange squares depict the analogous relation for the electronic energy penalties ($\Delta E_{GS\rightarrow SH}$ divided by $\Delta E_{GS\rightarrow planar}$).

In all cases, the relative deformation energy is lower than the relative LUMO lowering. In the case of SiH_4, for example, the deformation to the **SH** configuration is associated with an energy increase of 211 kJ mol^{-1} which corresponds to 56% of the energy demand for complete planarization (379 kJ mol^{-1}). At the same time, the LUMO of the **SH** structure

(**Figure 3.50B**) has already reached 80% of the lowering achievable through the D_{4h} symmetric structure. The observed effect is more pronounced for group 14 than for group 13-atom-based compounds. The results predict a more straightforward experimental realization of molecules with **SH** structurally constrained *p*-block atoms while maintaining large parts of the "electronic benefits" from complete planarization. The **SH** arrangement of carbon was already experimentally reported[360] and computationally investigated.[361]

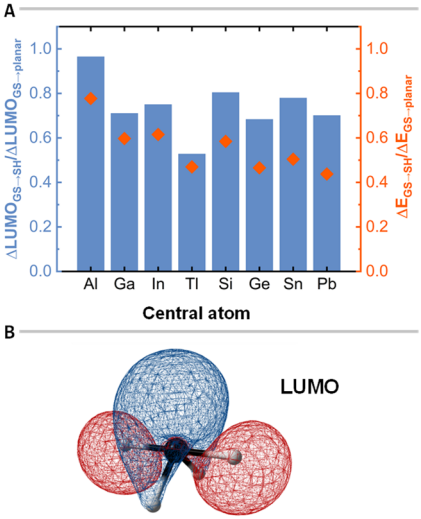

Figure 3.50: Comparison of the square planar and sawhorse deformation. ***A)*** *LUMO lowering for the SH configuration relative to the LUMO lowering achievable through full planarization (blue bars) and deformation energy required for the distortion to the SH structure relative to the planarization energy (orange squares) for* EH_4^n, *E = Al*$^-$, *Ga*$^-$, *In*$^-$, *Tl*$^-$, *Si, Ge, Sn, and Pb.* ***B)*** *Kohn-Sham LUMO of the SH structure of* SiH_4. *The MO energies were calculated with B97M-D3(BJ)/def2-QZVPP, the deformation energies with CCSD(T)/aug-cc-pwCVQZ(-PP).*[25]

Conclusion

The potential energy surfaces of 15 anionic, neutral, and cationic *p*-block atom-based element-hydrogen compounds ($\mathbf{EH_4^n}$, $\mathbf{E^n}$ = B^-, Al^-, Ga^-, In^-, Tl^-, C, Si, Ge, Sn, Pb, N^+, P^+, As^+, Sb^+, and Bi^+) was investigated with quantum chemical calculations at the MRCI+Q and CCSD(T) level of theory. Special emphasis was placed on the square planar states as well as on the possibility of stereoinversion. A new stepwise mechanism for stereoinversion was discovered. Ultimately, the results were related to reactions competing with the inversion process. The key findings for each compound are as follows (**Figure 3.51**):

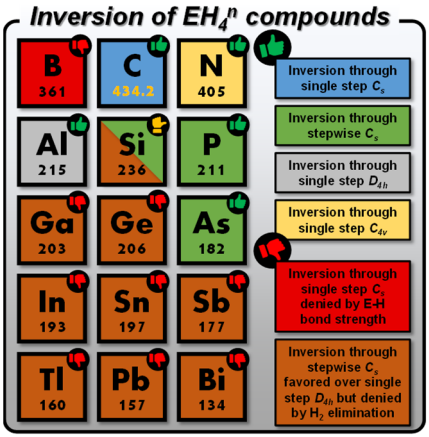

Figure 3.51: Stereochemical inversion of *p*-block element-hydrogen compounds? *The numbers specify the activation enthalpy of the rate-determining step of the lowest energy inversion mechanism in kJ mol^{-1}. The calculations were done at the CCSD(T)/aug-cc-pwCVQZ(-PP)//CCSD(T)/aug-cc-pwCVTZ(-PP) level of theory, except for CH_4, for which the mHEAT+ procedure was applied.*[25]

- A non-planar *single-step C_s inversion* transition state was found for BH_4^-. However, the molecule preferentially expels a hydride, prohibiting stereoinversion.
- Strikingly, the inversion of methane seems not to be forbidden by CH-bond rupture. The *single-step C_s inversion* is an enthalpically feasible process with an activation enthalpy of 434.2 kJ mol^{-1}.
- The ammonium cation can undergo inversion *via* a unique C_{4v} symmetric transition state, which is not prevented by other pathways.
- AlH_4^- is the only tetrahedral *p*-block element hydride that may invert *via* a square planar transition structure.[7]
- SiH_4, PH_4^+, and AsH_4^+ can invert through a *stepwise C_s symmetric* process that can be described as a partial reductive elimination, rotation of the H_2 fragment, and oxidative readdition sequence. For the three mentioned molecules, this process is enthalpically favored over H_2 expulsion and square planar inversion.
- The unimolecular stereoinversion of GaH_4^-, InH_4^-, TlH_4^-, GeH_4, SnH_4, PbH_4, SbH_4^+, and BiH_4^+ is enthalpically not feasible because H_2 elimination is preferred instead.

Lastly, pyramidal and sawhorse configurations were considered. The sawhorse constraint affects orbital energies in a similar fashion as complete planarization to D_{4h} symmetry at a significantly reduced energetic expense. This finding may guide new experimental approaches for ligand design regarding frontier molecular orbital engineering.

3.9 Automated Construction of a Fluoride Ion Affinity Dataset

By the time this dissertation was written, the results presented within this chapter were submitted for peer review: L. M. Sigmund, S. Sowndarya S. V., A. Albers, P. Erdmann, R. S. Paton, L. Greb, "Predicting Lewis Acidity: Machine Learning the Fluoride Ion Affinity of p-Block Atom-based Molecules". This chapter was written based on the mentioned paper draft. Some of the results shown below were generated in collaboration with ANDREAS ALBERS and PHILIPP ERDMANN. The generated FIA dataset and all developed Python code was published on GitHub (https://github.com/GrebGroup/fia-gnn) and figshare (https://figshare.com/projects/FIA-GNN/187050).

Introduction and background

The fluoride ion affinity (FIA) obtained through quantum chemical calculations is one of the most popular global scales for Lewis acidity (*cf.* **Chapter 1.4**) and simulated FIA values have been applied in many Lewis acidity-related studies. KIRSCHNER *et al.* used the FIA of organoboranes and developed phase transfer catalysts for nucleophilic fluorination reactions.[362] The group of LIST correlated FIA values with the activity of their Lewis acidic organocatalysts.[363-364] FIAs are also widely considered in studies on weakly coordinating anions[69, 365] and in the closely related field of Lewis superacidity.[17, 58, 366-385] The FIA has further been compared to other Lewis acidity scales, such as the global electrophilicity index (GEI)[60-61] or others.[386-389]

In this chapter, the computational workflow for the automatic generation of a FIA dataset, denoted FIA44k, is described. The FIA44k dataset has 44,877 datapoints. The entire workflow, based on a modular design principle, was implemented using the cheminformatics package RDKit within the Python programming language.[390] The resulting software package was termed *autoPAMS* (automatic generation of *p*-block atom-based molecular structures).

Dataset composition

The FIA44k dataset consists of quantum chemical data of Lewis acids (LA) and their fluoride adducts (FA). Although not all LA molecules might be classified as a "Lewis acid" in the sense of the IUPAC definition (*cf.* **Chapter 1.4** in the Introduction), nevertheless, this part of the dataset is termed LA regardless of that fact for the sake of simple nomenclature

and classification. Only neutral LAs were used, which results in monoanionic FAs. Bond rearrangements due to FA formation were excluded from the dataset (*vide infra*).

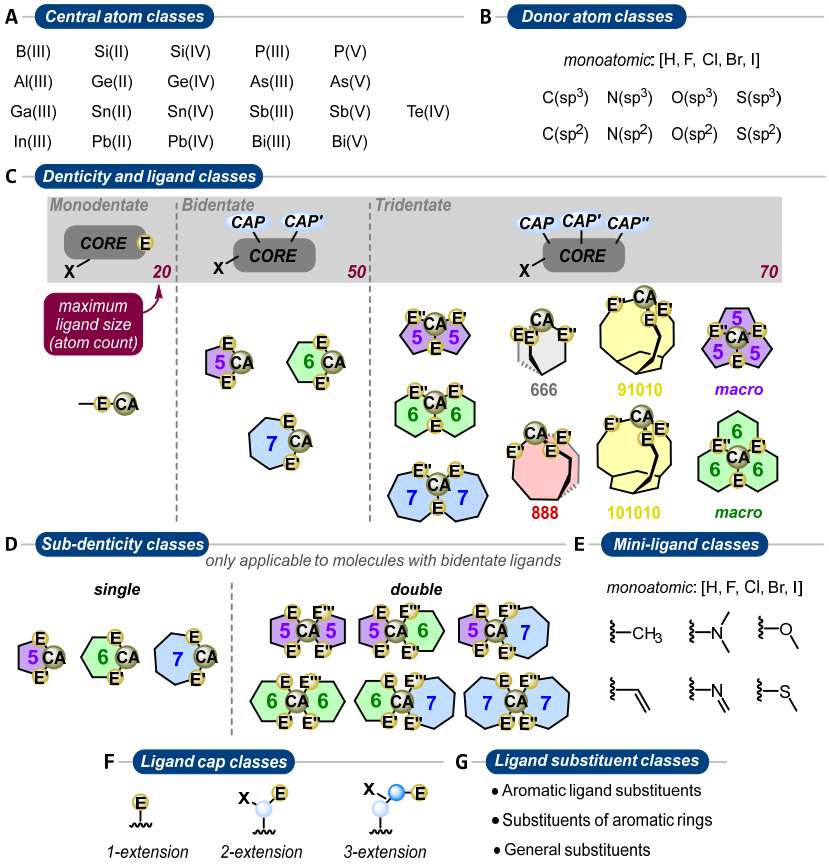

Figure 3.52: Molecular structure taxonomy for the construction of the FIA44k dataset. *"CA" stand for central atom.* ***A)*** *21 central atom classes.* ***B)*** *Nine donor atom classes.* ***C)*** *Three denticity classes which are further divided into ligand classes in the case of bi- and tridentate ligands (three and nine, respectively).* ***D)*** *Two sub-denticity classes (single, double) with three and six categories, respectively, relevant for molecules with bidentate ligands.* ***E)*** *Seven mini-ligand classes. The mini-ligands were used to fill remaining free valences during structure generation.* ***F)*** *Three ligand cap classes with ligand substituents X (applies also to the ligand cores).* ***G)*** *Three ligand substituent classes. The substituents of aromatic rings and the general substituents are shown in Figure 3.53.*

Molecules are considered as a combination of a central atom to which the ligands are connected. Each ligand consists of a ligand core to which a certain amount of ligand substituents is attached to form the final ligand. To allow for a clear and understandable

presentation, the logic with which the dataset was constructed (**Figure 3.52**) is now presented in bullet points.

- FIA44k is defined by 21 different *central atom classes*, coming from groups 13 to 16 of the periodic table (**Figure 3.52A**). Low- and high-valent central atoms are included for groups 14 and 15, *e.g.*, P(III) and P(V). The central atom is the position to which the fluoride anion is attached. Each molecule contains one central atom only.
- Ligand atoms were allowed to be H, C, N, O, S, F, Cl, Br, and I. These atom types were connected by single, aromatic, or double bonds.
- Bonds between two heteroatoms, for instance, N-O or O-O were not included.
- The atoms directly binding to the central atom are denoted donor atoms (**Figure 3.52B**). A total of 9 different *donor atom classes* was defined. This was done based on the hybridization of the respective atoms in each molecule.
- The FIA44k dataset includes mono-, bi-, and tridentate ligands (*denticity classes*, **Figure 3.52C**). The maximum size of the ligand was limited to 20, 50, and 70 atoms (including hydrogen atoms) for mono-, bi-, and tridentate ligands, respectively.
- The denticity class "mono" was not further subclassified. For the other two denticity classes ("bi" and "tri"), subclassification though *ligand classes* was implemented. The "bi" class was further divided into three, the "tri" class into nine different ligand classes (**Figure 3.52C**). The ring size that is formed when the bi- and tridentate ligand, respectively, is attached to the central atom was used as the classification criterion.
- The introduction of *sub-denticity classes* was necessary for molecules of the ligand class "bi" (**Figure 3.52D**) because multiple bidentate ligands were attached to certain central atoms. The defined sub-denticity classes are either of type "single" or "double". "Single" refers to the attachment of one bidentate ligand, "double" to the attachment of two. The number of "single" sub-denticity classes is equal to the amount of available "bi" ligand classes, which is three. The number of "double" sub-denticity classes is six. This results from the combination of all ligand classes with each other.
- Bidentate and tridentate ligands were not combined, *e.g.*, at central atoms of valency five.

- Free valences at central atoms, *e.g.*, after the attachment of a bidentate ligand to a central atom of valency three, were filled with so-called mini-ligands (**Figure 3.52E**). Mini-ligands were introduced to avoid steric overloading of the molecules, which could for example happen if a bulky tridentate ligand would be attached to a central atom and would then be combined with one or two bulky monodentate ligands. Seven different *mini-ligand classes* were defined, six of them only have one member.
- In general, the generation of homoleptic LAs (*e.g.*, for molecules of the "mono" denticity class) was not enforced; though, it can happen randomly.

The described taxonomy defines the general structure of the FIA44k dataset and provides rules for keeping it balanced (*vide infra*). It also provides the requirements for an automatic ligand generation routine. This is presented in the following sections of this chapter.

Building blocks of the dataset

For the automatic assembly of ligands, five different pools of information were compiled manually. The individual building blocks and their classification were obtained with the help of the ChemDraw software. To connect individual building blocks in a well-defined manner, a wildcard atom system was developed. Connectable building blocks possess mutually matching wildcard atoms (identical atom map numbers) which were removed after the actual chemical bond was formed. At the end of this chapter, a concrete example of a ligand and molecule assembly process is presented.

1) The *ligand cores* are the anchor point for the construction of a ligand (**Figure 3.52C**). They express attachment positions for caps and ligand substituents (*vide infra*). All cores are part of a hierarchical classification system of depth four. The first rung has three categories, corresponding to the three ligand classes "mono", "bi", and "tri" (*vide supra*). The second tier maps the donor atom classes in case of the monodentate ligands and the ligand classes in case of the bi- and tridentate ligands (*vide supra*). The third and fourth rung server for further chemical categorization. For example, the "mono" core class has the C(sp^3) subclass. This subclass is divided into "methyl" and "ethyl", whereby the "methyl" class is further divided into "alkyl" and "heteroatom". The "ethyl" class is split into "alkyl" and "vinyl". A total of 1,682 different ligand cores was used.

2) The *ligand caps* provide the donor atoms which make the connection to the central atom (**Figure 3.52F**). They were classified in a hierarchical system of depth three. The first rung has three categories which were implemented based on the amount of atoms a given ligand cap extends a ligand core (separation between central atom and ligand core). Extensions by one, two, or three atoms are possible. The second rung represents the donor atom classes (*vide supra*). The third rung serves for further chemical categorization. For example, the 2-extension cap class has the C(sp^2) subgroup. This subgroup is divided into "chain", "chain-vinyl-exo", "chain-vinyl-endo", "ring-phenyl", and "ring-heteroaryl". Caps were required only for the construction of bi- and tridentate ligands as the ligand cores of monodentate ligands are equipped with a donor atom. A total of 735 different ligand caps was used.

The final three ligand building block pools contain substituents, which are attached to the ligand cores and caps.

3) The *aromatic ligand substituents* allow for the introduction of aromatic substituents, for example, of a phenyl group (**Figure 3.52G**). They were categorized into a "phenyl" and "heteroaryl" subclass. A total of 62 aromatic ligand substituents was included.

4) With *aromatic ring substituents* (**Figure 3.53A**), chemical variation of the just described aromatic ligand substituents and all other aromatic portions of respective molecules is possible (**Figure 3.52G**). 15 substituents of that kind were used which were categorized into the three groups: "monoatomic", "carbon-based", and "heteroatom-based".

5) The 49 *general substituents* (**Figure 3.53B**) provide all other required substituents. Substituents for C(sp^3), C(sp^2) (either to form a new double bond or a vinylic bond), and heteroatoms (N, O, and S) are considered (**Figure 3.52G**). Some of them appeared in multiple of the four subclasses.

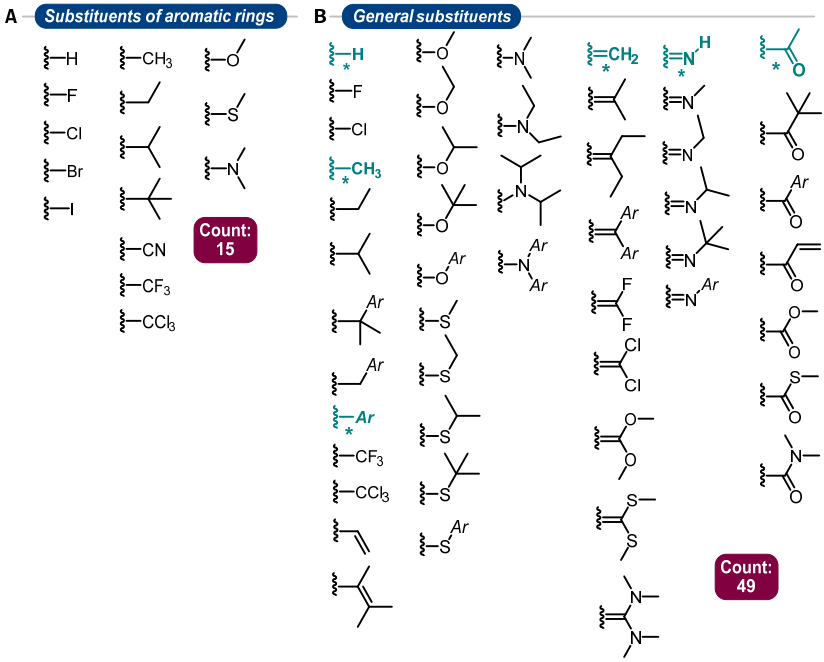

Figure 3.53: Molecular structures of ligand building blocks. ***A)*** *Substituents of aromatic rings.* ***B)*** *General substituents. The six green structures (marked with an asterisk) were used for constructing less functionalized ligands (see main text for further details). Ar stands for an aryl group.*

Python implementation

The so far described molecular logic of the FIA44k dataset was implemented in four separate Python modules:

- `autoPAMS` (automatic generation of *p*-block atom-based molecular structures)
- `autoPAMS_LG` (automatic generation of *p*-block atom-based molecular structures – ligand generation)
- `autoPAMS_F` (automatic generation of *p*-block atom-based molecular structures – fluoride adduct)
- `autoPAMS_DM` (automatic generation of *p*-block atom-based molecular structures – dataset manager).

autoPAMS_LG implements a generate_ligand(denticity_class, ligand_class, max_ligand_size) function. It is prompted with the desired denticity and ligand class as well as with the maximum ligand atom count. It returns a ligand SMILES string. The desired donor atom classes are not passed to generate_ligand. This keeps the autoPAMS_LG code more concise and consistent across all denticity classes. Ligand caps are chosen randomly, and autoPAMS_LG keeps getting called until the donor atoms of interest are contained in the generated ligand. Within autoPAMS_LG, the individual ligand building blocks are chosen randomly from the building block hierarchies (*vide supra*) under the constraint of the requested denticity and ligand class.

autoPAMS implements a generate_la_structure(central_atom, ligands, name) function. It is prompted with the desired central atom, the list of ligands, and the name string of the datapoint for identification. autoPAMS firstly assembles the individual building blocks of the molecule and secondly attempts the calculation of an initial three-dimensional molecular structure. If the 3D embedding is successful, the datapoint is added to the raw dataset along with general molecular information as well as a <name>.xyz file, which stores the three-dimensional structure of the LA. In case the 3D structure generation fails, the LA structure generation process is retriggered until successful embedding is achieved.

autoPAMS_F is responsible for the generation of the starting structure of the fluoride adducts (FAs). For that, a generate_fa_structure(path_to_la_structure_file) function was implemented, which takes as input the file path to the structurally optimized Lewis acid structure and uses that to calculate a FA three-dimensional starting structure. autoPAMS_F constrains the Euclidian distance between the central atom and the new fluorine atom to a central atom-specific approximate value. After that, the atomic position of the fluorine is optimized by maximizing the distance between the fluorine atom and all other atoms in the structure. This circumvents a second RDKit embedding step, as this step is prone to failure. The obtained FA structure is saved in a <name>__F.xyz file, which has the fluoride atom in last atomic position. The Lewis acidic central atom is always at the first position.

The autoPAMS_DM module is used to provide the main functionality for the generation of the dataset. It allows the generation of a new or the extension of an existing dataset. autoPAMS_DM is responsible for keeping the dataset balanced (*vide infra*). It requests ligands with certain properties (denticity and ligand class) from autoPAMS_LG and passes the output to autoPAMS. If all processes conclude as expected, and all criteria are satisfied,

the corresponding molecule, along with its structural information, is included in the raw dataset. Subsequently, the quantum chemical workflow is initiated with separate routines. Notably, `autoPAMS_DM` is responsible for the selection of the donor atoms within the generated ligands according to the following two criteria.

i) The least populated donor atom class (*cf.* **Figure 3.52B**) in the currently treated subset of the dataset must be present in the ligand.

ii) The ligand must not include the two most populated donor atom classes in the currently treated subset of the dataset.

Generation of the FIA44k dataset

The described autoPAMS workflow was initialized three times to construct the FIA44k dataset. This was done to generate structures with varying degree of chemical complexity. The three subsets of FIA44k are:

- The *normal* subset (14,599 datapoints); it was generated with the full set of building blocks.
- The *partially simplified* subset (16,077 datapoints); it was generated with a reduced set of building blocks by limiting the used general substituents to those marked with an asterisk in **Figure 3.53B**.
- The *simplified* subset (14,201 datapoints); it was generated with an even further reduced set of building blocks. In addition to the limited set of general substituents of the partially simplified subset, hydrogen was used as the only aromatic ring substituent (**Figure 3.53A**).

Concrete example for the generation of a LA and FA molecular structure

In this section of the chapter, the autoPAMS routines are illustrated with a concrete example (**Figure 3.54**). The LA starting structure generation process gets prompted as given in **Figure 3.54A**. This causes an inquiry of `autoPAMS_DM` to `autoPAMS_LG` to return a SMILES string corresponding to a bidentate ligand of ligand class "6". This is done until a ligand with an O(sp^2) donor atom is generated. O(sp^2) is in this example the lowest-populated donor atom class of the currently treated subset of the dataset (central atom class: Si(IV), denticity class: bi, sub-denticity class: single, ligand class: 6). C(sp^3) and N(sp^2) are the two highest-populated donor atom classes and must not be contained in the generated ligand.

In the example, autoPAMS_LG selects an imine-type core that expresses three wildcard atoms (**Figure 3.54B**). The wildcard atom labeled with "200" requests to be substituted with a cap that extends the core by two atoms. Accordingly, the label "100" of the other wildcard atom asks to be substituted with a cap that brings a one-atom extension. The request of these specific kinds of ligand caps ensures that a ligand is generated that will form a six-membered ring with the central atom when being attached. As 1-extension cap, autoPAMS_LG pics an oxygen atom, as 2-extension cap a carbothioic *S*-acid type cap (**Figure 3.54B**).

The wildcard atom labeled with "13" requests to be exchanged against a substituent for a sp^2-hybridized, *per se*, non-aromatic carbon atom by forming a single bond – a methylene bridge is picked (**Figure 3.54B**). The methylene group contains a wildcard atom labeled with "13" (connection to the core) and one labeled with "1000". The latter requests an aromatic ligand substituent, which, in the chosen example, is a 1,3,5-trisubstituted benzene ring. This aromatic ligand building block has a wildcard atom labeled with "1000" (connection to the core, cap, or other general ligand substituent, respectively) and one labeled with "2". This triggers the request of a substituent for an aromatic ring. A chlorine atom is chosen for that. It has only one wildcard atom (labeled "2") which is used for the connection to the aromatic ligand building block. Due to that, the building block selection is terminated, and the individual pieces are assembled recursively. Finally, the ligand (in form of its SMILES string) is obtained as shown in **Figure 3.54B**. It is the result of the ligand generation process.

autoPAMS_DM selects two mini-ligands (methyl and bromine) to complete Si(IV)'s valence and passes them together with the generated bidentate ligand to autoPAMS. Now, the entire molecule is assembled, a three-dimensional starting structure is calculated, and the structure and the structural data are saved and get added to the raw dataset. After the quantum chemical workflow (*vide infra*) is completed for the LA, the optimized structure is given to autoPAMS_F. It generates the FA starting structure, which is also submitted to the quantum chemical workflow.

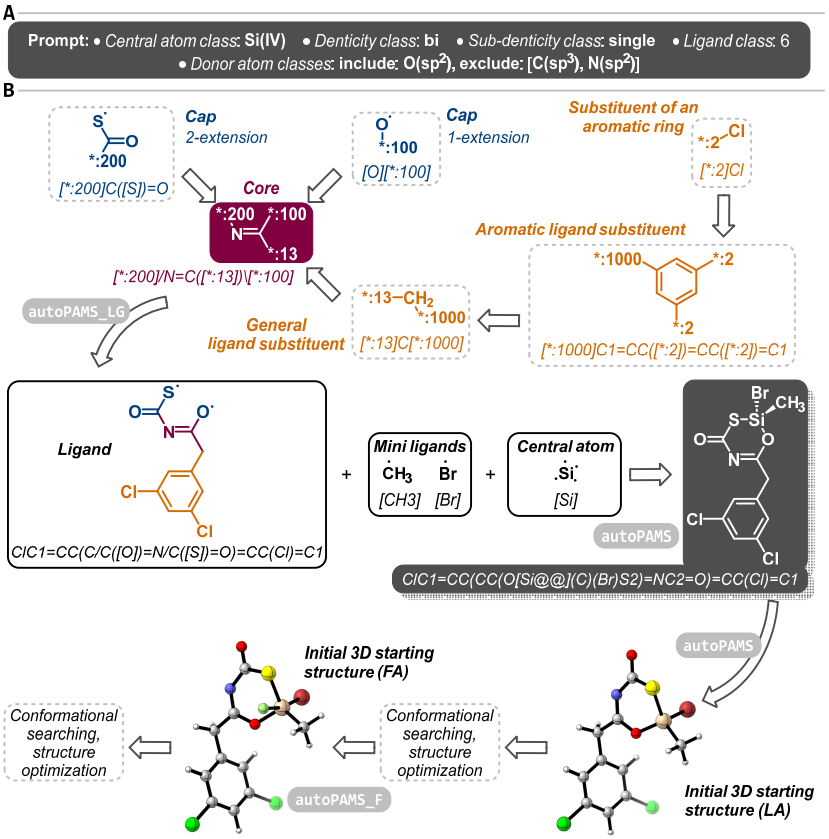

Figure 3.54: Workflow for the automated starting structure generation for the compilation of the FIA44k dataset. ***A)*** *Prompt that is passed to the Python modules (light-gray boxes).* ***B)*** *Structure generation process for Lewis acid (LA) and fluoride adduct (FA).*

Mechanisms to keep the dataset balanced

To conclude the presentation of how the FIA44k dataset was constructed, its individual categories and their relative proportion are described. In general, `autoPAMS_DM` ensures that molecules of the denticity classes “mono”, “bi”, and “tri” are represented in equal portions. Low-valent group 14-based molecules have an overall lower absolute count in the dataset as it is not possible to attach tridentate ligands to the respective central atoms while having the molecule remain neutral.

The molecules of denticity class "mono" were not categorized into further subgroups. Hence, autoPAMS_DM requests ligands from autoPAMS_LG such that the nine donor atom classes (*cf.* **Figure 3.52B**) are equally populated.

The denticity class "bi" was divided into its ligand and sub-denticity classes (**Figure 3.52C/D**). For each of these 3-tuples (*e.g.*, central atom class: Si(IV), denticity class: bi, ligand class: 5), autoPAMS_DM works toward an as balanced as possible donor atom distribution. Furthermore, it distributes the overall one third share of the denticity class "bi": the sub-denticity classes "single" and "double" are equally represented (1/6 each). The ligand classes obtain equal shares within each sub-denticity class. In total, nine different ligand classes are obtained, which are grouped into two different sub-denticity classes.

The denticity class "tri" was divided into its nine ligand classes, for which balanced donor atom distributions were sought. The one third share of the denticity class "tri" was equally divided between the nine ligand classes.

Given the chosen chemical space, autoPAMS_DM keeps track of 291 individual donor atom distributions ("mono": 21, "bi": 117, and "tri": 153) defined by the central atom, the denticity, and the ligand class.

Quantum chemical workflow

To close this chapter, the applied quantum chemical workflow for the construction of the FIA dataset is presented. Conformational searching was done with the CREST algorithm (conformer-rotamer ensemble sampling tool) using GFN2-xTB. Structure optimizations and frequency calculations were done at the PBEh-3c level of theory. For final single point energy calculations RI-DSD-BYLP-D3(BJ)/def2-QZVPP was used. The COSMO-RS scheme for CH_2Cl_2 (298.15 K) was applied to implicitly account for solvent influences during the calculation of the solution phase FIA (FIA_{solv}). The references to utilized software, methods, and basis sets are given in **Chapter 5.2**. Thermochemical corrections were obtained at 298.15 K and 1 bar. Gas phase FIA values (FIA_{gas}) were calculated with the fluorotrimethylsilane anchoring system (*cf.* **Figure 1.8** in the Introduction). FIA_{solv} was obtained with

$$FIA_{solv} = FIA_{gas} - \left(\Delta H_{corr}(FA) - \Delta H_{corr}(LA) - \Delta H_{corr}(F^-)\right), \tag{3.1}$$

in which ΔH_{corr} refers to the individual solvent corrections to enthalpy values.

The first step toward a FIA datapoint was the conformational searching and structure optimization for LA. The lowest energy conformer based on the ordering provided by the GFN2-xTB level of theory was used in the PBEh-3c calculation. After structure optimization, the atom connectivity of the optimized structure was compared to the expected one based on the known SMILES string. This was done with a modified version of `xyz2graph` (https://github.com/zotko/xyz2graph, last accessed on January 02, 2024). If the two connectivity arrays were found identical, the frequency calculation was done, if not, the datapoint was eliminated from the dataset. In case the frequency calculation resulted in the presence of at least one imaginary vibrational mode, the structure was displaced along this mode and was reoptimized, and the frequency calculation was repeated. This was done for a maximum of 30 cycles. If it was possible to remove the imaginary mode, the atom connectivity of the final optimized structure was checked again as described above.

If a LA structure with zero imaginary modes and expected atom connectivity was obtained, the FA starting structure was generated with the `autoPAMS_F` module. It was submitted to the same routine as the LA starting structure. If both an LA and FA structure with zero imaginary modes and expected atom connectivity were obtained, the final single point energy and COSMO-RS calculations were done. If they were successful, the datapoint was added to the dataset, if not, it was eliminated.

The deformation energies for all datapoints of the constructed FIA dataset were computed (*cf.* **Chapter 3.11**). 107 datapoints with a negative deformation energy were removed. The deformation energy is defined as the difference in electronic energy of the relaxed LA structure and the structure of the LA in the FA but with the fluoride anion removed (**Figure 1.7** in the Introduction).

Conclusion

Large and chemically diverse datasets as well as their efficient generation are crucial for the successful development of statistical models. By applying the developed Python routines (autoPAMS) and quantum chemical workflows presented within this chapter, a FIA dataset holding 44,877 unique datapoints was obtained (FIA44k). The collected data is of RI-DSD-BLYP-D3(BJ), COSMO-RS(CH_2Cl_2)/def2-QZVPP//PBEh-3c quality. The analysis of FIA44k is discussed in **Chapter 3.11**. To train, test, and apply machine learning models for FIA regression, the FIA44k dataset was expanded to the final FIA49k dataset, which has 48,986 datapoints. These expansions are described in the following chapter.

3.10 Augmentation of the FIA44k Dataset

By the time this dissertation was written, the results presented within this chapter were submitted for peer review: L. M. Sigmund, S. Sowndarya S. V., A. Albers, P. Erdmann, R. S. Paton, L. Greb, "Predicting Lewis Acidity: Machine Learning the Fluoride Ion Affinity of p-Block Atom-based Molecules". This chapter was written based on the mentioned paper draft. Some of the results shown below were generated in collaboration with PHILIPP ERDMANN. The generated FIA dataset and all developed Python code was published on GitHub (https://github.com/GrebGroup/fia-gnn) and figshare (https://figshare.com/projects/FIA-GNN/187050).

Introduction and background

In the previous chapter, the FIA44k dataset, its taxonomical details, and the underlying Python routines were presented. In this chapter, five extensions to FIA44k are introduced to yield the final FIA49k dataset with 48,986 datapoints. The extensions are as follows.

- FIA2k-CSD has 2,389 datapoints and contains examples which were extracted from the Cambridge Structural Database (CSD).
- FIA911-ring4 includes 911 datapoints. It is composed of molecules which all have the central atom embedded within a four-membered ring. This structural motive is not contained in the FIA44k dataset.
- FIA763-bimacro spans 763 datapoints. This subset contains structures which all feature a bidentate macrocyclic ligand (such as for example in 9-BBN). This structural motive is also not part of the FIA44k dataset.
- FIA31-cat has 31 datapoints (**Figure 3.59**). All molecules of the FIA31-cat subset have perfluoro- or perchlorocatecholato ligands. These ligands have been applied in multiple studies to prepare strong neutral *p*-block atom-based Lewis acids.[379-381, 391-393]
- FIA15-PTCat encompasses 15 datapoints which are differently substituted boranes (**Figure 3.60**). Some of the included molecules were investigated by KIRSCHNER *et al.* as phase transfer catalysts for fluoride anions.[362]

FIA2k-CSD dataset

The Cambridge Structural Database was consulted to search for additional molecules for the enlargement of the FIA44k dataset. This was done using the 2022.3.0 CSD software portfolio, leveraging its Python application programming interface (API), version 3.0.14.[394] The CSD was searched complying with the in **Chapter 3.9** formulated dataset construction rules. The concrete criteria to search the CSD were:

- All database entries classified as being polymeric were excluded.
- All entries classified as having at least one charged atom were excluded.
- Allowed ligand atoms were H, C, N, O, S, F, Cl, Br, and I (*cf.* **Figure 3.52B**).
- Only entries that have exactly one atom of the 21 different options as shown in **Figure 3.52A** were considered. These atoms are the central atom to which the fluoride anion binds in the fluoride adduct.
- Only the heaviest component of each entry was considered, and only if it was possible to obtain it as SMILES string representation. This was done to exclude co-crystallized solvent molecules.

For the actual search, the `SMARTSSubstructure` class of the `ccdc.search` module was used. The provided smarts were of the form

“`[<central_atom>X<valency>v<valency>]-[#6,#7,#8,#16]`”,

in which “`central_atom`” was the central atom symbol (*e.g.*, “Al”) and valency its oxidation state (*e.g.*, “3”) as given in **Figure 3.52A**. The described workflow resulted in 16,969 hits. The obtained SMILES representations were further filtered using RDKit:

- Hits with unpaired electrons at ligand atoms were removed. It was ensured that there are no unpaired electrons at central atoms except for lone electron pairs which are classified as unpaired by RDKit (*e.g.*, at Si(II) central atoms).
- Hits with triple bonds were removed. They are not part of the dataset.
- Hits with ligands which were not mono-, bi-, or tridentate were removed.
- Hits with heteroatom-heteroatom bonds (*e.g.*, S-S or N-O bonds) were removed.
- Hits with deuterium labels were removed.
- Hits with more than 120 atoms were removed.

These restrictions narrowed down the CSD dataset to 12,572 entries (**Figure 3.55A**). The distribution of hits among the central atom classes is highly unbalanced. It ranges from eleven hits for Si(II)-based molecules to 4,607 for compounds with Si(IV). This would be problematic when statistical models are trained with such a dataset as a significant bias toward the highly populated central atom classes would be introduced.

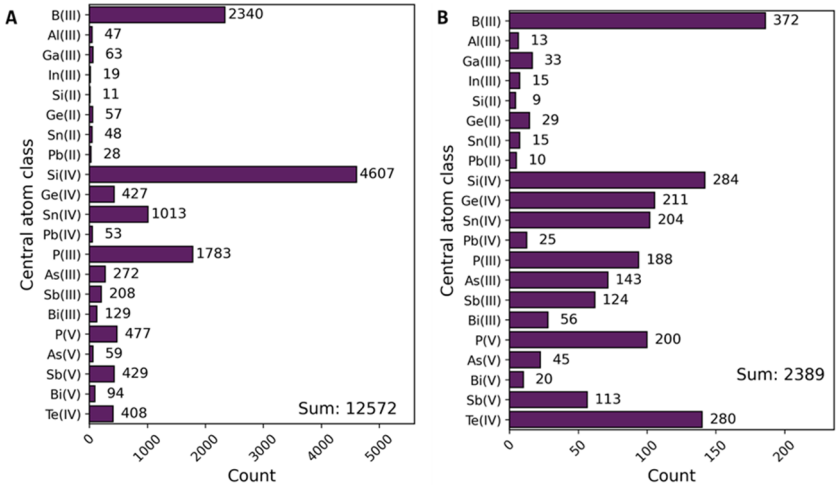

Figure 3.55: FIA dataset of molecules from the Cambridge Structural Database. ***A)*** *Distribution with respect to the 21 different central atom classes (cf. Figure 3.52A) after filtering the entire database.* ***B)*** *Distribution of the successfully obtained FIA values (FIA2k-CSD dataset).*

As it would be computationally to demanding to attempt the FIA calculation of all 12,572 molecules, a third selection step was implemented. For that, the maximum number of datapoints per central atom class was restricted to 500. If less than 500 datapoints were found in a given central atom class, all were selected for the submission to the quantum chemical workflow (*cf.* Chapter 3.9). If it was more than 500, a MinMax picking strategy (based on Tanimoto similarities[395] and Morgan fingerprints[396]) was followed to reduce the number of molecules.

In a final step, three-dimensional starting structures were calculated from the list of selected SMILES strings. This was done with the `ConformerGenerator` class of the `ccdc.conformer` module. Ultimately, 4,735 datapoints were subjected to the quantum chemical workflow of which 2,389 made it to the final FIA2k-CSD dataset (**Figure 3.55A**). The final distribution of successful datapoints still resembles the unbalanced situation of the initial filtering result, though to a lesser extent (**Figure 3.56**). The unbalanced situation

also transpires when analyzing FIA2k-CSD with respect to the three denticity classes "mono", "bi", and "tri", whereat the latter is clearly underrepresented (**Figure 3.56B**). The donor atom distribution (atom binding to the central atom, **Figure 3.56C**) is dominated by the carbon-based donor classes, while especially the two sulfur classes are clearly underrepresented.

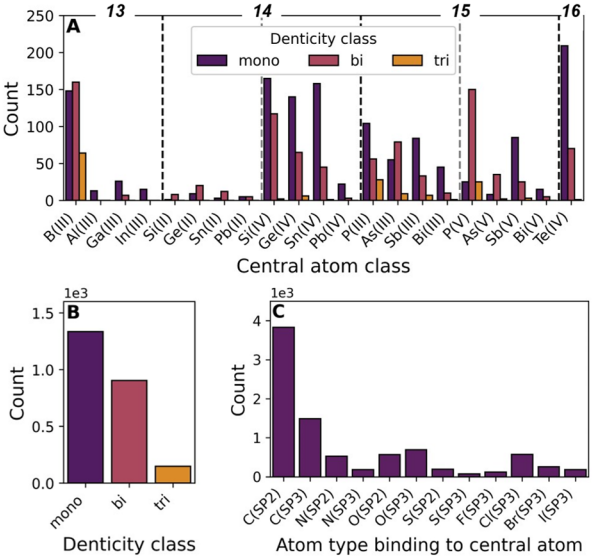

Figure 3.56: **The FIA2k-CSD dataset.** *Composition of the dataset with respect to **A)** the 21 different central atom and three denticity classes, **B)** the overall distribution among the three denticity classes, and **C)** the atom types directly binding to the central atoms.*

FIA911-ring4 dataset

The starting structures of the FIA911-ring4 dataset were obtained by composing 122 different ligands in ChemDraw, and the structure assembly functionality of *autoPAMS* (*cf.* **Chapter 3.9**) was used to build up the final three-dimensional starting structures. 80 starting structures were generated for each of the 21 central atom classes by randomly picking ligands from the pool of the available 122 bidentate ligands. Free valences at the central atoms after attaching the bidentate ligand were saturated with mini-ligands (**Figure 3.52E**).

Within FIA911-ring4, all central atom classes are represented, while the Al(III) and Pb(IV) subgroups are slightly underpopulated (**Figure 3.57A**). The donor atom distribution shows a significant presence of C-, N-, and S-donors (**Figure 3.57B**). The O(sp^2) subclass is underrepresented compared to the other non-monoatomic classes because only a small number of the 122 chosen bidentate ligands had sp^2-hybridized oxygen atoms.

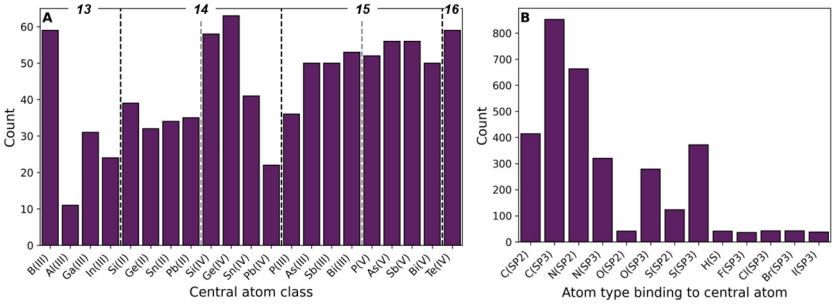

Figure 3.57: The FIA911-ring4 dataset. *Composition of the dataset with respect to **A)** the 21 different central classes and **B)** the atom types directly binding to the central atoms.*

FIA763-bimacro

The starting structures of the FIA763-bimacro dataset were obtained by composing 88 different ligands in ChemDraw, and the structure assembly functionality of *autoPAMS* (*cf.* **Chapter 3.9**) was used to build up the final three-dimensional starting structures. 60 starting structures were generated for each central atom class by randomly picking ligands from the ligand pool. Free valences after attaching the bidentate ligand were saturated with mini-ligands (**Figure 3.52E**).

All central atom classes are represented equally. Only the low-valent group 14 classes are slightly underrepresented (**Figure 3.58A**). Regarding the donor atom distribution, the O(sp^2) and S(sp^2) class are not populated as it is not possible to construct macrocyclic bidentate ligands with these atom types (**Figure 3.58A**). The populations of the respective sp^3 classes stem from the mini-ligands.

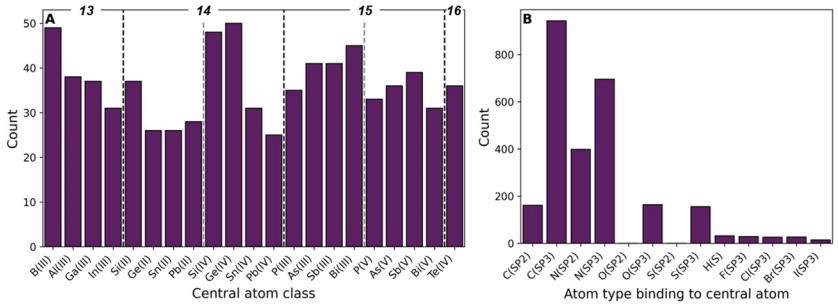

Figure 3.58: The FIA763-bimacro dataset. *Composition of the dataset with respect to* ***A)*** *the 21 different central classes and* ***B)*** *the atom types directly binding to the central atoms.*

FIA31-cat dataset

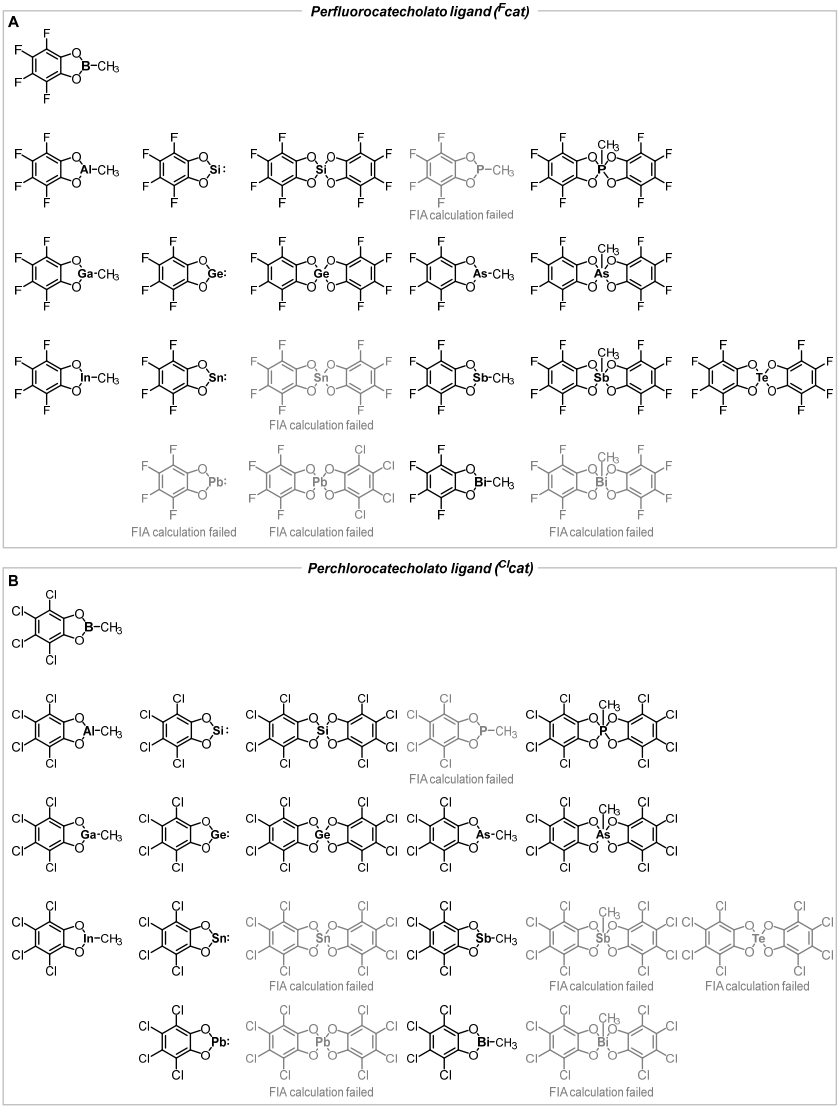

Figure 3.59: The FIA31-cat dataset.

FIA15-PTcat dataset

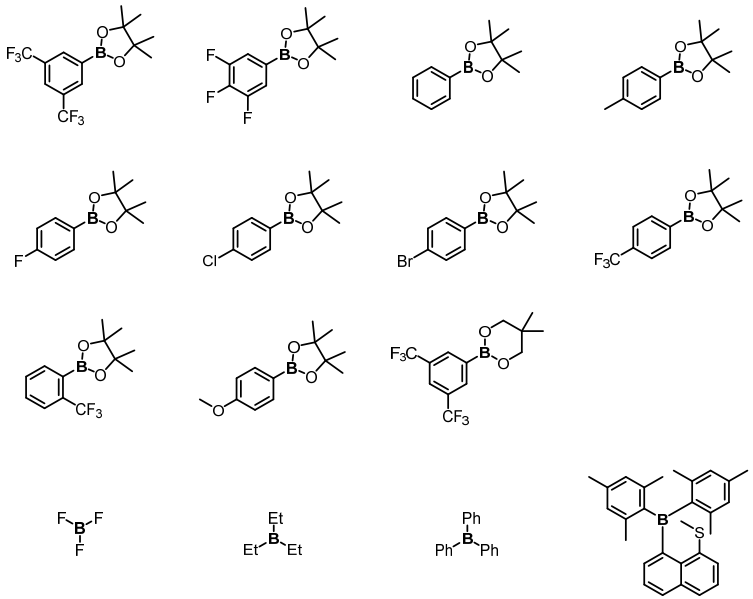

Figure 3.60: **The FIA15-PTcat dataset.**

Conclusion

In this chapter, the expansion of the FIA44k dataset (44,877 datapoints) to the final FIA49k dataset with 48,986 datapoints was presented. Five additional subsets were added, introducing molecules, for instance, from the CSD, from outside the structural scope of FIA44k, or from catalysis research from the literature. Most importantly, these expansions will allow an ample testing of ML models for FIA regression as it is described in **Chapter 3.12**. Before this was carried out, the FIA44k dataset, which is the major source of data, was analyzed. The obtained results are the subject of the following chapter.

3.11 Analysis of the FIA44k Dataset

By the time this dissertation was written, the results presented within this chapter were submitted for peer review: L. M. Sigmund, S. Sowndarya S. V., A. Albers, P. Erdmann, R. S. Paton, L. Greb, "Predicting Lewis Acidity: Machine Learning the Fluoride Ion Affinity of p-Block Atom-based Molecules". This chapter was written based on the mentioned paper draft. Some of the results shown below were generated in collaboration with ANDREAS ALBERS. The generated FIA dataset and all developed Python code was published on GitHub (https://github.com/GrebGroup/fia-gnn) and figshare (https://figshare.com/projects/FIA-GNN/187050).

Introduction and background

In the previous two chapters of this dissertation, the generation of FIA49k, a FIA dataset of *p*-block atom-based molecules with 48,986 datapoints, was presented. The major portion of FIA49k is the FIA44k subset with 44,877 datapoints. In **Chapter 3.12**, it is described how FIA49k was used to train, test, and deploy ML models for FIA regression. For the development of any ML model, it is essential to gain an as detailed as possible understanding of the used data. Therefore, the FIA44k dataset as the main source of training data for the developed statistical models is analyzed in detail within this chapter. This is done based on some of its underlying design principles (*cf.* **Chapter 3.9**). In the second part of this chapter, correlations and trends within the extracted data are investigated.

Composition and chemical balance

The FIA44k dataset is evenly distributed among the central atom classes (**Figure 3.61A**). The P(III) and Pb(IV) classes are slightly underrepresented. This is because the FIA calculations for these central atom classes were more prone to failure. P(III)-based molecules intrinsically show low FIA values, often resulting in dissociation of the fluoride adduct. Molecules with Pb(IV) central atoms tended to undergo reductive elimination to give Pb(II) compounds. Because the low-valent group 14 molecules cannot have tridentate ligands, they contribute less to FIA44k. Moreover, the compiled dataset is evenly distributed among the denticity classes "mono", "bi", and "tri" with relative shares of 32, 40, and 28%, respectively (**Figure 3.61B**).

Figure 3.61C shows the distribution of atoms directly binding to the central atoms. An even distribution of the non-monoatomic cases exists. During the construction of the dataset, the monoatomic ligands (hydrogen, halogens) were treated within a general

"monoatomic" class from which ligands were sampled. Due to that, they have a lower absolute contribution. The reason for that is that monoatomic ligands bring much less potential for molecular complexity and diversity compared to polyatomic groups. Therefore, it was decided to include monoatomic ligands to a lesser extent. The molecules of the FIA44k dataset possess a diverse set of functional groups in their ligands. 5,265 different substructures and 2,987 different ring systems were identified.

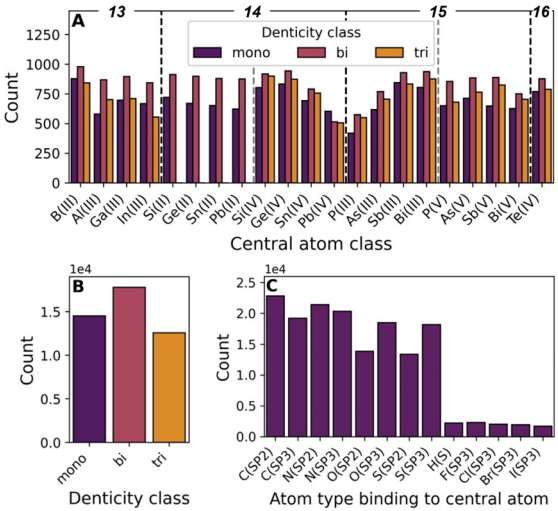

Figure 3.61: Composition of the FIA44k dataset. *Distribution of the dataset with respect to **A)** the 21 central atom and three denticity classes, **B)** the overall denticity classes, and **C)** the atom types directly binding to the central atoms.*

Trends and correlations

The FIA_{gas} values of FIA44k span a total range of 753 kJ mol^{-1}. The minimum value is 10, the maximum value 763, and the mean value 309 kJ mol^{-1}. For FIA_{solv}, the range is with 744 kJ mol^{-1} virtually identical compared to the gas phase data, with the extrema at −201 and 543 kJ mol^{-1}. The observed shift toward lower affinities is due to solvation damping. The mean FIA_{solv} value is 124 kJ mol^{-1}. Because FIA_{gas} and FIA_{solv} are strongly linearly correlated, the following discussion is limited to FIA_{gas}.

In general, the FIA distributions get sharper when going down a group of the periodic table (**Figure 3.62A**). The highest FIA values are found for group 13 molecules, with aluminum-based molecules being the most Lewis acidic (on the FIA scale) – the Al(III) central atom class has an average FIA_{gas} of 471 kJ mol^{-1}. B(III), as the only central atom of the

second period of the periodic table, is clearly separated from the other group 13 molecules toward lower FIA values.[397]

For molecules with group 14 centers, the low-valent central atom classes have higher FIA values compared to the high-valent cases. In general, the FIA decreases with increasing atomic number. This is an interesting observation, since previous research on neutral group 14 Lewis acids primarily focused on the high-valent congeners. For molecules with central atoms from group 15, the situation found for group 14 is inverted. The low-valent central atom classes have lower FIAs compared to their high-valent counterparts. Likewise, the FIA increases with the atomic number. When the FIA values were analyzed with respect to the three denticity classes, an increase in FIA as well as an increasingly wider distribution with higher ligand denticity was found (**Figure 3.62B**). Hence, the highest FIA values are achieved for molecules with tridentate ligands.

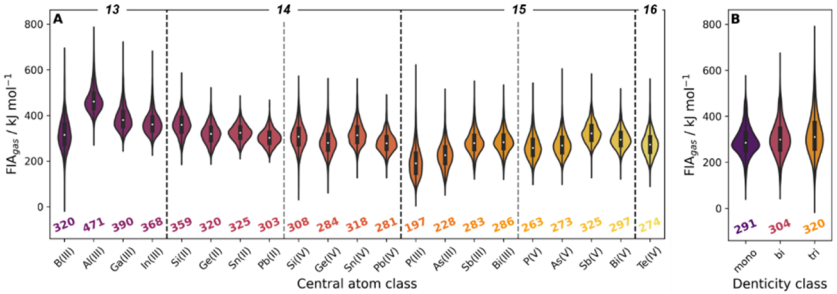

Figure 3.62: The distribution of FIA values within the FIA44k dataset. *Violin plots for the calculated FIA_{gas} values with respect to **A)** the 21 different central atom classes and **B)** the three denticity classes. Low-valent group 14 molecules were omitted in B) because they cannot have tridentate ligands. The calculations were done at the RI-DSD-BYLP-D3(BJ)/def2-QZVPP//PBEh-3c level of theory. The numbers below the violins are the class-specific mean values.*

Next, the correlation of the FIA with other intrinsic Lewis acidity descriptors was investigated. As already mentioned above, the linear correlation between FIA_{gas} and FIA_{solv} is with an r^2 value of 0.921 high (**Figure 3.63A**). On average, FIA_{solv} (calculated for CH_2Cl_2 as solvent) is 185 kJ mol^{-1} lower than FIA_{gas}. The line of best fit in the FIA_{solv} *versus* FIA_{gas} plot has a slope of 0.9077. This means that by trend high FIA_{gas} values get more strongly damped when converted to FIA_{solv}. Accordingly, relatively low FIA_{gas} values experience a less strong reduction. A practical estimate of FIA_{solv} (± 16 kJ mol^{-1}) can be obtained from FIA_{gas} with

$$FIA_{solv} = 0.9077 \cdot FIA_{gas} - 157\ kJ\ mol^{-1}. \quad (3.2)$$

Lastly, the FIA_{gas} values were related to descriptors obtained for the Lewis acids from the DFT calculations: the LUMO energy (**Figure 3.63B**), the GEI (**Figure 3.63C**), and the Mulliken charge of the central atom (**Figure 3.63D**). There is no linear correlation between any of these quantities and FIA_{gas} when considering the entire FIA44k dataset at once. This clearly distinguishes the FIA as a distinctive scale encoding more chemical information than the electronic descriptors. However, when the FIA and GEI were evaluated separately with respect to the central atom classes, r^2 values of up to 0.698 were found. Such correlations were noticed before by others for much smaller subsets of Lewis acids.[60-61]

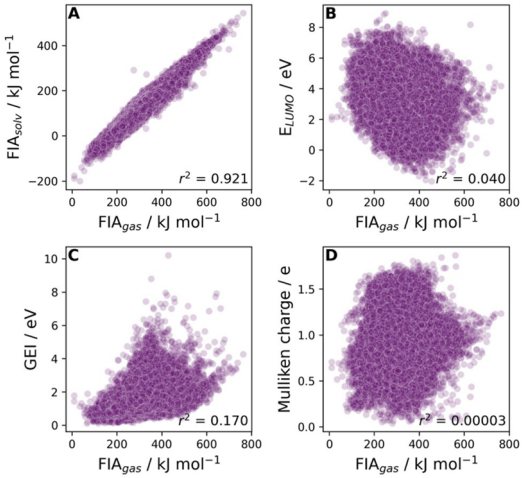

Figure 3.63: The linear correlation of the FIA with other quantum chemical descriptors. *Relation of FIA_{gas} to **A)** FIA_{solv}, **B)** the LUMO energy, **C)** the GEI, and **D)** the Mulliken charge of the central atom of the Lewis acid. The DFT descriptors were obtained at the PBEh-3c level of theory.*

Stereochemical considerations

With respect to stereochemistry, FAs with pentavalent central atoms (*e.g.*, Si(IV)-based molecules), *per se*, can adopt two different stereoisomeric conformations depending on the position of the added fluoride anion. It can either be in equatorial or apical site (**Figure 3.64**). Within the FIA44k dataset, this scenario applies to Si(IV)-, Ge(IV)-, Sn(IV)-, and Pb(IV)-based molecules.

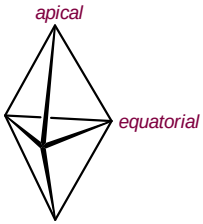

Figure 3.64: The trigonal bipyramid and its two distinct positions.

For further investigation, the FAs of the four mentioned central atom classes were analyzed by determining the maximum fluoride-central atom-X angle (X is any of the four other direct neighbors of the central atom). The obtained distribution revealed the coexistence of both isomeric forms within the FIA44k dataset, with a preference for the fluoride occupying the apical position (**Figure 3.65**). The ratio between the two isomeric forms is approximately 3:1. This aligns with the apicophilicity of the electronegative fluorine atom.[398-399] Notably, this distribution "naturally" emerged from the CREST conformational searches and structure optimizations. It was not specifically controlled whether the initial structure of the FA (which was fed to CREST) represented rather the apical or equatorial isomer. Given low isomerization barriers, the resulting distribution is expected to be valid and not an artifact of the random generation process of the FA starting structures.

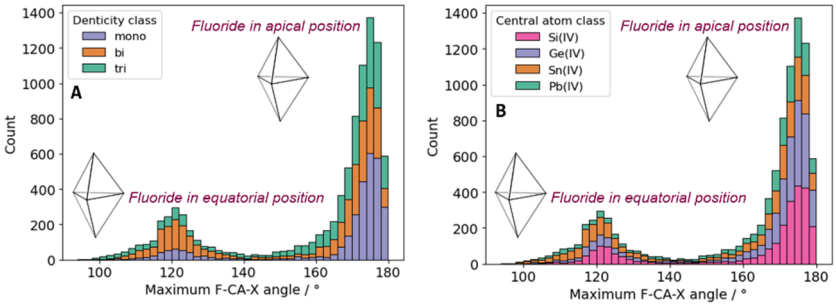

Figure 3.65: Stereochemistry of pentavalent fluoride adducts. *Maximum angle (fluoride-central atom-X) distribution within a subset of the FIA44k dataset (molecules with high-valent group 14 central atoms) with respect to* ***A)*** *the denticity classes and* ***B)*** *the central atom classes.*

Intriguingly, when the distribution was divided in half at an angle of 150° and the mean FIA_{gas} value was calculated, 327 for the equatorial half and 290 kJ mol^{-1} for the apical half were obtained – a difference of 37 kJ mol^{-1}. This indicates a clear difference between the two subgroups of molecules. As the difference between the two mean values is that large, it can be assumed that ML models must learn this classification in order to produce

accurate results. As shown at the end of **Chapter 3.12**, there is considerable evidence for the herein presented FIA model, FIA-GNN, having adapted to this additional task to a significant extent.

Deformation energy

The deformation energy (DE) required for fluoride anion binding (*cf.* **Figure 1.7** in the Introduction) was calculated for all LAs of the FIA44k dataset at the RI-DSD-BLYP-D3(BJ)/def2-QZVPP//PBEh-3c level of theory (**Figure 3.66**). The DE is an important factor influencing Lewis acidity of molecules in a universal sense and is important to be considered during the design of new LAs. The average DE of the FIA44k dataset is 100 kJ mol^{-1}. Generally, the mean DE decreases when going down a group of elements of the periodic table. It is lowest for molecules with a low-valent central atom from group 14 ranging between 54 and 31 kJ mol^{-1}. The highest DEs are found for their high-valent congeners. Si(IV)-based molecules have a mean DE of 203 kJ mol^{-1}. The archetypical building blocks for Lewis acids, that is, the group 13 elements have DEs between 192 and 68 kJ mol^{-1}, with boron being clearly the least flexible in terms of F^- binding.

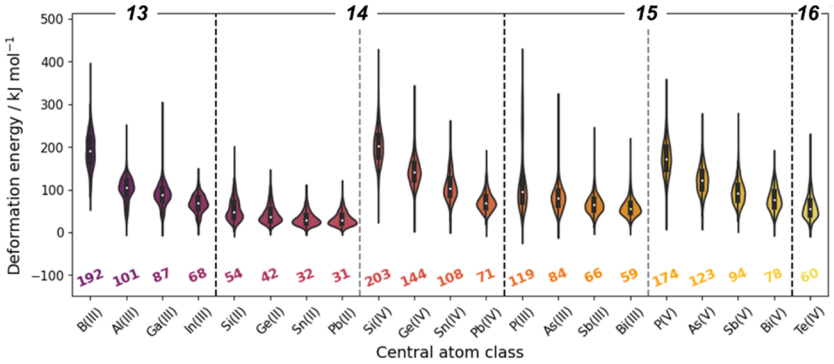

Figure 3.66: Molecular deformation due to fluoride anion binding. *Distribution of the calculated deformation energies due to fluoride anion binding of the FIA44k dataset with respect to the 21 different central atom classes (cf. Figure 3.52A).*

With increasing ligand denticity, the mean DE decreases from 119 kJ mol^{-1} for molecules with only monodentate ligands to 111 and 100 kJ mol^{-1} for bi- and tridentate cases, respectively.[d] This shows that structural constraint imposed by polydentate ligands

[d] Molecules with low-valent group 14 central atoms were omitted as they cannot have tridentate ligands.

indeed can reduce the energetic cost of structural deformation which contributes to an increase in FIA (*cf.* **Figure 3.62B**). **Figure 3.67** shows that the DEs mostly continuously decrease with increasing ligand denticity. Exceptions are for instance Ga(III) and In(III) for which molecules with a bidentate ligand on average have higher DEs than molecules with monodentate ligands. Simultaneously, group 13-based molecules show the largest drop in DE when going from bi- to tridentate ligands. Molecules with a B(III) central atom and a tridentate ligand on average require 37 kJ mol^{-1} less DE than analogous compounds with a bidentate ligand. This means that group 13 atoms can effectively capitalize on ligand-imposed structural constraint, which contributes to high FIA values (*cf.* **Figure 3.62A**).

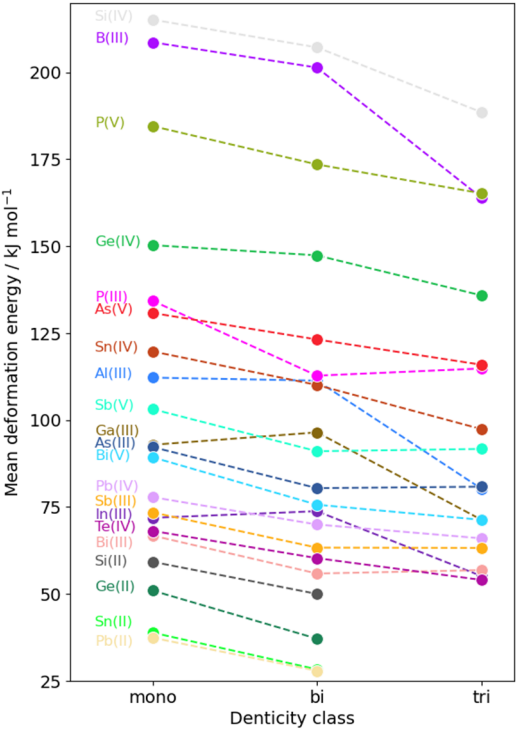

Figure 3.67: Mean deformation energies with respect to the 21 central atom and three denticity classes for the FIA44k dataset.

Lastly, the DE was directly correlated with the FIA (**Figure 3.68**). To avoid the influence of ligand-induced structural strain as much as possible, the FIA44k dataset was reduced to molecules of denticity class "mono" for this analysis. As expected, there is no overall linear correlation between the two quantities. This means that the FIA is representing more molecular properties (in terms of Lewis acidity) than sole structural flexibility during fluoride anion binding. However, **Figure 3.68** nicely illustrates the relevance of the DE for the FIA. Si(IV)-based molecules show the highest DEs and in turn only reach medium high FIA values. Contrastingly, the molecules with Si(II) centers have very low DEs; though, other electronic conditions imparted by the low-valent state prevent to reach maximum FIA values. At the same time, Al(III) LAs show low to medium large DEs and reach the highest FIA values within the FIA44k dataset.

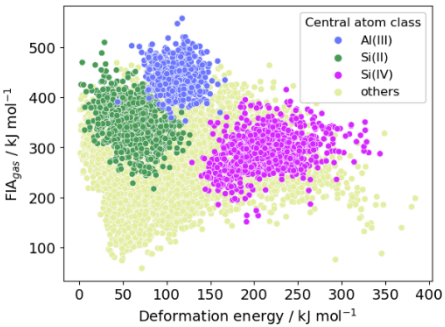

Figure 3.68: The fluoride ion affinity plotted against the deformation energy for the FIA44k dataset. *Only molecules with monodentate ligands were considered.*

Conclusion

Large datasets of high quality and an in detail understanding of them are essential for the development of ML models. Within this chapter, the FIA44k dataset was thoroughly analyzed regarding its composition and linear correlations. Stereochemical aspects were discussed, and the DEs for fluoride anion binding of the LAs of the dataset were investigated. Most importantly, the balanced distribution of FIA44k with respect to various parameters, as it was intended during the construction of the dataset with the autoPAMS workflow (*cf.* **Chapter 3.9**), was ensured. This is important, for example, for splitting the dataset into train, validation, and test portions which is required for the development of statistical models. In the following chapter, the construction of different ML models for FIA regression is presented, and the best performing models are applied in four different case studies.

3.12 Machine Learning Models for FIA Regression and their Application

By the time this dissertation was written, the results presented within this chapter were submitted for peer review: L. M. Sigmund, S. Sowndarya S. V., A. Albers, P. Erdmann, R. S. Paton, L. Greb, "Predicting Lewis Acidity: Machine Learning the Fluoride Ion Affinity of p-Block Atom-based Molecules". This chapter was written based on the mentioned paper draft. The FIA-GNN training was conducted by SHREE SOWNDARYA S. V.. The developed ML models and all further Python code was published on GitHub (https://github.com/GrebGroup/fia-gnn).

Introduction and background

In the past decade, data-driven and statistical models have gained increasingly large attention in many branches of chemical research.[162, 164-166, 400-402] As described in the Introduction in **Chapter 1.7**, ML algorithms like ANNs automatically extract potentially complex patterns from datasets. By that, they simplify or even open up the way to valuable information within a fraction of time compared to conventional approaches. ML models are thus well-suited to circumvent quantum chemical calculations of molecular or reaction properties.[163, 403-404] A huge number of ML regressors was trained for the prediction of various quantities, for example, orbital energies[405-408], bond dissociation enthalpies[173, 409-412], NMR chemical shifts[172, 413-418], atomic partial charges[419-421], and others.[175, 406, 422-425] Also, predictors for Mayr's electrophilicity parameter[426-428] and BF_3 affinities of organic Lewis bases[429] exist. However, a statistical model for the prediction of FIA values, one of the key descriptors for Lewis acidity, has not been reported.

In this chapter, ML models that can predict the gas and solution phase (CH_2Cl_2) FIA values of a chemically diverse set of *p*-block atom-based molecules comprising 13 different elements (B, Al, Ga, In, Si, Ge, Sn, Pb, P, As, Sb, Bi, and Te) are presented. The best-performing models are GNNs, and they operate with a mean absolute error of around 14 kJ mol^{-1} (r^2 = 0.93). Decision tree-based models trained with Morgan fingerprint and 2D molecular descriptor features were also tested and compared to the GNNs. For training of the FIA models, the FIA49k dataset was used (see **Chapter 3.9** and **3.10**). The applicability of the best models is demonstrated in four different case studies in the second half of this chapter.

Additional references to used software and version numbers are given in **Chapter 5.3**.

Splitting of the dataset

Before the ML models were trained, the FIA49k dataset was split in train, validate, and test portions. The FIA44k section of the entire dataset was randomly split in a 70 : 15 : 15 ratio into train, validate, and test sets. Next, the FIA2k-CSD dataset was divided into two equal portions. The first of which was added to the train and validate set respectively, in such a way that the 70 : 15 ratio of train and validate was maintained. The second half was held-out for testing the final best performing models. Because the FIA2k-CSD dataset shows significant central atom class imbalances (*cf.* **Figure 3.55**), it was split randomly but stratified by the central atom class label. The models were trained independently to either predict FIA_{gas} or FIA_{solv} and were evaluated with respect to mean absolute error (MAE) and squared Pearson correlation coefficient (r^2).

Decision tree-based FIA models

As baseline models, random forest (RF) regressors[154] with 100 trees were trained using Morgan fingerprints[396] (calculated for the whole molecules) of radius 3 and length 2048 as features. Baseline models are important as benchmark for further, more sophisticated models. A FIA_{gas} RF model that made predictions for the test set of FIA44k with an MAE of 32.2 kJ mol^{-1} (r^2 = 0.660) was obtained. The FIA_{solv} model's accuracy was marginally higher (MAE = 29.8 kJ mol^{-1}, r^2 = 0.661). As expected, FIA_{gas} and FIA_{solv} can be predicted to a similar degree of precision. The change to a LightGBM regressor with 2000 boosting rounds and early stopping instead of the RF model slightly increased the accuracy for both the FIA_{gas} (MAE = 28.3 kJ mol^{-1}, r^2 = 0.738) and FIA_{solv} model (MAE = 27.1 kJ mol^{-1}, r^2 = 0.728). The generated results indicate that molecular fingerprints (the way they were applied) are features of mediocre quality for FIA prediction.

Next, all two-dimensional molecular descriptors available in RDKit[390] and mordred[152] for the LAs (including hydrogen atoms) of the FIA49k dataset were calculated. After feature reduction, which was carried out in two rounds, a set of 296 features was obtained. Firstly, numerically malformatted (*e.g.*, NaN or infinite values) and linearly correlated features were removed. Secondly, LassoCV[154] (with FIA_{solv} as target value) was used to further reduce the features. All features with a coefficient below 0.1 were discarded.

When the LightGBM regressor was retrained with the 296-dimension molecular descriptor feature space, a significant improvement in accuracy was observed. The newly obtained FIA_{gas} model made predictions for the test set with an MAE of 17.4 kJ mol^{-1} (r^2 = 0.899), and the FIA_{solv} model with an MAE of 15.8 kJ mol^{-1} (r^2 = 0.902).

Understanding the 296-dimensional molecular descriptor feature space

The initial 296-dimensional feature space (*vide supra*) of the train set was subjected to a supervised partial least squares (PLS)[154] regression to 25 dimensions (using FIA_{gas}) followed by an unsupervised UMAP (Uniform Manifold Approximation and Projection) dimensionality reduction into 2D.[430] An embedding resulted that shows separation of the dataset into the central atom classes and also gathering of central atom classes of the same group of the periodic table (**Figure 3.69**). Moreover, it singularizes the central atom classes with the highest (Al(III), Ga(III), In(III)) and lowest (P(III), As(III)) mean FIA values. This illustrates that clustering of the data occurs primarily based on the central element type, which is thus identified as important parameter that influences the FIA as well as its prediction.

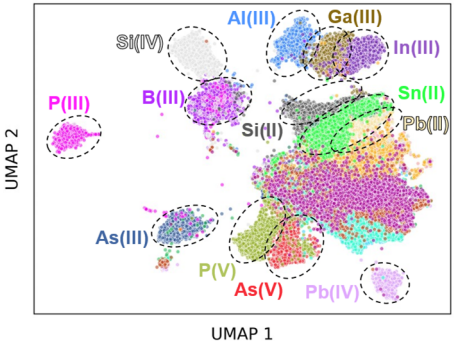

Figure 3.69: **Dimensionality reduction of the molecular descriptor feature space for FIA prediction.** *Two dimensional UMAP embedding of the train and test dataset of FIA44k obtained from a 25-dimensional PLS embedding. The reducers were trained with the train set. The supervised PLS regression was done with* FIA_{gas}.

SHAP analysis of the LightGBM model

To get further insights into the influence of the individual features on the FIA predictions of the LightGBM models, which used the 2D molecular descriptor features, SHAP (Shapley additive explanations)[431] values were calculated using the fitted FIA_{solv} model. The SHAP algorithm is a game theoretical approach which attempts to explain the output of ML models. It assigns each used feature an importance value; thus, it allows to better understand which part of the feature space was considered "important" by the ML model to obtained the results.[432]

For the present application, the by far highest ranked feature was the BCUTpe-1l descriptor. This is the first lowest eigenvalue of the Burden matrix weighted by Pauling electronegativity. The Burden matrix is a modified adjacency matrix.[433] For the FIA49k dataset, the BCUTpe-1l descriptor is the central atom Pauling electronegativity adjusted by the molecular framework (atom electronegativities and chemical bonds) around it. This is because the central atom is the most electropositive one for all molecules within the dataset, and therefore it is represented in the lowest eigenvalue of the weighted Burden matrix.

Remarkably, the BCUTpe-1l values of the FIA49k dataset show linear correlation (up to $r^2 = 0.580$ for Bi(III)-based molecules) with the Mulliken charges of the central atom. The correlation was done central atom class wise. This demonstrates that topological descriptors contain information about quantum chemical properties. Similar conclusions can be drawn for the second highest ranked feature (according to the SHAP analysis). It is the first highest eigenvalue of the Burden matrix weighted by van-der-Waals volume. Except for boron-based molecules, the central atom is the largest atom in each molecule of the FIA49k dataset. Overall, this analysis further demonstrates the importance of central atom features, namely "electronegativity" and "size" (fine-tuned by ligand influences), for FIA predictions with ML models. BCUT descriptors were also used before in previous studies.[434-435]

Graph neural networks for FIA prediction

To reach even higher predictive accuracy, message-passing graph neural networks (GNNs) were considered within the nfp Python package (*cf.* **Chapter 1.7** in the Introduction).[178] Firstly, the two-dimensional molecular graph was transformed to an atom and bond token vector, respectively, by following a small number of node and edge classification rules: for atoms, the atom symbol and degree (neighbor count) were used; for bonds, the participating atoms (start and end atom) and the bond order were applied (**Figure 3.70A**). Secondly, each token was used to obtain initial atom and bond embeddings of length 128. These embeddings were sequentially updated during six rounds of message passing on the molecular graph. Updates were performed in the order bond, atom, and finally global (**Figure 3.70B**). The overall model was also given molecule features. They were exploited to provide further information on the central atom: the period and group of the central atom in the periodic table, its oxidation state, the number of rings the central atom is part of, and the number of ligands that are attached to it were used (**Figure 3.70A**). They were passed through the final readout network together with the learned

graph embeddings. Models were optimized with the AdamW optimizer for 500 epochs with an inverse time decay schedule for learning rate and weight decay and the best of the 500 obtained models was taken as the final result. A FIA_{gas} model which made predictions for the test set with an MAE of 13.1 kJ mol^{-1} (r^2 = 0.931), and a FIA_{solv} model with an MAE of 12.3 kJ mol^{-1} (r^2 = 0.927) were obtained.

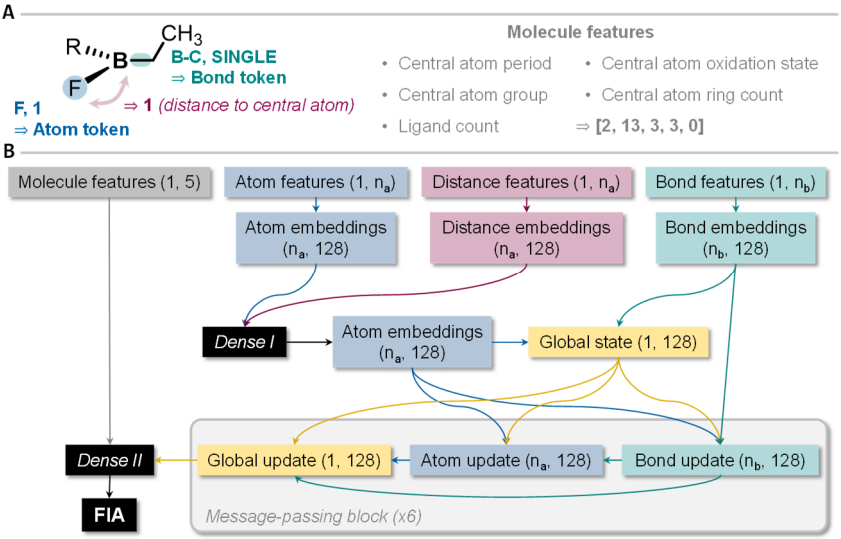

Figure 3.70: FIA prediction with message-passing graph neural networks. ***A)*** *Featurization of molecular graphs (obtained from SMILES strings) using atom, bond, and molecule features.* ***B)*** *Model architecture. n_a means number of atoms, n_b number of bonds. "Dense I" is a set of three fully connected layers (512, 256, and 128 neurons). "Dense II" expands the molecule features to 128 dimensions with a single layer and after concatenation provides a set of four fully connected layers for read-out (128, 64, 32, and 1 neuron(s)).*

Ultimately, the FIA GNN models were extended by another input layer taking in a vector of the shortest bond path length between a given atom and the central atom. This provides information on the concentricity of the problem at hand. Potentially, the influence of a certain atom depending on its distance to the central atom is learned. Indeed, this input of additional information resulted in a slight drop in MAE to 12.1 kJ mol^{-1} (r^2 = 0.939) for FIA_{gas} and 11.7 kJ mol^{-1} (r^2 = 0.935) for FIA_{solv}. These are the best FIA predictions which were obtained. The respective model is called FIA-GNN, and its overall architecture is depicted in **Figure 3.70B**.

To put these results into perspective, the FIA span of the FIA49k dataset is around 750 kJ mol^{-1}. Hence, the MAEs are less than 2% of this wide range. Also, they are on the

same order of magnitude as the error of the quantum chemical procedure (RI-DSD-BLYP-D3(BJ)/def2-QZVPP//PBEh-3c) which was used to construct the dataset.[436] At the same time, FIA-GNN entirely avoids quantum chemical calculations and processes only SMILES strings as input. SMILES strings can be easily obtained, *e.g.*, from ChemDraw.

The performance of FIA-GNN with respect to the central atom and ligand denticity classes was analyzed (**Figure 3.71**) before it was applied in different case studies (see next section of this Chapter). The FIA_{gas} values of datapoints with central atoms from group 13 (except for boron) and the low-valent group 14 atom-based molecules were most accurately predicted. Here, the MAEs were below 10 kJ mol^{-1}. The largest prediction errors showed phosphorus-based molecules (MAE of 19.6 and 18.4 kJ mol^{-1}). LAs with only mono or bidentate ligands had lower prediction MAEs (10.6 kJ mol^{-1}) compared to molecules with tridentate ligands (MAE = 16.1 kJ mol^{-1}).

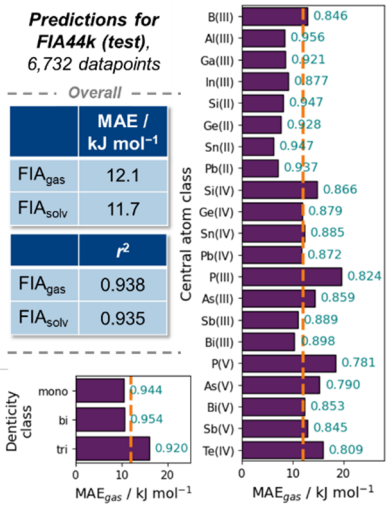

Figure 3.71: **Performance of the FIA-GNN model.** *Predictions of FIA_{gas} values of the test set of FIA44k evaluated overall, with respect to the 21 different central atom classes, and the three denticity classes (cf. Chapter 3.9). The dashed orange lines mark the overall MAE. The numeric labels at the bars are the central atom and denticity class-specific r^2 values.*

One way to investigate the operation of GNNs, is the inspection of the learned feature representations, which are molecular representations in the context of chemistry. These representations are of high dimensionality (up to 128 in the case of FIA-GNN) and cannot be visualized offhand. Therefore, dimensionality reduction was applied, and two different layer outputs were subjected to a UMAP dimensionality reduction into two dimensions.

The activations of the last message-passing block (128-dimensional) as well as the final 32-dimensional latent space vectors which are fed to FIA-GNN's output node were selected. The data of the model which was trained to predict FIA_{gas} was used.

The reduced 128-dimensional embeddings result in a granular data organization separating the dataset with respect to central atom and ligand denticity classes (**Figure 3.72A**). Intriguingly, molecules of ligand denticity class "bi" (*cf.* **Chapter 3.9**) were grouped in two separate clusters depending on the amount of attached bidentate ligands (either one or two). Contrastingly, the UMAP embedding of the 32-dimensional feature vectors is continuous (**Figure 3.72B**). The separation in the individual central atom and denticity classes is lost. A counterclockwise ordering of the data with increasing FIA_{gas} is observed that unexpectedly places the highest and lowest FIA values close in dimensionality reduced latent space.

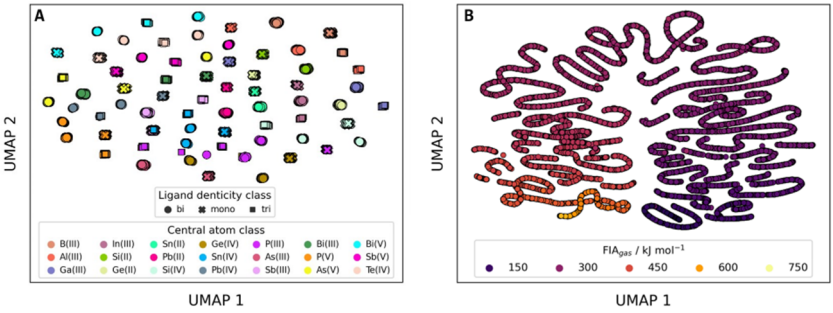

Figure 3.72: Dimensionality reduction of molecular representations of FIA-GNN. *Two dimensional UMAP embedding of the 128-dimensional output of* ***A)*** *the final message-passing block and of* ***B)*** *the 32-dimensional output of the penultimate layer of "Dense II". The reducers were trained with the train set and the* FIA_{gas} *model, and the embedding of the train and test set is shown.*

Application of FIA-GNN

The FIA-GNN model was applied in four separate case studies. First, it was applied to the second half of the FIA2k-CSD dataset, second, molecules from outside of the structural scope of FIA-GNN's training dataset were tested, third, results from a catalysis study taken from the literature were reproduced, and fourth, influences of catecholato ligands on *p*-block atoms were investigated.

Case study I. The FIA values of 1,200 molecules extracted from the CSD were predicted with FIA-GNN. FIA_{gas} and FIA_{solv} were predicted with MAEs of 14.4 (r^2 = 0.905) and 13.5 kJ mol^{-1} (r^2 = 0.895), respectively (**Figure 3.73A**). This is slightly less accurate in comparison to the regressions made for the test set of the FIA44k dataset (*cf.* **Figure 3.71**). The obtained results demonstrate the model's applicability to a broad variety of real-world examples, which are beyond the training dataset of FIA-GNN.

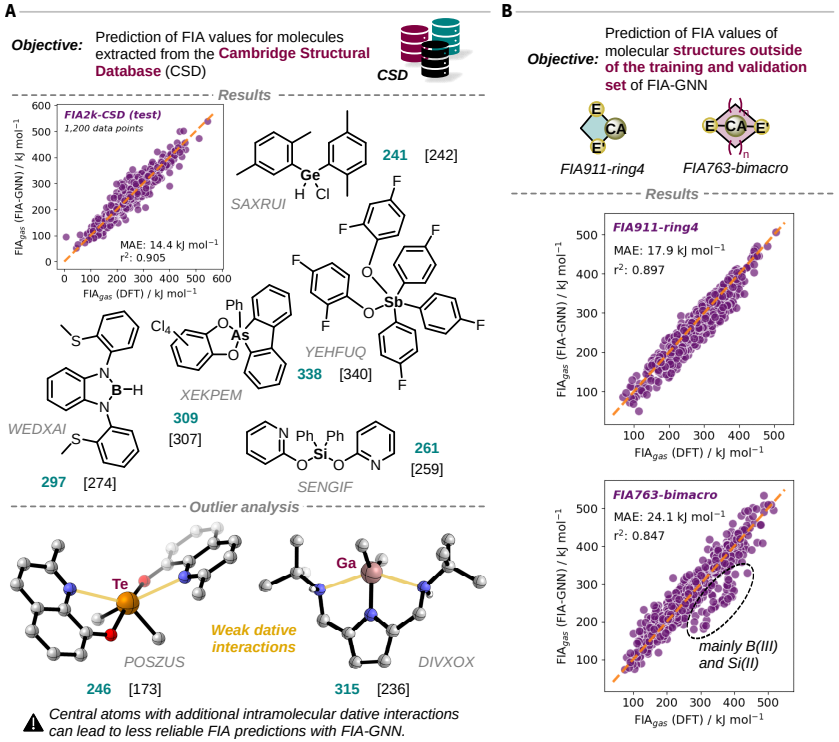

Figure 3.73: Application of FIA-GNN – part I. ***A)*** *FIA predictions for molecules from the Cambridge Structural Database. The explicitly shown molecules were randomly selected from the subset of datapoints which was added to the CSD in 2022. All shown numbers are FIA_{gas} values in kJ mol^{-1}. FIA-GNN predictions are given in bold and green, the data from the DFT calculations (ground truth) in brackets. The carbon-bound hydrogen atoms of the two molecular structures in the lower left section were omitted for clarity.* ***B)*** *FIA predictions for molecules with structures outside of the train and validation dataset of FIA-GNN. The FIA911-ring4 (molecules with the central atom embedded in a four-membered ring) and the FIA763-bimacro (molecules with a macrocyclic bidentate ligand) dataset were used (cf. Chapter 3.10).*

The molecules which showed the largest prediction errors were investigated. It was not possible to detect systematic structural features across all the poorly predicted cases. However, it was found that five of the 20 molecules with the highest error showed significant chemical bond rearrangement upon fluoride binding. The extraordinary reorganization in chemical bonding stems from a certain degree of hypercoordination of the central atom in the Lewis acid (**Figure 3.73A**). Even though, the observed hypervalencies are within the defined cutoff values used for the transformation of the continuous 3D structures to molecular graphs with discrete edges (chemical bonds) after structural optimization (*cf.* **Chapter 3.9**), it seems that they are not sufficiently represented in the training set of the model to be adequately accounted for during prediction. This means that when bond rearrangements are likely to occur after F^- binding, results from FIA-GNN could be less reliable and must be inspected carefully.

Case study II. Next, it was investigated how FIA-GNN deals with molecules with structural motifs that are systematically outside of the training dataset (**Figure 3.73B**). Structural properties have a strong influence on the FIA, and therefore, it is important to study such examples. Molecules with their central atom embedded in a four-membered ring (FIA911-ring4) or which feature a macrocyclic bidentate ligand (FIA763-bimacro) were chosen (*cf.* **Chapter 3.10**). These two structural characteristics are not present in FIA44k and in the training dataset in general. FIA-GNN predicted the data of the FIA911-ring4 dataset (MAE_{gas} = 17.9 kJ mol^{-1}, r^2_{gas} = 0.897) more accurately compared to the FIA763-bimacro set of molecules (MAE_{gas} = 24.1 kJ mol^{-1}, r^2_{gas} = 0.847). Generally though, a significant degree of predictive ability is conserved for both test sets. However, when FIA values of molecular structures beyond the training and validation set of FIA-GNN (*cf.* **Figure 3.52**) are predicted, results always should be interpreted with caution. The analysis of the prediction results for the FIA763-bimacro dataset showed that especially the FIA values of B(III)- and Si(II)-based molecules were underestimated by the model (MAE_{gas} of 46.1 and 44.2 kJ mol^{-1}). For the FIA911-ring4 dataset, molecules with high-valent central atoms from group 14 showed the highest prediction errors (MAE_{gas} values of around 32 kJ mol^{-1}).

Case study III. For the third application of FIA-GNN, a catalysis study conducted by KIRSCHNER *et al.* was used (**Figure 3.74A**).[362] In their research, computed FIA_{solv} values were employed to assist, guide, and provide a rationale for investigations on fluoride anion phase transfer catalysis. Their argumentation followed a Sabatier principle-type approach: catalysts with high FIA values facilitate the efficient removal of F^- from the solid cesium fluoride phase yet hinder the transfer of the fluoride anion to the substrate in

solution, resulting in an overall decrease in performance. Conversely, catalysts with too low FIAs are also detrimental, as they fail to extract F^- to solution in a sufficient concentration. The study identified triethylborane and a fluoroaryl pinacolatoborane as effective phase transfer catalysts and suggests that "[...] boranes with calculated fluoride affinity of 95-120 kJ mol^{-1} (vs. Me_3Si^+) appear to be suitable candidates as nucleophilic fluorination catalysts, [...].".[362]

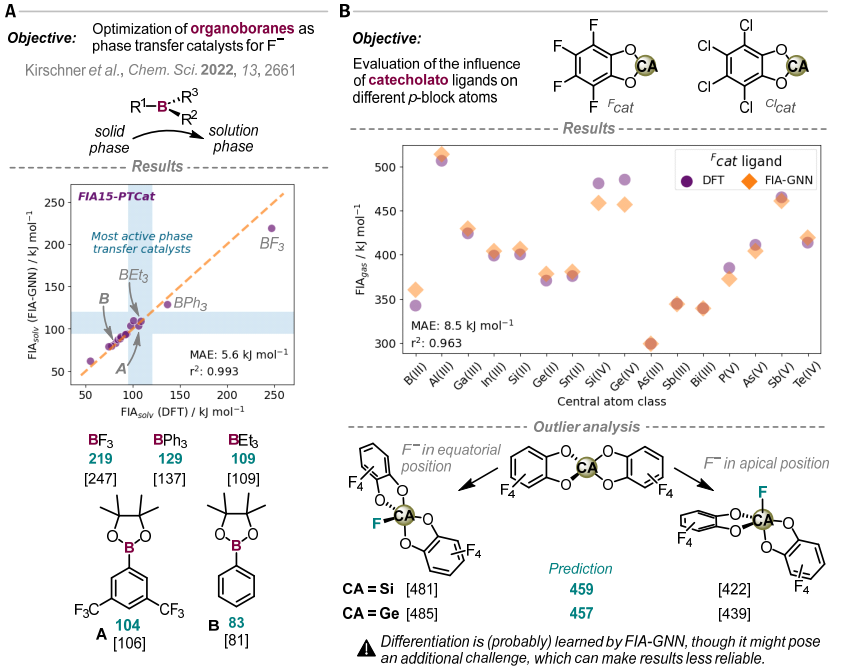

Figure 3.74: Application of FIA-GNN – part II. *FIA-GNN predictions are given in bold and green, the data from the DFT calculations (ground truth) in brackets.* ***A)*** *FIA predictions for organoboranes from a fluoride anion phase transfer catalysis study by KIRSCHNER et al. All shown numbers are FIA_{solv} values in kJ mol^{-1}.* ***B)*** *FIA predictions of perfluoro- and perchlorocatecholato-substituted p-block atoms. All given numbers are FIA_{gas} values in kJ mol^{-1}. The "apical FIA values" in the lower right section are approximate values.*

The FIA values for 15 boranes mentioned in the KIRSCHNER paper were recalculated (FIA15-PTCat dataset, **Figure 3.60**). Despite a notable prediction error (28 kJ mol^{-1}), FIA-GNN clearly pinpointed BF_3 as the most fluorophilic molecule within the specified scope, clearly surpassing the desired FIA range for effective catalysis (**Figure 3.74A**). The model correctly characterized BPh_3 as relatively strong and Ph-BPin (molecule **B** in **Figure 3.74A**) as a relatively weak Lewis acid on the FIA scale. Both fall outside the mentioned FIA span

and consequently yielded poor experimental results.[362] The FIA_{solv} values for two highly effective phase transfer catalysts, namely BEt_3 and 3,5-$(CF_3)_2C_6H_3$-BPin (molecule **A** in **Figure 3.74A**), were predicted very accurately by FIA-GNN. These findings suggest that the developed model can aid in optimizing Lewis acid-catalyzed reactions, provided there is experimental evidence establishing the correlation between catalyst performance and FIA values. Notably, FIA-GNN effectively handled well the distinction between 40% substrate conversion after 24 hours and 99% conversion after 8 hours. The difference between the two significantly different experimental outcomes is less than 20 kJ mol^{-1} on the FIA_{solv} scale.[362]

Case study IV. The previously presented application studied the influence of different ligands on the same central atom (boron). Thus, FIA-GNN was now employed to explore the impact of a single ligand system across the different central atom classes. The perfluoro- (^{F}cat) and perchlorocatecholato (^{Cl}cat) ligand were chosen for that as they have been applied in multiple previous studies to prepare strong neutral *p*-block atom-based Lewis acids (**Figure 3.74B**).[379-381, 391-393] To assemble the test molecules, the maximum number of catecholato ligands was placed at the central atom. Free valences in molecules with an odd central atom oxidation state (*e.g.*, in Ga(III)-based molecules) were saturated with methyl groups. For 31 of the 42 different combinations, FIA values were successfully calculated (FIA31-cat dataset, **Figure 3.59**). FIA-GNN accurately predicted the data of the FIA31-cat dataset with MAE_{gas} values of 8.5 (^{F}cat, r^2 = 0.963) and 8.6 (^{Cl}cat, r^2 = 0.968) kJ mol^{-1}. FIA_{solv} was equally well treated (MAE = 9.4 kJ mol^{-1}, r^2 = 0.945). The model detected the Al-based molecules as the strongest fluoride acceptors, and also suggests them as Lewis superacids (FIA_{gas} > $FIA_{gas}(SbF_5)$ = 495 kJ mol^{-1}).[17]

The FIA_{gas} values are on average 9.4 kJ mol^{-1} higher for molecules with the ^{Cl}cat ligand compared to its fluorine analog, and the values are also higher across the entire board of central atoms. When moving to FIA_{solv}, the difference between the two ligands with respect to the FIA decreases significantly (Δ = 0.8 kJ mol^{-1}). Gratifyingly, the GNN model was able to reproduce this fine effect in a qualitative manner (from Δ = 6.0 kJ mol^{-1} for FIA_{gas} to Δ = 3.2 kJ mol^{-1} for FIA_{solv}). Also, for compounds with a low-valent central atom from group 14, the minor change in the qualitative FIA trend (from Si>Sn>Ge>Pb for FIA_{gas} to Si>Ge>Sn>Pb for FIA_{solv}) when going from FIA_{gas} to FIA_{solv} was correctly modeled. These findings illustrate the effectiveness of FIA-GNN in examining how specific ligand systems affect the individual atoms of the *p*-block, and notably, also in regard of potentially varying solvent influences.

The predictions of FIA-GNN for the FIA31-cat dataset revealed a consistent underestimation of FIA values for high-valent group 14 atom-based molecules (Si(IV) and Ge(IV)). Pentavalent fluoride adducts can adopt two distinct conformations, with the fluoride located either in the equatorial or apical position. The FIA44k dataset was analyzed in this regard in **Chapter 3.11**. SCXRD analyses indicated that bis(catecholato)silanes and -germanes preferentially position fluoride in the equatorial position.[391, 437] The "apical FIA_{gas}" values for $(^{F}cat)_2Si$ and $(^{F}cat)_2Ge$ were approximately determined and found to be significantly lower than their equatorial counterparts (**Figure 3.74B**). This led to the hypothesis that FIA-GNN learned to differentiate between equatorial and apical fluoride acceptance during training for the FIA regression task. However, this differentiation potentially presents an additional challenge for the model when predicting molecules with fluoride adducts that can have multiple stereoisomers.

To test this hypothesis, the final 32-dimensional molecular features from FIA-GNN (FIA_{gas} model) were used to train a binary linear discriminant analysis (LDA) classifier.[154] A model making classifications with 79% prediction accuracy for the relevant part of the FIA44k test set was obtained. This suggests that FIA-GNN has learned information about the stereochemistry of high-valent group 14 atom-based fluoride adducts. It is worth noting that FIA-GNN was trained with the SMILES strings of the Lewis acids as input. The described apical/equatorial problem is concerned with the fluoride adducts and does not apply for most of the training dataset. Interestingly, the LDA model correctly classified all four bis(catecholato)tetrels as molecules hosting fluoride anions in the equatorial position, which is in line with the experimental findings (*vide supra*).

Conclusion

The FIA is one of the most popular descriptors for global Lewis acidity. However, FIA calculations with quantum chemistry, including the important solvation-corrected values, demand multiple steps with dedicated user input and require substantial computational power. Therefore, a ML tool (FIA-GNN) was developed that predicts FIA_{gas} and its solvation-corrected counterpart FIA_{solv} (CH_2Cl_2). FIA-GNN can generate several thousand FIA values within one minute with an average mean error of 14 kJ mol^{-1} ($r^2 = 0.93$) on a standard personal laptop. The only necessary input to the model is the Lewis structure of the compounds of interest (in form of SMILES strings). The execution of quantum chemical software is entirely avoided.

The application of FIA-GNN, exemplified in tasks involving molecules from the Cambridge Structural Database or catalysis research from the literature, has demonstrated the model's effectiveness in real-world scenarios. It is essential to highlight that a significant portion of FIA-GNN's training data originates from the FIA44k dataset (*cf.* **Chapter 3.9**), designed to encompass a broad chemical space of *p*-block atom-based molecules without specifically targeting those with exceptionally large FIA values, high halogenation levels, or unusually small sizes. Exploring these specific areas should be the focus of future research endeavors.

3.13 Dehydrogenation Chemistry of the Borane Adducts of hppH Ligands

Some of the results presented within this chapter were previously published and can be found under: L. Kistner, L. M. Sigmund, F. F. Grieser, J. Krauß, S. Leingang, E. Kaifer, L. Greb, and H.-J. Himmel, "Metal-Free B-B Dehydrocoupling Reaction of a Simple Borane Adduct: Convenient Access to a Nucleophilic Diborane(4)", Angew. Chem. Int. Ed. **2023**, *63*, *e202317463. This chapter was written based on the mentioned publication. All experimental work which is presented in the following was done by* LUCAS KISTNER.

Introduction and background

1,3,4,6,7,8-Hexahydro-2*H*-pyrimido[1,2-*a*]pyrimidine (hppH) is a bicyclic guanidine (**84**, **Figure 3.75B**).[438] As a strong base, it finds various applications, for example as organocatalyst for several different reactions[439-440], or, in its deprotonated, monoanionic form (hpp^-), as ligand in main group[441-445], transition metal[446-447], and *f*-block element chemistry.[438, 448-449] When hppH is treated with a monoborane source such as $H_3B{\cdot}N(CH_3)_3$ at elevated temperature, the borane-hppH adduct **85** is formed (**Figure 3.75A**).

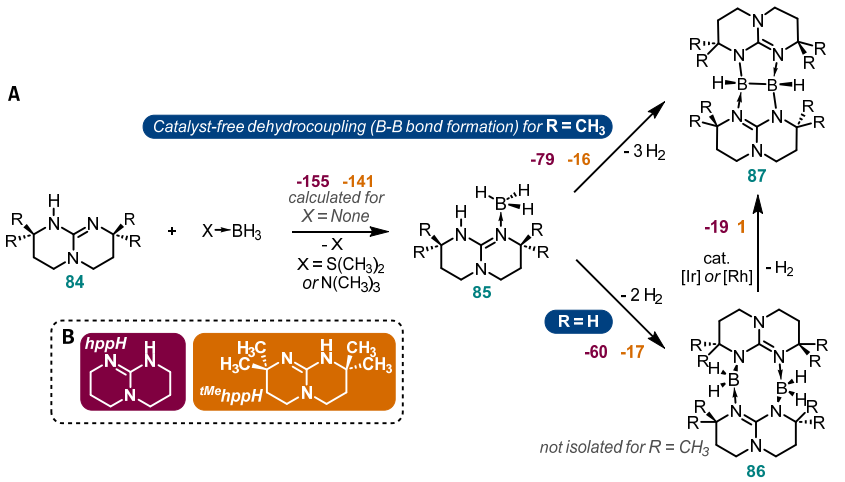

Figure 3.75: Dehydrogenation chemistry of borane adducts of hppH ligands. ***A)*** *Initial adduct formation and dehydrogenation as well as the calculated Gibbs free reaction energies (kJ mol^{-1}).* ***B)*** *Applied color scheme for the shown Gibbs free energies: the dark red numbers (left) refer to the hpp, the orange numbers (right) to the ^{tMe}hpp system.*

When **85** is heated in toluene under reflux conditions, dehydrogenative dimerization to **86** occurs.[442] The loss of a third equivalent of H_2 can be induced with the help of a rhodium- or iridium-based catalyst.[443] This results in the formation of a boron-boron bond in **87** (**Figure 3.75A**). B-B bond formation processes *via* a dehydrocoupling reaction often require a transition metal catalyst to facilitate the elimination of H_2.[450-451] Catalyst-free B-B dehydrocoupling reactions are rare.[452] This is because a potential system must be able to achieve a certain degree of umpolung of one of the hydridic hydrogen atoms connected to boron for the reaction to occur. Only then, sufficiently low activation barriers for H_2 elimination can be expected due the presence of a hydridic and protic hydrogen atom.

It was found by the HIMMEL group within the Department of Inorganic Chemistry at Heidelberg University that the introduction of four methyl groups at the 2- and 8-position of the hppH ligand framework (2,2,8,8-tetramethyl-1,3,4,6,7,8-hexahydro-2*H*-pyrimido[1,2-*a*]pyrimidine, ^{tMe}hppH, **Figure 3.75A**) allows for the catalyst free dehydrocoupling of two boron atoms resulting in diborane(4) **87** within 5 days at 120 °C in toluene as solvent. In this chapter, the results of quantum chemical calculations for the suggestion of a reaction mechanism for the transformation of hppH·BH_3 (**85**) to **86** and ^{tMe}hppH·BH_3 (**85**) to **87** are presented. All stated molecule index numbers generally refer to both the hpp and the ^{tMe}hpp system. If distinction is required, hpp or ^{tMe}hpp is prefixed to the respective number (*e.g.*, hpp-**85** and ^{tMe}hpp-**85**, respectively).

Applied computational methods

Conformational searching was done with the CREST algorithm using GFN2-xTB. For structure optimizations and frequency calculations PBEh-3c and final single point energy calculations RI-DSD-PBEB95-D3(BJ)/def2-QZVPP was used. The COSMO-RS scheme for toluene (298.15 K) was used to implicitly account for solvent influences. Thermochemical corrections were obtained at 298.15 K and 1 bar. All energies mentioned in the following sections are Gibbs free energies, given in kJ mol^{-1}. If two energy values (or any other quantity) are given, the number for the hpp system comes always first if not mentioned differently. The references to used software, methods, and basis sets are given in **Chapter 5.2**.

Overall thermodynamics

Before the individual elementary steps were investigated, the overall reaction Gibbs free energy for the transformation from **85** to **87** was calculated. It is −79 and −16 kJ mol^{-1}, respectively (**Figure 3.75A**). At the same time, the reaction from **85** to **86**, corresponding to the liberation of only two equivalents of H_2 without the formation of the B-B bond, is −60 and −17 kJ mol^{-1}. This means that in the case of the ^{tMe}hpp system, the final dehydrocoupling is slightly endergonic (+1 kJ mol^{-1}, with respect to the non-dehydrocoupled dimer), whereas for the ligand without the methyl groups, the elimination of the third equivalent of H_2 along B-B bond formation is exergonic by −19 kJ mol^{-1}. Hence, the experimentally observed preferred formation of hpp-**86** with the avoidance of B-B bond formation must be kinetically controlled. There must be a reaction pathway irreversibly trapping the hpp system in the non-dehydrogenated state (**86**). In the ^{tMe}hpp case, this pathway is absent or kinetically altered such that dehydrocoupling can occur to yield ^{tMe}hpp-**87**.

In general, the dehydrogenation reactions are much less exergonic for the ^{tMe}hpp system compared to the hpp case (*vide supra*). This can be ascribed to steric repulsions, which are introduced into the molecules by the four additional methyl groups – especially when dimerization occurs. This holds throughout the entire discussion following in the next sections. Exemplarily, this is illustrated by non-covalent interaction (NCI) plots of **86** and **87** (**Figure 3.76**). In situations, in which steric effects only play a secondary role, *e.g.*, during the intramolecular dehydrogenation of **85** (*vide infra*), the absolute and relative differences between the two different system are significantly reduced.

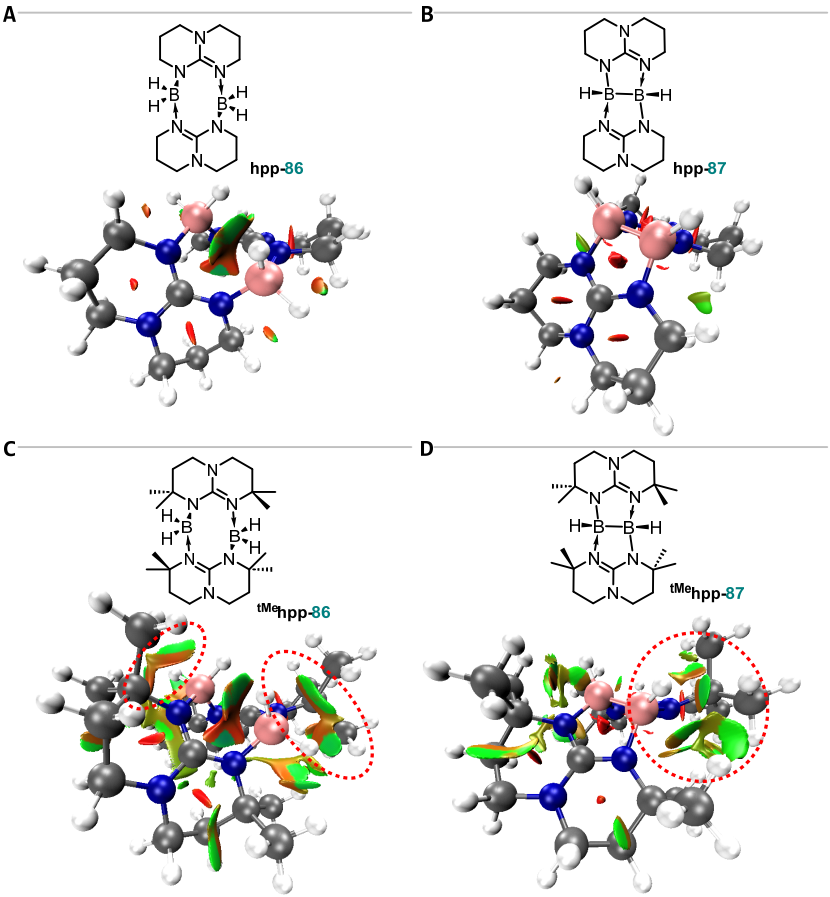

Figure 3.76: **Non-covalent interaction plots of bis-hpp- and ^{tMe}hpp-ligated diboranes.** *The plots were generated with Multiwfn (grid size of 0.116) and VMD (iso value of 0.45) using the electron density calculated at the PBEh-3c level of theory. Repulsive interactions are shown in orange-red to olive (marked with dashed red circles in C and D), weak van der Waals interactions in green.*

Detailed reaction mechanism: first and second H_2 elimination and dimerization

Initially, the H_2 elimination from borane adduct **85** was studied. Importantly, the B-N bond in **85** was calculated to be very stable. The dissociation to **84** and BH_3 is strongly endergonic (155 and 141 kJ mol^{-1}, **Figure 3.75A**). For the intramolecular elimination of H_2 from **85** an essentially identical activation energy of 123 and 122 kJ mol^{-1}, was found (TS-**88**, **Figure 3.77A**). The reaction to Int-**89** is endergonic by 42 and 46 kJ mol^{-1}. Further stabilization by 14 and 32 kJ mol^{-1}, is achieved by intramolecular adduct formation to give

Int-**90**. Also, a transition state was found that accounts for an intermolecular H_2 elimination reaction (TS-**91**). The associated activation energy is high (181 and 222 kJ mol^{-1}, with respect to two isolated **85**). Therefore, the intramolecular H_2 elimination from **85** to give Int-**90** is suggested to be the initial step of the reaction sequence.

Next, the dimerization of Int-**90** was investigated (**Figure 3.77B**). All Gibbs free energies mentioned in the following are relative to that of two isolated Int-**90**. The reaction is expected to commence with the opening of the four-membered 1,3,2-diazaborete ring in one of the two Int-**90**. This requires an activation energy of 65 and 66 kJ mol^{-1} (TS-**91**). Adduct formation between Int-**89** and Int-**90** most likely occurs *via* the formation of a new B-N bond between the Lewis acidic boron atom in Int-**89** and one of the nitrogen atoms in Int-**90**. It is endergonic by 12 and 52 kJ mol^{-1} (with respect to Int-**89** + Int-**90**).

Starting from Int-**93**, a brought variety of possible further reaction steps is conceivable (**Figure 3.77C**). Five different transition structures were found. The opening of the diazaborete in Int-**93** *via* TS-**94** to give directly **86** is with a transition state energy of 91 and 151 kJ mol^{-1} a high energy process (withing all possibilities). Notably, **86** is the experimentally observed species in the case of the hpp system (no B-B bond formation occurs), and it is in either case the energetically most favorable structure among all possibilities shown in **Figure 3.77C**.

The opening of the diazaborete in TS-**95** to form a 1,3,2,4-diazadiboretidine in Int-**96** is also unlikely to occur. In either case, it was not possible to locate the respective transition state, TS-**95**. Interestingly, a transition structure for the direct formation of Int-**96** from two isolated Int-**89** was found (TS-**97**). However, it is thermodynamically unlikely that two Int-**89** collide in the reaction mixture. Also, there are energetically more favorable pathways (*vide infra*).

The formation of a new six-membered ring featuring a B-H-B bridge in Int-**99** is possible through TS-**98**. The associated energy demand is 78 and 135 kJ mol^{-1}. This reaction step is exergonic for the hpp case (−45 kJ mol^{-1}) and only marginally endergonic (7 kJ mol^{-1}) for the ^{tMe}hpp system. Int-**99** will be of further relevance below. There is also a transition state (TS-**100**, 98 and 171 kJ mol^{-1}) for the direct formation of Int-**99** from Int-**89** and Int-**90**. It is in either case not the energetically most favorable option. This is due to the lack of stabilization of the uncoordinated borane moiety in TS-**100**.

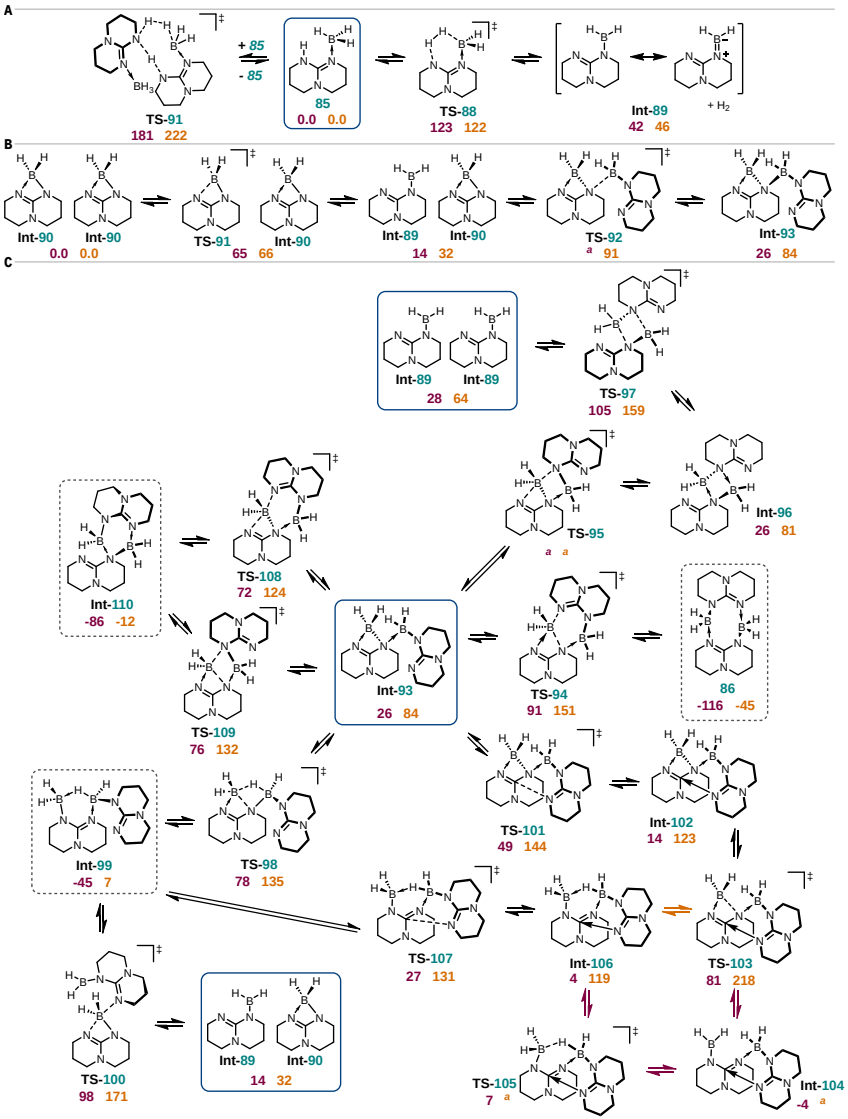

Figure 3.77: Reactivity scope of borane adducts of the hppH and ^{tMe}hppH ligand based on quantum chemical calculations – part I. *All calculations were performed at the RI-DSD-PBEB95-D3(BJ)/def2-QZVPP, COSMO-RS(toluene)//PBEh-3c level of theory. The dark red numbers (left) refer to the hpp, the orange numbers (right) to the ^{tMe}hpp system (see Figure 3.75B). They are Gibbs free energies given in kJ mol^{-1} (a: Structure was not found.)* ***A)*** *Dehydrogenation of borane adduct 85.* ***B)*** *Initial reaction steps for the dimerization of Int-90.* ***C)*** *Further reactivity of the initial dimerization product Int-93.*

In the case of the hpp system, the energetically most favorable transition state (49 kJ mol^{-1}) connected to Int-**93** is TS-**101**. It accounts for the formation of a new carbon-nitrogen bond in Int-**102**. As the following step, diazaborete ring opening was considered (TS-**103**). For both cases (hpp and ^{tMe}hpp), the transition state energy for this step (81 and 218 kJ mol^{-1}) is larger than that of the alternative route (*vide infra*). Therefore, also this pathway is not the energetically most favorable. Though, it can be connected to the formation of Int-**99**.

Ultimately, the formation of Int-**110** is presented. It is exergonic for both cases by −86 and −12 kJ mol^{-1}, respectively. Two distinct transition structures (TS-**108** and TS-**109**) were found connecting Int-**93** with Int-**110**. TS-**108** is lower in energy with values of 72 and 124 kJ mol^{-1}, respectively. Interestingly, TS-**108** and TS-**100** are closely related, only differing in the presence and absence, respectively, of a B-N bond aside the bond reorganization events of the transition states.

The results so far can be summarized as follows: starting from borane adduct **85**, an intramolecular H_2 elimination occurs affording diazaborete Int-**90**. The species can dimerize after the opening of one diazaborete ring to give Int-**93**, that subsequently can rearrange *via* TS-**108** to 1,3,5,2,4-triazadiborinane Int-**110**, which is exergonic for both considered systems.

Detailed reaction mechanism: third H_2 elimination and product formation

Next, the subsequent reaction pathways starting out from the triazadiborinane Int-**110** were studied (**Figure 3.78**). Three different transition states were found. TS-**111** accounts for the opening of the six-membered ring to give **86**. Its relative energy is 29 and 107 kJ mol^{-1}. **86** is the experimentally observed compound for the hpp system. Energetically more favorable is the traversal of TS-**112** (5 and 82 kJ mol^{-1}), which is cleaving one of the B-N bonds in Int-**110** to give short-lived intermediate Int-**113**. This can relax with minimal activation energy (TS-**114**, 12 and 86 kJ mol^{-1}) to Int-**99**. Surprisingly, the transition state for the direct transformation from Int-**110** to Int-**99** (which was only found for the ^{tMe}hpp case) is significantly higher in energy by more than 50 kJ mol^{-1} than the stepwise path (TS-**115**).

Intermediate Int-**99** has several options to undergo further transformation (**Figure 3.78**). It can rearrange *via* TS-**116** (49 and 132 kJ mol^{-1}) to give **86**. In either case, the activation energy for this step is higher than that for the direct rearrangement from Int-**110** to **86** (29 *versus* 49 and 107 *versus* 132 kJ mol^{-1}). Energetically more favorable than

traversing TS-**116** is the formation of a B-B bond owing to the intramolecular deprotonation of the B-H-B bridge by the free nitrogen atom of Int-**99**. The associated transition state energy is 31 and 74 kJ mol^{-1} (TS-**117**). This reaction step to Int-**118** is slightly endergonic relative to Int-**99** (10 and 3 kJ mol^{-1}). In a final, strongly exergonic reaction step (−100 and −54 kJ mol^{-1}), Int-**118** can eliminate H_2 to form diborane(4) **87** (TS-**119**, 57 and 98 kJ mol^{-1}, respectively). Interestingly, the direct dehydrogenation of Int-**99** (TS-**120**, 77 and 131 kJ mol^{-1}, respectively) is energetically less favorable than the stepwise reaction pathway, which makes use of the intramolecularly available base.

In Int-**118**, the nitrogen-bound hydrogen atom has a natural charge of +0.470 and +0.451, whereas the hydrogen atoms attached to boron in BH_3 adduct **85** have a mean natural charge of −0.064 and −0.063. This clearly shows the umpolung of one of the hydrogen atoms throughout the course of the reaction, which is necessary for the dehydrocoupling to occur. It also highlights the importance of the hpp ligand system not only to allow for dimerization due to its bidenticity and stabilization of the resulting diborane(4) substructure but also for the availability of a strong base. The presented conclusions are in close agreement with those ROCHETTE *et al.* drew for the dehydrocoupling occurring within the dimer of 2-boraneyl-*N,N*-dimethylaniline.[452] They succeeded in structurally characterizing the dimeric structure by SCXRD analysis and found a B-H-B bridge within a six-membered azadiboracycle (**Figure 3.78**). This is structurally closely related to Int-**99** and therefore provides further evidence for the here presented reaction mechanism.

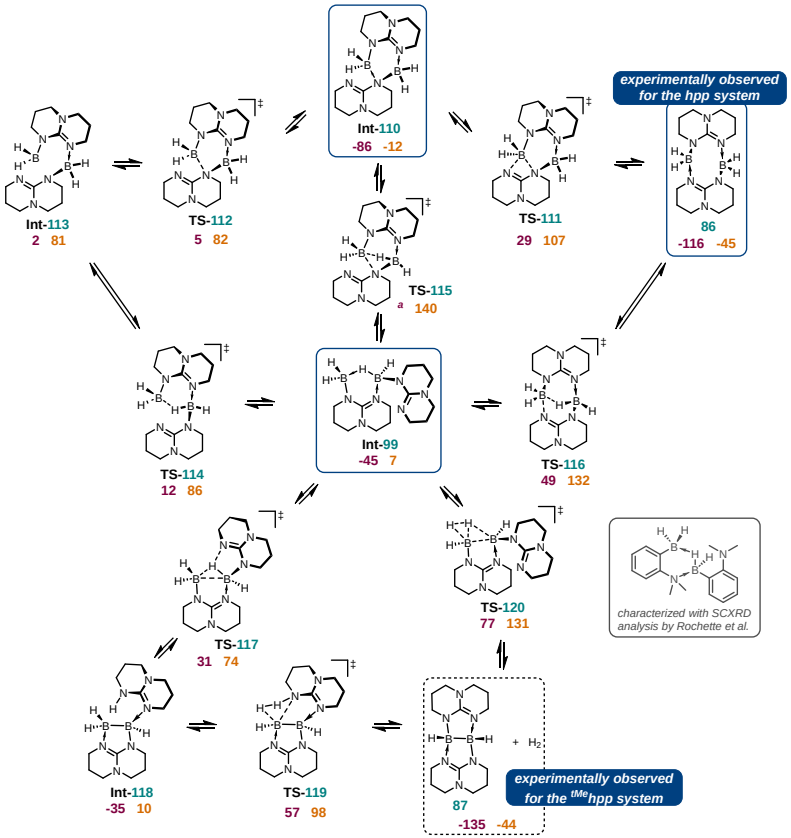

Figure 3.78: **Reactivity scope of borane adducts of the hppH and ^{tMe}hppH ligand based on quantum chemical calculations – part II.** *All calculations were performed at the RI-DSD-PBEB95-D3(BJ)/def2-QZVPP, COSMO-RS(toluene)//PBEh-3c level of theory. The dark red numbers (left) refer to the hpp, the orange numbers (right) to the ^{tMe}hpp system (see Figure 3.75B). They are Gibbs free energies given in kJ mol^{-1} (a: Structure was not found.). The insert in the lower right shows the dimeric structure which is formed by 2-boraneyl-N,N-dimethylaniline.*[452] *Its structure is closely related to Int-99.*

Detailed reaction mechanism: summary

The above-described barrier heights assist in explaining the difference in reactivity of the two systems. H_2 elimination from adduct **85** requires the same activation energy for both systems and is therefore not decisive. Staring from diazaborete Int-**90**, the formation of the thermodynamically favorable Int-**110** is the rate-determining step (TS-**108**) towards **86** and **87**, respectively, in both cases and thus also not decisive. Beginning from Int-**110**, the energetically most favorable pathway to **86** is *via* TS-**111**, which has an

energy of 29 and 107 kJ mol^{-1} (relative to two separated Int-**90**). The energetically highest lying transition state (rate-determining step starting from Int-**110**) on the path for dehydrocoupling to yield **87** is TS-**119**. Its energy is 57 and 98 kJ mol^{-1}. This means that there is a $\Delta\Delta G^{\ddagger}$ of −28 kJ mol^{-1} (29 *versus* 57 kJ mol^{-}) in favor of the formation of hpp-**86**. In contrast to that, this $\Delta\Delta G^{\ddagger}$ value for the ^{tMe}hpp case is +9 kJ mol^{-1} (107 *versus* 98 kJ mol^{-}) in favor of the dehydrocoupling toward ^{tMe}hpp-**87**. Even though dehydrocoupling going from **86** to **87** is exergonic by 19 kJ mol^{-1} for the hpp case, the system gets trapped in the state of **86**, which is strongly exergonic (−116 kJ mol^{-1}). This is 173 kJ mol^{-1} below the critical step for dehydrocoupling, which prohibits the final H_2 elimination to happen. For ^{tMe}hpp, the analogous energetic span is reduced to 143 kJ mol^{-1}. The overall reaction pathway from **85** to **86** and **87**, respectively, which is suggested based on the presented results of quantum chemical calculations, is summarized in **Figure 3.79**.

H_2 activation

It was experimentally found that when diborane(4) ^{tMe}hpp-**87** is heated in toluene-d_8 at 120 °C under a D_2 atmosphere (2 bar) a quantitative transformation to ^{tMe}hpp-**87**-d_2 occurs in which the boron-bound hydrogen atoms were exchanged against deuterium atoms. Furthermore, the chemical equilibrium could even be slightly shifted back to ^{tMe}hpp-**90** as observed by NMR spectroscopy. This kind of reactivity is not possible with the hpp system. These observations agree with the presented quantum chemical results. For the hpp system, the activation energy for H_2 activation is 192 kJ mol^{-1}, which is thermally inaccessible. For the ^{tMe}hpp case, this barrier is significantly reduced (142 kJ mol^{-1}), which allows for slow D_2 activation at elevated temperatures.

From the perspective of H_2 activation, the energetically preferred reaction channel is the boron-ligand cooperative pathway (*cf.* **Chapter 1.5** in the Introduction) in which the H_2 substrate inserts into the boron-nitrogen bond (TS-**119**). It is favored by more than 30 kJ mol^{-1} (^{tMe}hpp system) over the splitting of H_2 at the B-B bond (TS-**120**, *cf.* **Figure 3.78**).

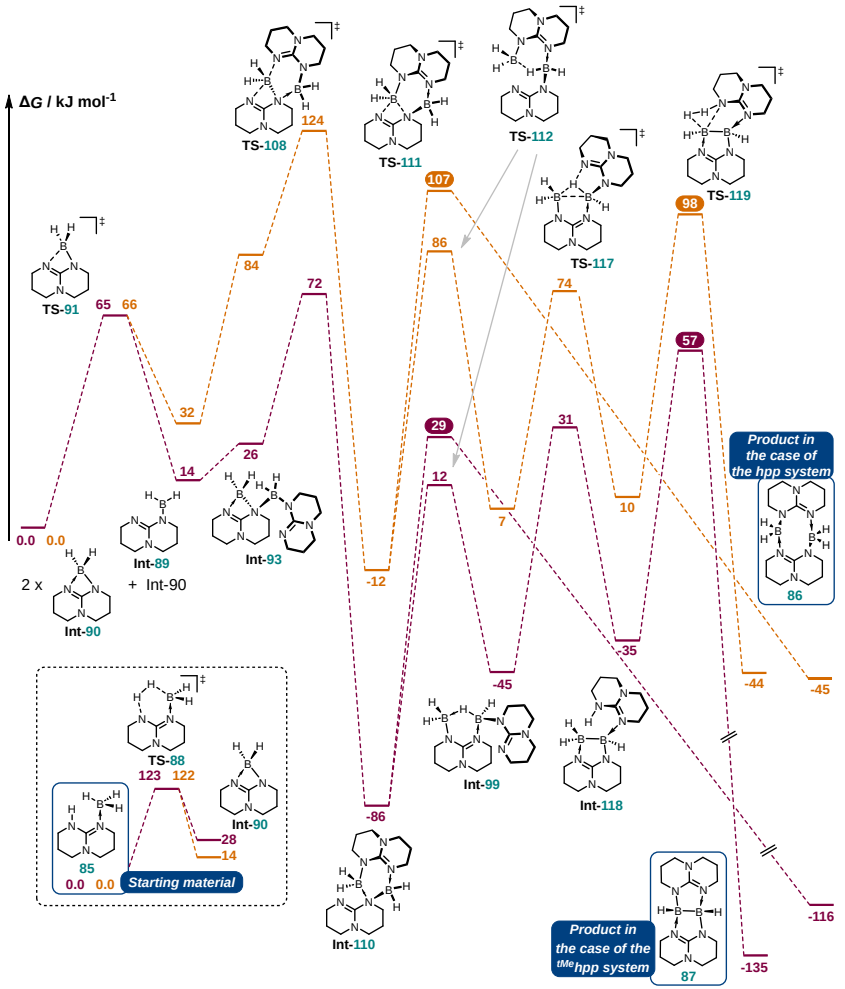

Figure 3.79: **Suggested reaction mechanism for the dehydrogenation of borane adduct 85 to 86 and 87, respectively, based on quantum chemical calculations.** *All calculations were performed at the RI-DSD-PBEB95-D3(BJ)/def2-QZVPP, COSMO-RS(toluene)//PBEh-3c level of theory. The dark red pathway refers to the hpp, the orange to the* ^{tMe}*hpp system (see Figure 3.75B).*[453]

To further understand this discrepancy between the two systems, TS-**119** (**Figure 3.80**) was analyzed with the activation-strain model by dissecting between the forming H_2 fragment and the remaining structure.[454] The numbers, which are mentioned in the following, are electronic energies. The separation of the H-atoms in the forming H_2 in the transition structure is 81.2 and 81.6 pm and therefore almost identical. The energy difference

between the two different H_2 moieties is below 1 kJ mol^{-1}, resulting from activation strain energies of 8.1 and 8.9 kJ mol^{-1}. The activation strain energy for the remaining bis(hpp)$(BH)_2$ and bis(^{tMe}hpp)$(BH)_2$ substructure, respectively, is much larger. It is 150 and 107 kJ mol^{-1}. This means that the ^{tMe}hpp system profits from a more than 40 kJ mol^{-1} reduced energy demand to transform **87** to the structure it adopts in TS-**119**. The reason for that is nicely illustrated with an NCI plot of ^{tMe}hpp-**119** (**Figure 3.80C**). It features a large green lobe on the open flank of the structure, which indicates weak attractive interactions. Regarding H_2 activation, the ^{tMe}hpp system benefits from a significant destabilization of the ground state **87** with reference to Int-**90** (−44 kJ mol^{-1} *versus* −135 kJ mol^{-1} for the hpp case) as well as from a clearly reduced activation strain energy demand to achieve the transition structure for H_2 splitting.

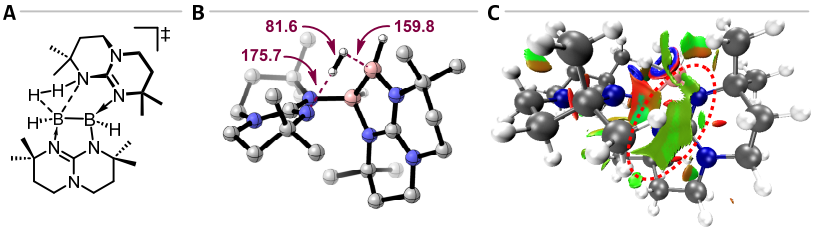

Figure 3.80: H_2 addition/elimination transition state TS-119 of the ^{tMe}hpp system. ***A)*** *Lewis structure.* ***B)*** *DFT-optimized molecular structure with selected bond lengths given in pm. Carbon-bound hydrogen atoms were omitted for clarity.* ***C)*** *NCI plot. The plot was generated with Multiwfn (grid size of 0.116) and VMD (iso value of 0.45) using the electron density calculated at the PBEh-3c level of theory. Repulsive interactions are shown in orange-red to olive, weak van der Waals interactions in green (marked with a dashed red circle).*

Aluminum and gallium analogs

A few of the most important calculations presented so far were repeated for the analogous aluminum- and gallium-based molecules – again for both the hpp and the ^{tMe}hpp ligand (**Figure 3.81**).[455] In general, the dehydrogenation reactions, either with the elimination of two or three equivalents of H_2, are more exergonic compared to the boron systems. For example, the reaction to digallane Ga-hpp-**86** is exergonic by −94 kJ mol^{-1}, whereas for the boron case, it was −79 kJ mol^{-1}. Regarding the dehydrocoupling from the perspective of the formal precursor **86**, the B-, Al-, and Ga-based systems differ significantly. While for the boron case, dehydrocoupling is exergonic (hpp, −19 kJ mol^{-1}) or essentially thermoneutral (^{tMe}hpp, 1 kJ mol^{-1}), it is strongly endergonic for aluminum by 65 and 54 kJ mol^{-1}. For gallium, it is exergonic for both ligand systems (−9 and −16 kJ mol^{-1}). The intramolecular H_2 elimination in TS-**88** is a key step for the presented reaction

pathways (**Figure 3.81B**). The activation energies for this step are lower for the Ga- (106 and 94 kJ mol^{-1}) and even lower for the Al-system (91 and 77 kJ mol^{-1}). Lastly, the H_2 activation transition state (TS-**119**) was reevaluated starting out from **87** (**Figure 3.81C**). Also here, lower activation barriers were obtained, with the Ga-system having the lowest. H_2 activation with Ga-hpp-**86** requires an activation energy of 141 kJ mol^{-1} which is essentially identical to the value obtained for B-^{tMe}hpp-**86** (142 kJ mol^{-1}). Thus, the homologous Al- and Ga-hpp/^{tMe}hpp-systems are predicted to be thermodynamically more stable (relative to the initial starting material **85**) while also having lower activation barriers for element-ligand cooperative H_2 activation.

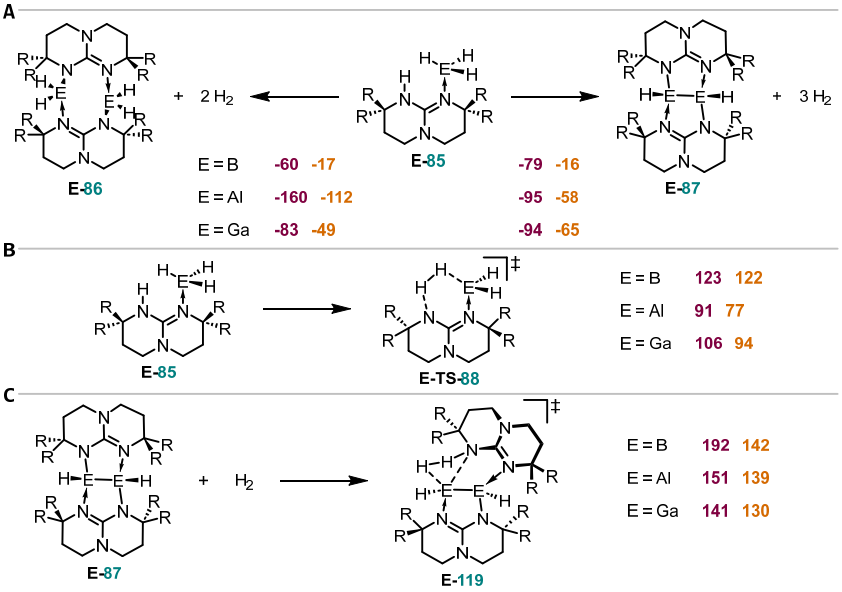

Figure 3.81: Group 13 element chemistry of the hppH and ^{tMe}hppH ligand as predicted by quantum chemical calculations. *All calculations were performed at the RI-DSD-PBEB95-D3(BJ)/def2-QZVPP, COSMO-RS(toluene)//PBEh-3c level of theory. The dark red numbers (left) refer to the hpp, the orange numbers (right) to the ^{tMe}hpp system (see Figure 3.75B). They are Gibbs free energies given in kJ mol^{-1}.* ***A)*** *Reaction energies for the overall dehydrogenation steps.* ***B)*** *H_2 elimination from the initial starting material 85.* ***C)*** *H_2 addition activation with 87.*

Conclusion

In summary, the dehydrogenation chemistry of hppH·BH_3 and ^{tMe}hppH·BH_3 (**85**) was explored with quantum chemical methods. A complex network of elementary steps was uncovered. Based on the results, suggestions were made for the explanation of why hpp-**85** preferentially dimerizes to 1,3,5,7,2,6-tetrazadiborocine hpp-**86** whereas ^{tMe}hpp-**85** undergoes dehydrocoupling to finally yield diborane(4) ^{tMe}hpp-**87**. A predicted difference between the two systems is that in the hpp case the transition state for tetrazadiborocine formation (TS-**111**) is lower than that for the elimination of the final equivalent of H_2 (TS-**119**). After the tetrazadiborocine has formed, the hpp system is trapped in a deep thermodynamic sink, which denies further reactivity. The opposite is the case for the ^{tMe}hpp system. Here, H_2 elimination is energetically more favorable and the thermodynamic sink of ^{tMe}hpp-**86** is less deep.

Like hpp-**86**, also diborane(4) hpp-**87** (which can be obtained with the help of a transition metal-based catalyst) is a thermodynamically very stable molecule. It cannot react with dihydrogen to revert the dehydrocoupling step. As found experimentally, this is however possible for ^{tMe}hpp-**87**, which was rationalized with the activation strain model and NCI plots. The analogous aluminum and gallium species were studied as well.

4 SUMMARY AND OUTLOOK

Lewis acids are molecules that can engage in chemical reactions by the acceptance of an electron pair. This dissertation presents various contributions to the chemistry of Lewis acids build upon *p*-block atoms such as aluminum or gallium. In particular, the influence of structural constraint on the reactivity and properties of respective molecules was studied.

The reactivity of *calix[4]pyrrolato aluminates* with various functional groups was investigated. These aluminates feature an aluminum(III) atom within a structurally constrained, square planar coordination environment, due to which they react through aluminum-ligand cooperativity. It was found that *meso*-octamethylcalix[4]pyrrolato aluminate reacts with *alcohols and carboxylic acids* by splitting the O-H bond, which can be reversed by temperature change or through the addition of strong Lewis bases (**Figure 4.1A**). The reaction mechanism, the property of the products, and further reactivities were researched using NMR spectroscopy, mass spectrometry, deuterium labeling, and quantum chemical simulations.

The reaction of calix[4]pyrrolato aluminate with *dioxygen* was investigated (**Figure 4.1B**). It selectively yields an alkyl peroxido aluminate through aluminum-ligand cooperativity, which is remarkably stable, and which was crystallographically characterized. The intersystem crossing, required for the experimentally observed product to be formed, was scrutinized with *ab initio* quantum chemistry. The cooperative reactivity of the aluminate – Lewis acidic central atom plus redox active ligand – was revealed essential for the reaction. It allows to separate the two unpaired electrons which in turn leads to the interconversion to the singlet potential energy surface. The findings were related to enzymatic reactions with dioxygen, for example, within iron porphyrins-containing proteins or flavoenzymes. The alkyl peroxido aluminate undergoes a rearrangement reaction that entirely breaks one of the pyrrole rings. An α,β-unsaturated carboxylato aluminate is formed, whose structure was elucidated with extensive NMR spectroscopical investigations including a $^{13}C,^{13}C$-INADEQUATE. Based on the results of quantum chemical simulations, a reaction mechanism was suggested.

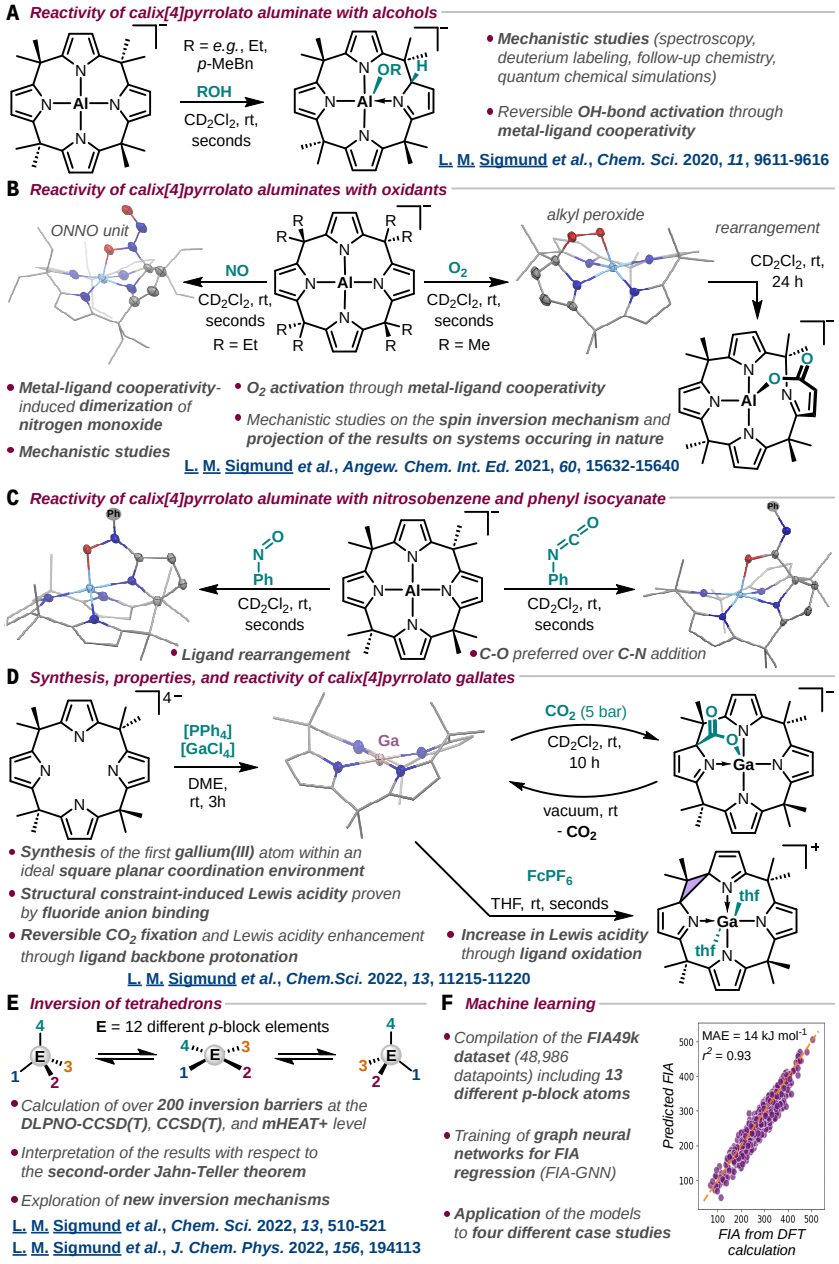

Figure 4.1: The results of this dissertation.

Nitrogen monoxide was found to dimerize at *meso*-octaethylcalix[4]pyrrolato aluminate to form a *N*-nitrosohydroxylaminato group as shown by SCXRD measurements (**Figure 4.1B**). The binding of the first NO molecule induces the formation of a N-N bond with a computed bond dissociation enthalpy of 140 kJ mol^{-1} which is more than ten times higher than the N-N bond strength in the unsupported NO dimer.

With *nitrosobenzene* as substrate, *meso*-octamethylcalix[4]pyrrolato aluminate is subjected to a ligand rearrangement reaction (**Figure 4.1C**) – most likely *via* a similar initial addition product as found for the reaction with NO. Further studies should attempt to verify this hypothesis which was formulated based on quantum chemical simulations. *Phenyl isocyanate* is selectively added to *meso*-octamethylcalix[4]pyrrolato aluminate *via* its C=O bond (**Figure 4.1C**). The C=N bond remains untouched and available for further reactions, for example, reductions. Future studies should also address the question on why the isocyanate group is chemoselectively added to the aluminate only though its C=O bond.

The synthesis of *calix[4]pyrrolato gallates* expanded the scope of the ligand family to aluminums heavier homolog gallium (**Figure 4.1D**). The gallates represent the first examples of Ga(III) atoms within an ideal anti-van't-Hoff-Le-Bel coordination environment as verified by spectroscopy and crystallography. The Lewis acidity of the gallates was demonstrated with the synthesis of a dianionic fluoride adduct. Also, the fully reversible binding of CO_2 was discovered which follows a gallium-ligand cooperative reaction mode. Ligand backbone protonation was observed as a tool to increase the Lewis acidity of the gallates. Ultimately, the exploration of the redox chemistry was initiated by two-electron oxidation of the ligand backbone (**Figure 4.1D**). Generally, the milder Lewis acidity of the gallates compared to the analogous aluminates can make reactions thermodynamically more balanced, which can be beneficial for the establishment of catalytic cycles.

The square planar arrangement of four substituents around a *p*-block atom in its highest oxidation state is generally perceived a high energy configuration which the calix[4]pyrrolato ligands made experimentally accessible for a range of *p*-block elements. In fact, square planar structures are typically associated with transition states for *stereochemical inversion*. To gain a deeper understanding of the square planar states, the stereoinversion of more than 250 small *p*-block atom-based molecules was studied with quantum chemical methods (**Figure 4.1E**). Inversion barriers even exceedable at ambient temperatures were found, rendering the tetrahedron as one of the major building blocks in *p*-block element chemistry much more structurally flexible as previously assumed. The

activation energies were related to a frontier molecular orbital approximation of the second-order Jahn-Teller effect. Generally, a small HOMO-LUMO gap in the square planar inversion transition state leads to a larger inversion barrier and *vice versa*.

The electronic structure of the *square planar element-hydrogen compounds* is more intricate than that of their heteroatom-substituted analogs. Therefore, they were studied separately with *ab initio* quantum chemical methods. The lowest energy electronic configuration in the square planar state was identified. Stereoinversion transition structures were discovered for BH_4^- and NH_4^+, which possess non-planar C_s and C_{4v} symmetry. In analogy to the second-row-based element hydrides, an alternative, stepwise mechanism for stereoinversion was discovered also for the heavier congeners and was revealed an energetically more favorable pathway than the square planar inversion mechanism, *e.g.*, for SiH_4 or PH_4^+. The two mechanisms for stereoinversion were weighted against competing dissociative reaction channels. Only for AlH_4^-, stereoinversion through the square planar state is feasible. Also, the stereoinversion barrier of methane was revisited with the mHEAT+ computational procedure, and an activation enthalpy 5 kJ mol^{-1} below the C-H bond dissociation enthalpy was determined.

The concept of Lewis acids and bases is the overarching paradigm of this work. The *fluoride ion affinity* (FIA) obtained through quantum chemical simulations is one of the most popular measures to quantify Lewis acidity. It was used for example to assess the calix[4]pyrrolato gallates. Herein, the *FIA49k* dataset was presented (**Figure 4.1F**). It includes in total 48,986 FIA values of neutral molecules based on 13 different *p*-block elements. The treatment of the covered chemical space was discussed in detail, and the developed structural taxonomy was implemented into automatic computational routines (autoPAMS) for the generation of the data. General statements on Lewis acidity were extracted from FIA49k. The dataset was used to train a *graph neural network machine learning model* denoted *FIA-GNN* that predicts FIA values both for the gas and condensed dichloromethane phase. The model operates only based on the Lewis structure of respective molecules (SMILES string), without the execution of quantum chemical software. It can process approximately 5,000 molecules in one minute on a standard personal computer with a mean absolute error of around 14 kJ mol^{-1} (r^2 = 0.93). FIA-GNN was trained and tested on a FIA range greater than 750 kJ mol^{-1}. The model was applied in four different case studies for example to molecules from the Cambridge Structural Database or to catalysis research from the literature.

In an additional project, related to the main scope of this dissertation, the *dehydrogenation chemistry of BH_3 adducts* of two different nitrogen Lewis bases (hppH ligands) was investigated computationally. A remarkably diverse reaction landscape was discovered and related to observations from experiments. In agreement with the experimental work, the simulations identified the introduction of methyl substituents to the hppH ligand as supportive for the thermal formation of a diborane(4) species without the help of a transition metal-based catalyst.

To conclude, this dissertation provided synthesis and reactivity studies of calix[4]pyrrolato complexes of aluminum and gallium. At the same time, the electronic structure of square planar coordinated *p*-block atoms was investigated with quantum chemical simulations, and contributions to the dehydrogenation chemistry of BH_3 and its Lewis adducts with hppH ligands were made. Lastly, a data-driven approach was followed to predict the Lewis acidity of *p*-block atom-based molecules, quantified by their affinity toward a fluoride anion, with a machine learning model.

5 METHODS

5.1 General Remarks on Experimental Work

Experimental details

All reagents, solvents, and further materials were purchased from commercial sources and were used as received if not stated differently. Dioxygen, carbon dioxide, and nitrogen monoxide gas was obtained from Air Liquide and was used without purification. The research group of PROF. DR. LUTZ GADE is acknowledged for providing access to nitrogen monoxide. Unless otherwise noted, all manipulations were carried out under an atmosphere of dry argon or nitrogen gas. Solvents were degassed prior to use with four freeze-pump-thaw cycles and were stored in sealed Schlenk ampulla over activated molecular sieve (3 or 4 Å, respectively) under a dry argon atmosphere. Acetonitrile was degassed by purging with dry argon gas.

All reactions on preparative scale were carried out in flame-dried standard laboratory glassware under a dry argon or nitrogen atmosphere using Schlenk line techniques and were permanently magnetically stirred, if not stated differently. Syringes, magnetic stirring bars, and needles were dried and/or flushed with argon prior to use. Reactions on the NMR sample scale were done in dry J. Young NMR tubes.

Compounds sensitive to ambient conditions were handled and stored in a Sylatech glovebox filled with dry nitrogen gas. Removal of solvents *in vacuo* was performed using a Heidolph VV2000 rotary evaporator or a Schlenk line.

Literature-known compounds were synthesized following published procedures. The respective publications are cited below. Analytical data of known compounds were compared to reference data and were found to be consistent. New compounds were characterized to the reported structures to the best of knowledge.

NMR spectroscopy

NMR spectra were collected with a Bruker BZH 200/52, a Bruker DPX200, a Bruker Avance II 400, or Bruker Avance III 600 spectrometers at 295 K. The measurements with the Bruker Avance II 400 and the Bruker Avance III 600 spectrometers were done by the staff of the NMR spectroscopy facilities of Heidelberg University. The 600 MHz spectrometers were equipped with a 5-mm $^{1}H\{^{13}C/^{15}N/^{31}P\}$ or a 5-mm BBFO z-axis gradient helium-cooled cryogenic probe. Spectra were acquired with field-frequency lock on the ^{2}H signal of the used solvent prior to data collection. Chemical shifts δ are generally reported in parts per million (ppm). Shifts of ^{1}H and ^{13}C nuclei are given relative to the tetramethylsilane resonance; ^{15}N chemical shifts are reported relative to the nitromethane reference system. ^{1}H and ^{13}C NMR spectra were calibrated on appropriate solvent signals before data extraction.[456] ^{15}N NMR chemical shifts relative to the NH_3 reference were extracted from $^{1}H,^{15}N$ HMBC NMR spectra without manual calibration and were converted to the nitromethane reference system by subtraction of 380.23 ppm. ^{19}F and ^{31}P chemical shifts are reported relative to the trichlorofluoromethane and the H_3PO_4 (85% aq) reference system, respectively. ^{19}F and ^{31}P NMR spectra were not manually calibrated after processing. ^{71}Ga NMR chemical shifts are reported relative to the signal of $Ga(NO_2)_3$ dissolved in D_2O and were obtained from spectra which were not manually calibrated.

NMR signal multiplicities are abbreviated as: s = singlet, br s = broad singlet, d = doublet, t = triplet, q = quartet, sept = septet, dd = doublet of doublets, dq = doublet of quartets, tq = triplet of quartets, m = multiplet. Where applicable, spin-spin coupling constants are given as $^{X}J_{AB}$ (X = number of chemical bonds between coupled nuclei; A, B = coupled nuclei). All signals were assigned to respective atoms or atom types, and ^{1}H NMR integration values are given.

The protons of the aromatic pyrrole rings of the calix[4]pyrrolato ligands are denoted "β-H", the directly attached carbon atoms "β-C". The quaternary carbon atoms of the aromatic pyrrole rings in the ligand are named "C_q-pyrrole". The atoms of the ligand's methyl and methylene (in case of the *meso*-octaethyl ligand) groups are called "α-Me" and "α-methylene", respectively. The quaternary carbon atoms to which they are bound are denoted "α-C".

NMR spectra were processed with TopSpin (versions 4.0.7 or 4.1.4)[457] and plotted with MNova (version v14.0.1-23559)[458] or TopSpin.

Mass spectrometry

High resolution mass spectrometry (HR-MS) was done with a Bruker ApexQe FT-ICR instrument coupled to an electrospray ionization (ESI) source operating in negative ion mode. Measurements were carried out by the staff of the mass spectrometry facilities of Heidelberg University. Samples were prepared with dichloromethane as solvent under inert conditions with an approximate analyte concentration of $c = 10^{-5}$ mol L^{-1}. They were immediately analyzed after being brought in contact with air.

UV-Vis spectroscopy

For UV-Vis absorption spectroscopy, a Varian Cary 5000 device and a quartz cuvette equipped with a J. Young valve was used. Measurements were carried out under a dry nitrogen atmosphere in dichloromethane as solvent at room temperature with an approximate analyte concentration of $c = 1.5 \cdot 10^{-4}$ mol L^{-1}. The maximum wavelengths λ_{max} (in nm) of the respective absorption bands are reported.

IR spectroscopy

Fourier-transform attenuated total reflection infrared spectroscopy (FT-ATR-IR) was done with an Agilent Cary 630 spectrometer with solid material at room temperature inside a dry nitrogen-filled glovebox. The obtained spectra were manually baseline-corrected. The data is reported as: maximum wavenumber $\tilde{\nu}_{max}$ [cm^{-1}] of the respective absorption band, intensity (s = strong, m = medium, w = weak).

Elemental analysis

Elemental analyses for the determination of C, H, and N contents were done with a vario EL or vario MICRO cube elemental analyzer. They were carried out by the staff of the microanalytical laboratory of the chemical institutes of Heidelberg University.

Single crystal X-ray diffraction

After removal from the crystallization sample, crystals were immersed in perfluorinated polyether oil (purchased from ABCR). A suitable crystal was picked and fixed on top of a CryoLoop. A Bruker D8 Venture dual wavelength Mo/Cu four-circle diffractometer with mirror optics as monochromator and an Oxford Cryostream 700 low-temperature device was used for φ and ω-scans. Data collection was performed at 100 K using Mo-K_α radiation (λ = 0.71073 Å). A strategy for data acquisition was calculated with Bruker's APEX3 or APEX4 software.[459-460] The data were integrated with the SAINT program[461] and

SADABS-2016/2 was used for multi-scan absorption correction.[462] Structures were solved with direct methods as implemented in the ShelXT 2018[463-464] structure solution program. Structure refinement was carried out by full matrix least squares minimization on F^2 using the 2018/3 or 2019/3 version of ShelXL[465-468]. All non-hydrogen atoms were refined anisotropically. Hydrogen atom positions were calculated geometrically and refined using a riding model. Handling of the structural data during refinement was performed with the ShelXle (Rev: 1246)[469] or Olex2 v1.3[470] graphical interface. Data finalization was done with FinalCif v104.[471] Crystallographic data for the structures reported here have been partly deposited with the Cambridge Crystallographic Data Centre. Copies of the data can be obtained free of charge from: www.ccdc.cam.ac.uk/structures.

For data visualization, Mercury was used.[472-474] The thermal displacement ellipsoids are shown at a probability level of 50%. Data collection and processing including structure refinement was carried out by the X-ray team of the HIMMEL and GREB group.

5.2 Supplementary Details on Quantum Chemical Simulations

Structure optimizations and frequency calculations

Throughout the presented research projects, various DFT and wavefunction-based levels of theory were applied. They are mentioned within each chapter. Generally, molecular structures were optimized toward minimum or transition structures. The obtained structures were verified as stationary points on the respective PES by the calculation of harmonic frequencies, either numerically or analytically. It was ensured that for minimum structures zero and for transition structures one negative force constant was present. In the case of transition states, it was confirmed that the correct first-order saddle point on the potential energy surface was located by animation of the imaginary frequency and by following the intrinsic reaction coordinate (IRC calculations) in both directions.

For the optimizations of small molecules in square planar structures (*cf.* **Chapter 3.7**), the two *trans*-valence angles of the central atom were added manually (with an initial value of 180°) to the set of redundant internal coordinates.

Where necessary, prior to the structure optimizations with DFT, conformational searching was done with CREST[475] using GFN2-xTB[476] within xTB.[477] The lowest energy conformer according to GFN2-xTB was carried over to the DFT structure optimization.

For structure optimizations and frequency calculations the PBEh-3c[478-481] and r^{2}SCAN-3c[479, 482-484] method, which include respective basis sets[485-486] were used. The B97M-D3(BJ)[487-488] functional together with the def2-TZVPP[489] or the cc-pVTZ[490-493] basis set was also applied for this purpose. The structures and harmonic frequencies of the element-hydrogen compounds (*cf.* **Chapter 3.8**) were obtained with the CCSD(T)[494-496] method and the aug-cc-pwCVTZ set of basis functions.[491-493, 497-499] The structures of the O_2 addition mechanism (*cf.* **Chapter 3.2**) were optimized and the vibrational frequencies calculated with the CASSCF[500] method and the def2-SVP[489] basis set.

Single point energy calculations and thermochemistry

In cases where an additional single point calculation was carried out after structure optimization, the final data which is reported was obtained by combination of the electronic energy from the higher-level computation with the thermal corrections from the frequency calculations on the lower computational level. Enthalpies were calculated at 298.15 K if not stated differently. For Gibbs free energies, the enthalpy values were merged

with the vibrational entropy terms according to the rigid-rotor-harmonic-oscillator approximation (QRRHO) of GRIMME.[501]

For the calculation[502] of implicit solvation influences on the thermochemical data, the conductor like screening model for real solvents (COSMO-RS)[503-505] as it is implemented in the Amsterdam Modeling suite (ADF and AMS, respectively) was used.[502, 506-507] The default program settings were applied (BP86/TZP). Only the maximum number of structure optimization iterations was set to zero. COSMO-RS correction for enthalpies was achieved by the calculation of ΔG-corrections at five different temperatures (278.15, 288.15, 298.15, 308.15, 318.15 K). Following $\Delta G = \Delta H - T\Delta S$, the plot of the obtained Gibbs free energy corrections against the temperature allows to fit a straight line from which the corrections for ΔH were obtained.

The CCSD(T)[494-496], its DLPNO version[508-511], MRCI+Q[512-513], CASSCF[500], NEVPT2[514-516], PW6B95-D3(BJ)[517], DSD-BLYP-D3(BJ)[518], DSD-PBEB95-D3(BJ)[519], DSD-PBEP86-D3(BJ)[520] method was used for single point energy calculations. The aug-cc-pwCVQZ[491-493, 497-499], cc-pVQZ[490-493], and def2-QZVPP[489] basis sets were employed. TD-DFT calculations were done with CAM-B3LYP.[521] Natural bond orbital (NBO) analyses were carried out based on the results of single point calculations with PBE0[522] (def2-TZVPP basis set).

Treatment of open-shell singlets

Open-shell singlet energies were estimated with an approximate spin projection method using YAMAGUCHI's equation.[523-524]

$$E_{OSS} = \frac{2\left(E_{BS} - E_{trip}\right)}{\langle S^2\rangle_{trip} - \langle S^2\rangle_{BS}} + E_{trip} \qquad (5.1)$$

The broken-symmetry energy E_{BS} as well as the triplet and broken-symmetry S^2 expectation values were obtained from broken-symmetry single point calculations.

Calculations of NMR chemical shifts

For the calculation of absolute isotropic chemical shielding values and spin-spin coupling constants at the DFT level, the gauge-independent atomic orbital (GIAO) method[525-528] was employed as it is implemented in ORCA. The conversion to NMR chemical shifts (for comparison to experimentally obtained values) was done by subtraction from reference data calculated for tetramethylsilane (TMS) and nitromethane ($MeNO_2$). The PBE0[522] functional and the IGLO-II basis set[529-530] was used.

Programs and computational resources

DFT, double-hybrid DFT, TD-DFT, DLPNO-CCSD(T), and CCSD(T) calculations were carried out with ORCA (versions 4.2.1, 5.0.1, 5.0.3, and 5.0.4).[531-533] ORCA was also used for the multiconfigurational and multireference calculations to model the addition reaction of O_2 to *meso*-octamethylcalix[4]pyrrolato aluminate. MOLPRO 2020.1 was used for the CASSCF and the MRCI+Q calculations.[534-535] The mHEAT+ protocol was executed with CFOUR v2.1.[339] The NBO7 program was used for NBO calculations through ORCA.[536-537] NCI plots[538] were generated with Multiwfn 3.8[539] and VMD 1.9.4a53[539]. The visualization and molecule editing programs Chemcraft[540], PyMol[541], IBOview[542-543], CYLView[544], and Avogadro[545] were used.

Computational resources were provided by the Baden-Württemberg High Performance Computing program through the bwForCluster JUSTUS2 at Ulm University. The support of the state of Baden-Württemberg through bwHPC and the German Research Foundation is acknowledged.

5.3 Additional Information on Python Programming

The Python programming language was used throughout. The cheminformatics packages RDKit 2023.03.3[390] and mordred 1.2.0[152] were utilized. The FIA-GNN models were built using Python 3.8.0 and nfp 0.3.8[178], which is based on TensorFlow 2.[546] The models were trained on the San Diego Supercomputer Center cluster (NVIDIA V100 SMX2 GPU nodes). The Scikit-learn library (version 1.2.2)[154] was used for data preprocessing and training of the random forest models. The LightGBM Python module was used in its 4.0.0 version.[547] The modules UMAP 0.5.3[430] and SHAP 0.43.0[431-432] were employed. Data handling and evaluation was achieved with pandas 1.5.0[548] and SciPy 1.9.1[549] and visualization with seaborn 0.12.0.[550-551]

5.4 Synthetic Procedures and Characterization Data

meso-Octamethylcalix[4]pyrrole (**19**)[8, 114, 149]

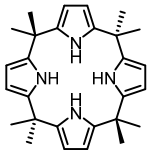

Procedure. In a 500 mL round-bottom flask equipped with a reflux condenser, acetone (13.0 g, 16.5 mL, 223.83 mmol, 1.0 equiv.) was dissolved in methanol (160 mL). Pyrrole (15.0 g, 15.5 mL, 223.83 mmol, 1.0 equiv.), which was freshly distilled, was added in one portion. Methanesulfonic acid (4 drops) was added to the colorless solution. While the mixture was heated to 60 °C for 3 h, a colorless solid precipitated. The reaction mixture was allowed to cool down to room temperature. The solvent was removed under reduced pressure. A pale green solid was obtained as the crude reaction product, which was purified by flash column chromatography on silica gel with dichloromethane/petroleum ether (60:40, R_f = 0.53) as eluent. The solvent was removed from the combined product fractions and *meso*-octamethylcalix[4]pyrrole (**19**) was isolated after drying under reduced pressure as a pale brown solid (13.7 g, 31.96 mmol, 57% yield), which is stable to ambient conditions.

^{1}H NMR (400 MHz, CD_2Cl_2, 295 K): δ [ppm] = **7.02** (br s, 4H, N-H), **5.88** (d, $^3J_{HH}$ = 2.8 Hz, 8H, β-H), **1.49** (s, 24H, α-Me).

^{13}C{^{1}H} NMR (100 MHz, CD_2Cl_2, 295 K): δ [ppm] = **138.8** (s, C_q, C_q-pyrrole), **103.1** (s, CH, β-C), **35.4** (s, C_q, α-C), **28.9** (s, CH_3, α-Me).

meso-Octaethylcalix[4]pyrrole[8, 114, 149]

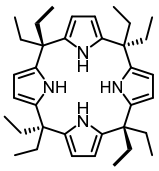

Procedure. In a 1000 mL round-bottom flask equipped with a reflux condenser, pentan-3-one (25.7 g, 31.5 mL, 298.37 mmol, 1.0 equiv.) was dissolved in methanol (320 mL). Pyrrole (20.0 g, 20.1 mL, 298.37 mmol, 1.0 equiv.) and catalytic amounts of methanesulfonic acid (8 drops) were added. Upon stirring for 18 h at 60 °C, the reaction mixture turned dark brown, and a colorless solid precipitated. The crude product was separated by filtration and was washed with methanol (3 × 40 mL). The obtained beige solid was dried under reduced pressure. It was then purified by flash column chromatography on silica gel with dichloromethane/petroleum ether (40:60, R_f = 0.59) as eluent. The solvent was removed from the combined product fractions, and after drying under reduced pressure *meso*-octaethylcalix[4]pyrrole was obtained as a colorless solid (18.4 g, 34.02 mmol, 46% yield). It was recognized that over several weeks the color of the material changes to pale orange when stored under ambient conditions. Therefore, the compound was brought into a nitrogen-filled glovebox after completion of the synthesis and was stored there.

^{1}H NMR (600 MHz, CD_2Cl_2, 295 K): δ [ppm] = **6.90** (br s, 4H, N-H), **5.90** (d, $^3J_{HH}$ = 2.6 Hz, 8H, β-H), **1.80** (br s, 16H, α-methylene), **0.58** (t, $^3J_{HH}$ = 7.4 Hz, 24H, α-Me).

^{13}C{^{1}H} NMR (151 MHz, CD_2Cl_2, 295 K): δ [ppm] = **136.5** (s, C_q, C_q-pyrrole), **105.1** (s, CH, β-C), **43.1** (s, C_q, α-C), **28.4** (s, CH_2, α-methylene), **8.0** (s, CH_3, α-Me).

Tetraphenylphosphonium *meso*-octamethylcalix[4]pyrrolato aluminate ([PPh_4][**21**])[140, 147]

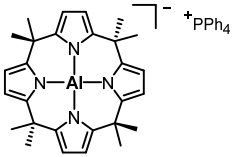

Procedure. In a nitrogen-filled glovebox, *meso*-octamethylcalix[4]pyrrole (**19**, 5.0 g, 11.67 mmol, 1.0 equiv.) and purified (*vide infra*) lithium aluminum hydride (1.1 g, 28.00 mmol, 2.4 equiv.) were dissolved in 1,2-dimethoxyethane (30 mL) in a 500 mL Schlenk flask. An overpressure valve was added, and the reaction mixture was stirred at 95 °C for 48 h. The solvent was removed under reduced pressure and the residue was re-dissolved in dichloromethane (70 mL). To the pale-yellow solution tetraphenylphosphonium chloride (4.4 g, 11.67 mmol, 1.0 equiv.), which was dried *in vacuo* at 80 °C for several hours prior to use, was added in one portion, and it was stirred for 1 h at room temperature. The formed colorless precipitate was separated by filtration through a fritted glass filter. The product (7.6 g, 9.61 mmol, 82% yield) was precipitated from its pale-yellow dichloromethane solution by addition of *n*-pentane (70 mL). It contains approximately an equimolar amount of dichloromethane which was considered for stoichiometric calculations. [PPh_4][**21**] was permanently handled under inert conditions.

^{1}H NMR (600 MHz, CD_2Cl_2, 295 K), δ [ppm] = **7.90-7.83** (m, 4H, PPh_4^+), **7.73-7.65** (m, 8H, PPh_4^+), **7.61-7.52** (m, 8H, PPh_4^+), **5.75** (s, 8H, β-H), **1.64** (s, 12H, α-Me), **1.47** (s, 12H, α-Me).

^{13}C{^{1}H} NMR (151 MHz, CD_2Cl_2, 295 K), δ [ppm] = **147.3** (s, C_q, C_q-pyrrole), **136.2** (d, $^4J_{CP}$ = 3.0 Hz, CH, PPh_4^+), **134.8** (d, $^2J_{CP}$ = 10.3 Hz, CH, PPh_4^+), **131.0** (d, $^3J_{CP}$ = 12.9 Hz, CH, PPh_4^+), **117.8** (d, $^1J_{CP}$ = 89.6 Hz, C_q, PPh_4^+), **100.8** (s, CH, β-C), **42.6** (s, C_q, α-C), **35.9** (s, CH_3, α-Me), **24.8** (s, CH_3, α-Me).

Procedure for $LiAlH_4$ purification. Gray $LiAlH_4$ powder (5.0 g) was mixed with diethyl ether (200 mL) in a 500 mL one-necked Schlenk flask, which was equipped with a Schlenk frit capped with a 250 mL Schlenk flask. The apparatus was flame-dried and flushed with dry argon prior to use. The suspension was stirred for 30 min at room temperature. The gray solid was separated by filtration from the colorless solution. The solvent was removed under reduced pressure to yield a colorless solid (2.9 g) after drying *in vacuo* at 80 °C. The product was used without further characterization and was permanently handled under inert conditions.

Tetraphenylphosphonium *meso*-octaethylcalix[4]pyrrolato aluminate ([PPh_4][**34**])[140, 142, 148]

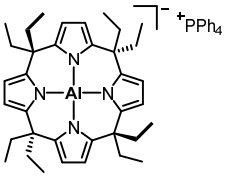

Procedure. In a nitrogen-filled glovebox, *meso*-octaethylcalix[4]pyrrole (3.0 g, 5.55 mmol, 1.0 equiv.) and lithium aluminum hydride (484.2 mg, 12.77 mmol, 2.3 equiv.) were dissolved in 1,2-dimethoxyethane (18 mL) in a 500 mL Schlenk flask. The procedure which was followed to purify lithium aluminum hydride is given above. An overpressure valve was added, and the reaction mixture was stirred at 95 °C for 48 h. The solvent was removed under reduced pressure. The material was redissolved in dichloromethane (20 mL). To the colorless solution, tetraphenylphosphonium chloride (2.1 g, 5.55 mmol, 1.0 equiv.), which was dried for several hours *in vacuo* at 80 °C, was added in one portion, and it was stirred for 1 h at room temperature. After PPh_4Cl addition, the color of the reaction mixture immediately changed to orange. After addition of further dichloromethane (20 mL), the formed colorless precipitate was separated by filtration through a fritted glass filter. The product (4.7 g, 5.20 mmol, 93% yield) was precipitated from its pale-yellow dichloromethane solution by the addition of *n*-pentane (80 mL). [PPh_4][**34**] was permanently handled under inert conditions.

If required, further purification can be achieved by redissolving the material (1.2 g) in dichloromethane (20 mL), filtration through a syringe filter, and precipitation with *n*-pentane (30 mL).

^{1}H NMR (600 MHz, CD_2Cl_2, 295 K), δ [ppm] = **7.91-7.83** (m, 4H, PPh_4^+), **7.74-7.65** (m, 8H, PPh_4^+), **7.62-7.53** (m, 8H, PPh_4^+), **5.73** (s, 8H, β-H) , **2.03** (q, $^3J_{HH}$ = 7.3 Hz, 8H, α-methylene), **1.68** (q, $^3J_{HH}$ = 7.3 Hz, 8H, α-methylene), **1.08** (t, $^3J_{HH}$ = 7.3 Hz, 12H, α-Me), **0.53** (t, $^3J_{HH}$ = 7.3 Hz, 12H, α-Me).

^{13}C{^{1}H} NMR (151 MHz, CD_2Cl_2, 295 K), δ [ppm] = **144.3** (s, C_q, C_q-pyrrole), **136.2** (d, $^4J_{CP}$ = 3.0 Hz, CH, PPh_4^+), **134.7** (d, $^2J_{CP}$ = 10.3 Hz, CH, PPh_4^+), **131.0** (d, $^3J_{CP}$ = 12.9 Hz, CH, PPh_4^+), **117.8** (d, $^1J_{CP}$ = 89.6 Hz, C_q, PPh_4^+), **102.5** (s, CH, β-C), **44.9** (s, CH_2, α-methylene), **43.8** (s, C_q, α-C), **26.7** (s, CH_3, α-methylene), **10.4** (s, CH_3, α-Me), **10.1** (s, CH_3, α-Me).

Lithium tetrapyrrolato aluminate[147, 189]

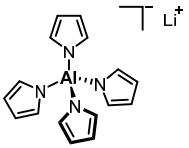

Procedure. In a flame-dried 100 mL Schlenk flask, purified lithium aluminum hydride (200.0 mg, 5.27 mmol, 1.0 eq, for purification procedure see above) was mixed with diethyl ether (10 mL). Freshly distilled pyrrole (366 µL, 354.0 mg, 5.27 mmol, 1.0 equiv.) was added dropwise, and the reaction mixture was stirred for 1 h at room temperature. The formation of gas was observed. The solvent was removed under reduced pressure, and after drying *in vacuo*, the desired product was obtained as a colorless solid. The exact yield was not determined. Lithium tetrapyrrolato aluminate was constantly handled under inert conditions.

^{1}H NMR (600 MHz, THF-d_8, 295 K), δ [ppm] = **6.69** (s, 8H, H-2/5), **6.00** (s, 8H, H-3/H-4).

^{13}C{^{1}H} NMR (151 MHz, THF-d_8, 295 K), δ [ppm] = **125.7** (s, CH, C-2/5), **108.3** (s, CH, C-3/4). Both signals showed poorly resolved ^{13}C-^{27}Al coupling and appeared, though expected as a sextet ($s_{^{27}Al}$ = 5/2), as doublet-type signals.

^{7}Li NMR (233 MHz, THF-d_8, 295 K), δ [ppm] = 2.45 (s).

Procedure for the addition reaction of alcohols to *meso*-octamethylcalix[4]pyrrolato aluminate[147]

Procedure. In a dry nitrogen-filled glovebox, tetraphenylphosphonium *meso*-octamethylcalix[4]pyrrolato aluminate ([PPh_4][**21**], 10.0 mg, 11.4 µmol, 1.0 equiv., including 1 equivalent of CH_2Cl_2) was dissolved in CD_2Cl_2 (0.5 mL). An equimolar amount of the respective alcohol substrate was dissolved in CD_2Cl_2 (0.3 mL) and was added to the stirring aluminate solution at room temperature. The reaction mixture turned yellow (orange in the case of *para*-nitrobenzyl alcohol) immediately after the addition of the first drop of the alcohol solution. After complete addition, the solution was transferred to a J. Young NMR tube and was analyzed by NMR spectroscopy. The addition products were also characterized by high resolution ESI(−) mass spectrometry.

Single crystals of the addition product of *para*-bromophenol to *meso*-octamethylcalix[4]pyrrolato aluminate were obtained at −40 °C from a dichloromethane/toluene solution.

Addition product of ethanol to *meso*-octamethylcalix[4]pyrrolato aluminate ([PPh_4][**30**])[147]

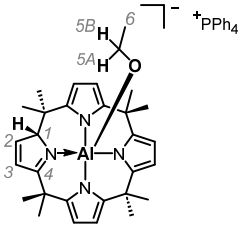

^{1}H NMR (600 MHz, CD_2Cl_2, 295 K), δ [ppm] = **7.92-7.86** (m, 4H, PPh_4^+), **7.75-7.68** (m, 8H, PPh_4^+), **7.62-7.55** (m, 8H, PPh_4^+), **7.56** (1 H, H-2, observed by ^{1}H,^{1}H COSY NMR spectroscopy, expected multiplicity is d), **6.82** (d, $^3J_{HH}$ = 5.1 Hz, 1H, H-3), **5.89** (d, $^3J_{HH}$ = 2.8 Hz, 1H, β-H), **5.83** (d, $^3J_{HH}$ = 2.8 Hz, 1H, β-H), **5.79** (d, $^3J_{HH}$ = 2.9 Hz, 1H, β-H), **5.78** (d, $^3J_{HH}$ = 2.9 Hz, 1H, β-H), **5.70** (d, $^3J_{HH}$ = 2.7 Hz, 1H, β-H), **5.67** (d, $^3J_{HH}$ = 2.7 Hz, 1H, β-H), **5.60** (s, 1H, H-1), **2.73-2.65** (m, 1H, H-5A/5B), **2.43-2.35** (m, 1H, H-5A/5B), **1.75** (s, 3H, α-Me), **1.69** (s, 3H, α-Me), **1.66** (s, 3H, α-Me), **1.63** (s, 3H, α-Me), **1.60** (s, 3H, α-Me), **1.51** (s, 3H, α-Me), **1.32** (s, 3H, α-Me), **0.65** (s, 3H, α-Me), **0.64** (t, $^3J_{HH}$ = 6.9 Hz, 3H, H-6).

^{13}C{^{1}H} NMR (151 MHz, CD_2Cl_2, 295 K), δ [ppm] = **186.9** (s, C_q, C-4), **156.2** (s, CH, C-2), **150.9** (s, C_q, C_q-pyrrole), **150.1** (s, C_q, C_q-pyrrole), **149.1** (s, C_q, C_q-pyrrole), **147.0** (s, C_q, C_q-pyrrole), **146.4** (s, C_q, C_q-pyrrole), **141.4** (s, C_q, C_q-pyrrole), **136.2** (d, $^4J_{CP}$ = 3.0 Hz, CH, PPh_4^+), **134.8** (d, $^2J_{CP}$ = 10.3 Hz, CH, PPh_4^+), **131.0** (d, $^3J_{CP}$ = 12.9 Hz, CH, PPh_4^+), **127.4** (s, CH, C-3), **117.8** (d, $^1J_{CP}$ = 89.6 Hz, C_q, PPh_4^+), **101.7** (s, CH, β-C), **101.4** (s, CH, β-C), **101.0** (s, CH, β-C), **100.6** (s, CH, β-C), **100.3** (s, CH, β-C), **98.2** (s, CH, β-C), **86.5** (s, CH, C-1), **55.4** (s, CH_2, C-5), **40.7** (s, C_q, α-Me), **39.6** (s, CH_3, α-Me), **38.3** (s, C_q, α-C), **36.7** (s, C_q, α-C), **36.6** (s, C_q, α-C), **36.4** (s, CH_3, α-Me), **33.4** (s, CH_3, α-Me), **32.0** (s, CH_3, α-Me), **28.5** (s, CH_3, α-Me), **28.0** (s, CH_3, α-Me), **27.4** (s, CH_3, α-Me), **26.1** (s, CH_3, α-Me), **20.5** (s, CH_3, C-6).

HR-MS (ESI, negative ion mode): *m/z* calculated for $C_{30}H_{38}AlN_4O$ $[M]^-$: **497.2866**, found: **497.2874**.

Addition product of isopropanol to *meso*-octamethylcalix[4]pyrrolato aluminate[147]

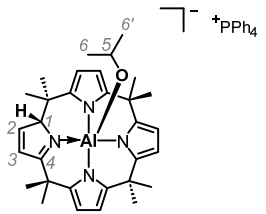

^{1}H NMR (600 MHz, CD_2Cl_2, 295 K), δ [ppm] = **7.92-7.85** (m, 4H, PPh_4^+), **7.76-7.68** (m, 8H, PPh_4^+), **7.62-7.55** (m, 8H, PPh_4^+), **7.56** (d, $^{3}J_{HH}$ = 5.6 Hz, 1H, H-2), **6.80** (dd, $^{3}J_{HH}$ = 5.3 Hz, $^{4}J_{HH}$ = 0.7 Hz, 1H, H-3), **5.90** (d, $^{3}J_{HH}$ = 3.0 Hz, 1H, β-H), **5.82** (d, $^{3}J_{HH}$ = 3.0 Hz, 1H, β-H), **5.81** (d, $^{3}J_{HH}$ = 3.0 Hz, 1H, β-H), **5.77** (d, $^{3}J_{HH}$ = 3.0 Hz, 1H, β-H), **5.72** (d, $^{3}J_{HH}$ = 2.9 Hz, 1H, β-H), **5.68** (d, $^{3}J_{HH}$ = 2.9 Hz, 1H, β-H), **5.66** (s, 1H, H-1), **3.11** (sept, $^{3}J_{HH}$ = 6.0 Hz, 1H, H-5), **1.75** (s, 3H, α-Me), **1.70** (s, 3H, α-Me), **1.66** (s, 3H, α-Me), **1.63** (s, 3H, α-Me), **1.59** (s, 3H, α-Me), **1.57** (s, 3H, α-Me), **1.27** (s, 3H, α-Me), **0.63** (s, 3H, α-Me), **0.46** (d, $^{3}J_{HH}$ = 6.0 Hz, 3H, H-6/6'), **0.37** (d, $^{3}J_{HH}$ = 6.0 Hz, 3H, H-6/6').

^{13}C{^{1}H} NMR (151 MHz, CD_2Cl_2, 295 K), δ [ppm] = **186.4** (s, C_q, C-4), **156.5** (s, CH, C-2), **150.5** (s, C_q, C_q-pyrrole), **150.4** (s, C_q, C_q-pyrrole), **149.3** (s, C_q, C_q-pyrrole), **146.6** (s, C_q, C_q-pyrrole), **146.2** (s, C_q, C_q-pyrrole), **141.2** (s, C_q, C_q-pyrrole), **136.2** (d, $^{4}J_{CP}$ = 3.0 Hz, CH, PPh_4^+), **134.8** (d, $^{2}J_{CP}$ = 10.3 Hz, CH, PPh_4^+), **131.0** (d, $^{3}J_{CP}$ = 12.9 Hz, CH, PPh_4^+), **127.4** (s, CH, C-3), **117.9** (d, $^{1}J_{CP}$ = 89.6 Hz, C_q, PPh_4^+), **102.3** (s, CH, β-C), **101.08** (s, CH, β-C), **101.05** (s, CH, β-C), **101.0** (s, CH, β-C), **100.6** (s, CH, β-C), **98.3** (s, CH, β-C), **85.6** (s, CH, C-1), **62.5** (s, CH, C-5), **41.14** (s, C_q, α-C), **41.09** (s, C_q, α-Me), **38.1** (s, C_q, α-C), **37.5** (s, C_q, α-Me), **36.8** (s, C_q, α-Me), **36.7** (s, C_q, α-C), **36.4** (s, C_q, α-Me), **31.1** (s, C_q, α-Me), **28.9** (s, C_q, α-Me), **28.0** (s, C_q, α-Me), **27.2** (s, C_q, α-Me), **26.9** (s, CH_3, C-6/6'), **26.7** (s, CH_3, C-6/6'), **25.3** (s, C_q, α-Me).

HR-MS (ESI, negative ion mode): *m/z* calculated for $C_{31}H_{40}AlN_4O$ $[M]^-$: **511.3023**, found: **511.3080**.

Addition product of *tert*-butyl alcohol to *meso*-octamethylcalix[4]pyrrolato aluminate[147]

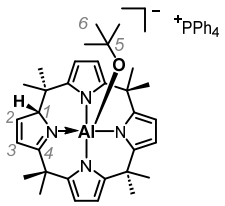

^{1}H NMR (600 MHz, CD_2Cl_2, 295 K), δ [ppm] = **7.91-7.85** (m, 4H, PPh_4^+), **7.75-7.68** (m, 8H, PPh_4^+), **7.62-7.54** (m, 8H, PPh_4^+), **7.57** (1 H, H-2, observed by ^{1}H,^{1}H COSY NMR spectroscopy, expected multiplicity is d), **6.82** (dd, $^3J_{HH}$ = 5.3 Hz, $^4J_{HH}$ = 0.7 Hz, 1H, H-3), **5.90** (s, 1H, H-1), **5.89** (d, $^3J_{HH}$ = 3.1 Hz, 1H, β-H), **5.88** (d, $^3J_{HH}$ = 3.1 Hz, 1H, β-H), **5.82** (d, $^3J_{HH}$ = 3.0 Hz, 1H, β-H), **5.78** (d, $^3J_{HH}$ = 3.0 Hz, 1H, β-H), **5.73** (d, $^3J_{HH}$ = 2.9 Hz, 1H, β-H), **5.69** (d, $^3J_{HH}$ = 2.9 Hz, 1H, β-H), **1.75** (s, 3H, α-Me), **1.74** (s, 3H, α-Me), **1.67** (s, 3H, α-Me), **1.63** (s, 3H, α-Me), **1.58** (s, 3H, α-Me), **1.55** (s, 3H, α-Me), **1.21** (s, 3H, α-Me), **0.61** (s, 3H, α-Me), **0.58** (s, 9H, H-6).

^{13}C{^{1}H} NMR (151 MHz, CD_2Cl_2, 295 K), δ [ppm] = **186.3** (s, C_q, C-4), **156.9** (s, CH, C-2), **150.9** (s, C_q, C_q-pyrrole), **150.3** (s, C_q, C_q-pyrrole), **149.5** (s, C_q, C_q-pyrrole), **146.6** (s, C_q, C_q-pyrrole), **146.0** (s, C_q, C_q-pyrrole), **141.2** (s, C_q, C_q-pyrrole), **136.2** (d, $^4J_{CP}$ = 3.0 Hz, CH, PPh_4^+), **134.8** (d, $^2J_{CP}$ = 10.3 Hz, CH, PPh_4^+), **131.0** (d, $^3J_{CP}$ = 12.9 Hz, CH, PPh_4^+), **127.8** (s, CH, C-3), **117.9** (d, $^1J_{CP}$ = 89.6 Hz, C_q, PPh_4^+), **102.4** (s, CH, β-C), **101.5** (s, CH, β-C), **100.8** (s, CH, β-C), **100.92** (s, CH, β-C), **100.90** (s, CH, β-C), **98.7** (s, CH, β-C), **84.7** (s, CH, C-1), **68.2** (s, C_q, C-5), **42.0** (s, CH_3, α-Me), **41.5** (s, C_q, α-C), **38.4** (s, CH_3, α-Me), **38.3** (s, CH_3, α-Me), **38.1** (s, C_q, α-C), **36.9** (s, C_q, α-C), **36.6** (s, C_q, α-C), **32.4** (s, CH_3, C-6), **31.0** (s, CH_3, α-Me), **28.4** (s, CH_3, α-Me), **28.1** (s, CH_3, α-Me), **27.0** (s, CH_3, α-Me), **25.2** (s, CH_3, α-Me).

HR-MS (ESI, negative ion mode): *m/z* calculated for $C_{32}H_{42}AlN_4O$ $[M]^-$: **525.3179**, found: **525.3129**.

Addition product of *para*-methylbenzyl alcohol to *meso*-octamethylcalix[4]pyrrolato aluminate[147]

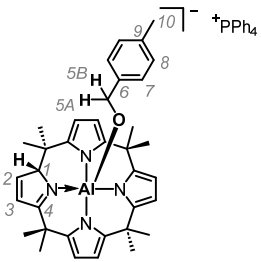

^{1}H NMR (600 MHz, CD_2Cl_2, 295 K), δ [ppm] = **7.90-7.84** (m, 4H, PPh_4^+), **7.74-7.67** (m, 8H, PPh_4^+), **7.60-7.53** (m, 8H, PPh_4^+), **7.48** (d, $^{3}J_{HH}$ = 5.2 Hz, 1H, H-2), **6.93-6.89** (m, 2H, H-7), **6.89-6.85** (m, 2H, H-8), **6.79** (d, $^{3}J_{HH}$ = 5.2 Hz, 1H, H-3), **5.90** (d, $^{3}J_{HH}$ = 2.9 Hz, 1H, β-H), **5.85** (d, $^{3}J_{HH}$ = 3.0 Hz, 1H, β-H), **5.84** (d, $^{3}J_{HH}$ = 3.0 Hz, 1H, β-H), **5.80** (d, $^{3}J_{HH}$ = 3.0 Hz, 1H, β-H), **5.73** (d, $^{3}J_{HH}$ = 2.9 Hz, 1H, β-H), **5.70** (d, $^{3}J_{HH}$ = 2.9 Hz, 1H, β-H), **5.54** (s, 1H, H-1), **3.70** (d, $^{2}J_{HH}$ = 13.2 Hz, 1H, H-5A/5B), **3.14** (d, $^{2}J_{HH}$ = 13.2 Hz, 1H, H-5A/5B), **2.20** (s, 3H, H-10), **1.74** (s, 3H, α-Me), **1.68** (s, 3H, α-Me), **1.63** (s, 3H, α-Me), **1.60** (s, 3H, α-Me), **1.55** (s, 3H, α-Me), **1.49** (s, 3H, α-Me), **1.34** (s, 3H, α-Me), **0.60** (s, 3H, α-Me).

^{13}C{^{1}H} NMR (151 MHz, CD_2Cl_2, 295 K), δ [ppm] = **186.9** (s, C_q, C-4), **156.4** (s, CH, C-2), **151.3** (s, C_q, C_q-pyrrole), **150.2** (s, C_q, C_q-pyrrole), **149.2** (s, C_q, C_q-pyrrole), **147.2** (s, C_q, C_q-pyrrole), **146.4** (s, C_q, C_q-pyrrole), **145.3** (s, C_q, C-6), **141.5** (s, C_q, C_q-pyrrole), **136.2** (d, $^{4}J_{CP}$ = 3.0 Hz, CH, PPh_4^+), **134.8** (d, $^{2}J_{CP}$ = 10.3 Hz, CH, PPh_4^+), **134.1** (s, C_q, C-9), **131.0** (d, $^{3}J_{CP}$ = 12.9 Hz, CH, PPh_4^+), **128.2** (s, CH, C-8), **127.3** (s, CH, C-3), **127.0** (s, CH, C-7), **117.8** (d, $^{1}J_{CP}$ = 89.6 Hz, C_q, PPh_4^+), **102.3** (s, CH, β-C), **101.4** (s, CH, β-C), **101.2** (s, CH, β-C), **100.8** (s, CH, β-C), **100.6** (s, CH, β-C), **98.0** (s, CH, β-C), **86.3** (s, CH, C-1), **62.3** (s, CH_2, C-5), **40.9** (s, C_q, α-C), **40.2** (s, CH_3, α-Me), **38.3** (s, C_q, α-C), **36.9** (s, CH_3, α-Me), **36.8** (s, C_q, α-Me), **36.6** (s, C_q, α-C), **33.7** (s, CH_3, α-Me), **31.2** (s, CH_3, α-Me), **28.2** (s, CH_3, α-Me), **27.6** (s, CH_3, α-Me), **27.5** (s, CH_3, α-Me), **25.6** (s, CH_3, α-Me), **21.1** (s, CH_3, C-10).

HR-MS (ESI, negative ion mode): *m/z* calculated for $C_{36}H_{42}AlN_4O$ $[M]^-$: **573.3179**, found: **573.3177**.

Addition product of *para*-nitrobenzyl alcohol to *meso*-octamethylcalix[4]pyrrolato aluminate[147]

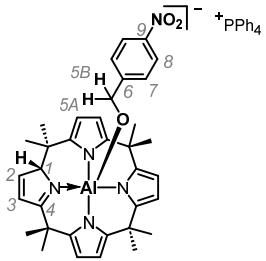

^{1}H NMR (600 MHz, CD_2Cl_2, 295 K), δ [ppm] = **7.92-7.89** (m, 2H, H-8), **7.89-7.85** (m, 4H, PPh_4^+), **7.74-7.67** (m, 8H, PPh_4^+), **7.61-7.55** (m, 8H, PPh_4^+), **7.51** (d, $^3J_{HH}$ = 5.3 Hz, 1H, H-2), **7.23-7.19** (m, 2H, H-7), **6.83** (dd, $^3J_{HH}$ = 5.3 Hz, $^4J_{HH}$ = 1.0 Hz, 1H, H-3), **5.87** (d, $^3J_{HH}$ = 2.9 Hz, 1H, β-H), **5.86** (d, $^3J_{HH}$ = 3.0 Hz, 1H, β-H), **5.81** (d, $^3J_{HH}$ = 3.0 Hz, 1H, β-H), **5.75** (d, $^3J_{HH}$ = 2.9 Hz, 1H, β-H), **5.72** (d, $^3J_{HH}$ = 2.9 Hz, 1H, β-H), **5.45** (s, 1H, H-1), **3.82** (d, $^2J_{HH}$ = 15.7 Hz, 1H, H-5A/5B), **3.27** (d, $^2J_{HH}$ = 15.7 Hz, 1H, H-5A/5B), **1.75** (s, 3H, α-Me), **1.69** (s, 3H, α-Me), **1.65** (s, 3H, α-Me), **1.57** (s, 3H, α-Me), **1.56** (s, 3H, α-Me), **1.42** (s, 3H, α-Me), **1.35** (s, 3H, α-Me), **0.60** (s, 3H, α-Me).

^{13}C{^{1}H} NMR (151 MHz, CD_2Cl_2, 295 K), δ [ppm] = **187.4** (s, C_q, C-4), **157.5** (s, C_q, C-9), **156.5** (s, CH, C-2), **151.5** (s, C_q, C_q-pyrrole), **150.2** (s, C_q, C_q-pyrrole), **149.0** (s, C_q, C_q-pyrrole), **147.2** (s, C_q, C_q-pyrrole), **146.3** (s, C_q, C-6), **145.9** (s, C_q, C_q-pyrrole), **141.4** (s, C_q, C_q-pyrrole), **136.2** (d, $^4J_{CP}$ = 3.0 Hz, CH, PPh_4^+), **134.8** (d, $^2J_{CP}$ = 10.3 Hz, CH, PPh_4^+), **131.0** (d, $^3J_{CP}$ = 12.9 Hz, CH, PPh_4^+), **127.41** (s, CH, C-3), **127.37** (s, CH, C-7), **122.8** (s, CH, C-8), **117.8** (d, $^1J_{CP}$ = 3.1 Hz, C_q, PPh_4^+), **102.6** (s, CH, β-C), **101.7** (s, CH, β-C), **101.4** (s, CH, β-C), **100.9** (s, CH, β-C), **100.8** (s, CH, β-C), **98.2** (s, CH, β-C), **86.4** (s, CH, C-1), **62.4** (s, CH_2, C-5), **40.9** (s, C_q, α-C), **40.0** (s, CH_3, α-Me), **38.3** (s, C_q, α-Me), **36.9** (s, CH_3, α-Me), **36.8** (s, C_q, α-Me), **36.6** (s, C_q, α-Me), **33.7** (s, CH_3, α-Me), **31.2** (s, CH_3, α-Me), **28.1** (s, CH_3, α-Me), **27.5** (s, CH_3, α-Me), **27.3** (s, CH_3, α-Me), **25.5** (s, CH_3, α-Me).

HR-MS (ESI, negative ion mode): *m/z* calculated for $C_{35}H_{39}AlN_5O_3$ $[M]^-$: **604.2874**, found: **604.2886**.

Addition product of bis(4-methoxyphenyl)methanol to *meso*-octamethylcalix[4]pyrrolato aluminate[147]

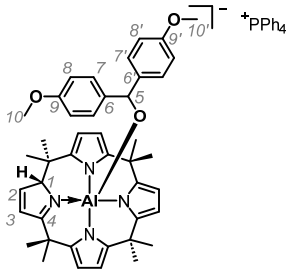

^{1}H NMR (600 MHz, CD_2Cl_2, 295 K), δ [ppm] = **7.91-7.85** (m, 4H, PPh_4^+), **7.75-7.67** (m, 8H, PPh_4^+), **7.62-7.53** (m, 8H, PPh_4^+), **7.33** (d, $^3J_{HH}$ = 5.2 Hz, 1H, H-2), **7.07-7.02** (m, 2H, H-7/7'), **6.77-6.74** (dd, $^3J_{HH}$ = 5.2 Hz, $^4J_{HH}$ = 0.7 Hz, 1H, H-3), **6.71-6.67** (m, 2H, H-8/8'), **6.28-6.24** (m, 2H, H-8/8'), **6.22-6.18** (m, 2H, H-7/7'), **5.93** (d, $^3J_{HH}$ = 2.9 Hz, 1H, β-H), **5.84** (d, $^3J_{HH}$ = 2.9 Hz, 1H, β-H), **5.80** (d, $^3J_{HH}$ = 3.0 Hz, 1H, β-H), **5.77** (d, $^3J_{HH}$ = 2.9 Hz, 1H, β-H), **5.70** (d, $^3J_{HH}$ = 3.0 Hz, 1H, β-H), **5.61** (d, $^3J_{HH}$ = 2.9 Hz, 1H, β-H), **5.34** (s, 1H, H-1), **4.20** (s, 1H, H-5), **3.74** (s, 3H, H-10/10'), **3.58** (s, 3H, H-10/10'), **1.77** (s, 3H, α-Me), **1.74** (s, 3H, α-Me), **1.58** (s, 3H, α-Me), **1.41** (s, 3H, α-Me), **1.31** (s, 3H, α-Me), **1.10** (s, 3H, α-Me), **0.94** (s, 3H, α-Me), **0.49** (s, 3H, α-Me).

^{13}C{^{1}H} NMR (151 MHz, CD_2Cl_2, 295 K), δ [ppm] = **186.4** (s, C_q, C-4), **157.7** (s, C_q, C-9/9'), **156.8** (s, C_q, C-9/9'), **156.5** (s, CH, C-2), **151.6** (s, C_q, C_q-pyrrole), **151.2** (s, C_q, C_q-pyrrole), **149.1** (s, C_q, C_q-pyrrole), **146.1** (s, C_q, C_q-pyrrole), **146.0** (s, C_q, C_q-pyrrole), **142.9** (s, C_q, C-6/6'), **141.7** (s, C_q, C-6/6'), **141.3** (s, C_q, C_q-pyrrole), **136.1** (d, $^4J_{CP}$ = 3.1 Hz, CH, PPh_4^+), **134.8** (d, $^2J_{CP}$ = 10.3 Hz, CH, PPh_4^+), **131.0** (d, $^3J_{CP}$ = 12.9 Hz, CH, PPh_4^+), **130.2** (s, CH, C-7/7'), **128.8** (s, CH, C-7/7'), **127.2** (s, CH, C-3), **117.8** (d, $^1J_{CP}$ = 89.6 Hz, C_q, PPh_4^+), **112.7** (s, CH, C-8/8'), **112.4** (s, CH, C-8/8'), **103.2** (s, CH, β-C), **101.34** (s, CH, β-C), **101.30** (s, CH, β-C), **101.04** (s, CH, β-C), **100.97** (s, CH, β-C), **98.2** (s, CH, β-C), **85.2** (s, CH, C-1), **74.4** (s, CH, C-5), **55.5** (s, CH_3, C-10/10'), **55.3** (s, CH_3, C-10/10'), **41.2** (s, CH_3, α-Me), **41.1** (s, C_q, α-C), **38.1** (s, C_q, α-C), **37.9** (s, CH_3, α-Me), **36.9** (s, C_q, α-Me), **36.4** (s, C_q, α-Me), **35.2** (s, CH_3, α-Me), **30.5** (s, CH_3, α-Me), **27.6** (s, CH_3, α-Me), **27.3** (s, CH_3, α-Me), **27.2** (s, CH_3, α-Me), **25.1** (s, CH_3, α-Me).

HR-MS (ESI, negative ion mode): *m/z* calculated for $C_{43}H_{48}AlN_4O_3$ $[M]^-$: **695.3547**, found: **695.3561**.

Addition product of *para*-bromophenol to *meso*-octamethylcalix[4]pyrrolato aluminate ([PPh_4][**29**])[147]

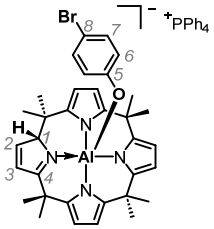

^{1}H NMR (600 MHz, CD_2Cl_2, 295 K), δ [ppm] = **7.90-7.84** (m, 4H, PPh_4^+), **7.74-7.66** (m, 8H, PPh_4^+), **7.61-7.55** (m, 8H, PPh_4^+), **7.54** (d, $^3J_{HH}$ = 5.2 Hz, 1H, H-2), **6.85** (dd, $^3J_{HH}$ = 5.3 Hz, $^4J_{HH}$ = 1.1 Hz, 1H, H-3), **6.75-6.71** (m, 2H, H-7), **5.90** (d, $^3J_{HH}$ = 3.0 Hz, 1H, β-H), **5.89** (d, $^3J_{HH}$ = 3.0 Hz, 1H, β-H), **5.84** (d, $^3J_{HH}$ = 3.0 Hz, 1H, β-H), **5.83** (d, $^3J_{HH}$ = 3.0 Hz, 1H, β-H), **5.73** (d, $^3J_{HH}$ = 2.9 Hz, 1H, β-H), **5.72** (d, $^3J_{HH}$ = 2.9 Hz, 1H, β-H), **5.55-5.51** (m, 2H, H-6), **5.20** (s, 1H, H-1), **1.76** (s, 3H, α-Me), **1.68** (s, 3H, α-Me), **1.66** (s, 3H, α-Me), **1.54** (s, 3H, α-Me), **1.47** (s, 3H, α-Me), **1.41** (s, 3H, α-Me), **1.35** (s, 3H, α-Me), **0.62** (s, 3H, α-Me).

^{13}C{^{1}H} NMR (151 MHz, CD_2Cl_2, 295 K), δ [ppm] = **187.4** (s, C_q, C-4), **160.6** (s, C_q, C-5), **156.7** (s, CH, C-2), **150.4** (s, C_q, C_q-pyrrole), **150.3** (s, C_q, C_q-pyrrole), **149.1** (s, C_q, C_q-pyrrole), **146.8** (s, C_q, C_q-pyrrole), **146.4** (s, C_q, C_q-pyrrole), **141.2** (s, C_q, C_q-pyrrole), **136.2** (d, $^4J_{CP}$ = 3.0 Hz, CH, PPh_4^+), **134.8** (d, $^2J_{CP}$ = 10.3 Hz, CH, PPh_4^+), **131.04** (s, CH, C-7), **131.01** (d, $^3J_{CP}$ = 12.9 Hz, CH, PPh_4^+), **127.5** (s, CH, C-3), **121.6** (s, CH, C-6), **117.8** (d, $^1J_{CP}$ = 89.5 Hz, C_q, PPh_4^+), **106.8** (s, C_q, C-8), **103.2** (s, CH, β-C), **102.1** (s, CH, β-C), **102.0** (s, CH, β-C), **101.7** (s, CH, β-C), **101.4** (s, CH, β-C), **98.9** (s, CH, β-C), **85.9** (s, CH, C-1), **40.9** (s, C_q, α-C), **40.6** (s, CH_3, α-Me), **38.3** (s, C_q, α-Me), **37.0** (s, CH_3, α-Me), **36.7** (s, C_q, α-C), **36.5** (s, C_q, α-C), **34.2** (s, CH_3, α-Me), **31.4** (s, CH_3, α-Me), **28.7** (s, CH_3, α-Me), **27.7** (s, CH_3, α-Me), **27.6** (s, CH_3, α-Me), **25.5** (s, CH_3, α-Me).

HR-MS (ESI, negative ion mode): *m/z* calculated for $C_{34}H_{37}Al^{79}BrN_4O$ $[M]^-$: **623.1972**, found: **623.1980**.

The constitution of the compound as shown was unambiguously confirmed by SCXRD measurements (cf. **Chapter 7.4***).*

Addition product of benzoic acid to *meso*-octamethylcalix[4]pyrrolato aluminate[147]

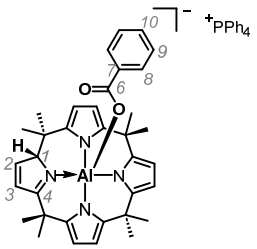

^{1}H NMR (600 MHz, CD_2Cl_2, 295 K), δ [ppm] = **7.91-7.83** (m, 4H, PPh_4^+), **7.74-7.65** (m, 8H, PPh_4^+), **7.61-7.52** (m, 8H, PPh_4^+), **7.58** (1 H, H-2, observed by ^{1}H,^{1}H COSY NMR spectroscopy, expected multiplicity is d), **7.51-7.46** (m, 2H, H-8), **7.23-19** (m, 1H, H-10), **7.12-7.06** (m, 2H, H-9), **6.87** (dd, $^3J_{HH}$ = 5.3 Hz, $^4J_{HH}$ = 1.0 Hz, 1H, H-3), **5.96** (d, $^3J_{HH}$ = 3.0 Hz, 1H, β-H), **5.92** (d, $^3J_{HH}$ = 3.0 Hz, 1H, β-H), **5.81** (d, $^3J_{HH}$ = 3.3 Hz, 1H, β-H), **5.80** (d, $^3J_{HH}$ = 3.3 Hz, 1H, β-H), **5.732** (d, $^3J_{HH}$ = 3.1 Hz, 1H, β-H), **5.728** (d, $^3J_{HH}$ = 3.1 Hz, 1H, β-H), **5.44** (s, 1H, H-1), **1.71** (s, 3H, α-Me), **1.54** (s, 3H, α-Me), **1.53** (s, 3H, α-Me), **1.51** (s, 3H, α-Me), **1.48** (s, 3H, α-Me), **1.46** (s, 3H, α-Me), **1.36** (s, 3H, α-Me), **0.76** (s, 3H, α-Me).

^{13}C{^{1}H} NMR (151 MHz, CD_2Cl_2, 295 K), δ [ppm] = **187.7** (s, C_q, C-4), **168.2** (s, C_q, C-6), **155.4** (s, CH, C-2), **150.3** (s, C_q, C_q-pyrrole), **149.9** (s, C_q, C_q-pyrrole), **148.2** (s, C_q, C_q-pyrrole), **147.0** (s, C_q, C_q-pyrrole), **146.6** (s, C_q, C_q-pyrrole), **142.3** (s, C_q, C_q-pyrrole), **136.9** (s, C_q, C-7), **136.2** (d, $^4J_{CP}$ = 3.1 Hz, CH, PPh_4^+), **134.8** (d, $^2J_{CP}$ = 10.3 Hz, CH, PPh_4^+), **131.0** (d, $^3J_{CP}$ = 12.9 Hz, CH, PPh_4^+), **130.5** (s, CH, C-10), **130.4** (s, CH, C-8), **127.8** (s, CH, C-3), **127.6** (s, CH, C-9), **117.8** (d, $^1J_{CP}$ = 89.6 Hz, C_q, PPh_4^+), **102.9** (s, CH, β-C), **102.0** (s, CH, β-C), **101.6** (s, CH, β-C), **101.2** (s, CH, β-C), **100.12** (s, CH, β-C), **100.12** (s, CH, β-C), **87.5** (s, CH, C-1), **39.2** (s, C_q, α-C), **38.5** (s, C_q, α-C), **36.8** (s, CH_3, α-Me), **36.43** (s, C_q, α-C), **36.42** (s, C_q, α-C), **35.5** (s, CH_3, α-Me), **34.2** (s, CH_3, α-Me), **30.67** (s, CH_3, α-Me), **30.65** (s, CH_3, α-Me), **28.7** (s, CH_3, α-Me), **28.2** (s, CH_3, α-Me), **26.6** (s, CH_3, α-Me).

HR-MS (ESI, negative ion mode): *m/z* calculated for $C_{35}H_{38}AlN_4O_2$ $[M]^-$: **573.2816**, found: **573.2839**.

General procedure for the autoprotolysis reaction of the alcohol addition products to *meso*-octamethylcalix[4]pyrrolato aluminate[147]

Procedure. In a dry nitrogen-filled glovebox, tetraphenylphosphonium *meso*-octamethylcalix[4]pyrrolato aluminate ([PPh_4][**21**], 45.0 mg, 51.4 µmol, 1.0 equiv., including 1 equivalent of CH_2Cl_2) was dissolved in CH_2Cl_2 (1.0 mL) in a crimp-top vial, and the equimolar amount of the alcohol substrate was added in one portion at room temperature. The solution turned yellow (orange in the case of *para*-nitrobenzyl alcohol) upon substrate addition. *n*-Pentane (5.0 mL) was added at room temperature what resulted in the precipitation of a yellow (orange in the case of *para*-nitrobenzyl alcohol) solid. The vial was sealed, and the reaction mixture was allowed to stand for several days (> 2 days) at room temperature. The supernatant was separated from the solid material at the bottom of the vial and was filtered through a PTFE syringe filter. The solvent was removed under reduced pressure to give in all cases, after drying *in vacuo*, pale yellow solids which are the protonated, neutral addition products. The orange precipitate (mixture of dianionic alcoholato complex and anionic addition product) was dried *in vacuo*. Both obtained substances were analyzed by NMR spectroscopy.

The described procedure produced crystals suitable for SCXRD measurements of both the neutral and dianionic species.

Neutral, protonated addition product of ethanol to *meso*-octamethylcalix[4]pyrrolato aluminate (**31**)[147]

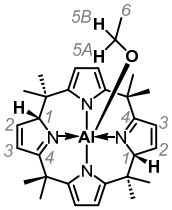

^{1}H NMR (600 MHz, CD_2Cl_2, 295 K), δ [ppm] = **7.61** (d, $^{3}J_{HH}$ = 5.3 Hz, 2H, H-2), **7.02** (dd, $^{3}J_{HH}$ = 5.3 Hz, $^{4}J_{HH}$ = 1.4 Hz, 2H, H-3), **6.04** (d, $^{3}J_{HH}$ = 3.2 Hz, 2H, β-H), **5.93** (d, $^{3}J_{HH}$ = 3.2 Hz, 2H, β-H), **4.88** (s, 2H, H-1), **3.39-3.32** (m, 1H, H-5A/5B), **3.11-3.04** (m, 1H, H-5A/5B), **1.84** (s, 6H, α-Me), **1.79** (s, 6H, α-Me), **1.54** (s, 6H, α-Me), **0.86** (t, $^{3}J_{HH}$ = 7.0 Hz, 3H, H-6), **0.38** (s, 6H, α-Me).

^{13}C{^{1}H} NMR (151 MHz, CD_2Cl_2, 295 K), δ [ppm] = **188.9** (s, C_q, C-4), **155.2** (s, CH, C-2), **149.6** (s, C_q, C_q-pyrrole), **143.5** (s, C_q, C_q-pyrrole), **129.1** (s, CH, C-3), **104.5** (s, CH, β-C), **102.5** (s, CH, β-C), **87.2** (s, CH, C-1), **56.8** (s, CH_2, C-5), **39.3** (s, C_q, α-C), **38.9** (s, C_q, α-C), **30.7** (s, CH_3, α-Me), **28.7** (s, CH_3, α-Me), **27.7** (s, CH_3, α-Me), **23.3** (s, CH_3, α-Me), **20.1** (s, CH_3, C-6).

The constitution of the compound as shown was unambiguously confirmed by SCXRD measurements (cf. **Chapter 7.4***).*

Dianionic ethanolato adduct of *meso*-octamethylcalix[4]pyrrolato aluminate ([PPh_4]$_2$[**32**])[147]

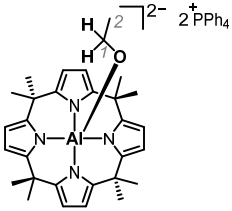

^{1}H NMR (600 MHz, CD_2Cl_2, 295 K), δ [ppm] = **7.90-7.82** (m, 8H, PPh_4^+), **7.75-7.66** (m, 16H, PPh_4^+), **7.62-7.53** (m, 16H, PPh_4^+), **5.61** (d, $^3J_{HH}$ = 2.8 Hz, 4H, β-H), **5.54** (d, $^3J_{HH}$ = 2.8 Hz, 4H, β-H), **2.33** (q, $^3J_{HH}$ = 6.8 Hz, 2H, H-1), **0.50** (t, $^3J_{HH}$ = 6.8 Hz, 3H, H-2).

^{13}C{^{1}H} / **^{1}H,^{13}C HSQC** / **^{1}H,^{13}C HMBC NMR** (600 / 151 MHz, CD_2Cl_2, 295 K), δ [ppm] = **148.3** (s, C_q, C_q-pyrrole), **147.3** (s, C_q, C_q-pyrrole), **136.1** (d, $^4J_{CP}$ = 3.0 Hz, CH, PPh_4^+), **134.8** (d, $^2J_{CP}$ = 10.3 Hz, CH, PPh_4^+), **131.0** (d, $^3J_{CP}$ = 12.9 Hz, CH, PPh_4^+), **117.8** (d, $^1J_{CP}$ = 89.6 Hz, C_q, PPh_4^+), **99.2** (s, CH, β-C), **96.8** (s, CH, β-C), **54.8** (s, CH_2, C-1), **42.6** (s, CH_3, α-Me), **36.9** (s, C_q, α-C), **36.1** (s, C_q, α-C), **35.6** (s, CH_3, α-Me), **32.6** (s, CH_3, α-Me), **26.6** (s, CH_3, α-Me), **19.6** (s, CH_3, C-2).

The constitution of the compound as shown was unambiguously confirmed by SCXRD measurements (cf. **Chapter 7.4***).*

Neutral, protonated addition product of *para*-methylbenzyl alcohol to *meso*-octamethyl-calix[4]pyrrolato aluminate[147]

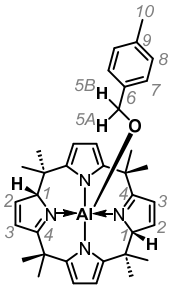

^{1}H NMR (600 MHz, CD_2Cl_2, 295 K), δ [ppm] = **7.65** (d, $^{3}J_{HH}$ = 5.3 Hz, 2H, H-2), **7.03** (dd, $^{3}J_{HH}$ = 5.3 Hz, $^{4}J_{HH}$ = 1.5 Hz, 2H, H-3), **7.01-6.98** (m, 2H, H-7), **6.96-6.92** (m, 2H, H-8), **6.05** (d, $^{3}J_{HH}$ = 3.2 Hz, 2H, β-H), **5.96** (d, $^{3}J_{HH}$ = 3.2 Hz, 2H, β-H), 4.99 (s, 2H, H-1), **4.45** (d, $^{3}J_{HH}$ = 13.4 Hz, 1H, H-5A/5B), **4.12** (d, $^{3}J_{HH}$ = 13.4 Hz, 1H, H-5A/5B), **2.22** (s, 3H, H-10), **1.82** (s, 6H, α-Me), **1.69** (s, 6H, α-Me), **1.57** (s, 6H, α-Me), **0.43** (s, 6H, α-Me).

^{13}C{^{1}H} NMR (151 MHz, CD_2Cl_2, 295 K), δ [ppm] = **189.0** (s, C_q, C-4), **155.3** (s, CH, C-2), **149.6** (s, C_q, C_q-pyrrole), **143.6** (s, C_q, C_q-pyrrole), **142.6** (s, C_q, C-7), **135.4** (s, C_q, C-9), **129.0** (s, CH, C-3), **128.6** (s, CH, C-8), **126.3** (s, CH, C-7), **104.6** (s, CH, β-C), **102.6** (s, CH, β-C), **87.2** (s, CH, C-1), **63.4** (s, CH_2, C-5), **39.3** (s, C_q, α-C), **38.9** (s, C_q, α-C), **31.0** (s, CH_3, α-Me), **28.7** (s, CH_3, α-Me), **27.7** (s, CH_3, α-Me), **23.4** (s, CH_3, α-Me), **21.6** (s, CH_3, C-10).

Dianionic *para*-methylbenzyl alcoholato adduct of *meso*-octamethylcalix[4]pyrrolato aluminate[147]

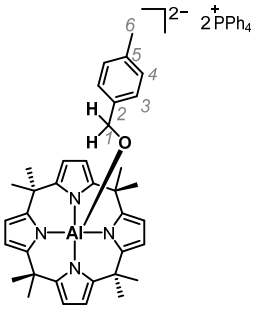

^{1}H NMR (600 MHz, CD_2Cl_2, 295 K), δ [ppm] = **7.87-7.79** (m, 8H, PPh_4^+), **7.72-7.63** (m, 16H, PPh_4^+), **7.59-7.50** (m, 16H, PPh_4^+), **6.79-6.76** (m, 2H, H-3), **6.63-6.59** (m, 2H, H-4), **5.59** (d, $^{3}J_{HH}$ = 2.8 Hz, 4H, β-H), **5.58** (d, $^{3}J_{HH}$ = 2.8 Hz, 4H, β-H), **3.49** (s, 2H, H-1), **2.06** (s, 3H, H-6), **1.57** (s, 6H, α-Me), **1.52** (s, 6H, α-Me), **1.49** (s, 6H, α-Me), **1.26** (s, 6H, α-Me).

^{13}C{^{1}H} / **^{1}H,^{13}C HSQC** / **^{1}H,^{13}C HMBC NMR** (600 / 151 MHz, CD_2Cl_2, 295 K), δ [ppm] = **148.2** (s, C_q, C_q-pyrrole), **147.4** (s, C_q, C-2), **147.3** (s, C_q, C_q-pyrrole), **136.1** (d, $^{4}J_{CP}$ = 3.0 Hz, CH, PPh_4^+), **134.8** (d, $^{2}J_{CP}$ = 10.3 Hz, CH, PPh_4^+), **132.3** (s, C_q, C-5), **131.0** (d, $^{3}J_{CP}$ = 12.9 Hz, CH, PPh_4^+), **127.5** (s, CH, C-4), **126.1** (s, CH, C-3), **117.9** (d, $^{1}J_{CP}$ = 89.6 Hz, C_q, PPh_4^+), **99.6** (s, CH, β-C), **97.1** (s, CH, β-C), **62.1** (s, CH_2, C-1), **42.9** (s, CH_3, α-Me), **36.9** (s, C_q, α-C), **36.3** (s, C_q, α-C), **35.7** (s, CH_3, α-Me), **32.7** (s, CH_3, α-Me), **26.8** (s, CH_3, α-Me), **21.0** (s, CH_3, C-6).

Neutral, protonated addition product of *para*-nitrobenzyl alcohol to *meso*-octamethyl-calix[4]pyrrolato aluminate[147]

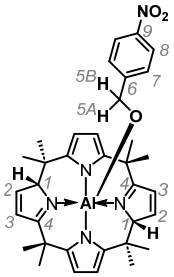

^{1}H NMR (600 MHz, CD_2Cl_2, 295 K), δ [ppm] = **8.01-9.97** (m, 2H, H-8), **7.68** (d, $^{3}J_{HH}$ = 5.3 Hz, 2H, H-2), **7.33-7.30** (m, 2H, H-7), **7.05** (dd, $^{3}J_{HH}$ = 5.3 Hz, $^{4}J_{HH}$ = 1.2 Hz, 2H, H-3), **6.06** (d, $^{3}J_{HH}$ = 3.2 Hz, 2H, β-H), **5.98** (d, $^{3}J_{HH}$ = 3.2 Hz, 2H, β-H), **5.03** (s, 2H, H-1), **4.63** (d, $^{3}J_{HH}$ = 16.1 Hz, 1H, H-5A/5B), **4.28** (d, $^{3}J_{HH}$ = 16.1 Hz, 1H, H-5A/5B), **1.82** (s, 6H, α-Me), **1.593** (s, 6H, α-Me), **1.590** (s, 6H, α-Me), **0.44** (s, 6H, α-Me).

^{13}C{^{1}H} NMR (151 MHz, CD_2Cl_2, 295 K), δ [ppm] = **189.2** (s, C_q, C-4), **155.5** (s, CH, C-2), **154.3** (s, C_q, C-9), **149.6** (s, C_q, C_q-pyrrole), **146.6** (s, C_q, C-6), **143.5** (s, C_q, C_q-pyrrole), **129.1** (s, CH, C-3), **126.4** (s, CH, C-7), **123.2** (s, CH, C-8), **104.8** (s, CH, β-C), **102.8** (s, CH, β-C), **87.3** (s, CH, C-1), **63.0** (s, CH_2, C-5), **39.4** (s, C_q, α-C), **38.9** (s, C_q, α-C), **30.9** (s, CH_3, α-Me), **28.7** (s, CH_3, α-Me), **27.7** (s, CH_3, α-Me), **23.4** (s, CH_3, α-Me).

Dianionic *para*-nitrobenzyl alcoholato adduct of *meso*-octamethylcalix[4]pyrrolato aluminate[147]

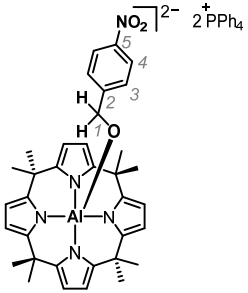

^{1}H NMR (600 MHz, CD_2Cl_2, 295 K), δ [ppm] = **7.87-7.80** (m, 8H, PPh_4^+), **7.71-7.64** (m, 16H, PPh_4^+), **7.62-7.59** (m, 2H, H-3), **7.59-7.51** (m, 16H, PPh_4^+), **7.08-7.04** (m, 2H, H-4), **5.63** (d, $^{3}J_{HH}$ = 2.7 Hz, 4H, β-H), **5.61** (d, $^{3}J_{HH}$ = 2.7 Hz, 4H, β-H), **3.57** (s, 2H, H-1), **1.59** (s, 6H, α-Me), **1.50** (s, 6H, α-Me), **1.47** (s, 6H, α-Me), **1.28** (s, 6H, α-Me).

^{13}C{^{1}H} / **^{1}H,^{13}C HSQC** / **^{1}H,^{13}C HMBC NMR** (600 / 151 MHz, CD_2Cl_2, 295 K), δ [ppm] = **160.5** (s, C_q, C-2), **148.2** (s, C_q, C_q-pyrrole), **147.4** (s, C_q, C_q-pyrrole), **144.9** (s, C_q, C-5), **136.2** (d, $^{4}J_{CP}$ = 3.0 Hz, CH, PPh_4^+), **134.8** (d, $^{2}J_{CP}$ = 10.3 Hz, CH, PPh_4^+), **131.0** (d, $^{3}J_{CP}$ = 12.9 Hz, CH, PPh_4^+), **126.9** (s, CH, C-4), **122.1** (s, CH, C-3), **117.8** (d, $^{1}J_{CP}$ = 89.5 Hz, C_q, PPh_4^+), **99.7** (s, CH, β-C), **97.4** (s, CH, β-C), **62.7** (s, CH_2, C-1), **42.8** (s, CH_3, α-Me), **36.6** (s, C_q, α-C), **36.2** (s, C_q, α-C), **35.6** (s, CH_3, α-Me), **32.8** (s, CH_3, α-Me), **26.8** (s, CH_3, α-Me).

Pyridine / dimethyl sulfoxide adduct of *meso*-octamethylcalix[4]pyrrolato aluminate[147]

Procedure. In a dry nitrogen-filled glovebox, tetraphenylphosphonium *meso*-octamethylcalix[4]pyrrolato aluminate ([PPh_4][**21**], 10.0 mg, 11.4 µmol, 1.0 equiv., including 1 equivalent of CH_2Cl_2) was dissolved in CD_2Cl_2 (0.6 mL) and the equimolar amount of pyridine or DMSO (0.92 and 0.81 µL, respectively, 11.4 µmol, 1.0 equiv.) was added to the solution at room temperature with a piston pipet. The reaction mixture turned pale yellow immediately after donor addition. The obtained solutions were analyzed by NMR spectroscopy. In both cases quantitative formation of the Lewis acid/base adduct was observed.

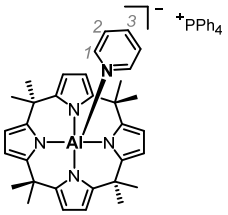

^{1}H NMR (600 MHz, CD_2Cl_2, 295 K), δ [ppm] = **7.90-7.82** (m, 4H, PPh_4^+), **7.74-7.65** (m, 8H, PPh_4^+), **7.61-7.56** (m, 1H, H-3), **7.60-7.53** (m, 8H, PPh_4^+), **7.12-7.07** (m, 2H, H-2), **6.84-6.81** (m, 2H, H-1), **5.84** (d, $^3J_{HH}$ = 2.9 Hz, 4H, β-H), **5.74** (d, $^3J_{HH}$ = 2.9 Hz, 4H, β-H), **1.70** (s, 6H, α-Me), **1.47** (s, 6H, α-Me), **1.46** (s, 6H, α-Me), **0.05** (s, 6H, α-Me).

^{13}C{^{1}H} NMR (151 MHz, CD_2Cl_2, 295 K), δ [ppm] = **149.5** (s, CH, C-1), **148.6** (s, C_q, C_q-pyrrole), **148.1** (s, C_q, C_q-pyrrole), **140.2** (s, CH, C-3), **136.2** (d, $^4J_{CP}$ = 3.0 Hz, CH, PPh_4^+), **134.8** (d, $^2J_{CP}$ = 10.3 Hz, CH, PPh_4^+), **131.0** (d, $^3J_{CP}$ = 12.9 Hz, CH, PPh_4^+), **125.3** (s, CH, C-2), **117.8** (d, $^1J_{CP}$ = 89.6 Hz, C_q, PPh_4^+), **102.1** (s, CH, β-C), **99.7** (s, CH, β-C), **40.8** (s, CH_3, α-Me), **36.3** (s, CH_3, α-Me), **36.1** (s, C_q, α-C), **35.9** (s, C_q, α-C), **34.5** (s, CH_3, α-Me), **26.4** (s, CH_3, α-Me).

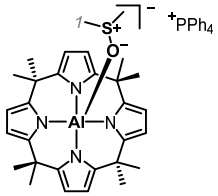

^{1}H NMR (600 MHz, CD_2Cl_2, 295 K), δ [ppm] = **7.87-7.81** (m, 4H, PPh_4^+), **7.70-7.64** (m, 8H, PPh_4^+), **7.58-7.51** (m, 8H, PPh_4^+), **5.83** (d, $^{3}J_{HH}$ = 2.9 Hz, 4H, β-H), **5.76** (d, $^{3}J_{HH}$ = 2.9 Hz, 4H, β-H), **2.05** (s, 6H, H-1), **1.66** (s, 6H, α-Me), **1.65** (s, 6H, α-Me), **1.29** (s, 6H, α-Me).

^{13}C{^{1}H} NMR (151 MHz, CD_2Cl_2, 295 K), δ [ppm] = **147.9** (s, C_q, C_q-pyrrole), **146.9** (s, C_q, C_q-pyrrole), **136.2** (d, $^{4}J_{CP}$ = 3.0 Hz, CH, PPh_4^+), **134.8** (d, $^{2}J_{CP}$ = 10.3 Hz, CH, PPh_4^+), **131.0** (d, $^{3}J_{CP}$ = 12.9 Hz, CH, PPh_4^+), **117.8** (d, $^{1}J_{CP}$ = 89.6 Hz, C_q, PPh_4^+), **101.8** (s, CH, β-C), **99.8** (s, CH, β-C), **41.7** (s, CH_3, α-Me), **38.4** (s, CH_3, α-Me), **36.4** (s, C_q, α-C), **35.9** (s, C_q, α-C), **34.5** (s, CH_3, C-1), **33.5** (s, CH_3, α-Me), **26.3** (s, CH_3, α-Me).

Procedure for the addition reaction of dioxygen to *meso*-octaalkylcalix[4]pyrrolato aluminates ([PPh_4][**35**] and [PPh_4][**36**])[148]

Procedure. A J. Young NMR tube was charged with tetraphenylphosphonium *meso*-octamethylcalix[4]pyrrolato aluminate or the analogous ethyl-substituted version ([PPh_4][**21**] or [PPh_4][**34**], between 10.0 and 50.0 mg). The material was dissolved in dichloromethane-d_2 (0.7 mL). The sample was pressurized multiple times with 1 bar of dioxygen gas (excess) at room temperature. The color of the reaction mixture changed within seconds from colorless to orange. Immediately after pressurizing, the sample was degassed with four freeze-pump-thaw cycles. The completion of the reaction was monitored with ^{1}H NMR spectroscopy, and the sample was used for respective experiments.

To obtain solid material for FT-ATR-IR measurements, the solvent was removed under reduced pressure, and the obtained solids were dried *in vacuo* at room temperature for 60 min. Single crystals of the dioxygen addition product [PPh_4][**35**] for SCXRD measurements were obtained at −40 °C from a dichloromethane/*n*-pentane solution.

Addition product of O_2 to *meso*-octamethylcalix[4]pyrrolato aluminate ([PPh_4][**35**])[148]

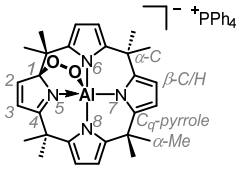

^{1}H NMR (600 MHz, CD_2Cl_2, 295 K), δ [ppm] = **7.88-7.83** (m, 4H, PPh_4^+), **7.72-7.66** (m, 8H, PPh_4^+), **7.60-7.53** (m, 8H, PPh_4^+), **7.23** (d, $^3J_{HH}$ = 5.3 Hz, 1H, H-2), **6.59** (d, $^3J_{HH}$ = 5.3 Hz, 1H, H-3), **5.90** (d, $^3J_{HH}$ = 3.0 Hz, 1H, β-H), **5.86** (d, $^3J_{HH}$ = 3.0 Hz, 1H, β-H), **5.79** (d, $^3J_{HH}$ = 3.0 Hz, 1H, β-H), **5.77** (d, $^3J_{HH}$ = 3.0 Hz, 1H, β-H), **5.68** (s, 2H, β-H), **1.73** (s, 3H, α-Me), **1.66** (s, 3H, α-Me), **1.63** (s, 3H, α-Me), **1.62** (s, 3H, α-Me), **1.56** (s, 3H, α-Me), **1.46** (s, 3H, α-Me), **1.34** (s, 3H, α-Me), **1.07** (s, 3H, α-Me).

^{13}C{^{1}H} NMR (151 MHz, CD_2Cl_2, 295 K), δ [ppm] = **189.8** (s, C_q, C-4), **154.9** (s, CH, C-2), **150.8** (s, C_q, C_q-pyrrole), **147.9** (s, C_q, C_q-pyrrole), **147.1** (s, C_q, C_q-pyrrole), **147.0** (s, C_q, C_q-pyrrole), **146.6** (s, C_q, C_q-pyrrole), **139.9** (s, C_q, C_q-pyrrole), **136.2** (d, $^4J_{CP}$ = 3.0 Hz, CH, PPh_4^+), **134.8** (d, $^2J_{CP}$ = 10.3 Hz, CH, PPh_4^+), **131.0** (d, $^3J_{CP}$ = 12.9 Hz, CH, PPh_4^+), **128.2** (s, CH, C-3), **117.8** (d, $^1J_{CP}$ = 89.6 Hz, C_q, PPh_4^+), **115.1** (s, C_q, C-1), **103.1** (s, CH, β-C), **102.9** (s, CH, β-C), **101.7** (s, CH, β-C), **101.4** (s, CH, β-C), **101.2** (s, CH, β-C), **99.9** (s, CH, β-C), **41.6** (s, C_q, α-C), **41.5** (s, CH_3, α-Me), **39.4** (s, C_q, α-C), **36.51** (s, C_q, α-C), **36.48** (s, C_q, α-C), **36.1** (s, CH_3, α-Me), **35.9** (s, CH_3, α-Me), **30.1** (s, CH_3, α-Me), **27.9** (s, CH_3, α-Me), **27.0** (s, CH_3, α-Me), **26.5** (s, CH_3, α-Me).

^{1}H,^{15}N HMBC NMR (600 MHz, 61 MHz, CD_2Cl_2, 295 K), δ [ppm] (with respect to nitromethane as reference) = **−102.1** (N-5), **−184.4** (N-8), **−185.7** (N-6), **−194.8** (N-7).

HR-MS (ESI, negative ion mode): *m/z* calculated for $C_{28}H_{32}AlN_4O_2$ $[M]^-$: **483.2346**, found: **483.2365**.

UV-Vis (CH_2Cl_2, room temperature), λ_{max} [nm] = **430**, **320**, **276**, **268**, **262**.

FT-ATR-IR (solid state, room temperature), $\tilde{\nu}_{max}$ [cm^{-1}] = **3083** (m), **3058** (m), **2961** (s), **2905** (s), **2860** (m), **1662** (w), **1634** (w), **1587** (m), **1544** (m), **1533** (m), **1484** (m), **1462** (w), **1436** (s), **1402** (w), **1374** (m), **1357** (m), **1346** (m), **1316** (w), **1278** (m), **1226** (w), **1215** (w), **1189** (w), **1156** (m), **1107** (s), **1067** (s), **996** (m), **952** (m), **894** (w), **877** (w), **849** (w), **826** (w), **783** (m), **754** (s), **719** (s), **688** (s).

The constitution of the compound as shown was unambiguously confirmed by SCXRD measurements (cf. **Chapter 7.4***).*

Addition product of dioxygen to *meso*-octaethylcalix[4]pyrrolato aluminate ([PPh_4][**36**])[148]

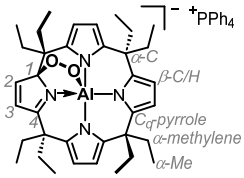

^{1}H NMR (600 MHz, CD_2Cl_2, 295 K), δ [ppm] = **7.89-7.81** (m, 4H, PPh_4^+), **7.73-7.65** (m, 8H, PPh_4^+), **7.60-7.52** (m, 8H, PPh_4^+), **7.30** (d, $^3J_{HH}$ = 5.3 Hz, 1H, H-2), **6.53** (d, $^3J_{HH}$ = 5.3 Hz, 1H, H-3), **5.85** (d, $^3J_{HH}$ = 3.0 Hz, 1H, β-H), **5.79** (d, $^3J_{HH}$ = 3.0 Hz, 1H, β-H), **5.78** (d, $^3J_{HH}$ = 3.0 Hz, 1H, β-H), **5.71** (d, $^3J_{HH}$ = 3.0 Hz, 1H, β-H), **5.68** (d, $^3J_{HH}$ = 2.9 Hz, 1H, β-H), **5.66** (d, $^3J_{HH}$ = 2.9 Hz, 1H, β-H), **2.37-2.26** (dq, 2H, α-methylene), **2.19-2.01** (dq, 4H, α-methylene), **1.98-1.84** (dq, 4H, α-methylene), **1.82-1.74** (dq, 1H, α-methylene), **1.62-1.51** (dq, 4H, α-methylene), **1.45-1.36** (dq, 1H, α-methylene), **1.06** (t, $^3J_{HH}$ = 7.4 Hz, 1H, α-Me), **1.05** (t, $^3J_{HH}$ = 7.4 Hz, 1H, α-Me), **0.99** (t, $^3J_{HH}$ = 7.4 Hz, 3H, α-Me), **0.97** (t, $^3J_{HH}$ = 7.2 Hz, 3H, α-Me), **0.56** (t, $^3J_{HH}$ = 7.2 Hz, 3H, α-Me), **0.51** (t, $^3J_{HH}$ = 7.4 Hz, 3H, α-Me), **0.48** (t, $^3J_{HH}$ = 7.4 Hz, 3H, α-Me), **0.40** (t, $^3J_{HH}$ = 7.4 Hz, 3H, α-Me).

^{13}C{^{1}H} NMR (151 MHz, CD_2Cl_2, 295 K), δ [ppm] = **189.2** (s, C_q, C-4), **154.0** (s, CH, C-2), **149.7** (s, C_q, C_q-pyrrole), **144.9** (s, C_q, C_q-pyrrole), **143.2** (s, C_q, C_q-pyrrole), **142.8** (s, C_q, C_q-pyrrole), **140.8** (s, C_q, C_q-pyrrole), **136.2** (d, $^4J_{CP}$ = 3.0 Hz, CH, PPh_4^+), **135.7** (s, C_q, C_q-pyrrole), **134.7** (d, $^2J_{CP}$ = 10.3 Hz, CH, PPh_4^+), **131.0** (d, $^3J_{CP}$ = 12.9 Hz, CH, PPh_4^+), **128.7** (s, CH, C-3), **117.8** (d, $^1J_{CP}$ = 89.5 Hz, C_q, PPh_4^+), **114.0** (s, C_q, C-1), **105.4** (s, CH, β-C), **104.4** (s, CH, β-C), **104.1** (s, CH, β-C), **102.9** (s, CH, β-C), **102.8** (s, CH, β-C), **101.7** (s, CH, β-C), **48.3** (s, C_q, α-C), **47.4** (s, C_q, α-C), **46.3** (s, CH_2, α-methylene), **45.4** (s, C_q, α-C), **44.5** (s, C_q, α-C), **36.3** (s, CH_2, α-methylene, was identified by ^{1}H,^{13}C HMBC and ^{1}H,^{13}C HSQC NMR spectroscopy), **35.24** (s, CH_2, α-methylene), **35.19** (s, CH_2, α-methylene), **32.0** (s, CH_2, α-methylene), **29.5** (s, CH_2, α-methylene), **27.7** (s, CH_2, α-methylene), **23.5** (s, CH_2, α-methylene), **10.82** (s, CH_3, α-Me), **10.80** (s, CH_3, α-Me), **10.79** (s, CH_3, α-Me), **10.13** (s, CH_3, α-Me), **10.05** (s, CH_3, α-Me), **9.9** (s, CH_3, α-Me), **9.4** (s, CH_3, α-Me), **8.3** (s, CH_3, α-Me).

HR-MS (ESI, negative ion mode): *m/z* calculated for $C_{36}H_{48}AlN_4O_2$ $[M]^-$: **595.3598**, found: **595.3597**.

UV-Vis (CH_2Cl_2, room temperature), λ_{max} [nm] = **450**, **322**, **276**, **268**, **261**.

FT-ATR-IR (solid state, room temperature), $\tilde{\nu}_{max}$ [cm^{-1}] = **3084** (m), **3060** (m), **2962** (s), **2925** (s), **2869** (s), **1665** (w), **1628** (m), **1587** (m), **1538** (w), **1484** (m), **1460** (m), **1437** (s), **1401** (w), **1385** (m), **1372** (m), **1352** (w), **1338** (w), **1319** (m), **1294** (w), **1246** (m), **1209** (w), **1187** (w), **1166** (w), **1149** (w), **1130** (w), **1108** (s), **1078** (s), **1056** (m), **1030** (w), **1011** (w), **996** (m), **969** (m), **953** (m), **924** (m), **885** (w), **858** (m), **846** (m), **794** (w), **747** (s), **721** (s), **689** (s).

Procedure for the rearrangement reaction of the dioxygen addition products to *meso*-octaalkylcalix[4]pyrrolato aluminates[148]

Procedure. In a J. Young NMR tube, [PPh_4][**35**] or [PPh_4][**36**] was prepared as described above. The sample was incubated for 30 min at 60 °C in an NMR tube heating block without stirring. The color of the reaction mixture slightly brightened to yellow-orange. The sample was then analyzed by ^{1}H NMR spectroscopy and further used for respective experiments. The relative conversion to [PPh_4][**40**] and [PPh_4][**41**], respectively, (R = Me: 51%, R = Et: 66%) was determined by ^{1}H NMR signal integration using the most downfield-shifted PPh_4^+ multiplet (4H) as internal reference and one well-separated doublet signal of a proton of an aromatic pyrrole ring in [**40**]$^-$ and [**41**]$^-$, respectively. The given values are the result of one single reaction. It was found that in both cases the reaction also takes place at room temperature within 24 h.

[PPh_4][**36**] was also prepared on preparative scale. For that, tetraphenylphosphonium *meso*-octaethylcalix[4]pyrrolato aluminate ([PPh_4][**34**], 424.0 mg) was dissolved in dichloromethane (6 mL) in a Schlenk flask. The flask was capped with a rubber septum. With a slight overpressure, dioxygen gas was passed through the headspace of the flask for 3 min, while the reaction mixture was rigorously stirred at room temperature. The color of the solution changed from colorless to orange within seconds. Immediately after reacting with dioxygen, the rubber septum was replaced with a glass cap, and the solution was degassed with three freeze-pump-thaw cycles. The closed system was heated for 80 min at 60 °C while stirring. The solvent was removed under reduced pressure. The obtained intensely orange material was analyzed by ^{1}H NMR spectroscopy and was further used for respective experiments.

Discussion. It was extensively attempted to purify the obtained material either by crystallization or washing. Various solvents (dichloromethane, tetrahydrofuran, fluorobenzene, chlorobenzene, *ortho*-dichlorobenzene, benzene, toluene, acetone, acetonitrile, 1,2-dimethoxyethane, diethyl ether, *n*-pentane, *n*-hexane, *n*-heptane, hexamethyldisiloxane) were used in different manners. However, in all cases the entire material or none of which dissolved preventing purification and crystallization. This is also why no isolated yields are reported in the above-described procedure. Also, all attempts to grow single crystals either at room temperature, −40, or −80 °C from [PPh_4][**40**] or [PPh_4][**41**] remained unfruitful.

One reason for the moderate relative conversion from [**35**]$^-$/[**36**]$^-$ to [**40**]$^-$/[**41**]$^-$ is a ligand degradation process occurring as a side reaction. This becomes obvious from ^{1}H NMR spectroscopy. Peaks in the ^{1}H NMR spectrum occurred which can be assigned to acetone (in the case of [**35**]$^-$ ⟶ [**40**]$^-$, singlet at 2.12 ppm) and pentan-3-one (in the case of [**36**]$^-$ ⟶ [**41**]$^-$, quartet at 2.40 and triplet at 1.01 ppm).

[PPh_4][**40**][148]

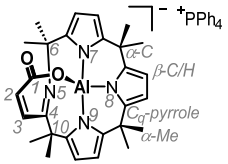

^{1}H NMR (600 MHz, CD_2Cl_2, 295 K), δ [ppm] = **7.86-7.79** (m, 4H, PPh_4^+), **7.71-7.63** (m, 8H, PPh_4^+), **7.59-7.51** (m, 8H, PPh_4^+), **6.94** (d, $^3J_{HH}$ = 12.4 Hz, 1H, H-3), **5.97** (d, $^3J_{HH}$ = 3.0 Hz, 1H, β-H), **5.90** (d, $^3J_{HH}$ = 3.0 Hz, 1H, β-H), **5.87** (d, $^3J_{HH}$ = 3.0 Hz, 1H, β-H), **5.81** (d, $^3J_{HH}$ = 12.4 Hz, 1H, H-2), **5.766** (d, $^3J_{HH}$ = 3.0 Hz, 1H, β-H), **5.761** (d, $^3J_{HH}$ = 3.0 Hz, 1H, β-H), **5.64** (d, $^3J_{HH}$ = 3.0 Hz, 1H, β-H), **1.61** (s, 3H, α-Me), **1.59** (s, 3H, α-Me), **1.58** (s, 3H, α-Me), **1.57** (s, 3H, α-Me), **1.56** (s, 3H, α-Me), **1.40** (s, 3H, α-Me), **1.38** (s, 3H, α-Me), **1.32** (s, 3H, α-Me).

^{13}C{^{1}H} NMR (151 MHz, CD_2Cl_2, 295 K), δ [ppm] = **185.0** (s, C_q, C-4), **165.6** (s, CH, C-1), **148.6** (s, C_q, C_q-pyrrole), **147.8** (s, C_q, C_q-pyrrole), **146.8** (s, C_q, C_q-pyrrole), **145.7** (s, C_q, C_q-pyrrole), **145.6** (s, C_q, C_q-pyrrole), **143.0** (s, C_q, C_q-pyrrole), **139.5** (s, CH, C-3), **136.2** (d, $^4J_{CP}$ = 3.0 Hz, CH, PPh_4^+), **134.8** (d, $^2J_{CP}$ = 10.3 Hz, CH, PPh_4^+), **131.0** (d, $^3J_{CP}$ = 12.9 Hz, CH, PPh_4^+), **117.8** (d, $^1J_{CP}$ = 89.5 Hz, C_q, PPh_4^+), **127.8** (s, CH, C-2), **104.4** (s, CH, β-C), **103.4** (s, CH, β-C), **102.5** (s, CH, β-C), **102.0** (s, CH, β-C), **101.2** (s, CH, β-C), **100.3** (s, CH, β-C), **61.7** (s, C_q, C-6), **48.7** (s, C_q, C-10), **39.9** (s, CH_3, α-Me), **38.8** (s, CH_3, α-Me), **37.5** (s, C_q, α-C), **36.4** (s, C_q, α-C), **36.2** (s, CH_3, α-Me), **31.5** (s, CH_3, α-Me), **31.1** (s, CH_3, α-Me), **30.1** (s, CH_3, α-Me), **30.0** (s, CH_3, α-Me), **27.6** (s, CH_3, α-Me).

^{1}H,^{15}N HMBC NMR (600 MHz, 61 MHz, CD_2Cl_2, 295 K), δ [ppm] (with respect to nitromethane as reference) = **−34.5** (N-5), **−201.0** (N-7), **−202.9** (N-8), **−206.6** (N-9).

HR-MS (ESI, negative ion mode): *m/z* calculated for $C_{28}H_{32}AlN_4O_2$ $[M]^-$: **483.2346**, found: **483.2331**.

FT-ATR-IR (solid state, room temperature), $\tilde{\nu}_{max}$ [cm^{-1}] = **3085** (w), **3056** (w), **2959** (m), **2904** (m), **2857** (m), **1661** (s), **1635** (m), **1586** (s), **1544** (m), **1483** (m), **1461** (w), **1436** (s), **1416** (w), **1400** (m), **1372** (m), **1358** (w), **1278** (s), **1236** (m), **1187** (w), **1156** (m), **1106** (s), **1067** (s), **1027** (w), **1014** (w), **995** (m), **952** (w), **827** (m), **753** (s), **719** (s), **687** (s).

[PPh_4][**41**][148]

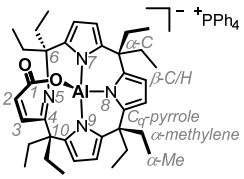

^{1}H NMR (600 MHz, CD_2Cl_2, 295 K), δ [ppm] = **7.92-7.85** (m, 4H, PPh_4^+), **7.76-7.70** (m, 8H, PPh_4^+), **7.66-7.59** (m, 8H, PPh_4^+), **6.70** (d, $^3J_{HH}$ = 12.4 Hz, 1H, H-3), **6.04** (d, $^3J_{HH}$ = 3.0 Hz, 1H, β-H), **5.86** (d, $^3J_{HH}$ = 2.9 Hz, 1H, β-H), **5.85** (d, $^3J_{HH}$ = 3.0 Hz, 1H, β-H), **5.84** (d, $^3J_{HH}$ = 3.0 Hz, 1H, β-H), **5.80** (d, $^3J_{HH}$ = 2.9 Hz, 1H, β-H), **5.74** (d, $^3J_{HH}$ = 3.0 Hz, 1H, β-H), **5.70** (d, $^3J_{HH}$ = 12.4 Hz, 1H, H-2), **2.35-2.26** (dq, 1H, α-methylene), **2.15-1.98** (dq, 5H, α-methylene), **1.98-1.84** (dq, 5H, α-methylene), **1.79-1.70** (dq, 3H, α-methylene), **1.66-1.58** (dq, 1H, α-methylene), **1.46-1.39** (dq, 1H, α-methylene), **1.02** (t, $^3J_{HH}$ = 7.5 Hz, 3H, α-Me), **0.93** (t, $^3J_{HH}$ = 7.5 Hz, 3H, α-Me), **0.83** (t, $^3J_{HH}$ = 7.1 Hz, 3H, α-Me), **0.64** (t, $^3J_{HH}$ = 7.3 Hz, 3H, α-Me), **0.63** (t, $^3J_{HH}$ = 7.5 Hz, 3H, α-Me), **0.59** (t, $^3J_{HH}$ = 7.3 Hz, 3H, α-Me), **0.49** (t, $^3J_{HH}$ = 7.3 Hz, 3H, α-Me), **0.41** (t, $^3J_{HH}$ = 7.3 Hz 3H, α-Me).

^{13}C{^{1}H} NMR (151 MHz, CD_2Cl_2, 295 K), δ [ppm] = **183.9** (s, C_q, C-4), **165.3** (s, CH, C-1), **144.9** (s, C_q, C_q-pyrrole), **142.7** (s, C_q, C_q-pyrrole), **142.4** (s, C_q, C_q-pyrrole), **141.5** (s, C_q, C_q-pyrrole), **140.1** (s, CH, C-3), **139.9** (s, C_q, C_q-pyrrole), **139.6** (s, C_q, C_q-pyrrole), **136.0** (d, $^4J_{CP}$ = 2.9 Hz, CH, PPh_4^+), **134.5** (d, $^2J_{CP}$ = 10.3 Hz, CH, PPh_4^+), **130.9** (d, $^3J_{CP}$ = 12.9 Hz, CH, PPh_4^+), **127.6** (s, CH, C-2), **117.6** (d, $^1J_{CP}$ = 89.5 Hz, C_q, PPh_4^+), **108.5** (s, CH, β-C), **105.3** (s, CH, β-C), **104.6** (s, CH, β-C), **102.5** (s, CH, β-C), **102.0** (s, CH, β-C), **101.8** (s, CH, β-C), **66.9** (s, C_q, C-6), **56.7** (s, C_q, C-10), **47.3** (s, C_q, α-C), **45.1** (s, C_q, α-C), **44.8** (s, CH_2, α-methylene), **39.0** (s, CH_2, α-methylene), **38.0** (s, CH_2, α-methylene), **37.0** (s, CH_2, α-methylene), **31.3** (s, CH_2, α-methylene), **29.8** (s, CH_2, α-methylene), **29.6** (s, CH_2, α-methylene), **28.0** (s, CH_2, α-methylene), **10.44** (s, CH_3, α-Me), **10.40** (s, CH_3, α-Me), **10.2** (s, CH_3, α-Me), **9.9** (s, CH_3, α-Me), **9.7** (s, CH_3, α-Me), **9.13** (s, CH_3, α-Me), **9.10** (s, CH_3, α-Me), **8.2** (s, CH_3, α-Me).

^{1}H,^{15}N HMBC NMR (600 MHz, 61 MHz, CD_2Cl_2, 295 K), δ [ppm] (with respect to nitromethane as reference) = −**26.9** (N-5), −**197.1** (N-7 or N-8), −**197.5** (N-7 or N-8), −**202.2** (N-9). Due to the extremely similar ^{15}N chemical shift of N-7 and N-8, the exact signal assignment was not possible.

HR-MS (ESI, negative ion mode): *m/z* calculated for $C_{36}H_{48}AlN_4O_2$ $[M]^-$: **595.3598**, found: **595.3596**.

FT-ATR-IR (solid state, room temperature), $\tilde{\nu}_{max}$ [cm^{-1}] = **3084** (w), **3060** (w), **2962** (s), **2925** (s), **2870** (s), **1662** (s), **1626** (m), **1587** (m), **1484** (m), **1460** (m), **1437** (s), **1373** (m), **1317** (m), **1264** (m), **1189** (w), **1167** (m), **1149** (m), **1107** (s), **1089** (s), **1079** (s), **1028** (w), **996** (m), **971** (m), **925** (m), **873** (w), **856** (m), **834** (m), **751** (s), **721** (s), **688** (s).

Addition product of phenyl isocyanate to *meso*-octamethylcalix[4]pyrrolato aluminate ([PPh_4][**61**])

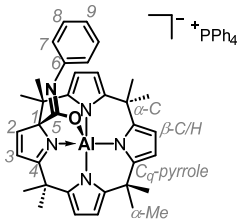

Procedure. A J. Young NMR tube was charged with *meso*-octamethylcalix[4]pyrrolato aluminate ([PPh_4][**21**], 10.0 mg, 11.4 µmol, 1.0 equiv., including 1 equivalent of CH_2Cl_2) in a nitrogen-filled glovebox. The material was dissolved in dichloromethane-d_2 (0.6 mL), and phenyl isocyanate (1.25 µL, 11.4 µmol, 1.0 equiv.) was added with a piston pipette at room temperature. The reaction mixture immediately turned yellow. It was analyzed by NMR spectroscopy.

Single crystals for SCXRD measurements were obtained at room temperature from a dichloromethane/toluene solution.

^{1}H NMR (600 MHz, CD_2Cl_2, 295 K), δ [ppm] = **7.85** (d, $^3J_{HH}$ = 5.0 Hz, 1H, H-2), **7.84-7.79** (m, 4H, PPh_4^+), **7.69-7.63** (m, 8H, PPh_4^+), **7.56-7.49** (m, 8H, PPh_4^+), **6.93-6.88** (m, 2H, H-7), **6.81-6.77** (m, 2H, H-8), **6.68-6.64** (m, 1H, H-9), **6.66** (d, $^3J_{HH}$ = 5.0 Hz, 1H, H-3), **5.90** (d, $^3J_{HH}$ = 3.0 Hz, 1H, β-H), **5.85** (d, $^3J_{HH}$ = 3.0 Hz, 1H, β-H), **5.76** (d, $^3J_{HH}$ = 3.0 Hz, 1H, β-H), **5.75** (d, $^3J_{HH}$ = 3.0 Hz, 1H, β-H), **5.67** (d, $^3J_{HH}$ = 3.0 Hz, 1H, β-H), **5.66** (d, $^3J_{HH}$ = 3.0 Hz, 1H, β-H), **1.92** (s, 3H, α-Me), **1.78** (s, 3H, α-Me), **1.71** (s, 3H, α-Me), **1.60** (s, 3H, α-Me), **1.54** (s, 3H, α-Me), **1.35** (s, 3H, α-Me), **1.33** (s, 3H, α-Me), **0.98** (s, 3H, α-Me).

$^{13}C\{^1H\}$ NMR (151 MHz, CD_2Cl_2, 295 K), δ [ppm] = **189.2** (s, C_q, C-4), **160.7** (s, CH, C-2), **159.9** (s, C_q, C-5), **150.4** (s, C_q, C_q-pyrrole), **149.9** (s, C_q, C-6), **148.5** (s, C_q, C_q-pyrrole), **147.7** (s, C_q, C_q-pyrrole), **146.89** (s, C_q, C_q-pyrrole), **146.86** (s, C_q, C_q-pyrrole), **141.7** (s, C_q, C_q-pyrrole), **136.2** (d, $^4J_{CP}$ = 3.0 Hz, CH, PPh_4^+), **134.7** (d, $^2J_{CP}$ = 10.4 Hz, CH, PPh_4^+), **131.0** (d, $^3J_{CP}$ = 12.8 Hz, CH, PPh_4^+), **128.0** (s, CH, C-7), **125.7** (s, CH, C-3), **123.8** (s, CH, C-8), **121.6** (s, CH, C-9), **117.8** (d, $^1J_{CP}$ = 89.6 Hz, C_q, PPh_4^+), **103.4** (s, CH, β-C), **102.4** (s, CH, β-C), **101.68** (s, CH, β-C), **101.67** (s, CH, β-C), **101.3** (s, CH, β-C), **99.8** (s, CH, β-C), **96.4** (s, C_q, C-1), **44.5** (s, C_q, α-C), **41.4** (s, CH_3, α-Me), **38.9** (s, C_q, α-C), **36.5** (s, C_q, α-C), **36.35** (s, C_q, α-C), **36.33** (s, CH_3, α-Me), **35.2** (s, CH_3, α-Me), **28.1** (s, CH_3, α-Me), **28.0** (s, CH_3, α-Me), **27.8** (s, CH_3, α-Me), **26.4** (s, CH_3, α-Me), **24.0** (s, CH_3, α-Me).

The constitution of the compound as shown was unambiguously confirmed by SCXRD measurements (cf. **Chapter 7.4***).*

Addition product of nitrogen monoxide to *meso*-octaethylcalix[4]pyrrolato aluminate ([PPh_4][**62**])

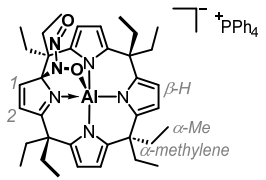

Procedure. In a nitrogen-filled glovebox, a J. Young NMR tube was charged with tetraphenylphosphonium *meso*-octaethylcalix[4]pyrrolato aluminate ([PPh_4][**34**], 12 mg). The material was dissolved in dichloromethane-d_2 (0.6 mL). The sample was pressurized multiple times with approximately 1 bar of nitrogen monoxide gas at room temperature. The color of the reaction mixture changed within seconds from colorless to dark red. Immediately after pressurizing, the sample was degassed with four freeze-pump-thaw cycles. It was analyzed by NMR spectroscopy.

Single crystals for SCXRD measurements were obtained at −40 °C from a THF/diethyl ether solution.

^{1}H NMR (600 MHz, CD_2Cl_2, 295 K), δ [ppm] = **7.96** (d, $^3J_{HH}$ = 5.2 Hz, 1H, H-1), **7.85-7.82** (m, 4H, PPh_4^+), **7.69-7.65** (m, 8H, PPh_4^+), **7.58-7.54** (m, 8H, PPh_4^+), **6.66** (d, $^3J_{HH}$ = 5.2 Hz, 1H, H-2), **5.89** (d, $^3J_{HH}$ = 3.0 Hz, 1H, β-H), **5.89** (d, $^3J_{HH}$ = 3.0 Hz, 1H, β-H), **5.85** (d, $^3J_{HH}$ = 3.1 Hz, 1H, β-H), **5.74** (d, $^3J_{HH}$ = 3.0 Hz, 1H, β-H), **5.72** (d, $^3J_{HH}$ = 3.0 Hz, 1H, β-H), **5.69** (d, $^3J_{HH}$ = 3.1 Hz, 1H, β-H), **2.26-2.14** (m, 2H, α-methylene), **2.13-1.80** (m, 10H, α-methylene), **1.64-1.43** (m, 4H, α-methylene), **1.08** (t, $^3J_{HH}$ = 7.3, 3H, α-Me), **0.94** (t, $^3J_{HH}$ = 7.1 Hz, 2 × 3H, α-Me), **0.92** (t, $^3J_{HH}$ = 7.4, 3H, α-Me), **0.46** (t, $^3J_{HH}$ = 7.4, 3H, α-Me), 0.45 (t, $^3J_{HH}$ = 7.3, 3H, α-Me).

^{31}P{^{1}H} NMR (243 MHz, CD_2Cl_2, 295 K), δ [ppm] = **23.2** (s, PPh_4^+).

HR-MS (ESI, negative ion mode): *m/z* calculated for $[M\text{-}NO]^{\bullet -}$: **593.3680**, found: **593.3804**.

A $^{13}C\{^1H\}$ NMR spectrum was not collected. However, the constitution of the compound as shown was unambiguously confirmed by SCXRD measurements (cf. **Chapter 7.4***).*

Addition product of nitrosobenzene to *meso*-octamethylcalix[4]pyrrolato aluminate ([PPh_4][**64**])

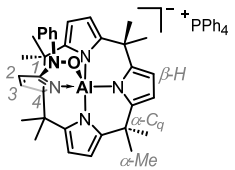

Procedure. In a nitrogen-filled glovebox, a J. Young NMR tube was charged with tetraphenylphosphonium *meso*-octamethylcalix[4]pyrrolato aluminate ([PPh_4][**21**], 15.0 mg, 17.1 µmol, 1.0 equiv., including 1 equivalent of CH_2Cl_2) and nitrosobenzene (1.8 mg, 17.1 µmol, 1.0 equiv.). Dichloromethane-d_2 (0.6 mL) was added at room temperature, and the sample was vigorously shaken. An orange solution was obtained which was analyzed by NMR spectroscopy.

Single crystals for SCXRD measurements were obtained at −40 °C from a CH_2Cl_2/toluene/*n*-pentane solution.

^{1}H NMR (600 MHz, CD_2Cl_2, 295 K), δ [ppm] = **7.83-7.80** (m, 4H, PPh_4^+), **7.66-7.63** (m, 8H, PPh_4^+), 7.58 (d, $^3J_{HH}$ = 5.2 Hz, 1H, H-3), **7.54-7.49** (m, 8H, PPh_4^+), **7.38-7.36** (m, 2H, Ph_{PhNO}), **7.24-7.21** (m, 2H, Ph_{PhNO}), **6.93-6.90** (m, 1H, Ph_{PhNO}), **6.62** (d, $^3J_{HH}$ = 5.2 Hz, 1H, H-2), **5.60** (s, 2H, β-H), **5.57** (d, $^3J_{HH}$ = 2.8 Hz, 2H, β-H), **5.56** (d, $^3J_{HH}$ = 2.8 Hz, 2H, β-H), **1.69** (s, 6H, α-Me), **1.57** (s, 6H, α-Me), **1.42** (s, 6H, α-Me), **1.21** (s, 6H, α-Me).

^{13}C{^{1}H} NMR (151 MHz, CD_2Cl_2, 295 K), δ [ppm] = **161.2** (s, CH, C-3), **157.9** (s, C_q, C-1), **149.0** (s, C_q, C_q-pyrrole), **148.3** (s, C_q, C_q-pyrrole), **147.4** (s, C_q, C_q-pyrrole), **136.1** (d, $^4J_{CP}$ = 3.0 Hz, CH, PPh_4^+), **134.7** (d, $^2J_{CP}$ = 10.6 Hz, CH, PPh_4^+), **131.0** (d, $^3J_{CP}$ = 13.6 Hz, CH, PPh_4^+), **129.0** (s, CH, Ph_{PhNO}), **122.3** (s, CH, Ph_{PhNO}), **120.8** (s, CH, C-2), **117.8** (d, $^1J_{CP}$ = 90.6 Hz, C_q, PPh_4^+), **116.6** (CH, Ph_{PhNO}), **102.0** (s, CH, β-C), **100.0** (s, CH, β-C), **99.2** (s, CH, β-C), **81.3** (s, C_q, C-4), **46.2** (s, C_q, α-C), **37.3** (s, C_q, α-C), **37.0** (s, CH_3, α-Me), **32.2** (s, CH_3, α-Me), **30.0** (s, CH_3, α-Me), **27.0** (s, CH_3, α-Me).

The constitution of the compound as shown was unambiguously confirmed by SCXRD measurements (cf. **Chapter 7.4***).*

Deprotonation of *meso*-octamethylcalix[4]pyrrole to give its tetrasodium salt ($Na_4(thf)_4$[**69**])[129, 149]

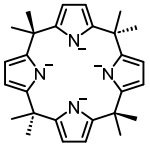

Procedure. *meso*-Octamethylcalix[4]pyrrole (**19**, 1.0 g, 2.33 mmol, 1.0 equiv.) was dissolved in THF (20 mL) in a Schlenk tube. Sodium bis(trimethylsilyl)amide (1 M solution in THF, 9.6 mL, 9.57 mmol, 4.1 equiv.) was added dropwise to the rapidly stirring solution within 5 min at room temperature. After approximately four fifths of the solution were added, a colorless precipitate formed. The reaction was stirred for 1 h at room temperature after complete addition. The mixture was filtered over a fritted glass filter inside a nitrogen-filled glovebox. The obtained solid was washed with THF (3 × 7 mL). Drying for 30 min under reduced pressure afforded the desired product as a colorless solid (1.8 g, 2.25 mmol, 95% yield). The acquired ^{1}H NMR spectrum showed the presence of four equivalents of THF as well as slight contamination. The material was found sufficient for subsequent usage.

^{1}H NMR (600 MHz, DMSO-d_6, 295 K): δ [ppm] = **5.38** (s, 8H, β-H), **3.65-3.58** (m, 4 × 4H, THF), **1.80-1.74** (m, 4 × 4H, THF), **1.32** (s, 24H, α-Me).

^{13}C{^{1}H} NMR (151 MHz, DMSO-d_6, 295 K): δ [ppm] = **148.8** (s, C_q, C_q-pyrrole), **96.5** (s, CH, β-C), **67.0** (s, CH, THF), **38.3** (s, C_q, α-C), **33.1** (s, CH_3, α-Me), **25.2** (s, CH, THF).

Deprotonation of *meso*-octaethylcalix[4]pyrrole to give its tetrasodium salt ($Na_4(thf)_4$[**70**])[129, 149]

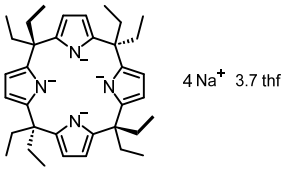

Procedure. *meso*-Octaethylcalix[4]pyrrole (600.0 mg, 1.11 mmol, 1.0 equiv.) was dissolved in THF (6 mL) in a Schlenk tube. Sodium bis(trimethylsilyl)amide (1 M solution in THF, 4.6 mL, 4.55 mmol, 4.1 equiv.) was added dropwise to the rapidly stirring solution within 5 min at room temperature. The clear solution was stirred for 1 h at room temperature, and the solvent was evaporated under reduced pressure. The obtained solid was suspended in *n*-hexane (6 mL) and was filtered over a fritted glass filter inside a nitrogen-filled glovebox. The obtained solid was washed with *n*-hexane (4 × 4 mL). Further purification was achieved by dissolving the entire material in THF (5 mL) and subsequent precipitation with *n*-pentane (approximately 80 mL). The solid was isolated by filtration using a fritted glass filter. After drying *in vacuo* for 30 min, the desired product was obtained as colorless solid (566.0 mg, 0.63 mmol, 57% yield). The acquired ^{1}H NMR spectrum showed the presence of 3.7 equivalents of THF as well as slight contamination. The material was found sufficient for subsequent usage.

^{1}H NMR (600 MHz, DMSO-d_6, 295 K): δ [ppm] = **5.35** (s, 8H, β-H), **3.63-3.56** (m, 3.7 × 4H, THF), **1.80-1.73** (m, 3.7 × 4H, THF), **1.65** (br q, $^3J_{HH}$ = 6.7 Hz, 16H, α-methylene), **0.45** (t, $^3J_{HH}$ = 6.7 Hz, 24H, α-Me).

^{13}C{^{1}H} NMR (151 MHz, DMSO-d_6, 295 K): δ [ppm] = **147.7** (s, C_q, C_q-pyrrole), **97.2** (s, CH, β-C), **67.0** (s, CH, THF), **45.4** (s, C_q, α-C), **28.7** (s, CH_2, α-methylene), **25.2** (s, CH, THF), **9.3** (s, CH_3, α-Me).

Tetraphenylphosphonium tetrachloridogallate(III) ([PPh_4][$GaCl_4$])[149, 269]

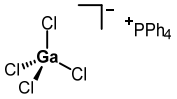

Procedure. Gallium trichloride (1.0 g, 5.68 mmol, 1.0 equiv.) was dissolved in ice-cold concentrated hydrochloric acid (35 mL). Next, a solution of dry tetraphenylphosphonium chloride (2.1 g, 5.68 mmol, 1.0 equiv.) in ethanol (25 mL) was added. This caused the immediate precipitation of a colorless solid. The mixture was stirred for 10 min at room temperature. The solid was isolated by filtration using a Büchner funnel. It was washed with ethanol (in total 60 mL over several washing steps) and diethyl ether (in total 40 mL over several washing steps). The product was obtained as a colorless solid after drying *in vacuo* (2.9 g, 5.20 mmol, 92% yield).

^{1}H NMR (600 MHz, CD_2Cl_2, 295 K): δ [ppm] = **7.96-7.90** (m, 4H, PPh_4^+), **7.80-7.72** (m, 8H, PPh_4^+), **7.66-7.59** (m, 8H, PPh_4^+).

^{13}C{^{1}H} NMR (151 MHz, CD_2Cl_2, 295 K), δ [ppm] = **136.1** (d, CH, $^{4}J_{CP}$ = 3.0 Hz, PPh_4^+), **134.8** (d, CH, $^{2}J_{CP}$ = 10.3 Hz, PPh_4^+), **131.0** (d, CH, $^{3}J_{CP}$ = 12.9 Hz, PPh_4^+), **117.9** (d, C_q, $^{1}J_{CP}$ = 89.7 Hz, PPh_4^+).

^{31}P{^{1}H} NMR (243 MHz, CD_2Cl_2, 295 K), δ [ppm] = **23.3** (s, PPh_4^+).

^{71}Ga{^{1}H} NMR (183 MHz, CD_2Cl_2, 295 K), δ [ppm] = **250.9** (s, $GaCl_4^-$).

Tetraphenylphosphonium *meso*-octamethylcalix[4]pyrrolato gallate ([PPh_4][**71**])[149]

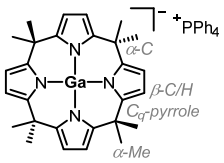

Procedure. In a nitrogen-filled glovebox, the tetrasodium salt of deprotonated *meso*-octamethylcalix[4]pyrrole ($Na_4(thf)_4$[**69**], 500.0 mg, 0.62 mmol, 1.0 equiv.) was dissolved in 1,2-dimethoxyethane (DME, 5 mL). Tetraphenylphosphonium tetrachloridogallate ([PPh_4][$GaCl_4$], 332.0 mg, 0.60 mmol, 0.97 equiv.) was added in one portion at room temperature. The reaction mixture turned intensively red. It was stirred for 3 h at room temperature. Over time, the color changed to pale orange, and a colorless precipitate formed. The solid was separated from the orange solution by filtration over a fritted glass filter. It was washed with DME (3 × 2 mL) and *n*-pentane (2 × 2 mL) and was subsequently suspended in CH_2Cl_2 (5 mL). The suspension was stirred for 5 min at room temperature. It was filtered over a fritted glass filter covered with a pad of celite to remove NaCl. The product was isolated from its CH_2Cl_2 solution by precipitation with *n*-pentane (approximately 20 mL) and subsequent filtration. After drying *in vacuo,* it was obtained as a pale rose solid (390.0 mg, 0.43 mmol, 69% yield). The material was found to contain 0.9 equivalents of CH_2Cl_2 as determined by ^{1}H NMR spectroscopy using $CDCl_3$ as solvent. This is consistent with the obtained result from the elemental analysis. The CH_2Cl_2 content was considered for stoichiometric calculations.

Single crystals for SCXRD measurements were obtained at −40 °C from a CH_2Cl_2/*n*-pentane solution. The THF adduct of the gallate ([PPh_4][**74**]) crystallized from THF-d_8 at room temperature.

^{1}H NMR (600 MHz, CD_2Cl_2, 295 K), δ [ppm] = **7.89-7.84** (m, 4H, PPh_4^+), **7.72-7.66** (m, 8H, PPh_4^+), **7.60-7.53** (m, 8H, PPh_4^+), **5.79** (s, 8H, β-H), **1.65** (s, 12H, α-Me), **1.46** (s, 12H, α-Me).

^{13}C{^{1}H} NMR (151 MHz, CD_2Cl_2, 295 K), δ [ppm] = **146.2** (s, C_q, C_q-pyrrole), **136.2** (d, $^4J_{CP}$ = 3.0 Hz, CH, PPh_4^+), **134.8** (d, $^2J_{CP}$ = 10.3 Hz, CH, PPh_4^+), **131.0** (d, $^3J_{CP}$ = 12.9 Hz, CH, PPh_4^+), **117.8** (d, $^1J_{CP}$ = 89.6 Hz, C_q, PPh_4^+), **100.7** (s, CH, β-C), **42.4** (s, C_q, α-C), **35.6** (s, CH_3, α-Me), **25.0** (s, CH_3, α-Me).

^{31}P{^{1}H} NMR (162 MHz, CD_2Cl_2, 295 K), δ [ppm] = **23.2** (s, PPh_4^+).

HR-MS (ESI, negative ion mode): *m/z* calculated for $C_{28}H_{32}{}^{69}GaN_4$ $[M]^-$: **493.1888**, found: **493.1877**.

FT-ATR-IR (solid state, room temperature), $\tilde{\nu}_{max}$ [cm^{-1}] = **3094** (w), **3040** (w), **2966** (m), **2937** (m), **2902** (m), **2867** (w), **2840** (w), **1613** (w), **1587** (w), **1485** (m), **1460** (w), **1435** (s), **1371** (s), **1348** (s), **1316** (w), **1303** (w), **1278** (s), **1263** (s), **1224** (m), **1213** (m), **1190** (w), **1153** (s), **1107** (s), **1064** (s), **994** (m), **929** (w), **890** (w), **854** (w), **807** (w), **756** (s), **723** (s), **688** (s).

Elemental analysis. calc. **C 69.81**, **H 5.96**, **N 6.16** ($[PPh_4][$**71**$] \cdot 0.9\ CH_2Cl_2$), found: **C 69.80**, **H 5.71**, **N 6.59** (content of CH_2Cl_2 was verified by ^1H NMR spectroscopy in $CDCl_3$).

The constitution of the compound as shown was unambiguously confirmed by SCXRD measurements (cf. **Chapter 7.4***).*

Tetraphenylphosphonium *meso*-octaethylcalix[4]pyrrolato gallate ([PPh_4][**72**])[149]

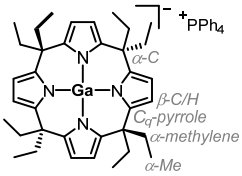

Procedure. In a nitrogen-filled glovebox, the tetrasodium salt of deprotonated *meso*-octaethylcalix[4]pyrrole ($Na_4(thf)_4$[**70**], 200.0 mg, 0.22 mmol, 1.0 equiv.) was dissolved in 1,2-dimethoxyethane (DME, 2 mL). Tetraphenylphosphonium tetrachloridogallate ([PPh_4][$GaCl_4$], 119.0 mg, 0.22 mmol, 0.97 equiv.) was added in one portion at room temperature. The reaction mixture turned intensively red. It was stirred for 3 h at room temperature. Over time, the color changed to pale orange, and a colorless precipitate formed. The solid was separated from the orange solution by filtration over a fritted glass filter. It was washed with DME (3 × 0.5 mL) and *n*-pentane (2 × 1 mL) and was subsequently suspended in CH_2Cl_2 (3 mL). The suspension was stirred for 5 min at room temperature. It was filtered over a fritted glass filter covered with a pad of celite to remove NaCl. The product was isolated from its CH_2Cl_2 solution by precipitation with *n*-pentane (approximately 20 mL) and subsequent filtration. After drying *in vacuo,* it was obtained as a slightly pale rose solid (120.0 mg, 0.13 mmol, 57% yield).

Single crystals for SCXRD measurements were obtained at −40 °C from a CH_2Cl_2/*n*-pentane solution.

^{1}H NMR (600 MHz, CD_2Cl_2, 295 K), δ [ppm] = **7.90-7.84** (m, 4H, PPh_4^+), **7.73-7.66** (m, 8H, PPh_4^+), **7.61-7.53** (m, 8H, PPh_4^+), **5.77** (s, 8H, β-H), **2.04** (q, $^3J_{HH}$ = 7.3 Hz, 8H, α-methylene), **1.48** (q, $^3J_{HH}$ = 7.2 Hz, 8H, α-methylene), **1.07** (t, $^3J_{HH}$ = 7.2 Hz, 12H, α-Me), **0.52** (t, $^3J_{HH}$ = 7.2 Hz, 12H, α-Me).

^{13}C{^{1}H} NMR (151 MHz, CD_2Cl_2, 295 K), δ [ppm] = **143.2** (s, C_q, C_q-pyrrole), **136.2** (d, $^4J_{CP}$ = 3.0 Hz, CH, PPh_4^+), **134.7** (d, $^2J_{CP}$ = 10.3 Hz, CH, PPh_4^+), **131.0** (d, $^3J_{CP}$ = 12.9 Hz, CH, PPh_4^+), **117.8** (d, $^1J_{CP}$ = 89.6 Hz, C_q, PPh_4^+), **102.4** (s, CH, β-C), **44.5** (s, C, α-methylene), **43.7** (s, C_q, α-C), **27.4** (s, CH_2, α-methylene), **10.5** (s, CH_3, α-Me), **10.2** (s, CH_3, α-Me).

^{31}P{^{1}H} NMR (243 MHz, CD_2Cl_2, 295 K), δ [ppm] = **23.3** (s, PPh_4^+).

HR-MS (ESI, negative ion mode): *m/z* calculated for $C_{36}H_{48}{}^{69}GaN_4$ $[M]^-$: **605.3135**, found: **605.3154**.

FT-ATR-IR (solid state, room temperature), $\tilde{\nu}_{max}$ [cm^{-1}] = **3087** (w), **3056** (w), **2959** (m), **2923** (m), **2869** (m), **2834** (w), **1587** (m), **1483** (m), **1454** (m), **1439** (s), **1374** (s), **1319** (s), **1292** (m), **1246** (m), **1188** (w), **1149** (m), **1108** (s), **1073** (s), **1026** (m), **996** (m), **971** (m), **924** (m), **883** (m), **858** (m), **749** (s), **719** (s), **688** (s).

Elemental analysis. calc. **C 76.19**, **H 7.25**, **N 5.92**, found: **C 76.08**, **H 7.04**, **N 5.96**.

The constitution of the compound as shown was unambiguously confirmed by SCXRD measurements (cf. **Chapter 7.4***).*

Fluoride adduct of *meso*-octamethylcalix[4]pyrrolato gallate ([PPh_4][*n*-Bu_4N][**73**])[149]

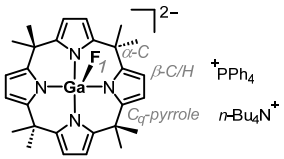

Procedure. In a nitrogen-filled glovebox, tetraphenylphosphonium *meso*-octamethylcalix[4]pyrrolato gallate ([PPh_4][**71**], 15.0 mg, 16.5 µmol, 1.0 equiv., including 0.9 equivalents of CH_2Cl_2) and tetrabutylammonium difluorotriphenylsilicate (TBAT, 8.9 mg, 16.5 µmol, 1.0 equiv.) were placed in a 10 mL snap cap vial and were dissolved in acetonitrile (1 mL) at room temperature. A pale-orange solution was obtained, which was stirred at room temperature for 4 h. Diethyl ether (3 mL) was added. Upon further addition of *n*-pentane (10 mL) an orange oil formed, which was separated by centrifugation. The clear and colorless supernatant was removed. The oil was washed with *n*-pentane (4 × 1 mL), what transformed it into a dark-orange, sticky solid. Drying under reduced pressure over night at room temperature gave the desired product as an orange solid ([PPh_4][*n*-Bu_4N][**73**], 14.6 mg, 13.3 µmol, 80% yield).

A sample for mass spectrometry was prepared by mixing *meso*-octamethylcalix[4]pyrrolato gallate ([PPh_4][**71**], 7.0 mg, 7.7 µmol, 1.0 equiv., including 0.9 equivalents of CH_2Cl_2) and tetrabutylammonium difluorotriphenylsilicate (12.5 mg, 23.1 µmol, 3.0 equiv.) in CH_2Cl_2 (0.5 mL). This solution was diluted with CH_2Cl_2 to approximately reach a concentration of $c = 10^{-5}$ mol L^{-1} and was subsequently analyzed. However, it was later noted that the fluoride adduct of [**71**]$^-$ is significantly more stable in acetonitrile.

^{1}H NMR (600 MHz, CD_3CN, 295 K), δ [ppm] = **7.93-7.87** (m, 4H, PPh_4^+), **7.76-7.70** (m, 8H, PPh_4^+), **7.70-7.63** (m, 8H, PPh_4^+), **5.66** (d, $^3J_{HH}$ = 2.9 Hz, 4H, β-H), **5.61** (d, $^3J_{HH}$ = 2.9 Hz, 4H, β-H), **3.12-3.03** (m, 8H, *n*-Bu_4N^+), **1.74** (d, J_{FH} = 3.1 Hz, 6H, α-Me), **1.64-1.56** (m, 8H, *n*-Bu_4N^+), **1.61** (s, 6H, α-Me), **1.60** (s, 6H, α-Me), **1.36** (tq, $^3J_{HH}$ = 7.4, 7.4 Hz, 8H, *n*-Bu_4N^+), **1.22** (s, 6H, α-Me), **0.97** (t, $^3J_{HH}$ = 7.4 Hz, 12H, *n*-Bu_4N^+).

$^{13}C\{^1H\}$ NMR (151 MHz, CD_3CN, 295 K), δ [ppm] = **148.0** (s, C_q, C_q-pyrrole), **145.9** (s, C_q, C_q-pyrrole), **136.4** (d, $^4J_{CP}$ = 3.0 Hz, CH, PPh_4^+), **135.7** (d, $^2J_{CP}$ = 10.4 Hz, CH, PPh_4^+), **131.3** (d, $^3J_{CP}$ = 12.9 Hz, CH, PPh_4^+), **118.9** (d, $^1J_{CP}$ = 89.7 Hz, C_q, PPh_4^+), **100.2** (s, CH, β-C), **98.6** (s, CH, β-C), **59.3** (t, CH_2, $^1J_{CN}$ = 2.9 Hz, *n*-Bu_4N^+), **42.0** (s, CH_3, α-Me), **36.8** (s, C_q, α-C), **36.6** (d, CH_3, J_{CF} = 18.3 Hz, α-Me), **36.4** (s, C_q, α-C), **31.7** (s, CH_3, α-Me), **26.9** (s, CH_3, α-Me), **24.3** (s, CH_2, *n*-Bu_4N^+), **20.3** (t, CH_2, $^3J_{CN}$ = 1.5 Hz, *n*-Bu_4N^+), **13.8** (s, CH_3, *n*-Bu_4N^+).

^{19}F NMR (376 MHz, CD_3CN, 295 K), δ [ppm] = −**146.4** (br s, F-1).

$^{31}P\{^1H\}$ NMR (243 MHz, CD_3CN, 295 K), δ [ppm] = **22.9** (s, PPh_4^+).

HR-MS (ESI, negative ion mode): *m/z* calculated for $C_{28}H_{35}F^{69}GaN_4O$ $[M+H_3O]^-$: **531.2056**, found: **531.2075**.

Addition product of carbon dioxide to *meso*-octamethylcalix[4]pyrrolato gallate ([PPh_4][**75**])[149]

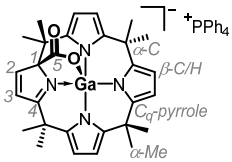

Procedure. In a nitrogen-filled glovebox, tetraphenylphosphonium *meso*-octamethylcalix[4]pyrrolato gallate ([PPh_4][**71**], 15.0 mg) was placed in a J. Young NMR pressure tube and was dissolved in CD_2Cl_2 (0.5 mL). To the sample, gaseous CO_2 (5 bar) was applied at room temperature. The reaction mixture was shaken with a rocking shaker at room temperature for 10 h. Over the course of the reaction, the color of the solution turned to yellow. The sample was analyzed by NMR spectroscopy and mass spectrometry. The ratio between free [**71**]$^-$ and [**75**]$^-$ under the reaction conditions was determined to 1:24 by ^{1}H NMR spectroscopy.

CO_2 elimination procedure. The pressure was released from the sample, CH_2Cl_2 (1 mL) was added, and the solution was transferred by syringe to a normal J. Young NMR tube. The open NMR tube was placed inside a large Schlenk flask. The solvent was slowly evaporated at room temperature over the course of several hours. The obtained solid was kept under static vacuum overnight at room temperature and was analyzed by NMR spectroscopy. A 1:1 ratio between free [**71**]$^-$ and [**75**]$^-$ was observed. Subsequently, this process was repeated twice to achieve quantitative CO_2 removal as found by ^{1}H NMR spectroscopy.

^{1}H NMR (600 MHz, CD_2Cl_2, 295 K), δ [ppm] = **7.87-7.80** (m, 4H, [PPh_4]$^+$), **7.71-7.63** (m, 8H, PPh_4^+), **7.65** (1H, H-2, identified by ^{1}H,^{1}H COSY NMR spectroscopy, expected multiplicity is d), **7.60-7.53** (m, 8H, PPh_4^+), **6.64** (d, $^3J_{HH}$ = 5.0 Hz, 1H, H-3), **5.94** (d, $^3J_{HH}$ = 3.1 Hz, 1H, β-H), **5.91** (d, $^3J_{HH}$ = 3.1 Hz, 1H, β-H), **5.84** (d, $^3J_{HH}$ = 3.1 Hz, 1H, β-H), **5.81** (d, $^3J_{HH}$ = 3.1 Hz, 1H, β-H), **5.79** (d, $^3J_{HH}$ = 3.0 Hz, 1H, β-H), **5.77** (d, $^3J_{HH}$ = 3.0 Hz, 1H, β-H), **1.79** (s, 3H, α-Me), **1.78** (s, 3H, α-Me), **1.68** (s, 3H, α-Me), **1.66** (s, 3H, α-Me), **1.60** (s, 3H, α-Me), **1.38** (s, 3H, α-Me), **1.36** (s, 3H, α-Me), **0.95** (s, 3H, α-Me).

$^{13}C\{^1H\}$ NMR (151 MHz, CD_2Cl_2, 295 K), δ [ppm] = **184.8** (s, C_q, C-4), **168.0** (s, C_q, C-5), **158.1** (s, CH, C-2), **149.0** (s, C_q, C_q-pyrrole), **148.3** (s, C_q, C_q-pyrrole), **146.2** (s, C_q, C_q-pyrrole), **146.1** (s, C_q, C_q-pyrrole), **145.6** (s, C_q, C_q-pyrrole), **140.0** (s, C_q, C_q-pyrrole), **136.2** (d, $^4J_{CP}$ = 3.0 Hz, CH, PPh_4^+), **134.8** (d, $^2J_{CP}$ = 10.3 Hz, CH, PPh_4^+), **131.0** (d, $^3J_{CP}$ = 12.9 Hz, CH, PPh_4^+), **126.6** (s, CH, C-3), **117.9** (d, $^1J_{CP}$ = 89.6 Hz, C_q, PPh_4^+), **104.2** (s, CH, β-C), **102.5** (s, CH, β-C), **102.1** (s, CH, β-C), **101.9** (s, CH, β-C), **101.8** (s, CH, β-C), **100.1** (s, CH, β-C), **97.2** (s, C_q, C-1), **44.1** (s, C_q, α-C), **40.8** (s, CH_3, α-Me), **38.5** (s, C_q, α-C), **36.4** (s, C_q, α-C), **36.14** (s, CH_3, α-Me), **36.10** (s, C_q, α-C), **35.9** (s, CH_3, α-Me), **27.4** (s, CH_3, α-Me), **27.2** (s, CH_3, α-Me), **26.8** (s, CH_3, α-Me), **26.6** (s, CH_3, α-Me), **24.1** (s, CH_3, α-Me).

$^{31}P\{^1H\}$ NMR (243 MHz, CD_2Cl_2, 295 K), δ [ppm] = **23.2** (s, PPh_4^+).

HR-MS (ESI, negative ion mode): *m/z* calculated for $C_{29}H_{32}{}^{69}GaN_4O_2$ $[M]^-$: **537.1781**, found: **537.1769**.

Addition product of carbon dioxide to *meso*-octaethylcalix[4]pyrrolato gallate ([PPh$_4$][**76**])[149]

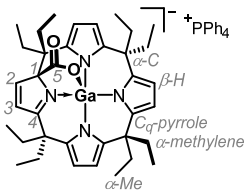

Procedure. In a nitrogen-filled glovebox, tetraphenylphosphonium *meso*-octaethylcalix[4]pyrrolato gallate ([PPh$_4$][**71**], 15.0 mg) was placed in a J. Young NMR pressure tube and was dissolved in CD_2Cl_2 (0.5 mL). To the sample, gaseous CO_2 (5 bar) was applied. The reaction mixture was shaken with a rocking shaker at room temperature for 10 h. Over the course of the reaction, the color of the solution turned to yellow. The sample was analyzed by NMR spectroscopy. The ratio between free [**71**]$^-$ and [**76**]$^-$ under the reaction conditions was determined to 2:1 by ^{1}H NMR spectroscopy. Detection of the addition product by mass spectrometry was not possible.

CO_2 elimination procedure. The pressure was released from the sample, CH_2Cl_2 (1 mL) was added, and the solution was transferred by syringe to a normal J. Young NMR tube. The open NMR tube was placed inside a large Schlenk flask. The solvent was slowly evaporated under reduced pressure over the course of several hours at room temperature. The obtained solid was kept under static vacuum overnight at room temperature and was subsequently analyzed by ^{1}H NMR spectroscopy. Quantitative CO_2 removal was found.

^{1}H NMR (600 MHz, CD_2Cl_2, 295 K), δ [ppm] = **7.89-7.82** (m, 4H, PPh_4^+), **7.77** (d, $^3J_{HH}$ = 5.1 Hz, 1H, H-2), **7.72-7.65** (m, 8H, PPh_4^+), **7.60-7.53** (m, 8H, PPh_4^+), **6.54** (d, $^3J_{HH}$ = 5.1 Hz, 1H, H-3), **5.95** (d, $^3J_{HH}$ = 3.3 Hz, 1H, β-H), **5.89** (d, $^3J_{HH}$ = 3.1 Hz, 1H, β-H), **5.85** (d, $^3J_{HH}$ = 3.2 Hz, 1H, β-H), **5.81** (d, $^3J_{HH}$ = 3.0 Hz, 1H, β-H), **5.76** (d, $^3J_{HH}$ = 3.1 Hz, 1H, β-H), **5.74** (d, $^3J_{HH}$ = 3.0 Hz, 1H, β-H). Evaluation of the signals of the ethyl groups was not fully possible due to signal overlapping (with unreacted [**71**]$^-$) and diastereotopicity of the methylene protons. Six of the eight methyl triplets were well resolved: **1.03** (t, $^3J_{HH}$ = 7.4 Hz, 3H, α-Me), **1.00** (t, $^3J_{HH}$ = 7.3 Hz, 3H, α-Me), **0.65** (t, $^3J_{HH}$ = 7.3 Hz, 3H, α-Me), **0.56** (t, $^3J_{HH}$ = 7.4 Hz, 3H, α-Me), **0.48** (t, $^3J_{HH}$ = 7.4 Hz, 3H, α-Me), **0.39** (t, $^3J_{HH}$ = 7.3 Hz, 3H, α-Me).

$^{13}C\{^1H\}$, NMR (151 MHz, CD_2Cl_2, 295 K), Due to the low concentration of [**76**]$^-$, complete characterization by $^{13}C\{^1H\}$ NMR spectroscopy was not possible. Only the well resolved and reliably assignable signals are listed. Some of them were identified by two-dimensional experiments. δ [ppm] = **184.6** (s, C_q, C-4), **168.6** (s, C_q, C-5), **158.6** (s, CH, C-2), **126.5** (s, CH, C-3), **105.0** (s, CH, β-C), **104.5** (s, CH, β-C), **103.5** (s, CH, β-C), **103.5** (s, CH, β-C), **102.4** (s, CH, β-C), **101.4** (s, CH, β-C), **97.3** (s, C_q, C-1), **11.1** (s, CH_3, α-Me), **11.0** (s, CH_3, α-Me), **10.7** (s, CH_3, α-Me), **10.0** (s, CH_3, α-Me), **9.7** (s, CH_3, α-Me), **9.1** (s, CH_3, α-Me), **8.7** (s, CH_3, α-Me).

$^{31}P\{^1H\}$ NMR (243 MHz, CD_2Cl_2, 295 K), δ [ppm] = **23.2** (s, PPh_4^+).

A mass spectrum of [**76**]$^-$ *was not collected due to very weak binding of* CO_2 *to the gallate.*

Reaction of *meso*-octamethylcalix[4]pyrrolato gallate ([PPh_4][**71**]) with $HNTf_2$ in THF-d_8[149]

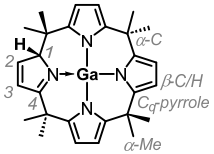

Dissolved in THF-d_8

Procedure. In a nitrogen-filled glovebox, tetraphenylphosphonium *meso*-octamethylcalix[4]pyrrolato gallate ([PPh_4][**71**], 10.0 mg, 11.0 µmol, 1.0 equiv., including 0.9 equivalents of CH_2Cl_2) and bis(trifluoromethyl)sulfonimide ($HNTf_2$, 3.0 mg, 10.7 µmol, 0.97 equiv.) were placed in a J. Young NMR tube. THF-d_8 (0.5 mL) was added at room temperature, the sample was closed and was vigorously shaken. A yellow solution was obtained which was analyzed by NMR spectroscopy.

^{1}H NMR (600 MHz, THF-d_8, 295 K), δ [ppm] = **7.95-7.90** (m, 4H, $[PPh_4]^+$), **7.85** (d, $^3J_{HH}$ = 5.4 Hz, 1H, H-2), **7.80-7.74** (m, 16H, PPh_4^+), **7.18** (dd, $^3J_{HH}$ = 5.4 Hz, $^4J_{HH}$ = 1.3 Hz, 1H, H-3), **6.08** (d, $^3J_{HH}$ = 3.3 Hz, 1H, β-H), **5.96** (d, $^3J_{HH}$ = 3.3 Hz, 1H, β-H), **5.95** (d, $^3J_{HH}$ = 3.2 Hz, 1H, β-H), **5.92** (d, $^3J_{HH}$ = 3.2 Hz, 1H, β-H), **5.81** (d, $^3J_{HH}$ = 3.1 Hz, 1H, β-H), **5.79** (d, $^3J_{HH}$ = 3.1 Hz, 1H, β-H), **5.02** (s, 1H, H-1), **1.77** (s, 3H, α-Me), **1.65** (s, 2 × 3H, α-Me), **1.56** (s, 3H, α-Me), **1.51** (s, 3H, α-Me), **1.47** (s, 3H, α-Me), **1.43** (s, 3H, α-Me), **0.86** (s, 3H, α-Me).

^{13}C{^{1}H} NMR (151 MHz, THF-d_8, 295 K), δ [ppm] = **190.3** (s, C_q, C-4), **156.6** (s, CH, C-2), **150.0** (s, C_q, C_q-pyrrole), **149.5** (s, C_q, C_q-pyrrole), **147.3** (s, C_q, C_q-pyrrole), **145.6** (s, C_q, C_q-pyrrole), **145.5** (s, C_q, C_q-pyrrole), **141.3** (s, C_q, C_q-pyrrole), **136.1** (d, $^4J_{CP}$ = 3.1 Hz, CH, PPh_4^+), **135.5** (d, $^2J_{CP}$ = 10.4 Hz, CH, PPh_4^+), **131.2** (d, $^3J_{CP}$ = 12.9 Hz, CH, PPh_4^+), **129.5** (s, CH, C-3), **121.0** (q, $^1J_{CF}$ = 322.4 Hz, C_q, NTf_2^-, the outer two peaks of the quartet were only barely visible), **118.9** (d, $^1J_{CP}$ = 89.5 Hz, C_q, PPh_4^+), **106.4** (s, CH, β-C), **103.8** (s, CH, β-C), **103.8** (s, CH, β-C), **103.6** (s, CH, β-C), **102.1** (s, 2 × CH, β-C), **87.6** (s, CH, C-1), **39.8** (s, C_q, α-C), **39.3** (s, C_q, α-C), **36.5** (s, C_q, α-C), **36.4** (s, C_q, α-C), **36.2** (s, CH_3, α-Me), **35.0** (s, CH_3, α-Me), **33.91** (s, CH_3, α-Me), **33.87** (s, CH_3, α-Me), **31.9** (s, CH_3, α-Me), **29.5** (s, CH_3, α-Me), **28.3** (s, CH_3, α-Me), **24.8** (s, CH_3, α-Me).

^{19}F NMR (188 MHz, THF-d_8, 295 K), δ [ppm] = −**79.9** (s, NTf_2^-).

^{31}P{^{1}H} NMR (243 MHz, THF-d_8, 295 K), δ [ppm] = **21.1** (s, PPh_4^+).

The ^{1}H,^{1}H COSY NMR spectrum showed characteristic cross peaks between the signals at 5.02 (transferred proton) and 7.18 ppm (H-3) and between the signals at 7.18 (H-3) and 7.85 ppm (H-2).

Reaction of *meso*-octamethylcalix[4]pyrrolato gallate ([PPh_4][**71**]) with $HNTf_2$ in CD_2Cl_2/diethyl ether (2:1 %vol)[149]

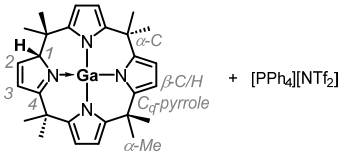

Dissolved in CD_2Cl_2 / Et_2O (2:1 %vol)

Procedure. In a nitrogen-filled glovebox, tetraphenylphosphonium *meso*-octamethyl-calix[4]pyrrolato gallate (10.0 mg, 11.0 µmol, 1.0 equiv., including 0.9 equivalents of CH_2Cl_2) were suspended in a mixture of CD_2Cl_2 and diethyl ether (2:1 %vol, 0.5 mL) in a 1 mL vial. bis(Trifluoromethyl)sulfonimide ($HNTf_2$, 2.8 mg, 10.66 µmol, 0.9 equiv.) was dissolved in the same solvent mixture (0.3 mL). The $HNTf_2$ solution was dropwise added to the gallate suspension over the course of 5 min at room temperature while shaking the latter. The reaction mixture turned yellow. It was filtered into a J. Young NMR tube and was analyzed by NMR spectroscopy.

^{1}H NMR (600 MHz, CD_2Cl_2 / Et_2O (2:1 %vol), 295 K), spectrum was calibrated with the signal of $CHDCl_2$ to 5.32 ppm, δ [ppm] = **7.92-7.86** (m, 4H, PPh_4^+), **7.77-7.71** (m, 8H, PPh_4^+), **7.73** (1H, H-2, identified by ^{1}H,^{1}H COSY NMR spectroscopy, expected multiplicity is d), **7.66-7.59** (m, 8H, PPh_4^+), **7.05** (dd, $^3J_{HH}$ = 5.4 Hz, $^4J_{HH}$ = 1.3 Hz, 1H, H-3), **6.14** (d, $^3J_{HH}$ = 3.3 Hz, 1H, β-H), **6.05** (d, $^3J_{HH}$ = 3.3 Hz, 1H, β-H), **6.03** (d, $^3J_{HH}$ = 3.3 Hz, 1H, β-H), **6.00** (d, $^3J_{HH}$ = 3.2 Hz, 1H, β-H), **5.90** (s, 2 × 1H, β-H), **4.91** (s, 1H, H-1), **1.82** (s, 3H, α-Me), **1.63** (s, 3H, α-Me), **1.574** (s, 3H, α-Me), **1.568** (s, 3H, α-Me), **1.52** (s, 3H, α-Me), **1.46** (s, 3H, α-Me), **1.44** (s, 3H, α-Me), **0.81** (s, 3H, α-Me).

$^{13}C\{^1H\}$ NMR (151 MHz, CD_2Cl_2 / Et_2O (2:1 %vol), 295 K), spectrum was calibrated with the signal of CD_2Cl_2 to 53.84 ppm, δ [ppm] = **190.0** (s, C_q, C-4), **156.6** (s, CH, C-2), **151.1** (s, C_q, C_q-pyrrole), **150.7** (s, C_q, C_q-pyrrole), **148.3** (s, C_q, C_q-pyrrole), **146.0** (s, C_q, C_q-pyrrole), **145.3** (s, C_q, C_q-pyrrole), **141.4** (s, C_q, C_q-pyrrole), **136.4** (d, $^4J_{CP}$ = 3.1 Hz, CH, PPh_4^+), **135.1** (d, $^2J_{CP}$ = 10.3 Hz, CH, PPh_4^+), **131.3** (d, $^3J_{CP}$ = 12.9 Hz, CH, PPh_4^+), **129.8** (s, CH, C-3), **120.6** (q, $^1J_{CF}$ = 321.2 Hz, C_q, NTf_2^-, the outer two peaks of the quartet were only barely visible), **118.3** (d, $^1J_{CP}$ = 89.7 Hz, C_q, PPh_4^+), **106.9** (s, CH, β-C), **104.7** (s, CH, β-C), **104.4** (s, CH, β-C), **104.1** (s, CH, β-C), **102.8** (s, CH, β-C), **102.4** (s, CH, β-C), **87.4** (s, CH, C-1), **42.7** (s, CH, α-Me), **40.5** (s, C_q, α-C), **39.1** (s, C_q, α-C), **37.5** (s, CH, α-Me), **36.43** (s, C_q, α-C), **36.38** (s, C_q, α-C), **35.5** (s, CH, α-Me), **32.2** (s, CH, α-Me), **31.7** (s, CH, α-Me), **26.7** (s, CH, α-Me), **25.3** (s, CH, α-Me), **25.2** (s, CH, α-Me).

^{19}F NMR (376 MHz, CD_2Cl_2 / Et_2O (2:1 %vol), 295 K), δ [ppm] = **−79.8** (s, NTf_2^-).

$^{31}P\{^1H\}$ NMR (243 MHz, CD_2Cl_2 / Et_2O (2:1 %vol), 295 K), δ [ppm] = **23.2** (s, PPh_4^+).

The identical pattern in the $^1H,^1H$ COSY NMR spectrum as for the reaction in THF-d_8 was found (*vide supra*).

Protonated addition product of isopropanol to *meso*-octamethylcalix[4]pyrrolato gallate (**82**)[149]

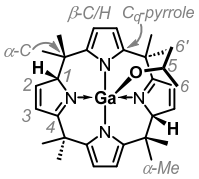

Procedure. In a nitrogen-filled glovebox, tetraphenylphosphonium *meso*-octamethylcalix[4]pyrrolato gallate ([PPh_4][**71**], 10.0 mg, 11.0 µmol, 1.0 equiv., including 0.9 equivalents of CH_2Cl_2) was suspended in a mixture of CH_2Cl_2 and diethyl ether (2:1 %vol, 2 mL) in a 10 mL snap cap vial and was vigorously stirred at room temperature. bis(Trifluoromethyl)sulfonimide ($HNTf_2$, 3.0 mg, 10.66 µmol, 0.97 equiv.) was dissolved in the same solvent mixture (0.5 mL). The $HNTf_2$ solution was added dropwise to the gallate suspension over the course of 5 min at room temperature. The reaction mixture turned yellow. Isopropanol (0.9 µL, 11.8 µmol, 1.07 equiv.) was added in one portion at room temperature using a piston pipette. It was continued to stir for 1 min. All volatiles were removed under reduced pressure. From the obtained solid, it was extracted with a *n*-pentane/diethyl ether mixture (4:1 %vol, 2.5 mL in total, used over three extraction cycles). After removing the solvent from the extract under reduced pressure and drying the residue *in vacuo*, a pale-yellow solid was isolated, which was characterized to the protonated addition product of isopropanol to *meso*-octamethylcalix[4]pyrrolato gallate (**83**) by NMR spectroscopy (4.4 mg, 7.92 µmol, 72% yield).

It was noted by ^{1}H NMR spectroscopy that a small quantity (approximately 8% relative to the shown compound) of another molecule was formed. Based on the acquired NMR data, this is assigned to a constitutional isomer in which the two dearomatization-inducing protons are convertible into each other by means of a mirror plane. One proton is located at the 2- the other at the 5-position of the respective dearomatized pyrrole ring.

^{1}H NMR (600 MHz, CD_2Cl_2, 295 K), δ [ppm] = **7.61** (dd, $^3J_{HH}$ = 5.4, 0.7 Hz, 2H, H-2), **7.00** (dd, $^3J_{HH}$ = 5.4 Hz, $^4J_{HH}$ = 1.4 Hz, 2H, H-3), **6.09** (d, $^3J_{HH}$ = 3.3 Hz, 2H, β-H), **6.00** (d, $^3J_{HH}$ = 3.3 Hz, 2H, β-H), **4.87** (br s, 2H, H-1), **3.52** (sept, $^3J_{HH}$ = 6.0 Hz, 1H, H-5), **1.88** (s, 6H, α-Me), **1.84** (s, 6H, α-Me), **1.57** (s, 6H, α-Me), **0.89** (d, $^3J_{HH}$ = 6.0 Hz, 3H, H-6), **0.69** (d, $^3J_{HH}$ = 6.0 Hz, 3H, H-6'), **0.44** (s, 6H, α-Me).

$^{13}C\{^1H\}$ NMR (151 MHz, CD_2Cl_2, 295 K), δ [ppm] = **188.4** (s, C_q, C-4), **155.3** (s, CH, C-2), **147.7** (s, C_q, C_q-pyrrole), **142.7** (s, C_q, C_q-pyrrole), **129.1** (s, CH, C-3), **104.7** (s, CH, β-C), **102.9** (s, CH, β-C), **87.1** (s, CH, C-1), **64.4** (s, CH, C-5), **39.4** (s, C_q, α-C), **38.8** (s, C_q, α-C), **32.4** (s, CH_3, α-Me), **28.7** (s, CH_3, α-Me), **28.4** (s, CH_3, α-Me), **27.2** (s, CH_3, C-6), **26.9** (s, CH_3, C-6'), **23.0** (s, CH_3, α-Me).

The ^1H,^1H COSY NMR spectrum showed characteristic cross peaks between the signals at 4.87 (protons at the 2-positions) and 7.00 ppm (H-3) and between the signals at 7.00 (H-3) and 7.61 ppm (H-2). Moreover, the ^1H,^1H NOESY NMR spectrum revealed spatial proximity of the isopropyl group and the ligand framework. This further confirms the attachment of the *i*-PrO^- group to the gallium center.

Doubly oxidized *meso*-octamethylcalix[4]pyrrolato gallate as its bis-thf hexafluorophosphate salt ([**83**][PF_6])

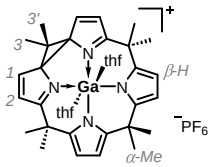

Procedure. In a nitrogen-filled glovebox, tetraphenylphosphonium *meso*-octamethylcalix[4]pyrrolato gallate (10.0 mg, 11.0 µmol, 1.0 equiv., including 0.9 equivalents of CH_2Cl_2) and ferrocenium hexafluorophosphate (7.3 mg, 22.0 µmol, 2.0 equiv.) were placed in a J. Young NMR tube. THF-d_8 (0.5 mL) was added at room temperature, the sample was closed and was vigorously shaken. A dark brown solution was obtained which was analyzed by NMR spectroscopy.

Single crystals for SCXRD measurements were obtained at −40 °C from a THF/diethyl ether solution.

^{1}H NMR (400 MHz, THF-d_8, 295 K), δ [ppm] = **8.43** (d, $^3J_{HH}$ = 5.3 Hz, 2H, H-1), **7.45** (d, $^3J_{HH}$ = 5.3 Hz, 2H, H-2), **6.16** (d, $^3J_{HH}$ = 3.2 Hz, 2H, β-H), **6.14** (d, $^3J_{HH}$ = 3.2 Hz, 2H, β-H), **1.91** (s, 3H, H-3 or H-3'), **1.80** (s, 6H, α-Me), **1.72** (s, 6H, α-Me), **1.61** (s, 6H, α-Me), **1.53** (s, 3H, H-3 or H-3').

^{19}F NMR (376 MHz, THF-d_8, 295 K), δ [ppm] = −**73.3** (d, $^1J_{PF}$ = 709 Hz, PF_6^-).

^{31}P{^{1}H} NMR (162 MHz, THF-d_8, 295 K), δ [ppm] = −**144.2** (sept, $^1J_{PF}$ = 709 Hz, PF_6^-).

A $^{13}C\{^1H\}$ NMR spectrum was not collected. However, the constitution of the compound as shown was unambiguously confirmed by SCXRD measurements (cf. **Chapter 7.4***).*

6 REFERENCES

1. L. Meyer, *Die modernen Theorien der Chemie und ihre Bedeutung für die chemische Statik*. Maruschke & Berendt: Breslau, **1864**.
2. D. Mendelejew, *Z. Chem.* **1869,** *12*, 173.
3. P. Schwerdtfeger, O. R. Smits, P. Pyykkö, *Nat. Rev. Chem.* **2020,** *4*, 359-380.
4. I. Langmuir, *J. Am. Chem. Soc.* **1919,** *41*, 868-934.
5. J. H. van't Hoff, *Arch. Neerl. Sci. Exactes Nat.* **1874,** *9*, 445-454.
6. J. A. Le Bel, *Bull. Soc. Chim. Fr.* **1874,** *22*, 337-347.
7. L. M. Sigmund, R. Maier, L. Greb, *Chem. Sci.* **2022,** *13*, 510-521.
8. A. Baeyer, *Ber. Dtsch. Chem. Ges.* **1886,** *19*, 2184-2185.
9. P. A. Gale, J. L. Sessler, V. Král, V. Lynch, *J. Am. Chem. Soc.* **1996,** *118*, 5140-5141.
10. P. A. Gale, J. L. Sessler, V. Král, *Chem. Commun.* **1998**, 1-8.
11. D. S. Kim, J. L. Sessler, *Chem. Soc. Rev.* **2015,** *44*, 532-546.
12. I. A. Rather, S. A. Wagay, M. S. Hasnain, R. Ali, *RSC Adv.* **2019,** *9*, 38309-38344.
13. S. Peng, Q. He, G. I. Vargas-Zúñiga, L. Qin, I. Hwang, S. K. Kim, N. J. Heo, C.-H. Lee, R. Dutta, J. L. Sessler, *Chem. Soc. Rev.* **2020,** *49*, 865-907.
14. Z. Lai, T. Zhao, J. L. Sessler, Q. He, *Coord. Chem. Rev.* **2020,** *425*, 213528.
15. H. Ruppert, L. M. Sigmund, L. Greb, *Chem. Commun.* **2021,** *57*, 11751-11763.
16. G. N. Lewis, *J. Frank. Inst.* **1938,** *226*, 293-313.
17. L. Greb, *Chem. Eur. J.* **2018,** *24*, 17881-17896.
18. J. C. Haartz, D. H. McDaniel, *J. Am. Chem. Soc.* **1973,** *95*, 8562-8565.
19. L. Greb, F. Ebner, Y. Ginzburg, L. M. Sigmund, *Eur. J. Inorg. Chem.* **2020,** *2020*, 3030-3047.
20. J. R. Khusnutdinova, D. Milstein, *Angew. Chem. Int. Ed.* **2015,** *54*, 12236–12273.
21. T. A. Albright, J. K. Burdett, M.-H. Whangbo, *Orbital interactions in chemistry*. Wiley: Hoboken, NJ, **2013**.
22. A. F. Saturno, *Theor. Chem. Acc.* **1967,** *8*, 273-276.
23. B. M. Gimarc, *Acc. Chem. Res.* **1974,** *7*, 384-392.
24. K. Yoshizawa, A. Suzuki, *Chem. Phys.* **2001,** *271*, 41-54.
25. L. M. Sigmund, C. Ehlert, G. Gryn'ova, L. Greb, *J. Chem. Phys.* **2022,** *156*, 194113.
26. M. B. Krogh-Jespersen, J. Chandrasekhar, E.-U. Würthwein, J. B. Collins, P. v. R. Schleyer, *J. Am. Chem. Soc.* **1980,** *102*, 2263-2268.
27. E.-U. Würthwein, P. v. R. Schleyer, *Angew. Chem. Int. Ed.* **1979,** *18*, 553-554.
28. M. S. Gordon, M. W. Schmidt, *J. Am. Chem. Soc.* **1993,** *115*, 7486-7492.
29. M. J. M. Pepper, I. Shavitt, P. v. R. Schleyer, M. N. Glukhovtsev, R. Janoschek, M. Quack, *J. Comput. Chem.* **1995,** *16*, 207-225.
30. D. A. Dixon, A. J. Arduengo III, *J. Phys. Chem.* **1987,** *91*, 3195-3200.
31. D. A. Dixon, A. J. Arduengo III, *J. Chem. Soc., Chem. Commun.* **1987**, 498-500.
32. D. A. Dixon, A. J. Arduengo III, *Int. J. Quantum Chem.* **1988,** *34*, 85-98.
33. A. J. Arduengo III, D. A. Dixon, D. C. Roe, M. Kline, *J. Am. Chem. Soc.* **1988,** *110*, 4437-4438.

34. J. C. Martin, W. H. Stevenson III, D. Y. Lee, In *Organosilicon and bioorganosilicon chemistry: structure bonding, reactivity and synthetic application*, H. Sakurai, Ed. Horwood, Chichester: Kyoto, **1985**.
35. I. G. Johnston, K. Dingle, S. F. Greenbury, C. Q. Camargo, J. P. K. Doye, S. E. Ahnert, A. A. Louis, *Proc. Natl. Acad. Sci. U.S.A.* **2022,** *119*, e2113883119.
36. B. Fink, N. Neave, J. T. Manning, K. Grammer, *Pers. Individ. Differ.* **2006,** *41*, 491-499.
37. P. O. Folgerø, L. Hodne, C. Johansson, A. E. Andresen, L. C. Sætren, K. Specht, Ø. O. Skaar, R. Reber, *Front. Hum. Neurosci.* **2016,** *10*.
38. N. A. Harun, K. B. C. Adam, N. A. Abdullah, N. Rusli, *Int. J. Oral Maxillofac. Surg.* **2023,** *52*, 703-709.
39. B. C. Jones, L. M. DeBruine, A. C. Little, *Percept. psychophys.* **2007,** *69*, 1273-1277.
40. G. Rhodes, F. Proffitt, J. M. Grady, A. Sumich, *Psychon. Bull. Rev.* **1998,** *5*, 659-669.
41. R. Thornhill, S. W. Gangestad, *Trends Cogn. Sci.* **1999,** *3*, 452-460.
42. H. A. Jahn, E. Teller, *Proc. R. Soc. London, Ser. A* **1937,** *161*, 220-235.
43. I. B. Bersuker, *Chem. Rev.* **2021,** *121*, 1463-1512.
44. R. Englman, *The Jahn-Teller effect in molecules and crystals*. Wiley-Interscience London: London, **1972**.
45. I. B. Bersuker, *Chem. Rev.* **2013,** *113*, 1351-1390.
46. I. B. Bersuker, *Pure Appl. Chem.* **1988,** *60*, 1167-1174.
47. I. B. Bersuker, N. N. Gorinchoi, V. Z. Polinger, *Theor. Chem. Acc.* **1984,** *66*, 161-172.
48. W. Hermoso, A. R. Ilkhani, I. B. Bersuker, *Comput. Theor. Chem.* **2014,** *1049*, 109-114.
49. H. B. Wedler, P. Wendelboe, P. P. Power, *Organometallics* **2018,** *37*, 2929-2936.
50. C. C. Levin, *J. Am. Chem. Soc.* **1975,** *97*, 5649-5655.
51. P. Schwerdtfeger, P. D. W. Boyd, T. Fischer, P. Hunt, M. Liddell, *J. Am. Chem. Soc.* **1994,** *116*, 9620-9633.
52. P. Schwerdtfeger, L. J. Laakkonen, P. Pyykkö, *J. Chem. Phys.* **1992,** *96*, 6807-6819.
53. M. Atanasov, D. Reinen, *J. Phys. Chem. A* **2001,** *105*, 5450-5467.
54. M. Atanasov, D. Reinen, *J. Am. Chem. Soc.* **2002,** *124*, 6693-6705.
55. I. B. Bersuker, N. N. Gorinchoi, V. Z. Polinger, *J. Mol. Struct.* **1992,** *270*, 369-380.
56. IUPAC, *Compendium of Chemical Terminology, 2nd ed. (the "Gold Book")*. Blackwell Scientific Publications: Oxford, **1997**.
57. D. Rodrigues Silva, L. de Azevedo Santos, M. P. Freitas, C. F. Guerra, T. A. Hamlin, *Chem. Asian J.* **2020,** *15*, 4043-4054.
58. A. Ben Saida, A. Chardon, A. Osi, N. Tumanov, J. Wouters, A. I. Adjieufack, B. Champagne, G. Berionni, *Angew. Chem. Int. Ed.* **2019,** *58*, 16889-16893.
59. H. Fleischer, *Eur. J. Inorg. Chem.* **2001,** *2001*, 393-404.
60. A. R. Jupp, T. C. Johnstone, D. W. Stephan, *Dalton Trans.* **2018,** *47*, 7029-7035.
61. A. R. Jupp, T. C. Johnstone, D. W. Stephan, *Inorg. Chem.* **2018,** *57*, 14764-14771.
62. K. Müther, P. Hrobárik, V. Hrobáriková, M. Kaupp, M. Oestreich, *Chem. Eur. J.* **2013,** *19*, 16579-16594.
63. A. E. Ashley, T. J. Herrington, G. G. Wildgoose, H. Zaher, A. L. Thompson, N. H. Rees, T. Krämer, D. O'Hare, *J. Am. Chem. Soc.* **2011,** *133*, 14727-14740.
64. K. F. Purcell, R. S. Drago, *J. Am. Chem. Soc.* **1966,** *88*, 919-924.
65. M. A. Beckett, G. C. Strickland, J. R. Holland, K. Sukumar Varma, *Polymer* **1996,** *37*, 4629-4631.
66. R. F. Childs, D. L. Mulholland, A. Nixon, *Can. J. Chem.* **1982,** *60*, 809-812.

67. K. O. Christe, D. A. Dixon, D. McLemore, W. W. Wilson, J. A. Sheehy, J. A. Boatz, *J. Fluorine Chem.* **2000,** *101*, 151-153.
68. P. Erdmann, J. Leitner, J. Schwarz, L. Greb, *ChemPhysChem* **2020,** *21*, 987-994.
69. H. Böhrer, N. Trapp, D. Himmel, M. Schleep, I. Krossing, *Dalton Trans.* **2015,** *44*, 7489-7499.
70. A. P. Altshuller, *J. Am. Chem. Soc.* **1955,** *77*, 6187-6188.
71. H. D. B. Jenkins, H. K. Roobottom, J. Passmore, *Inorg. Chem.* **2003,** *42*, 2886-2893.
72. K. A. G. MacNeil, J. C. J. Thynne, *J. Phys. Chem.* **1970,** *74*, 2257-2262.
73. T. E. Mallouk, G. L. Rosenthal, G. Mueller, R. Brusasco, N. Bartlett, *Inorg. Chem.* **1984,** *23*, 3167-3173.
74. J. A. Stockdale, D. R. Nelson, F. J. Davis, R. N. Compton, *J. Chem. Phys.* **2003,** *56*, 3336-3341.
75. R. G. Pearson, *J. Am. Chem. Soc.* **1963,** *85*, 3533-3539.
76. R. S. Drago, B. B. Wayland, *J. Am. Chem. Soc.* **1965,** *87*, 3571-3577.
77. R. S. Drago, G. C. Vogel, T. E. Needham, *J. Am. Chem. Soc.* **1971,** *93*, 6014-6026.
78. R. S. Drago, *Coord. Chem. Rev.* **1980,** *33*, 251-277.
79. R. S. Drago, M. K. Kroeger, J. R. Stahlbush, *Inorg. Chem.* **1981,** *20*, 306-308.
80. R. S. Drago, N. Wong, C. Bilgrien, G. C. Vogel, *Inorg. Chem.* **1987,** *26*, 9-14.
81. R. S. Drago, D. C. Ferris, N. Wong, *J. Am. Chem. Soc.* **1990,** *112*, 8953-8961.
82. R. S. Drago, G. C. Vogel, *J. Am. Chem. Soc.* **1992,** *114*, 9527-9532.
83. R. S. Drago, A. P. Dadmun, G. C. Vogel, *Inorg. Chem.* **1993,** *32*, 2473-2479.
84. R. S. Drago, S. Joerg, *J. Am. Chem. Soc.* **1996,** *118*, 2654-2663.
85. G. C. Vogel, R. S. Drago, *J. Chem. Educ.* **1996,** *73*, 701.
86. J. R. Khusnutdinova, D. Milstein, *Angew. Chem. Int. Ed.* **2015,** *54*, 12236-12273.
87. C. Gunanathan, D. Milstein, *Acc. Chem. Res.* **2011,** *44*, 588-602.
88. D. Milstein, *Philos. Trans. R. Soc. A* **2015,** *373*.
89. F. Ebner, L. M. Sigmund, L. Greb, *Angew. Chem. Int. Ed.* **2020,** *59*, 17118-17124.
90. J. Zhang, G. Leitus, Y. Ben-David, D. Milstein, *Angew. Chem. Int. Ed.* **2006,** *45*, 1113-1115.
91. E. Balaraman, C. Gunanathan, J. Zhang, L. J. W. Shimon, D. Milstein, *Nat. Chem.* **2011,** *3*, 609-614.
92. S. W. Kohl, L. Weiner, L. Schwartsburd, L. Konstantinovski, L. J. W. Shimon, Y. Ben-David, M. A. Iron, D. Milstein, *Science* **2009,** *324*, 74-77.
93. C. Gunanathan, Y. Ben-David, D. Milstein, *Science* **2007,** *317*, 790-792.
94. M. Montag, J. Zhang, D. Milstein, *J. Am. Chem. Soc.* **2012,** *134*, 10325–10328.
95. A. Kumar, P. Daw, N. A. Espinosa-Jalapa, G. Leitus, L. J. W. Shimon, Y. Ben-David, D. Milstein, *Dalton Trans.* **2019,** *48*, 14580-14584.
96. M. Vogt, A. Nerush, Y. Diskin-Posner, Y. Ben-David, D. Milstein, *Chem. Sci.* **2014,** *5*, 2043-2051.
97. M. Feller, E. Ben-Ari, Y. Diskin-Posner, D. Milstein, *J. Coord. Chem.* **2018,** *71*, 1679-1689.
98. M. L. Scheuermann, U. Fekl, W. Kaminsky, K. I. Goldberg, *Organometallics* **2010,** *29*, 4749-4751.
99. M. L. Scheuermann, K. I. Goldberg, *Chem. Eur. J.* **2014,** *20*, 14556-14568.
100. M. L. Scheuermann, A. T. Luedtke, S. K. Hanson, U. Fekl, W. Kaminsky, K. I. Goldberg, *Organometallics* **2013,** *32*, 4752-4758.

101. T. W. Myers, L. A. Berben, *J. Am. Chem. Soc.* **2013,** *135*, 9988-9990.
102. T. J. Sherbow, C. R. Carr, T. Saisu, J. C. Fettinger, L. A. Berben, *Organometallics* **2016,** *35*, 9-14.
103. T. W. Myers, L. A. Berben, *Chem. Sci.* **2014,** *5*, 2771-2777.
104. M.-A. Légaré, M.-A. Courtemanche, É. Rochette, F.-G. Fontaine, *Science* **2015,** *349*, 513-516.
105. I. L. Fedushkin, A. S. Nikipelov, K. A. Lyssenko, *J. Am. Chem. Soc.* **2010,** *132*, 7874-7875.
106. I. L. Fedushkin, A. S. Nikipelov, A. G. Morozov, A. A. Skatova, A. V. Cherkasov, G. A. Abakumov, *Chem. Eur. J.* **2012,** *18*, 255-266.
107. W. Zhang, V. A. Dodonov, W. Chen, Y. Zhao, A. A. Skatova, I. L. Fedushkin, P. W. Roesky, B. Wu, X.-J. Yang, *Chem. Eur. J.* **2018,** *24*, 14994-15002.
108. V. A. Dodonov, W. Chen, Y. Zhao, A. A. Skatova, P. W. Roesky, B. Wu, X.-J. Yang, I. L. Fedushkin, *Chem. Eur. J.* **2019,** *25*, 8259-8267.
109. G. A. Abakumov, A. I. Poddel'sky, E. V. Grunova, V. K. Cherkasov, G. K. Fukin, Y. A. Kurskii, L. G. Abakumova, *Angew. Chem. Int. Ed.* **2005,** *44*, 2767-2771.
110. V. K. Cherkasov, G. A. Abakumov, E. V. Grunova, A. I. Poddel'sky, G. K. Fukin, E. V. Baranov, Y. V. Kurskii, L. G. Abakumova, *Chem. Eur. J.* **2006,** *12*, 3916-3927.
111. V. V. Chelintzev, B. V. Tronov, *J. Russ. Phys. Chem. Soc.* **1916**, 105 - 155.
112. P. A. Gale, P. Anzenbacher Jr, J. L. Sessler, *Coord. Chem. Rev.* **2001,** *222*, 57-102.
113. F. H. Kohnke, *Eur. J. Org. Chem.* **2020,** *2020*, 4261-4272.
114. S. Depraetere, M. Smet, W. Dehaen, *Angew. Chem. Int. Ed.* **1999,** *38*, 3359-3361.
115. S. Dey, K. Pal, S. Sarkar, *Tetrahedron Lett.* **2006,** *47*, 5851-5854.
116. J. S. Park, J. L. Sessler, *Acc. Chem. Res.* **2018,** *51*, 2400-2410.
117. A. Aydogan, J. L. Sessler, A. Akar, V. Lynch, *Supramol. Chem.* **2008,** *20*, 11-21.
118. Y. Inaba, Y. Nomata, Y. Ide, J. Pirillo, Y. Hijikata, T. Yoneda, A. Osuka, J. L. Sessler, Y. Inokuma, *J. Am. Chem. Soc.* **2021,** *143*, 12355-12360.
119. Y. Inaba, J. Yang, Y. Kakibayashi, T. Yoneda, Y. Ide, Y. Hijikata, J. Pirillo, R. Saha, J. L. Sessler, Y. Inokuma, *Angew. Chem. Int. Ed.* **2023,** *62*, e202301460.
120. J. Jubb, C. Floriani, A. Chiesi-Villa, C. Rizzoli, *J. Am. Chem. Soc.* **1992,** *114*, 6571-6573.
121. U. Piarulli, E. Solari, C. Floriani, A. Chiesi-Villa, C. Rizzoli, *J. Am. Chem. Soc.* **1996,** *118*, 3634-3642.
122. K. M. Kadish, K. M. Smith, R. Guilard, *The porphyrin handbook. Vol. 3*. Academic: San Diego, Calif.; London, **2000**.
123. J. Bachmann, D. G. Nocera, *J. Am. Chem. Soc.* **2004,** *126*, 2829-2837.
124. J. Bachmann, D. G. Nocera, *J. Am. Chem. Soc.* **2005,** *127*, 4730-4743.
125. G. Cafeo, G. Carbotti, A. Cuzzola, M. Fabbi, S. Ferrini, F. H. Kohnke, G. Papanikolaou, M. R. Plutino, C. Rosano, A. J. P. White, *J. Am. Chem. Soc.* **2013,** *135*, 2544-2551.
126. S.-K. Ko, S. K. Kim, A. Share, V. M. Lynch, J. Park, W. Namkung, W. Van Rossom, N. Busschaert, P. A. Gale, J. L. Sessler*, et al.*, *Nat. Chem.* **2014,** *6*, 885-892.
127. R. Lappano, C. Rosano, A. Pisano, M. F. Santolla, E. M. De Francesco, P. De Marco, V. Dolce, M. Ponassi, L. Felli, G. Cafeo*, et al.*, *Dis. Model. Mech.* **2015,** *8*, 1237-1246.
128. I. B. Toumia, M. Ponassi, P. Barboro, E. Iervasi, G. C. Vargas, B. Banelli, S. Fiordoro, L. C. Ghedira, F. H. Kohnke, A. Izzotti*, et al.*, *Investig. New Drugs* **2022,** *40*, 1185-1193.
129. W. J. Transue, Y. Dai, M.-L. Y. Riu, G. Wu, C. C. Cummins, *Inorg. Chem.* **2021,** *60*, 9254-9258.

130. K. Anjali, M. S. Aswini, P. Aswin, V. Ganesh, A. Sakthivel, *Eur. J. Inorg. Chem.* **2019,** *2019*, 4087-4094.
131. K. Anjali, M. Ahmed, J. Christopher, A. Sakthivel, *Dalton Trans.* **2018,** *47*, 12353-12361.
132. G. B. Deacon, Z. Guo, P. C. Junk, J. Wang, *Angew. Chem. Int. Ed.* **2017,** *56*, 8486-8489.
133. G. B. Deacon, M. G. Gardiner, P. C. Junk, J. P. Townley, J. Wang, *Organometallics* **2012,** *31*, 3857-3864.
134. G. T. Kent, J. Murillo, G. Wu, S. Fortier, T. W. Hayton, *Inorg. Chem.* **2020,** *59*, 8629-8634.
135. J. T. Brewster, H. Zafar, H. D. Root, G. D. Thiabaud, J. L. Sessler, *Inorg. Chem.* **2020,** *59*, 32-47.
136. S. K. Kim, J. L. Sessler, *Acc. Chem. Res.* **2014,** *47*, 2525-2536.
137. D. Jacoby, C. Floriani, A. Chiesi-Villa, C. Rizzoli, *J. Chem. Soc., Chem. Commun.* **1991**, 220-222.
138. D. Jacoby, C. Floriani, A. Chiesi-Villa, C. Rizzoli, *J. Am. Chem. Soc.* **1993,** *115*, 3595-3602.
139. F. Ebner, L. Greb, *J. Am. Chem. Soc.* **2018,** *140*, 17409-17412.
140. F. Ebner, H. Wadepohl, L. Greb, *J. Am. Chem. Soc.* **2019,** *141*, 18009-18012.
141. F. Ebner, L. Greb, *Chem* **2021,** *7*, 2151-2159.
142. F. Ebner, P. Mainik, L. Greb, *Chem. Eur. J.* **2021,** *27*, 5120-5124.
143. H. Ruppert, L. Greb, *Angew. Chem. Int. Ed.* **2022,** *61*, e202116615.
144. M. Schorpp, R. Yadav, D. Roth, L. Greb, *Angew. Chem. Int. Ed.* **2022,** *61*, e202207963.
145. F. Schön, L. M. Sigmund, F. Schneider, D. Hartmann, M. A. Wiebe, I. Manners, L. Greb, *Angew. Chem. Int. Ed.* **2022,** *61*, e202202176.
146. R. Yadav, P. Janßen, M. Schorpp, L. Greb, *J. Am. Chem. Soc.* **2023,** *145*, 17746-17754.
147. L. M. Sigmund, L. Greb, *Chem. Sci.* **2020,** *11*, 9611-9616.
148. L. M. Sigmund, C. Ehlert, M. Enders, J. Graf, G. Gryn'ova, L. Greb, *Angew. Chem. Int. Ed.* **2021,** *60*, 15632-15640.
149. L. M. Sigmund, E. Engels, N. Richert, L. Greb, *Chem. Sci.* **2022,** *13*, 11215-11220.
150. S. Nandi, T. Vegge, A. Bhowmik, *Sci. Data* **2023,** *10*, 783.
151. Y. Zhang, C. Ling, *Npj Comput. Mater.* **2018,** *4*, 25.
152. H. Moriwaki, Y.-S. Tian, N. Kawashita, T. Takagi, *J. Cheminform.* **2018,** *10*, 4.
153. L. David, A. Thakkar, R. Mercado, O. Engkvist, *J. Cheminform.* **2020,** *12*, 56.
154. F. Pedregosa, G. Varoquaux, A. Gramfort, V. Michel, B. Thirion, O. Grisel, M. Blondel, P. Prettenhofer, R. Weiss, V. Dubourg, *J. Mach. Learn. Res.* **2011,** *12*, 2825-2830.
155. H. Kinsley, D. Kukieła, *Neural networks from scratch in Python*. USA, **2020**.
156. J. Gilmer, S. S. Schoenholz, P. F. Riley, O. Vinyals, G. E. Dahl In *Neural message passing for quantum chemistry*, International conference on machine learning, PMLR: 2017; 1263-1272.
157. C. W. Coley, R. Barzilay, T. S. Jaakkola, W. H. Green, K. F. Jensen, *ACS Cent. Sci.* **2017,** *3*, 434-443.
158. K. T. Butler, D. W. Davies, H. Cartwright, O. Isayev, A. Walsh, *Nature* **2018,** *559*, 547-555.
159. C. W. Coley, W. H. Green, K. F. Jensen, *Acc. Chem. Res.* **2018,** *51*, 1281-1289.
160. F. Strieth-Kalthoff, F. Sandfort, M. H. S. Segler, F. Glorius, *Chem. Soc. Rev.* **2020,** *49*, 6154-6168.

161. K. Jorner, A. Tomberg, C. Bauer, C. Sköld, P.-O. Norrby, *Nat. Rev. Chem.* **2021,** *5*, 240-255.
162. A. Karthikeyan, U. D. Priyakumar, *J. Chem. Sci.* **2021,** *134*, 2.
163. J. A. Keith, V. Vassilev-Galindo, B. Cheng, S. Chmiela, M. Gastegger, K.-R. Müller, A. Tkatchenko, *Chem. Rev.* **2021,** *121*, 9816-9872.
164. M. Meuwly, *Chem. Rev.* **2021,** *121*, 10218-10239.
165. A. Bender, N. Schneider, M. Segler, W. Patrick Walters, O. Engkvist, T. Rodrigues, *Nat. Rev. Chem.* **2022,** *6*, 428-442.
166. Y.-F. Shi, Z.-X. Yang, S. Ma, P.-L. Kang, C. Shang, P. Hu, Z.-P. Liu, *Engineering (Beijing)* **2023**.
167. P. Reiser, M. Neubert, A. Eberhard, L. Torresi, C. Zhou, C. Shao, H. Metni, C. van Hoesel, H. Schopmans, T. Sommer*, et al.*, *Commun. Mater.* **2022,** *3*, 93.
168. D. Jiang, Z. Wu, C.-Y. Hsieh, G. Chen, B. Liao, Z. Wang, C. Shen, D. Cao, J. Wu, T. Hou, *J. Cheminform.* **2021,** *13*, 12.
169. J. S. Smith, O. Isayev, A. E. Roitberg, *Chem. Sci.* **2017,** *8*, 3192-3203.
170. C. Devereux, J. S. Smith, K. K. Huddleston, K. Barros, R. Zubatyuk, O. Isayev, A. E. Roitberg, *J. Chem. Theory Comput.* **2020,** *16*, 4192-4202.
171. J. S. Smith, R. Zubatyuk, B. Nebgen, N. Lubbers, K. Barros, A. E. Roitberg, O. Isayev, S. Tretiak, *Sci. Data* **2020,** *7*, 134.
172. Y. Guan, S. Sowndarya S. V., L. C. Gallegos, P. C. St. John, R. S. Paton, *Chem. Sci.* **2021,** *12*, 12012-12026.
173. P. C. St. John, Y. Guan, Y. Kim, S. Kim, R. S. Paton, *Nat. Commun.* **2020,** *11*, 2328.
174. S. Sowndarya S. V., Y. Kim, S. Kim, P. C. St. John, R. S. Paton, *Digit. Discov.* **2023,** *2*, 1900-1910.
175. W. Nie, D. Liu, S. Li, H. Yu, Y. Fu, *J. Chem. Inf. Model.* **2022**.
176. Connor W. Coley, W. Jin, L. Rogers, T. F. Jamison, T. S. Jaakkola, W. H. Green, R. Barzilay, K. F. Jensen, *Chem. Sci.* **2019,** *10*, 370-377.
177. Z. Wu, J. Wang, H. Du, D. Jiang, Y. Kang, D. Li, P. Pan, Y. Deng, D. Cao, C.-Y. Hsieh*, et al.*, *Nat. Commun.* **2023,** *14*, 2585.
178. P. C. St. John, C. Phillips, T. W. Kemper, A. N. Wilson, Y. Guan, M. F. Crowley, M. R. Nimlos, R. E. Larsen, *J. Chem. Phys.* **2019,** *150*.
179. L. M. Sigmund. Masterthesis. Heidelberg University, 2019.
180. U. Gellrich, Y. Diskin-Posner, L. J. W. Shimon, D. Milstein, *J. Am. Chem. Soc.* **2016,** *138*, 13307-13313.
181. T. W. Myers, L. A. Berben, *Organometallics* **2013,** *32*, 6647-6649.
182. E. J. Thompson, T. W. Myers, L. A. Berben, *Angew. Chem. Int. Ed.* **2014,** *53*, 14132-14134.
183. M. V. Moskalev, A. N. Lukoyanov, E. V. Baranov, I. L. Fedushkin, *Dalton Trans.* **2016,** *45*, 15872-15878.
184. P. Wang, M. Zhang, C. Zhu, *Organometallics* **2020,** *39*, 2732-2738.
185. T. P. Robinson, D. M. De Rosa, S. Aldridge, J. M. Goicoechea, *Angew. Chem. Int. Ed.* **2015,** *54*, 13758-13763.
186. S. Volodarsky, R. Dobrovetsky, *Chem. Commun.* **2018,** *54*, 6931-6934.
187. P. Vasko, M. Á. Fuentes, J. Hicks, S. Aldridge, *Dalton Trans.* **2019,** *48*, 2896-2899.
188. W. Zhao, S. M. McCarthy, T. Y. Lai, H. P. Yennawar, A. T. Radosevich, *J. Am. Chem. Soc.* **2014,** *136*, 17634-17644.

189. T. A. Whitney, L. P. Klemann, Alkali metal salts of complex anions containing heteroatom substituents and electrolyte compositions containing these, US4117213A. **1978**.
190. B. G. Malmstrom, *Annu. Rev. Biochem* **1982,** *51*, 21-59.
191. B. A. Palfey, D. P. Ballou, V. Massey, Oxygen Activation by Flavins and Pterins. In *Active Oxygen in Biochemistry*, J. S. Valentine; C. S. Foote; A. Greenberg; J. F. Liebman, Eds. Springer Netherlands: Dordrecht, **1995**; pp 37-83.
192. T. D. H. Bugg, *Curr. Opin. Chem. Biol.* **2001,** *5*, 550-555.
193. A. Decker, E. I. Solomon, *Curr. Opin. Chem. Biol.* **2005,** *9*, 152-163.
194. E. Romero, J. R. Gómez Castellanos, G. Gadda, M. W. Fraaije, A. Mattevi, *Chem. Rev.* **2018,** *118*, 1742-1769.
195. E. G. Kovaleva, J. D. Lipscomb, *Nat. Chem. Biol.* **2008,** *4*, 186-193.
196. M. Costas, M. P. Mehn, M. P. Jensen, L. Que, *Chem. Rev.* **2004,** *104*, 939-986.
197. X. Huang, J. T. Groves, *Chem. Rev.* **2018,** *118*, 2491-2553.
198. M. Wikström, K. Krab, V. Sharma, *Chem. Rev.* **2018,** *118*, 2469-2490.
199. J. Rosenthal, D. G. Nocera, *Acc. Chem. Res.* **2007,** *40*, 543-553.
200. V. R. I. Kaila, M. I. Verkhovsky, M. Wikström, *Chem. Rev.* **2010,** *110*, 7062-7081.
201. T. Wongnate, P. Surawatanawong, S. Visitsatthawong, J. Sucharitakul, N. S. Scrutton, P. Chaiyen, *J. Am. Chem. Soc.* **2014,** *136*, 241-253.
202. S. Visitsatthawong, P. Chenprakhon, P. Chaiyen, P. Surawatanawong, *J. Am. Chem. Soc.* **2015,** *137*, 9363-9374.
203. B. F. Minaev, H. Ågren, V. O. Minaeva, Spin-Orbit Coupling in Enzymatic Reactions and the Role of Spin in Biochemistry. In *Handbook of Computational Chemistry*, J. Leszczynski; A. Kaczmarek-Kedziera; T. Puzyn; M. G. Papadopoulos; H. Reis; M. K. Shukla, Eds. Springer International Publishing: Cham, **2017**; pp 1557-1587.
204. G. K. Fukin, E. V. Baranov, A. I. Poddel'sky, V. K. Cherkasov, G. A. Abakumov, *ChemPhysChem* **2012,** *13*, 3773-3776.
205. M. V. Arsenyev, M. P. Shurygina, A. I. Poddel'sky, N. O. Druzhkov, S. A. Chesnokov, G. K. Fukin, V. K. Cherkasov, G. A. Abakumov, *J. Polym. Res.* **2013,** *20*, 98.
206. S. A. Chesnokov, N. A. Lenshina, M. V. Arsenyev, R. S. Kovylin, M. A. Baten'kin, A. I. Poddel'sky, G. A. Abakumov, *Applied Organometallic Chemistry* **2017,** *31*, e3553.
207. K. Huber, G. Herzberg, *Molecular spectra and molecular structure: iv. constants of diatomic molecules*. Springer-Verlag New York: New York, **2013**.
208. S. Dutta, S.-M. Peng, S. Bhattacharya, *Inorg. Chem.* **2000,** *39*, 2231-2234.
209. P. Kumar, S. V. Lindeman, A. T. Fiedler, *J. Am. Chem. Soc.* **2019,** *141*, 10984-10987.
210. A. Rola-Noworyta, T. Pietrzak, V. Szejko, I. Justyniak, J. Lewiński, *Inorg. Chem.* **2020,** *59*, 13807-13811.
211. G. Sosnovsky, J. H. Brown, *Chem. Rev.* **1966,** *66*, 529-566.
212. P. B. Brindley, Organometallic peroxides. In *Peroxides (1983)*, **1983**; pp 807-828.
213. W. Adam, *Peroxide chemistry : mechanistic and preparative aspects of oxygen transfer*. Wiley-VCH Weinheim: Weinheim, 2011.
214. B. Meunier, *Metal-Oxo and Metal-Peroxo Species in Catalytic Oxidations*. Springer Berlin: Berlin, **2013**.
215. W. T. Borden, R. Hoffmann, T. Stuyver, B. Chen, *J. Am. Chem. Soc.* **2017,** *139*, 9010-9018.

216. R. Prabhakar, P. E. M. Siegbahn, B. F. Minaev, H. Ågren, *J. Phys. Chem. B* **2002,** *106*, 3742-3750.
217. B. F. Minaev, *Chem. Phys.* **2019,** *521*, 61-68.
218. C. M. Marian, *WIREs Comput. Mol. Sci.* **2012,** *2*, 187-203.
219. C. M. Marian, *Annu. Rev. Phys. Chem.* **2021,** *72*, 617-640.
220. T. J. Penfold, E. Gindensperger, C. Daniel, C. M. Marian, *Chem. Rev.* **2018,** *118*, 6975-7025.
221. Z. Wang, Y. Wang, Y. Yuan, Y. Gu, Y. Zhu, L. Liu, Z. Zhuang, L. Kong, Y. Li, *Org. Lett.* **2023,** *25*, 3094-3098.
222. J. K. Howard, K. J. Rihak, A. C. Bissember, J. A. Smith, *Chem. Asian J.* **2016,** *11*, 155-167.
223. J. Clayden, R. Turnbull, I. Pinto, *Org. Lett.* **2004,** *6*, 609-611.
224. S. Panda, N. Pradhan, D. Manna, *ACS Comb. Sci.* **2018,** *20*, 573-578.
225. P. Xu, E.-U. Würthwein, C. G. Daniliuc, A. Studer, *Angew. Chem. Int. Ed.* **2017,** *56*, 13872-13875.
226. E. G. Palacios, G. Juárez-López, A. J. Monhemius, *Hydrometallurgy* **2004,** *72*, 139-148.
227. J. Buddrus, H. Bauer, *Angew. Chem. Int. Ed.* **1987,** *26*, 625-642.
228. O. W. Sørensen, R. Freeman, T. Frenkiel, T. H. Mareci, R. Schuck, *J. Magn. Reson.* **1982,** *46*, 180-184.
229. A. Bax, R. Freeman, T. A. Frenkiel, *J. Am. Chem. Soc.* **1981,** *103*, 2102-2104.
230. E. Theuergarten, J. Schlösser, D. Schlüns, M. Freytag, C. G. Daniliuc, P. G. Jones, M. Tamm, *Dalton Trans.* **2012,** *41*, 9101-9110.
231. C. Rosorius, G. Kehr, R. Fröhlich, S. Grimme, G. Erker, *Organometallics* **2011,** *30*, 4211-4219.
232. I. Heuermann, B. Heitmann, R. Stichauer, D. Duvinage, M. Vogt, *Organometallics* **2019,** *38*, 1787-1799.
233. D. L. H. Williams, *Nitrosation reactions and the chemistry of nitric oxide*. 1st ed.; Elsevier Amsterdam: Amsterdam, 2004.
234. A. Ray, K. Gulati, *Nitric oxide: from research to therapeutics*. Springer Cham: Chem (Germany), 2023.
235. W. H. Koppenol, *Free Radical Biol. Med.* **1998,** *25*, 385-391.
236. S. H. Snyder, D. S. Bredt, *Sci. Am.* **1992,** *266*, 68-77.
237. R. González-Luque, M. Merchán, B. O. Roos, *Theor. Chem. Acc.* **1994,** *88*, 425-435.
238. A. R. W. McKellar, J. K. G. Watson, B. J. Howard, *Mol. Phys.* **1995,** *86*, 273-286.
239. A. L. L. East, *J. Chem. Phys.* **1998,** *109*, 2185-2193.
240. J. K. Park, H. Sun, *Chem. Phys.* **2001,** *263*, 61-68.
241. J. A. Hrabie, L. K. Keefer, *Chem. Rev.* **2002,** *102*, 1135-1154.
242. D. H. Magers, H. Qiong, J. Leszczyński, *Struct. Chem.* **2002,** *13*, 165-172.
243. E. A. Wade, J. I. Cline, K. T. Lorenz, C. Hayden, D. W. Chandler, *J. Chem. Phys.* **2002,** *116*, 4755-4757.
244. Y.-L. Zhao, M. D. Bartberger, K. Goto, K. Shimada, T. Kawashima, K. N. Houk, *J. Am. Chem. Soc.* **2005,** *127*, 7964-7965.
245. S. V. Levchenko, H. Reisler, A. I. Krylov, O. Gessner, A. Stolow, H. Shi, A. L. L. East, *J. Chem. Phys.* **2006,** *125*, 084301.
246. N. Taguchi, Y. Mochizuki, T. Ishikawa, K. Tanaka, *Chem. Phys. Lett.* **2008,** *451*, 31-36.

247. D. Srivastava, C. H. Turner, E. E. Santiso, K. E. Gubbins, *J. Phys. Chem. B* **2018,** *122*, 3604-3614.
248. S. Amirkhalili, A. J. Conway, J. D. Smith, *J. Organomet. Chem.* **1978,** *149*, 407-411.
249. S. Amirkhalili, P. B. Hitchcock, J. D. Smith, J. G. Stamper, *Dalton Trans.* **1980**, 2493-2497.
250. T.-Y. Luh, *Coord. Chem. Rev.* **1984,** *60*, 255-276.
251. A. J. P. Cardenas, B. J. Culotta, T. H. Warren, S. Grimme, A. Stute, R. Fröhlich, G. Kehr, G. Erker, *Angew. Chem. Int. Ed.* **2011,** *50*, 7567-7571.
252. M. Sajid, A. Stute, A. J. P. Cardenas, B. J. Culotta, J. A. M. Hepperle, T. H. Warren, B. Schirmer, S. Grimme, A. Studer, C. G. Daniliuc*, et al.*, *J. Am. Chem. Soc.* **2012,** *134*, 10156-10168.
253. M. Sajid, G. Kehr, T. Wiegand, H. Eckert, C. Schwickert, R. Pöttgen, A. J. P. Cardenas, T. H. Warren, R. Fröhlich, C. G. Daniliuc*, et al.*, *J. Am. Chem. Soc.* **2013,** *135*, 8882-8895.
254. R. Liedtke, F. Scheidt, J. Ren, B. Schirmer, A. J. P. Cardenas, C. G. Daniliuc, H. Eckert, T. H. Warren, S. Grimme, G. Kehr*, et al.*, *J. Am. Chem. Soc.* **2014,** *136*, 9014-9027.
255. J. C. M. Pereira, M. Sajid, G. Kehr, A. M. Wright, B. Schirmer, Z.-W. Qu, S. Grimme, G. Erker, P. C. Ford, *J. Am. Chem. Soc.* **2014,** *136*, 513-519.
256. T. Wang, L. Wang, C. G. Daniliuc, K. Samigullin, M. Wagner, G. Kehr, G. Erker, *Chem. Sci.* **2017,** *8*, 2457-2463.
257. C. M. Mömming, G. Kehr, B. Wibbeling, R. Fröhlich, G. Erker, *Dalton Trans.* **2010,** *39*, 7556-7564.
258. W. N. Lipscomb, *J. Chem. Phys.* **1971,** *54*, 3659-3660.
259. W. N. Lipscomb, F. E. Wang, W. R. May, E. L. Lippert, *Acta Crystallogr.* **1961,** *14*, 1100-1101.
260. W. J. Dulmage, E. A. Meyers, W. N. Lipscomb, *Acta Crystallogr.* **1953,** *6*, 760-764.
261. D. R. Lide, *CRC Handbook of Chemistry and Physics*. 85 ed.; Taylor & Francis: **2004**.
262. K. A. Gudun, S. Tussupbayev, A. Slamova, A. Y. Khalimon, *Org. Biomol. Chem.* **2022,** *20*, 6821-6830.
263. V. K. Pandey, S. Sahoo, A. Rit, *Chem. Commun.* **2022,** *58*, 5514-5517.
264. R. K. Sahoo, N. Sarkar, S. Nembenna, *Angew. Chem. Int. Ed.* **2021,** *60*, 11991-12000.
265. M. Ziche, S. Donnini, L. Morbidelli, E. Monzani, R. Roncone, R. Gabbini, L. Casella, *ChemMedChem* **2008,** *3*, 1039-1047.
266. S. Gama, R. Hermenau, M. Frontauria, D. Milea, S. Sammartano, C. Hertweck, W. Plass, *Chem. Eur. J.* **2021,** *27*, 2724-2733.
267. L. M. Blomberg, M. R. A. Blomberg, P. E. M. Siegbahn, *J. Biol. Inorg. Chem.* **2007,** *12*, 79-89.
268. J. Jubb, D. Jacoby, C. Floriani, A. Chiesi-Villa, C. Rizzoli, *Inorg. Chem.* **1992,** *31*, 1306-1308.
269. L. E. Maelia, S. A. Koch, *Inorg. Chem.* **1986,** *25*, 1896-1904.
270. L. Yang, D. R. Powell, R. P. Houser, *Dalton Trans.* **2007**, 955-964.
271. W. P. Ozimiński, J. C. Dobrowolski, *J. Phys. Org. Chem.* **2009,** *22*, 769-778.
272. I. L. Fedushkin, V. A. Dodonov, A. A. Skatova, V. G. Sokolov, A. V. Piskunov, G. K. Fukin, *Chem. Eur. J.* **2018,** *24*, 1877-1889.
273. D. A. Razborov, A. N. Lukoyanov, M. V. Moskalev, E. V. Baranov, I. L. Fedyushkin, *Russ. J. Coord. Chem.* **2018,** *44*, 380-387.

274. I. L. Fedushkin, A. N. Lukoyanov, S. Y. Ketkov, M. Hummert, H. Schumann, *Chem. Eur. J.* **2007,** *13*, 7050-7056.
275. A. V. Piskunov, I. V. Ershova, G. K. Fukin, A. S. Shavyrin, *Inorg. Chem. Commun.* **2013,** *38*, 127-130.
276. J. A. B. Abdalla, I. M. Riddlestone, R. Tirfoin, S. Aldridge, *Angew. Chem. Int. Ed.* **2015,** *54*, 5098-5102.
277. M. Vogt, M. Gargir, M. A. Iron, Y. Diskin-Posner, Y. Ben-David, D. Milstein, *Chem. Eur. J.* **2012,** *18*, 9194-9197.
278. D. Sieh, D. C. Lacy, J. C. Peters, C. P. Kubiak, *Chem. Eur. J.* **2015,** *21*, 8497-8503.
279. R. Stichauer, A. Helmers, J. Bremer, M. Rohdenburg, A. Wark, E. Lork, M. Vogt, *Organometallics* **2017,** *36*, 839-848.
280. M. A. Dureen, D. W. Stephan, *J. Am. Chem. Soc.* **2010,** *132*, 13559-13568.
281. D. A. Dickie, E. N. Coker, R. A. Kemp, *Inorg. Chem.* **2011,** *50*, 11288-11290.
282. L. J. Hounjet, C. B. Caputo, D. W. Stephan, *Angew. Chem. Int. Ed.* **2012,** *51*, 4714-4717.
283. M.-A. Courtemanche, J. Larouche, M.-A. Légaré, W. Bi, L. Maron, F.-G. Fontaine, *Organometallics* **2013,** *32*, 6804-6811.
284. D. A. Dickie, R. A. Kemp, *Organometallics* **2014,** *33*, 6511-6518.
285. D. A. Dickie, M. T. Barker, M. A. Land, K. E. Hughes, J. A. C. Clyburne, R. A. Kemp, *Inorg. Chem.* **2015,** *54*, 11121-11126.
286. N. von Wolff, G. Lefèvre, J. C. Berthet, P. Thuéry, T. Cantat, *ACS Catal.* **2016,** *6*, 4526-4535.
287. T. S. Koptseva, V. G. Sokolov, S. Y. Ketkov, E. A. Rychagova, A. V. Cherkasov, A. A. Skatova, I. L. Fedushkin, *Chem. Eur. J.* **2021,** *27*, 5745-5753.
288. C. M. Mömming, E. Otten, G. Kehr, R. Fröhlich, S. Grimme, D. W. Stephan, G. Erker, *Angew. Chem. Int. Ed.* **2009,** *48*, 6643-6646.
289. F. Buß, P. Mehlmann, C. Mück-Lichtenfeld, K. Bergander, F. Dielmann, *J. Am. Chem. Soc.* **2016,** *138*, 1840-1843.
290. L. F. B. Wilm, T. Eder, C. Mück-Lichtenfeld, P. Mehlmann, M. Wünsche, F. Buß, F. Dielmann, *Green Chem.* **2019,** *21*, 640-648.
291. Y. Yang, L. Yan, Q. Xie, Q. Liang, D. Song, *Org. Biomol. Chem.* **2017,** *15*, 2240-2245.
292. A. Caise, J. Hicks, M. Ángeles Fuentes, J. M. Goicoechea, S. Aldridge, *Chem. Eur. J.* **2021,** *27*, 2138-2148.
293. M. Xu, A. R. Jupp, D. W. Stephan, *Angew. Chem. Int. Ed.* **2017,** *56*, 14277-14281.
294. J. N. Gayton, Q. Li, L. Sanders, R. R. Rodrigues, G. Hill, J. H. Delcamp, *ACS Omega* **2020,** *5*, 11687-11694.
295. H. Yamamoto, K. Futatsugi, *Angew. Chem. Int. Ed.* **2005,** *44*, 1924-1942.
296. E. J. Corey, T. Shibata, T. W. Lee, *J. Am. Chem. Soc.* **2002,** *124*, 3808-3809.
297. D. H. Ryu, E. J. Corey, *J. Am. Chem. Soc.* **2003,** *125*, 6388-6390.
298. D. H. Ryu, T. W. Lee, E. J. Corey, *J. Am. Chem. Soc.* **2002,** *124*, 9992-9993.
299. R. J. Gillespie, *Coord. Chem. Rev.* **2008,** *252*, 1315-1327.
300. A. I. Boldyrev, J. Simons, *J. Am. Chem. Soc.* **1998,** *120*, 7967-7972.
301. M. Driess, J. Aust, K. Merz, C. van Wullen, *Angew. Chem. Int. Ed.* **1999,** *38*, 3677-3680.
302. X. Li, L.-S. Wang, A. I. Boldyrev, J. Simons, *J. Am. Chem. Soc.* **1999,** *121*, 6033-6038.
303. L.-S. Wang, A. I. Boldyrev, X. Li, J. Simons, *J. Am. Chem. Soc.* **2000,** *122*, 7681-7687.
304. D. W. Stephan, *Angew. Chem. Int. Ed.* **2000,** *39*, 501-502.
305. A. I. Boldyrev, X. Li, L.-S. Wang, *Angew. Chem. Int. Ed.* **2000,** *39*, 3307-3310.

306. N. L. Dunn, M. Ha, A. T. Radosevich, *J. Am. Chem. Soc.* **2012,** *134*, 11330-11333.
307. T. P. Robinson, D. M. De Rosa, S. Aldridge, J. M. Goicoechea, *Angew. Chem. Int. Ed.* **2015,** *54*, 13758-63.
308. K. Lee, A. V. Blake, A. Tanushi, S. M. McCarthy, D. Kim, S. M. Loria, C. M. Donahue, K. D. Spielvogel, J. M. Keith, S. R. Daly*, et al.*, *Angew. Chem. Int. Ed.* **2019,** *58*, 6993-6998.
309. T. M. Bass, C. R. Carr, T. J. Sherbow, J. C. Fettinger, L. A. Berben, *Inorg. Chem.* **2020,** *59*, 13517-13523.
310. P. Ghana, J. Rump, G. Schnakenburg, M. I. Arz, A. C. Filippou, *J. Am. Chem. Soc.* **2021,** *143*, 420-432.
311. J. M. Lipshultz, G. Li, A. T. Radosevich, *J. Am. Chem. Soc.* **2021,** *143*, 1699-1721.
312. J. M. Lehn, Nitrogen inversion. In *Top. Curr. Chem.*, Springer Berlin Heidelberg: **1970**; Vol. 15/3, pp 311-377.
313. A. Rauk, L. C. Allen, K. Mislow, *Angew. Chem. Int. Ed.* **1970,** *9*, 400-414.
314. A. I. Boldyrev, O. P. Charkin, *J. Struct. Chem.* **1985,** *26*, 451-475.
315. W. Cherry, N. Epiotis, *J. Am. Chem. Soc.* **1976,** *98*, 1135-1140.
316. R. F. See, A. D. Dutoi, K. W. McConnell, R. M. Naylor, *J. Am. Chem. Soc.* **2001,** *123*, 2839-2848.
317. L. T. Xu, T. Y. Takeshita, T. H. Dunning, *Theor. Chem. Acc.* **2014,** *133*, 1493.
318. S. Pelzer, K. Wichmann, R. Wesendrup, P. Schwerdtfeger, *J. Phys. Chem. A* **2002,** *106*, 6387-6394.
319. Z. Varga, P. Verma, D. G. Truhlar, *J. Phys. Chem. A* **2019,** *123*, 301-312.
320. A. Najibi, L. Goerigk, *J. Comput. Chem.* **2020,** *41*, 2562-2572.
321. J. C. Southern, A Review of Alumina Production, Characterization, and Use. In *Materials & Equipment/Whitewares: Ceramic Engineering and Science Proceedings*, 2 ed.; W. M. Carty, Ed. The American Ceramic Society: Westerville, OH, **2001**; Vol. 22, pp 59-59.
322. P. R. Wells, Group Electronegativities. In *Progress in Physical Organic Chemistry*, A. J. Streitwieser; R. W. Taft, Eds. John Wiley and Sons, Inc. : New York, **1968**; Vol. 6, pp 111-145.
323. H. J. Monkhorst, *Chem. Commun.* **1968**, 1111-1112.
324. R. Hoffmann, R. W. Alder, C. F. Wilcox, *J. Am. Chem. Soc.* **1970,** *92*, 4992-4993.
325. R. Hoffmann, *Pure Appl. Chem.* **1971,** *28*, 181-194.
326. J. B. Collins, J. D. Dill, E. D. Jemmis, Y. Apeloig, P. v. R. Schleyer, R. Seeger, J. A. Pople, *J. Am. Chem. Soc.* **1976,** *98*, 5419-5427.
327. K. Yoshizawa, A. Suzuki, T. Yamabe, *J. Am. Chem. Soc.* **1999,** *121*, 5266-5273.
328. K. Yoshizawa, *J. Organomet. Chem.* **2001,** *635*, 100-109.
329. R. Keese, *Chem. Rev.* **2006,** *106*, 4787-4808.
330. L.-M. Yang, E. Ganz, Z. Chen, Z.-X. Wang, P. v. R. Schleyer, *Angew. Chem. Int. Ed.* **2015,** *54*, 9468-9501.
331. O. Dobis, S. W. Benson, *Int. J. Chem. Kinet.* **1987,** *19*, 691-708.
332. Y.-R. Luo, *Comprehensive Handbook of Chemical Bond Energies*. CRC Press: Hoboken, **2007**.
333. D. J. Goebbert, P. G. Wenthold, *Int. J. Mass spectrom.* **2006,** *257*, 1-11.
334. D. B. Workman, R. R. Squires, *Inorg. Chem.* **1988,** *27*, 1846-1848.

335. A. Tajti, P. G. Szalay, A. G. Császár, M. Kállay, J. Gauss, E. F. Valeev, B. A. Flowers, J. Vázquez, J. F. Stanton, *J. Chem. Phys.* **2004,** *121*, 11599-11613.
336. Y. J. Bomble, J. Vázquez, M. Kállay, C. Michauk, P. G. Szalay, A. G. Császár, J. Gauss, J. F. Stanton, *J. Chem. Phys.* **2006,** *125*, 064108.
337. M. E. Harding, J. Vázquez, B. Ruscic, A. K. Wilson, J. Gauss, J. F. Stanton, *J. Chem. Phys.* **2008,** *128*, 114111.
338. J. H. Thorpe, C. A. Lopez, T. L. Nguyen, J. H. Baraban, D. H. Bross, B. Ruscic, J. F. Stanton, *J. Chem. Phys.* **2019,** *150*, 224102.
339. D. A. Matthews, L. Cheng, M. E. Harding, F. Lipparini, S. Stopkowicz, T.-C. Jagau, P. G. Szalay, J. Gauss, J. F. Stanton, *J. Chem. Phys.* **2020,** *152*, 214108.
340. R. S. Grev, H. F. Schaefer, *J. Chem. Soc., Chem. Commun.* **1983**, 785-786.
341. M. S. Gordon, D. R. Gano, J. S. Binkley, M. J. Frisch, *J. Am. Chem. Soc.* **1986,** *108*, 2191-2195.
342. C. Sosa, H. B. Schlegel, *J. Am. Chem. Soc.* **1984,** *106*, 5847-5852.
343. I. S. Ignatyev, H. F. Schaefer, *J. Am. Chem. Soc.* **1997,** *119*, 12306-12310.
344. R. Becerra, S. E. Boganov, M. P. Egorov, V. I. Faustov, O. M. Nefedov, R. Walsh, *Can. J. Chem.* **2000,** *78*, 1428-1433.
345. G. Merino, S. Escalante, A. Vela, *J. Phys. Chem. A* **2004,** *108*, 4909-4915.
346. Y. Wang, J. Ma, *J. Organomet. Chem.* **2009,** *694*, 2567-2575.
347. S. E. Boganov, V. M. Promyslov, V. I. Faustov, M. P. Egorov, O. M. Nefedov, *Russ. Chem. Bull.* **2011,** *60*, 2147-2160.
348. X. Wang, L. Andrews, G. V. Chertihin, P. F. Souter, *J. Phys. Chem. A* **2002,** *106*, 6302-6308.
349. X. Wang, L. Andrews, G. P. Kushto, *J. Phys. Chem. A* **2002,** *106*, 5809-5816.
350. L. Andrews, X. Wang, *J. Phys. Chem. A* **2002,** *106*, 7696-7702.
351. X. Wang, L. Andrews, *J. Am. Chem. Soc.* **2003,** *125*, 6581-6587.
352. R. P. Bell, C. N. Hinshelwood, *Proc. R. Soc. A: Math. Phys. Sci.* **1936,** *154*, 414-429.
353. M. G. Evans, M. Polanyi, *T. Faraday Soc.* **1938,** *34*, 11-24.
354. P. Muller, *Pure Appl. Chem.* **1994,** *66*, 1077-1184.
355. Y.-C. Lin, E. Hatzakis, S. M. McCarthy, K. D. Reichl, T.-Y. Lai, H. P. Yennawar, A. T. Radosevich, *J. Am. Chem. Soc.* **2017,** *139*, 6008-6016.
356. S. Volodarsky, R. Dobrovetsky, *Chem. Commun.* **2018,** *54*, 6931-6934.
357. J. C. Gilhula, A. T. Radosevich, *Chem. Sci.* **2019,** *10*, 7177-7182.
358. A. Brand, W. Uhl, *Chem. Eur. J.* **2019,** *25*, 1391-1404.
359. G. T. Cleveland, A. T. Radosevich, *Angew. Chem. Int. Ed.* **2019,** *58*, 15005-15009.
360. R. E. von H. Spence, D. J. Parks, W. E. Piers, M.-A. MacDonald, M. J. Zaworotko, S. J. Rettig, *Angew. Chem. Int. Ed.* **1995,** *34*, 1230-1233.
361. U. Radius, S. J. Silverio, R. Hoffmann, R. Gleiter, *Organometallics* **1996,** *15*, 3737-3745.
362. S. Kirschner, M. Peters, K. Yuan, M. Uzelac, M. J. Ingleson, *Chem. Sci.* **2022,** *13*, 2661-2668.
363. D. Höfler, M. van Gemmeren, P. Wedemann, K. Kaupmees, I. Leito, M. Leutzsch, J. B. Lingnau, B. List, *Angew. Chem. Int. Ed.* **2017,** *56*, 1411-1415.
364. L. Ratjen, M. van Gemmeren, F. Pesciaioli, B. List, *Angew. Chem. Int. Ed.* **2014,** *53*, 8765-8769.
365. I. Krossing, I. Raabe, *Chem. Eur. J.* **2004,** *10*, 5017-5030.

366. N. Bormann, J. S. Ward, A. K. Bergmann, P. Wenz, K. Rissanen, Y. Gong, W.-B. Hatz, A. Burbaum, F. F. Mulks, *Chem. Eur. J.* **2023,** *29*, e202302089.
367. A. Hermannsdorfer, M. Driess, *Angew. Chem. Int. Ed.* **2020,** *59*, 23132-23136.
368. C. Foroutan-Nejad, J. Vicha, R. Marek, *Chem. Eur. J.* **2014,** *20*, 11584-11590.
369. J. F. Kögel, D. A. Sorokin, A. Khvorost, M. Scott, K. Harms, D. Himmel, I. Krossing, J. Sundermeyer, *Chem. Sci.* **2018,** *9*, 245-253.
370. F. S. Tschernuth, T. Thorwart, L. Greb, F. Hanusch, S. Inoue, *Angew. Chem. Int. Ed.* **2021,** *60*, 25799-25803.
371. A. Osi, N. Niessen, D. Mahaut, B. Champagne, A. Chardon, N. Tumanov, J. Wouters, G. Berionni, *Z. Anorg. Allg. Chem.* **2023,** *649*, e202300009.
372. J. Brzeski, *J. Comput. Chem.* **2023,** *44*, 1454-1463.
373. L. O. Müller, D. Himmel, J. Stauffer, G. Steinfeld, J. Slattery, G. Santiso-Quiñones, V. Brecht, I. Krossing, *Angew. Chem. Int. Ed.* **2008,** *47*, 7659-7663.
374. L. S. Warring, J. E. Walley, D. A. Dickie, W. Tiznado, S. Pan, R. J. Gilliard, Jr., *Inorg. Chem.* **2022,** *61*, 18640-18652.
375. D. Duvinage, L. A. Malaspina, S. Grabowsky, S. Mebs, J. Beckmann, *Eur. J. Inorg. Chem.* **2023,** *26*, e202200482.
376. K. F. Hoffmann, A. Wiesner, S. Steinhauer, S. Riedel, *Chem. Eur. J.* **2022,** *28*, e202201958.
377. A. Hermannsdorfer, M. Driess, *Angew. Chem. Int. Ed.* **2021,** *60*, 13656-13660.
378. Y. Gong, J. S. Ward, K. Rissanen, F. F. Mulks, *Molbank* **2023,** *29*, M1710.
379. R. Maskey, M. Schädler, C. Legler, L. Greb, *Angew. Chem. Int. Ed.* **2018,** *57*, 1717-1720.
380. D. Hartmann, M. Schädler, L. Greb, *Chem. Sci.* **2019,** *10*, 7379-7388.
381. D. Roth, H. Wadepohl, L. Greb, *Angew. Chem. Int. Ed.* **2020,** *59*, 20930-20934.
382. D. Roth, J. Stirn, D. W. Stephan, L. Greb, *J. Am. Chem. Soc.* **2021,** *143*, 15845-15851.
383. T. Thorwart, D. Roth, L. Greb, **2021,** *27*, 10422-10427.
384. T. Thorwart, D. Hartmann, L. Greb, **2022,** *28*, e202202273.
385. D. Roth, T. Thorwart, C. Douglas, L. Greb, *Chem. Eur. J.* **2023,** *29*, e202203024.
386. J. R. Gaffen, J. N. Bentley, L. C. Torres, C. Chu, T. Baumgartner, C. B. Caputo, *Chem* **2019,** *5*, 1567-1583.
387. R. J. Mayer, N. Hampel, A. R. Ofial, *Chem. Eur. J.* **2021,** *27*, 4070-4080.
388. P. Erdmann, L. Greb, *Angew. Chem. Int. Ed.* **2022,** *61*, e202114550.
389. L. Zapf, M. Riethmann, S. A. Föhrenbacher, M. Finze, U. Radius, *Chem. Sci.* **2023,** *14*, 2275-2288.
390. *RDKit: Open-source cheminformatics*. https://www.rdkit.org (accessed January 31, 2024).
391. A. L. Liberman-Martin, R. G. Bergman, T. D. Tilley, *J. Am. Chem. Soc.* **2015,** *137*, 5328-5331.
392. A. T. Henry, D. A. R. Nanan, K. M. Baines, *Dalton Trans.* **2023,** *52*, 10363-10371.
393. L. Greb, *Synlett* **2023,** *34*, A-Q.
394. C. R. Groom, I. J. Bruno, M. P. Lightfoot, S. C. Ward, *Acta Crystallogr. B* **2016,** *72*, 171-179.
395. D. Bajusz, A. Rácz, K. Héberger, *J. Cheminform.* **2015,** *7*, 20.
396. H. L. Morgan, *J. Chem. Doc.* **1965,** *5*, 107-113.
397. Z.-L. Wang, H.-S. Hu, L. von Szentpály, H. Stoll, S. Fritzsche, P. Pyykkö, W. H. E. Schwarz, J. Li, *Chem. Eur. J.* **2020,** *26*, 15558-15564.

398. R. G. Cavell, D. D. Poulin, K. I. The, A. J. Tomlinson, *J. Chem. Soc., Chem. Commun.* **1974**, 19-21.
399. J. Kobayashi, T. Kawashima, *C. R. Chim.* **2010,** *13*, 1249-1259.
400. N. Artrith, K. T. Butler, F.-X. Coudert, S. Han, O. Isayev, A. Jain, A. Walsh, *Nat. Chem.* **2021,** *13*, 505-508.
401. P. M. Pflüger, F. Glorius, *Angew. Chem. Int. Ed.* **2020,** *59*, 18860-18865.
402. W. L. Williams, L. Zeng, T. Gensch, M. S. Sigman, A. G. Doyle, E. V. Anslyn, *ACS Cent. Sci.* **2021,** *7*, 1622-1637.
403. F. A. Faber, L. Hutchison, B. Huang, J. Gilmer, S. S. Schoenholz, G. E. Dahl, O. Vinyals, S. Kearnes, P. F. Riley, O. A. von Lilienfeld, *J. Chem. Theory Comput.* **2017,** *13*, 5255-5264.
404. L. C. Gallegos, G. Luchini, P. C. St. John, S. Kim, R. S. Paton, *Acc. Chem. Res.* **2021,** *54*, 827-836.
405. C. Gaul, S. Cuesta-Lopez, *Phys. Status Solidi B* **2023**, 2200553.
406. F. Sandfort, F. Strieth-Kalthoff, M. Kühnemund, C. Beecks, F. Glorius, *Chem* **2020,** *6*, 1379-1390.
407. T. Kirschbaum, B. von Seggern, J. Dzubiella, A. Bande, F. Noé, *J. Chem. Theory Comput.* **2023,** *19*, 4461-4473.
408. F. E. Storm, L. M. Folkmann, T. Hansen, K. V. Mikkelsen, *J. Mol. Model.* **2022,** *28*, 313.
409. W. Li, Y. Luan, Q. Zhang, J. Aires-de-Sousa, *Mol. Inform.* **2023,** *42*, 2200193.
410. H. Yu, Y. Wang, X. Wang, J. Zhang, S. Ye, Y. Huang, Y. Luo, E. Sharman, S. Chen, J. Jiang, *J. Phys. Chem. A* **2020,** *124*, 3844-3850.
411. M. Wen, S. M. Blau, E. W. C. Spotte-Smith, S. Dwaraknath, K. A. Persson, *Chem. Sci.* **2021,** *12*, 1858-1868.
412. M. Nakajima, T. Nemoto, *Sci. Rep.* **2021,** *11*, 20207.
413. M. Cordova, E. A. Engel, A. Stefaniuk, F. Paruzzo, A. Hofstetter, M. Ceriotti, L. Emsley, *J. Phys. Chem. C* **2022,** *126*, 16710-16720.
414. E. Jonas, S. Kuhn, *J. Cheminform.* **2019,** *11*, 50.
415. J. B. Kleine Büning, S. Grimme, *J. Chem. Theory Comput.* **2023,** *19*, 3601-3615.
416. A. A. Ksenofontov, Y. I. Isaev, M. M. Lukanov, D. M. Makarov, V. A. Eventova, I. A. Khodov, M. B. Berezin, *Phys. Chem. Chem. Phys.* **2023,** *25*, 9472-9481.
417. E. E. Ondar, M. V. Polynski, V. P. Ananikov, *ChemPhysChem* **2023,** *24*, e202200940.
418. F. M. Paruzzo, A. Hofstetter, F. Musil, S. De, M. Ceriotti, L. Emsley, *Nat. Commun.* **2018,** *9*, 4501.
419. P. Bleiziffer, K. Schaller, S. Riniker, *J. Chem. Inf. Model.* **2018,** *58*, 579-590.
420. R. Martin, D. Heider, *Front. Genet.* **2019,** *10*, 990.
421. J. Wang, D. Cao, C. Tang, X. Chen, H. Sun, T. Hou, *Bioinformatics* **2020,** *36*, 4721-4728.
422. A. Jinich, B. Sanchez-Lengeling, H. Ren, R. Harman, A. Aspuru-Guzik, *ACS Cent. Sci.* **2019,** *5*, 1199-1210.
423. R. Fedorov, G. Gryn'ova, *J. Chem. Theory Comput.* **2023,** *19*, 4796-4814.
424. S. S. S. V, J. N. Law, C. E. Tripp, D. Duplyakin, E. Skordilis, D. Biagioni, R. S. Paton, P. C. St. John, *Nat. Mach. Intell.* **2022,** *4*, 720-730.
425. M. Orlandi, M. Escudero-Casao, G. Licini, *J. Org. Chem.* **2021,** *86*, 3555-3564.
426. G. Hoffmann, M. Balcilar, V. Tognetti, P. Héroux, B. Gaüzère, S. Adam, L. Joubert, *J. Comput. Chem.* **2020,** *41*, 2124-2136.

427. S. A. Cuesta, M. Moreno, R. A. López, J. R. Mora, J. L. Paz, E. A. Márquez, *J. Chem. Inf. Model.* **2023,** *63*, 507-521.
428. Y. Liu, Q. Yang, J. Cheng, L. Zhang, S. Luo, J.-P. Cheng, *ChemPhysChem* **2023,** *24*, e202300162.
429. H. Huynh, K. Le, L. Vu, T. Nguyen, M. Holcomb, S. Forli, H. Phan, **2023**, ChemRxiv preprint, DOI: 10.26434/chemrxiv-2023-lcxn0.
430. K. Jorner, T. Brinck, P.-O. Norrby, D. Buttar, *Chem. Sci.* **2021,** *12*, 1163-1175.
431. S. M. Lundberg, G. Erion, H. Chen, A. DeGrave, J. M. Prutkin, B. Nair, R. Katz, J. Himmelfarb, N. Bansal, S.-I. Lee, *Nat. Mach. Intell.* **2020,** *2*, 56-67.
432. S. M. Lundberg, S.-I. Lee, *Adv. Neural. Inf. Process. Syst.* **2017,** *30*.
433. F. R. Burden, *J. Chem. Inf. Comput. Sci.* **1989,** *29*, 225-227.
434. M. P. González, C. Terán, M. Teijeira, P. Besada, M. J. González-Moa, *Bioorg. Med. Chem. Lett.* **2005,** *15*, 3491-3495.
435. D. T. Stanton, *J. Chem. Inf. Comput. Sci.* **1999,** *39*, 11-20.
436. L. Goerigk, A. Hansen, C. Bauer, S. Ehrlich, A. Najibi, S. Grimme, *Phys. Chem. Chem. Phys.* **2017,** *19*, 32184-32215.
437. N. Ansmann, D. Hartmann, S. Sailer, P. Erdmann, R. Maskey, M. Schorpp, L. Greb, *Angew. Chem. Int. Ed.* **2022,** *61*, e202203947.
438. M. P. Coles, *Chem. Commun.* **2009**, 3659-3676.
439. R. C. Pratt, B. G. G. Lohmeijer, D. A. Long, R. M. Waymouth, J. L. Hedrick, *J. Am. Chem. Soc.* **2006,** *128*, 4556-4557.
440. M. K. Kiesewetter, M. D. Scholten, N. Kirn, R. L. Weber, J. L. Hedrick, R. M. Waymouth, *J. Org. Chem.* **2009,** *74*, 9490-9496.
441. S. L. Aeilts, M. P. Coles, D. C. Swenson, R. F. Jordan, V. G. Young, *Organometallics* **1998,** *17*, 3265-3270.
442. O. Ciobanu, P. Roquette, S. Leingang, H. Wadepohl, J. Mautz, H.-J. Himmel, *Eur. J. Inorg. Chem.* **2007,** *2007*, 4530-4534.
443. A. Wagner, S. Litters, J. Elias, E. Kaifer, H.-J. Himmel, *Chem. Eur. J.* **2014,** *20*, 12514-12527.
444. A. Widera, D. Vogler, H. Wadepohl, E. Kaifer, H.-J. Himmel, *Angew. Chem. Int. Ed.* **2018,** *57*, 11456-11459.
445. H.-J. Himmel, *Angew. Chem. Int. Ed.* **2019,** *58*, 11600-11617.
446. F. A. Cotton, C. A. Murillo, X. Wang, C. C. Wilkinson, *Inorg. Chem.* **2006,** *45*, 5493-5500.
447. F. A. Cotton, J. P. Donahue, D. L. Lichtenberger, C. A. Murillo, D. Villagrán, *J. Am. Chem. Soc.* **2005,** *127*, 10808-10809.
448. W. J. Evans, E. Montalvo, D. J. Dixon, J. W. Ziller, A. G. DiPasquale, A. L. Rheingold, *Inorg. Chem.* **2008,** *47*, 11376-11381.
449. W. J. Evans, E. Montalvo, J. W. Ziller, A. G. DiPasquale, A. L. Rheingold, *Inorg. Chem.* **2010,** *49*, 222-228.
450. H. Braunschweig, F. Guethlein, *Angew. Chem. Int. Ed.* **2011,** *50*, 12613-12616.
451. E. C. Neeve, S. J. Geier, I. A. I. Mkhalid, S. A. Westcott, T. B. Marder, *Chem. Rev.* **2016,** *116*, 9091-9161.
452. É. Rochette, N. Bouchard, J. Légaré Lavergne, C. F. Matta, F.-G. Fontaine, *Angew. Chem. Int. Ed.* **2016,** *55*, 12722-12726.

453. L. Kistner, L. M. Sigmund, F. F. Grieser, J. Krauß, S. Leingang, E. Kaifer, L. Greb, H.-J. Himmel, *Angew. Chem. Int. Ed.* **2024,** *63*, e202317462.
454. F. M. Bickelhaupt, K. N. Houk, **2017,** *56*, 10070-10086.
455. G. Robinson, C. Y. Tang, R. Köppe, A. R. Cowley, H.-J. Himmel, *Chem. Eur. J.* **2007,** *13*, 2648-2654.
456. G. R. Fulmer, A. J. M. Miller, N. H. Sherden, H. E. Gottlieb, A. Nudelman, B. M. Stoltz, J. E. Bercaw, K. I. Goldberg, *Organometallics* **2010,** *29*, 2176-2179.
457. *Bruker corp., TopSpin | NMR Data Analysis*. https://www.bruker.com/en/products-and-solutions/mr/nmr-software/topspin.html (accessed January 31, 2024).
458. *Mestrelab Research S.L., Mnova*. https://mestrelab.com/download/mnova/ (accessed January 31, 2024).
459. Z. Otwinowski, W. Minor, *Methods Enzymol.* **1997,** *276*, 307-26.
460. *Bruker corp., Apex Software*. https://www.bruker.com/en/products-and-solutions/diffractometers-and-x-ray-microscopes/single-crystal-x-ray-diffractometers/sc-xrd-software/apex.html (accessed January 31, 2024).
461. SAINT, Bruker AXS GmbH, Karlsruhe, Germany, 2016.
462. G. M. Sheldrick, SADABS, Bruker AXS GmbH, Karlsruhe, Germany, 2016.
463. G. M. Sheldrick, SHELXT, Program for Crystal Structure Solution, University of Göttingen, Germany, 2014.
464. G. M. Sheldrick, *Acta Crystallogr. A* **2015**, 3-8.
465. W. Robinson, G. M. Sheldrick, Crystallographic Computing 4. N. W. Isaaks; M. R. Taylor, Eds. Ch. 22, IUCr and Oxford University Press, Oxford, UK, 1988.
466. G. M. Sheldrick, *Acta Crystallogr. A* **2008,** *64*, 112-122.
467. G. M. Sheldrick, SHELXL-20xx, University of Göttingen and Bruker AXS GmbH, Karlsruhe, Germany, 2012.
468. G. M. Sheldrick, *Acta Crystallogr. C* **2015,** *71*, 3-8.
469. C. B. Hubschle, G. M. Sheldrick, B. Dittrich, *J. Appl. Crystallogr.* **2011,** *44*, 1281-1284.
470. O. V. Dolomanov, L. J. Bourhis, R. J. Gildea, J. A. K. Howard, H. Puschmann, *J. Appl. Crystallogr.* **2009,** *42*, 339-341.
471. D. Kratzert, *FinalCif*. https://dkratzert.de/finalcif.html (accessed January 31, 2024).
472. I. J. Bruno, J. C. Cole, P. R. Edgington, M. Kessler, C. F. Macrae, P. McCabe, J. Pearson, R. Taylor, *Acta Crystallogr. B* **2002,** *58*, 389-397.
473. C. F. Macrae, P. R. Edgington, P. McCabe, E. Pidcock, G. P. Shields, R. Taylor, M. Towler, J. van de Streek, *J. Appl. Crystallogr.* **2006,** *39*, 453-457.
474. C. F. Macrae, I. Sovago, S. J. Cottrell, P. T. A. Galek, P. McCabe, E. Pidcock, M. Platings, G. P. Shields, J. S. Stevens, M. Towler, *et al.*, *J. Appl. Crystallogr.* **2020,** *53*, 226-235.
475. P. Pracht, F. Bohle, S. Grimme, *Phys. Chem. Chem. Phys.* **2020,** *22*, 7169-7192.
476. C. Bannwarth, S. Ehlert, S. Grimme, *J. Chem. Theory Comput.* **2019,** *15*, 1652-1671.
477. C. Bannwarth, E. Caldeweyher, S. Ehlert, A. Hansen, P. Pracht, J. Seibert, S. Spicher, S. Grimme, *WIREs Comput. Mol. Sci.* **2021,** *11*, e1493.
478. S. Grimme, J. G. Brandenburg, C. Bannwarth, A. Hansen, *J. Chem. Phys.* **2015,** *143*.
479. H. Kruse, S. Grimme, *J. Chem. Phys.* **2012,** *136*, 154101.
480. S. Grimme, J. Antony, S. Ehrlich, H. Krieg, *J. Chem. Phys.* **2010,** *132*, 154104.
481. S. Grimme, S. Ehrlich, L. Goerigk, *J. Comput. Chem.* **2011,** *32*, 1456-1465.
482. S. Grimme, A. Hansen, S. Ehlert, J.-M. Mewes, *J. Chem. Phys.* **2021,** *154*, 064103.
483. E. Caldeweyher, C. Bannwarth, S. Grimme, *J. Chem. Phys.* **2017,** *147*, 034112.

484. E. Caldeweyher, S. Ehlert, A. Hansen, H. Neugebauer, S. Spicher, C. Bannwarth, S. Grimme, *J. Chem. Phys.* **2019,** *150*, 154122.
485. F. Weigend, *Phys. Chem. Chem. Phys.* **2006,** *8*, 1057-1065.
486. G. L. Stoychev, A. A. Auer, F. Neese, *J. Chem. Theory Comput.* **2017,** *13*, 554-562.
487. N. Mardirossian, M. Head-Gordon, *J. Chem. Phys.* **2015,** *142*.
488. A. Najibi, L. Goerigk, *J. Chem. Theory Comput.* **2018,** *14*, 5725-5738.
489. F. Weigend, R. Ahlrichs, *Phys. Chem. Chem. Phys.* **2005,** *7*, 3297-3305.
490. T. H. Dunning, Jr., *J. Chem. Phys.* **1989,** *90*, 1007-1023.
491. D. E. Woon, T. H. Dunning, Jr., *J. Chem. Phys.* **1993,** *98*, 1358-1371.
492. A. K. Wilson, D. E. Woon, K. A. Peterson, T. H. Dunning Jr., *J. Chem. Phys.* **1999,** *110*, 7667-7676.
493. B. P. Prascher, D. E. Woon, K. A. Peterson, T. H. Dunning, A. K. Wilson, *Theor. Chem. Acc.* **2011,** *128*, 69-82.
494. G. D. Purvis III, R. J. Bartlett, *J. Chem. Phys.* **1982,** *76*, 1910-1918.
495. K. Raghavachari, G. W. Trucks, J. A. Pople, M. Head-Gordon, *Chem. Phys. Lett.* **1989,** *157*, 479-483.
496. J. D. Watts, J. Gauss, R. J. Bartlett, *J. Chem. Phys.* **1993,** *98*, 8718-8733.
497. R. A. Kendall, T. H. Dunning, Jr., R. J. Harrison, *J. Chem. Phys.* **1992,** *96*, 6796-6806.
498. K. A. Peterson, T. H. D. Jr., *J. Chem. Phys.* **2002,** *117*, 10548-10560.
499. N. J. DeYonker, K. A. Peterson, A. K. Wilson, *J. Phys. Chem. A* **2007,** *111*, 11383-11393.
500. B. O. Roos, P. R. Taylor, P. E. M. Sigbahn, *Chem. Phys.* **1980,** *48*, 157-173.
501. S. Grimme, *Chem. Eur. J.* **2012,** *18*, 9955-9964.
502. *SCM, Theoretical Chemistry, Vrije Universiteit, Amsterdam, The Netherlands, http://www.scm.com*. (accessed January 31, 2024).
503. A. Klamt, *J. Phys. Chem.* **1995,** *99*, 2224-2235.
504. A. Klamt, V. Jonas, T. Bürger, J. C. W. Lohrenz, *J. Phys. Chem. A* **1998,** *102*, 5074-5085.
505. A. Klamt, *COSMO-RS From Quantum Chemistry to Fluid Phase Thermodynamics and Drug Design*. Elsevier Science Amsterdam, **2005**.
506. G. te Velde, F. M. Bickelhaupt, E. J. Baerends, C. Fonseca Guerra, S. J. A. van Gisbergen, J. G. Snijders, T. Ziegler, *J. Comput. Chem.* **2001,** *22*, 931-967.
507. C. C. Pye, T. Ziegler, E. van Lenthe, J. N. Louwen, *Can. J. Chem.* **2009,** *87*, 790-797.
508. F. Neese, A. Hansen, D. G. Liakos, *J. Chem. Phys.* **2009,** *131*, 064103.
509. C. Riplinger, F. Neese, *J. Chem. Phys.* **2013,** *138*, 034106.
510. C. Riplinger, B. Sandhoefer, A. Hansen, F. Neese, *J. Chem. Phys.* **2013,** *139*, 134101.
511. C. Riplinger, P. Pinski, U. Becker, E. F. Valeev, F. Neese, *J. Chem. Phys.* **2016,** *144*, 024109.
512. H. J. Werner, P. J. Knowles, *J. Chem. Phys.* **1988,** *89*, 5803-5814.
513. P. J. Knowles, H.-J. Werner, *Chem. Phys. Lett.* **1988,** *145*, 514-522.
514. C. Angeli, R. Cimiraglia, S. Evangelisti, T. Leininger, J.-P. Malrieu, *J. Chem. Phys.* **2001,** *114*, 10252-10264.
515. C. Angeli, R. Cimiraglia, J.-P. Malrieu, *Chem. Phys. Lett.* **2001,** *350*, 297-305.
516. C. Angeli, R. Cimiraglia, J.-P. Malrieu, *J. Chem. Phys.* **2002,** *117*, 9138-9153.
517. Y. Zhao, D. G. Truhlar, *J. Phys. Chem. A* **2005,** *109*, 5656-5667.
518. S. Kozuch, D. Gruzman, J. M. L. Martin, *J. Phys. Chem. C* **2010,** *114*, 20801-20808.
519. S. Kozuch, J. M. L. Martin, *J. Comput. Chem.* **2013,** *34*, 2327-2344.
520. S. Kozuch, J. M. L. Martin, *Phys. Chem. Chem. Phys.* **2011,** *13*, 20104-20107.

521. T. Yanai, D. P. Tew, N. C. Handy, *Chem. Phys. Lett.* **2004,** *393*, 51-57.
522. C. Adamo, V. Barone, *J. Chem. Phys.* **1999,** *110*, 6158-6170.
523. T. Soda, Y. Kitagawa, T. Onishi, Y. Takano, Y. Shigeta, H. Nagao, Y. Yoshioka, K. Yamaguchi, *Chem. Phys. Lett.* **2000,** *319*, 223-230.
524. K. Yamaguchi, Y. Takahara, T. Fueno, *Applied Quantum Chemistry* **1986**, 155-184.
525. F. London, *J. Phys. Radium* **1937,** *8*, 397-409.
526. H. F. Hameka, *Mol. Phys.* **1958,** *1*, 203-215.
527. R. Ditchfield, *J. Chem. Phys.* **1972,** *56*, 5688-5691.
528. K. Wolinski, J. F. Hinton, P. Pulay, *J. Am. Chem. Soc.* **1990,** *112*, 8251-8260.
529. W. Kutzelnigg, *Isr. J. Chem.* **1980,** *19*, 193-200.
530. M. Schindler, W. Kutzelnigg, *J. Chem. Phys.* **1982,** *76*, 1919-1933.
531. F. Neese, *WIREs Comput. Mol. Sci.* **2012,** *2*, 73-78.
532. F. Neese, *WIREs Comput. Mol. Sci.* **2018,** *8*, e1327.
533. F. Neese, *WIREs Comput. Mol. Sci.* **2022,** *12*, e1606.
534. H.-J. Werner, P. J. Knowles, G. Knizia, F. R. Manby, M. Schütz, *WIREs Comput. Mol. Sci.* **2012,** *2*, 242-253.
535. H.-J. Werner, P. J. Knowles, F. R. Manby, J. A. Black, K. Doll, A. Heßelmann, D. Kats, A. Köhn, T. Korona, D. A. Kreplin, *et al.*, *J. Chem. Phys.* **2020,** *152*, 144107.
536. E. D. Glendening, C. R. Landis, F. Weinhold, *J. Comput. Chem.* **2013,** *34*, 1429-1437.
537. E. D. Glendening, C. R. Landis, F. Weinhold, *J. Comput. Chem.* **2019,** *40*, 2234-2241.
538. J. Contreras-García, E. R. Johnson, S. Keinan, R. Chaudret, J.-P. Piquemal, D. N. Beratan, W. Yang, *J. Chem. Theory Comput.* **2011,** *7*, 625-632.
539. T. Lu, F. Chen, *J. Comput. Chem.* **2012,** *33*, 580-592.
540. G. A. Andrienko, *Chemcraft 1.8*. https://www.chemcraftprog.com (accessed January 31, 2024).
541. Schrodinger, LLC, The PyMOL Molecular Graphics System, Version 2.4. **2021**.
542. G. Knizia, *IboView*. http://www.iboview.org/ (accessed January 31, 2024).
543. G. Knizia, *J. Chem. Theory Comput.* **2013,** *9*, 4834-4843.
544. C. Y. Legault, *CYLview 2.0*. http://www.cylview.org (accessed January 31, 2024).
545. M. D. Hanwell, D. E. Curtis, D. C. Lonie, T. Vandermeersch, E. Zurek, G. R. Hutchison, *J. Cheminform.* **2012,** *4*, 17.
546. M. Abadi, P. Barham, J. Chen, Z. Chen, A. Davis, J. Dean, M. Devin, S. Ghemawat, G. Irving, M. Isard, *et al.*, *12th USENIX Symposium on Operating Systems Design and Implementation* **2016**, 265-283.
547. G. Ke, Q. Meng, T. Finley, T. Wang, W. Chen, W. Ma, Q. Ye, T.-Y. Liu, *Adv. Neural. Inf. Process. Syst.* **2017,** *30*.
548. W. McKinney, *Proceedings of the 9th Python in Science Conference* **2010**, 51-56.
549. P. Virtanen, R. Gommers, T. E. Oliphant, M. Haberland, T. Reddy, D. Cournapeau, E. Burovski, P. Peterson, W. Weckesser, J. Bright, *et al.*, *Nat. Methods* **2020,** *17*, 261-272.
550. J. D. Hunter, *Comput. Sci. Eng.* **2007,** *9*, 90-95.
551. M. L. Waskom, *J. Open Source Softw.* **2021,** *6*, 3021.
552. C. H. DePuy, S. Gronert, S. E. Barlow, V. M. Bierbaum, R. Damrauer, *J. Am. Chem. Soc.* **1989,** *111*, 1968-1973.
553. D. Polino, A. Barbato, C. Cavallotti, *Phys. Chem. Chem. Phys.* **2010,** *12*, 10622-10632.

7 APPENDIX

7.1 List of Abbreviations

A

AILC · *Aluminum-ligand cooperativity*
ANN · *Artificial neural network*
API · *Application programming interface*
autoPAMS · *Automatic generation of p-block atom-based molecular structures*

B

Bn · *Benzyl (group)*
BS · *Broken-symmetry*

C

CASSCF · *Complete active space self-consistent field (method)*
cat · *Catecholato ligand*
CBS · *Complete basis set (extrapolation)*
CCSD(T) · *Coupled cluster (including) singles, doubles, and perturbative triples*
CD_2Cl_2 · *Dichloromethane-d_2*
CH_2Cl_2 · *Dichloromethane*
^{Cl}cat · *Perchlorocatecholato ligand*
CO_2 · *Carbon dioxide*
COSMO-RS · *Conductor like screening model for real solvents*
COSY · *Correlation (NMR) spectroscopy*
CREST · *Conformer-rotamer ensemble sampling tool*
CSD · *Cambridge Structural Database*
CSS · *Closed-shell singlet*

D

DE · *Deformation energy*
DEPT · *Distortionless enhancement by polarization transfer*
DFT · *Density functional theory*
DLPNO · *Domain-based local pair natural orbital*
dme · *1,2-Dimethoxyethane (ligand)*
DME · *1,2-Dimethoxyethane (solvent)*

E

ECP · *Effective core potential*
ECW model · *Electrostatic, covalent, and steric parameter model for the prediction of Lewis adduct stabilities*
ELC · *Element-ligand cooperativity*
equiv. · *Equivalents*
ESI · *Electrospray ionization*
Et · *Ethyl (group)*
exc. · *Excess*
EXSY · *Exchange (NMR) spectroscopy*

F

FA · *Fluoride adduct*
Fc · *Ferrocene*
^{F}cat · *Perfluorocatecholato ligand*
FIA · *Fluoride ion affinity*
FIA_{gas} · *Gas phase fluoride ion affinity*
FIA_{solv} · *Solution phase fluoride ion affinity (dichloromethane)*
FLP · *Frustrated Lewis pair*
FMO · *Frontier molecular orbital*

FT-ATR-IR · *Fourier-transform attenuated total reflection infrared (spectroscopy)*

G

GaLC · *Gallium-ligand cooperativity*
GEI · *Global electrophilicity index*
GIAO · *Gauge-independent atomic orbital*
GNN · *Graph neural network*

H

HMBC · *Heteronuclear multiple-bond correlation (NMR) spectroscopy*
HMDS · *Hexamethyldisilazide ≙ bis(trimethylsilyl)amide*
$HNTf_2$ · *Bis(trifluoromethyl)sulfonimide*
HOMO · *Highest occupied molecular orbital*
hppH · *1,3,4,6,7,8-Hexahydro-2H-pyrimido[1,2-a]pyrimidine*
HR-MS · *High resolution mass spectrometry*
HSAB · *(Theory of) hard and soft Lewis acids and bases*
HSQC · *Heteronuclear single-quantum correlation (NMR) spectroscopy*

I

INADEQUATE · *Incredible natural abundance double quantum transfer (NMR) experiment*
Int · *Intermediate*
***i*-Pr** · *iso-Propyl (group)*
IPUAC · *International Union of Pure and Applied Chemistry*
IR · *Infrared*
IRC · *Intrinsic reaction coordinate*
ISC · *Intersystem crossing*

J

JTE · *Jahn-Teller effect*

L

LA · *Lewis acid*
LDA · *Linear discriminant analysis*
LightGBM · *Light gradient-boosting machine*
LUMO · *Lowest unoccupied molecular orbital*

M

m/z · *Mass-to-charge ratio*
MAE · *Mean absolute error*
Me · *Methyl (group)*
mHEAT+ · *Modified high-accuracy extrapolated ab initio thermochemistry*
ML · *Machine learning*
MLC · *Metal-ligand cooperativity*
MO · *Molecular orbital*
MRCI · *Multireference configuration interaction*

N

NaN · *Not a number*
NBO · *Natural bond orbital*
***n*-Bu** · *n-Butyl (group)*
NCI · *Non-covalent interaction*
NEVPT2 · *N-electron valence perturbation theory to second order*
NMR · *Nuclear magnetic resonance*
NOESY · *Nuclear Overhauser effect (NMR) spectroscopy*

O

o/n · *over night*
***o*DFB** · *ortho-Difluorobenzene*
OSS · *Open-shell singlet*

P

PCET · *Proton-coupled electron transfer*
PES · *Potential energy surface*
Ph · *Phenyl (group)*
PLS · *Partial least squares*
PNP · *Bis(triphenylphosphine)iminium*
PPh_4 or PPh_4^+ · *Tetraphenylphosphonium*
ppm · *Parts per million*
PTCat · *Phase transfer catalysis*

R

r^2 · *Squared Pearson correlation coefficient*
ReLU · *Rectified linear unit*
RF · *Random forest*
rt · *Room temperature*

S

SCXRD · *Single crystal X-ray diffraction*
SH · *Sawhorse*
SHAP · *Shapley additive explanations*
SMILES · *Simplified molecular-input line-entry system*
SOC · *Spin-orbit coupling*

T

TBAT · *Tetrabutylammonium difluorotriphenylsilicate*
***t*-Bu** · *tert-Butyl (group)*
TD-DFT · *Time-dependent density functional theory*
TEP · *Tolman electronic parameter*
thf · *Tetrahydrofuran (ligand)*
THF · *Tetrahydrofuran (solvent)*
trip · *triplet*
TS · *Transition state/structure*

U

UMAP · *Uniform manifold approximation and projection*
UV · *Ultraviolet*

V

Vis · *Visible region of the electromagnetic spectrum*

7.2 Terminology

Stereoinversion

Within this dissertation, the term “stereoinversion” (of molecules with a tetrahedral structure in their ground state) refers to a process in which the four individual substituents are defined to be distinguishable despite being potentially of the same atom type. For example, the stereoinversion of methane effectively does not lead to the inversion of CH_4’s stereochemistry as the carbon atom is not a chiral center. The initial and final structure are superimposable. A true mirror image is only obtained if the four hydrogen atoms are labeled, *e.g.*, as H-1, H-2, H-3, and H-4 (*cf.* **Figure 1.3**). For the sake of concise wording, the term stereoinversion was used throughout and options like “pseudo stereoinversion” were avoided.

Square planar *p*-block atom

The phrase “square planar *p*-block atom” refers to an atom whose nearest neighbors (bonding partners) define a square. This definition is for example based on the results of a quantum chemical structure optimization or an SCXRD measurement. It does not refer to the actual shape of the atom within the molecule. This also applies to similar phrase, *e.g.*, “trigonal pyramidal nitrogen atom” or “square planar aluminate”.

7.3 NMR Spectra

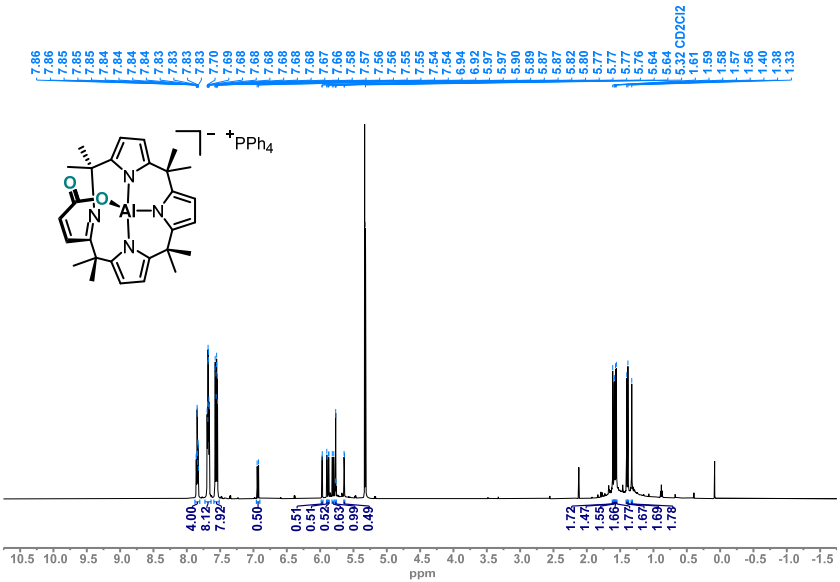

Figure 7.1: ^{1}H NMR spectrum (600 MHz, CD_2Cl_2, 295 K) of $[PPh_4][40]$. *The singlet at 2.12 ppm is assigned to acetone, which is formed in a side reaction when going from $[35]^-$ to $[40]^-$.*[148]

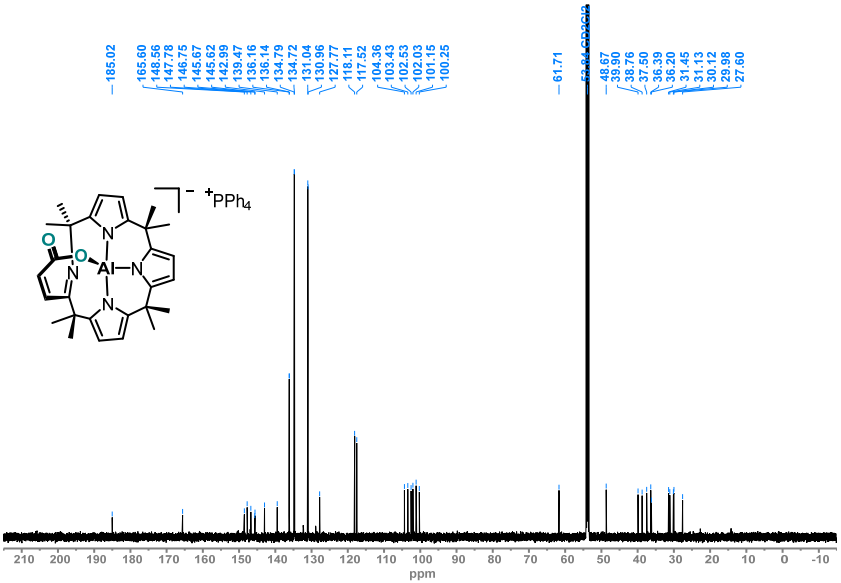

Figure 7.2: $^{13}C\{^1H\}$ NMR spectrum (151 MHz, CD_2Cl_2, 295 K) of $[PPh_4][40]$.[148]

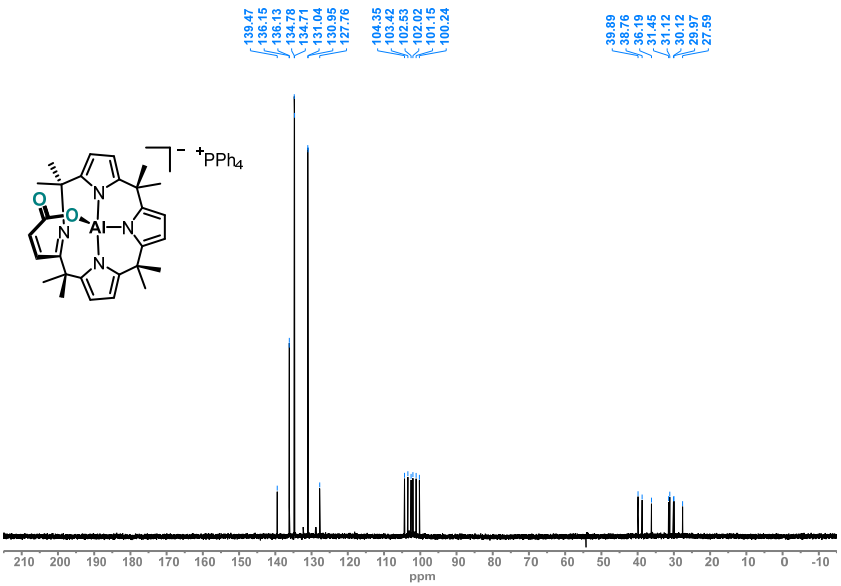

Figure 7.3: DEPT-135 $^{13}C\{^1H\}$ NMR spectrum (151 MHz, CD_2Cl_2, 295 K) of $[PPh_4][40]$.[148]

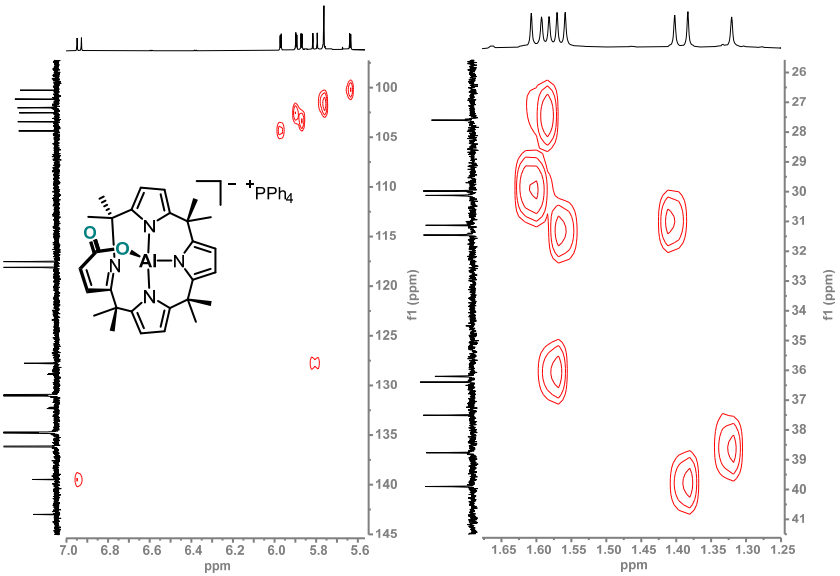

Figure 7.4: $^{1}H,^{13}C$ NMR HSQC spectrum (600, 151 MHz, CD_2Cl_2, 295 K) of $[PPh_4][40]$.[148]

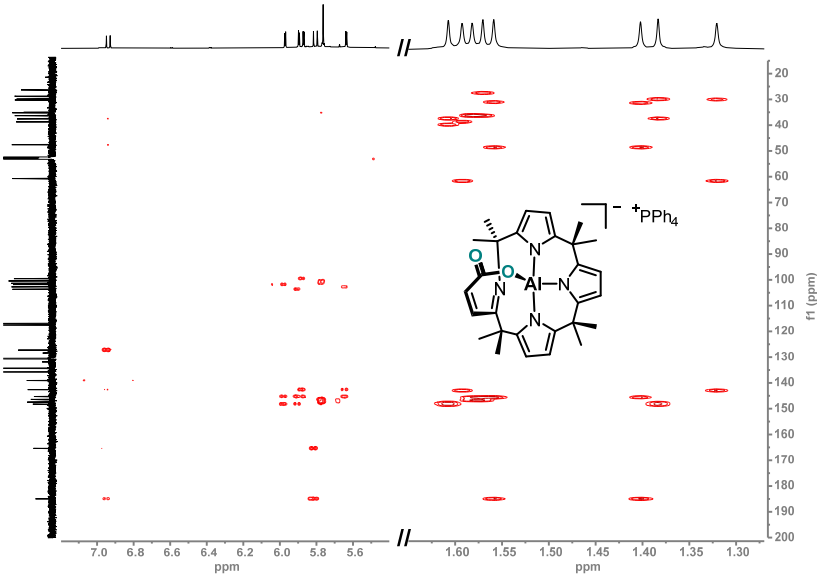

Figure 7.5: $^{1}H,^{13}C$ NMR HMBC spectrum (600, 151 MHz, CD_2Cl_2, 295 K, long-range J_{CH} = 7 Hz) of $[PPh_4][40]$.[148]

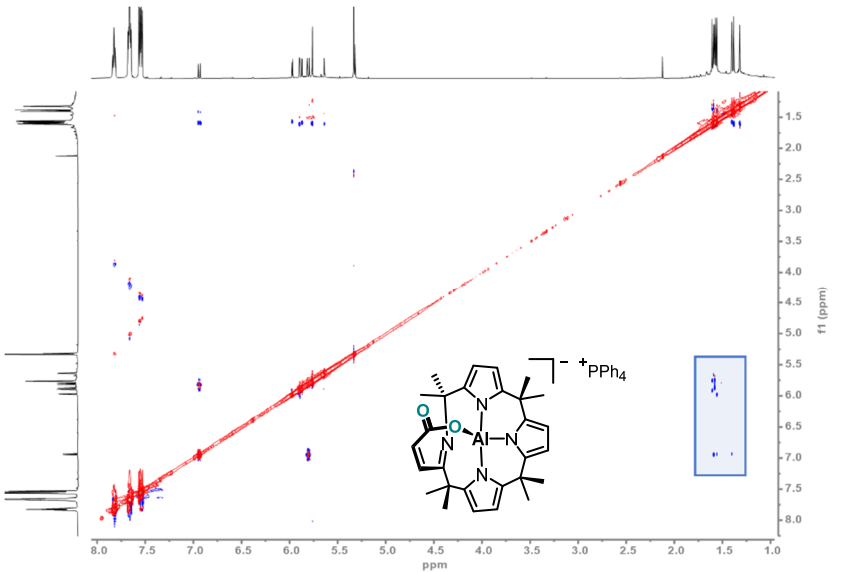

Figure 7.6: $^1H,^1H$ NMR NOESY spectrum (600, CD_2Cl_2, 295 K, t_m = 0.5 s) of $[PPh_4][40]$. *The singlet at 2.12 ppm is assigned to acetone, which is formed in a side reaction when going from $[35]^-$ to $[40]^-$. The marked region is shown in Figure 7.7.*[148]

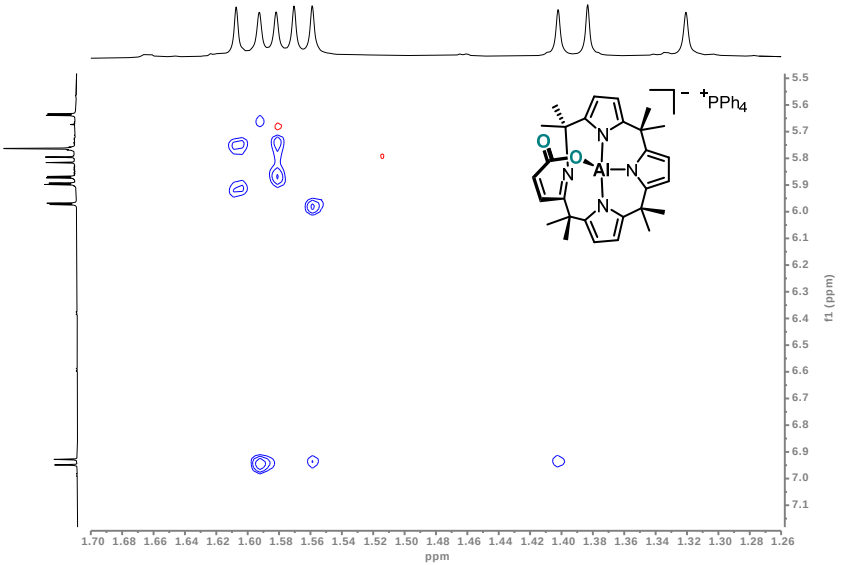

Figure 7.7: Excerpt of the $^1H,^1H$ NMR NOESY spectrum (600, CD_2Cl_2, 295 K, t_m = 0.5 s) of $[PPh_4][40]$. *The full spectrum is given in Figure 7.6.*[148]

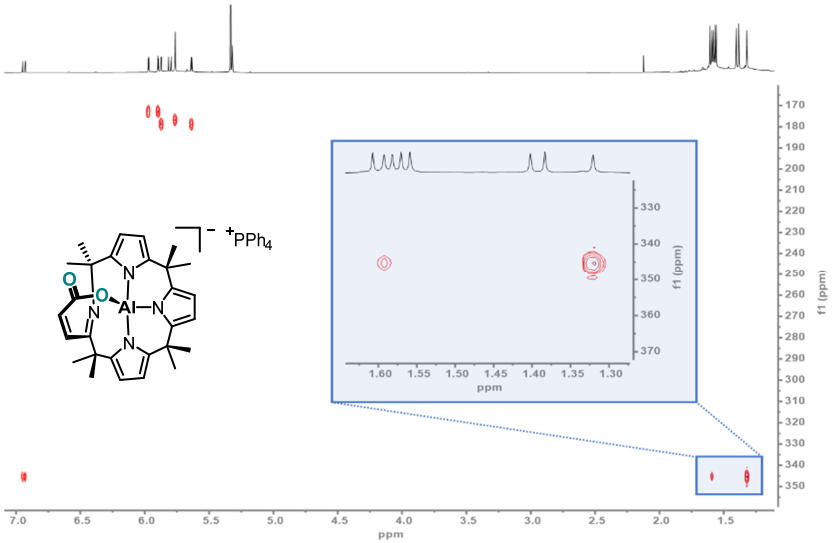

Figure 7.8: $^{1}H,^{15}N$ NMR HMBC spectrum (600, 61 MHz, CD_2Cl_2, 295 K, long-range J_{NH} = 3 Hz) of [PPh_4][40]. *The ^{15}N chemical shifts are plotted with respect to the ammonia reference system. Conversion to the nitromethane reference system (as it is used for the discussion in the main text) was achieved by subtraction with 380.23 ppm.*[148]

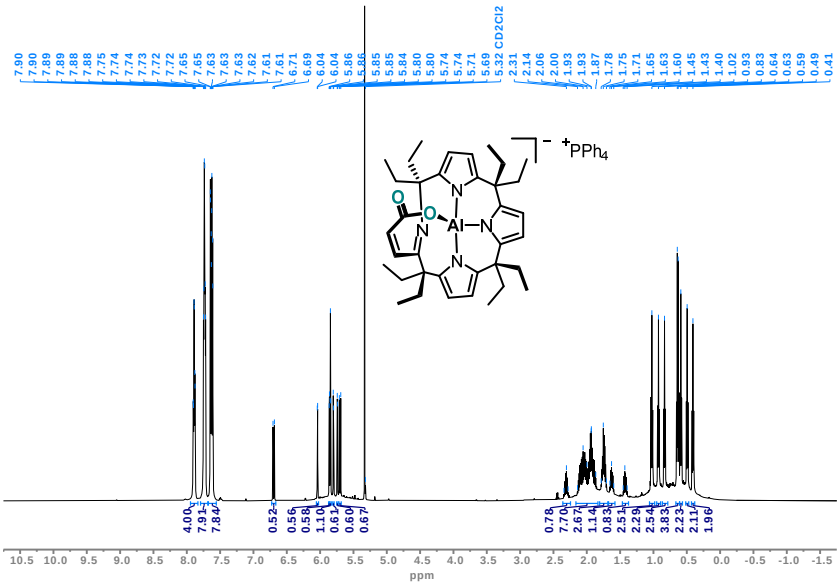

Figure 7.9: ^{1}H NMR spectrum (600 MHz, CD_2Cl_2, 295 K) of [PPh_4][41]. *The weak quartet at 2.44 ppm is assigned to pentan-3-one, which is formed in a side reaction when going from [36]⁻ to [41]⁻.*[148]

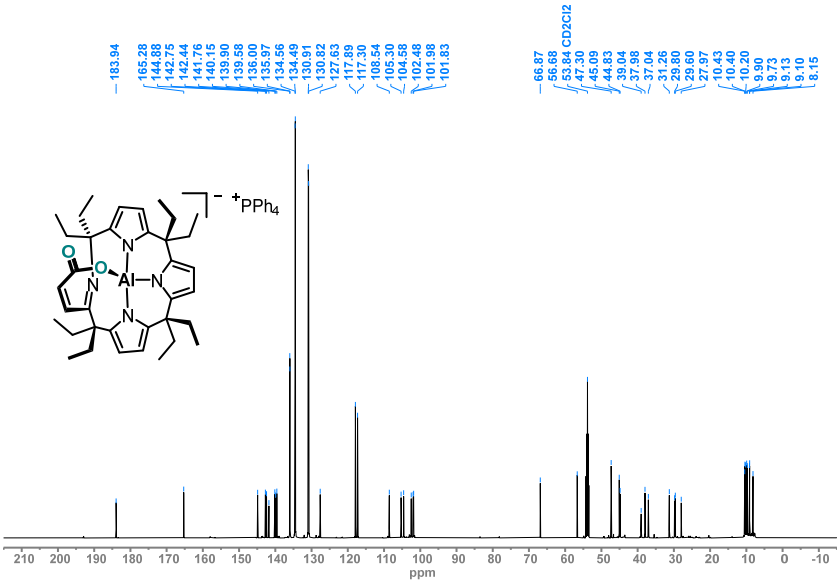

Figure 7.10: $^{13}C\{^{1}H\}$ NMR spectrum (151 MHz, CD_2Cl_2, 295 K) of $[PPh_4][41]$.[148]

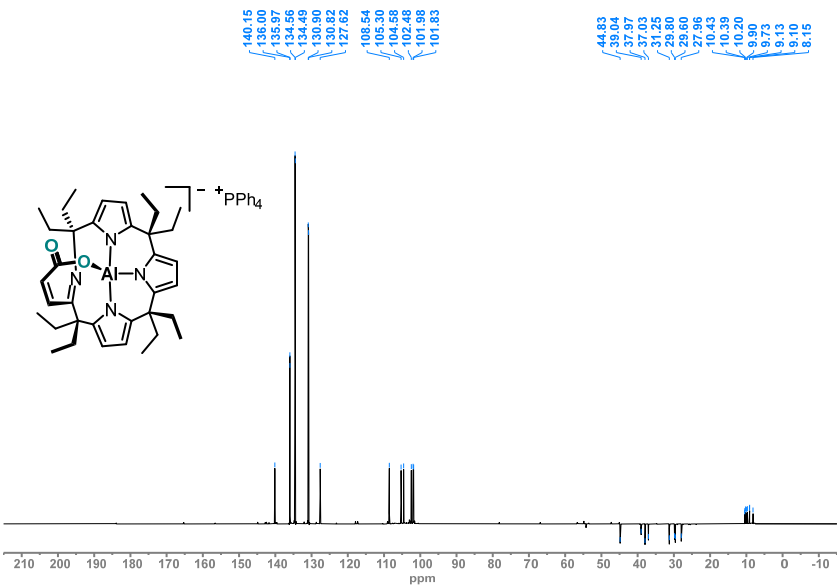

Figure 7.11: DEPT-135 $^{13}C\{^{1}H\}$ NMR spectrum (151 MHz, CD_2Cl_2, 295 K) of $[PPh_4][41]$.[148]

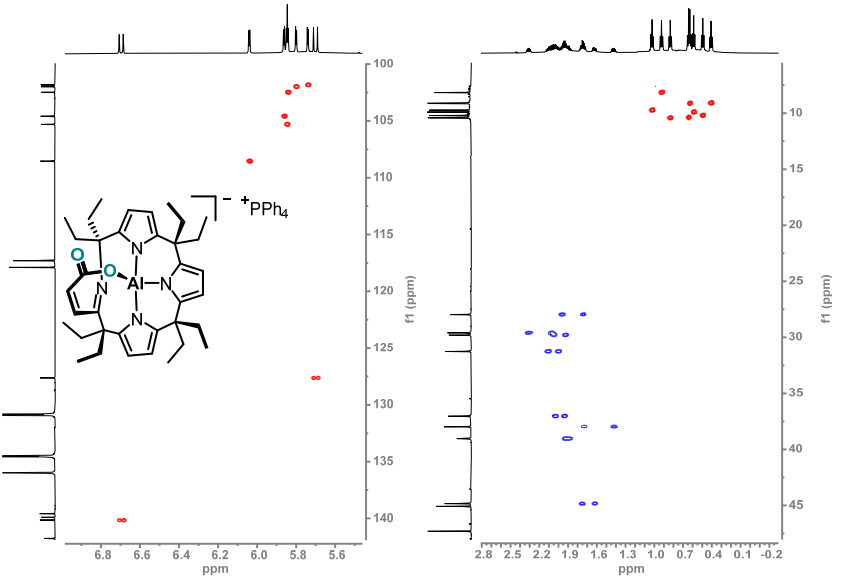

Figure 7.12: Multiplicity-edited $^{1}H,^{13}C$ NMR HSQC spectrum (600, 151 MHz, CD_2Cl_2, 295 K) of $[PPh_4][41]$.[148]

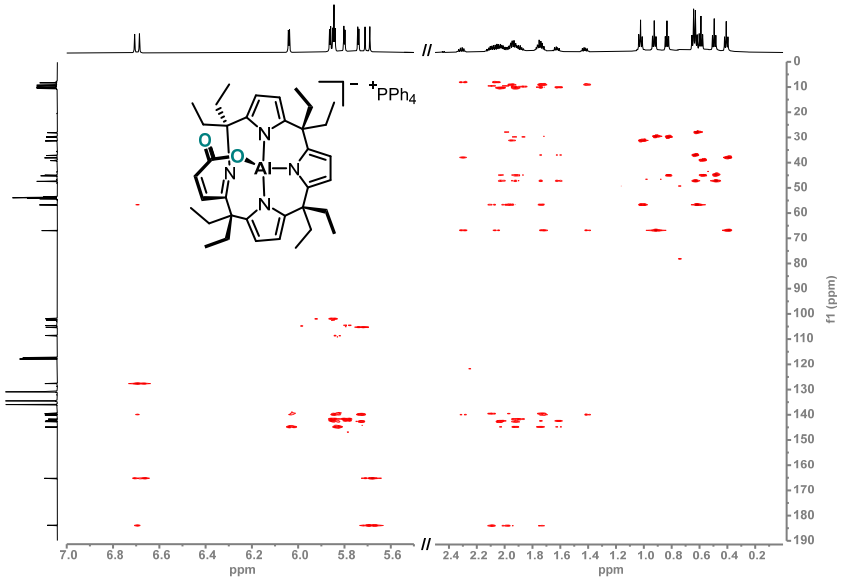

Figure 7.13: $^{1}H,^{13}C$ NMR HMBC spectrum (600, 151 MHz, CD_2Cl_2, 295 K, long-range J_{CH} = 8 Hz) of $[PPh_4][41]$.[148]

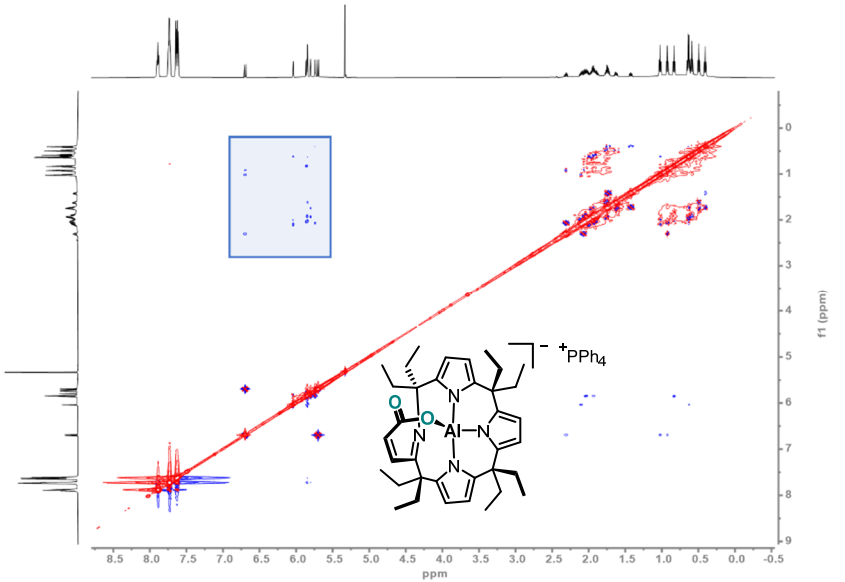

Figure 7.14: $^{1}H,^{1}H$ NMR NOESY spectrum (600, CD_2Cl_2, 295 K, t_m = 0.5 s) of [PPh_4][41]. *The marked region is shown in Figure 7.15.*[148]

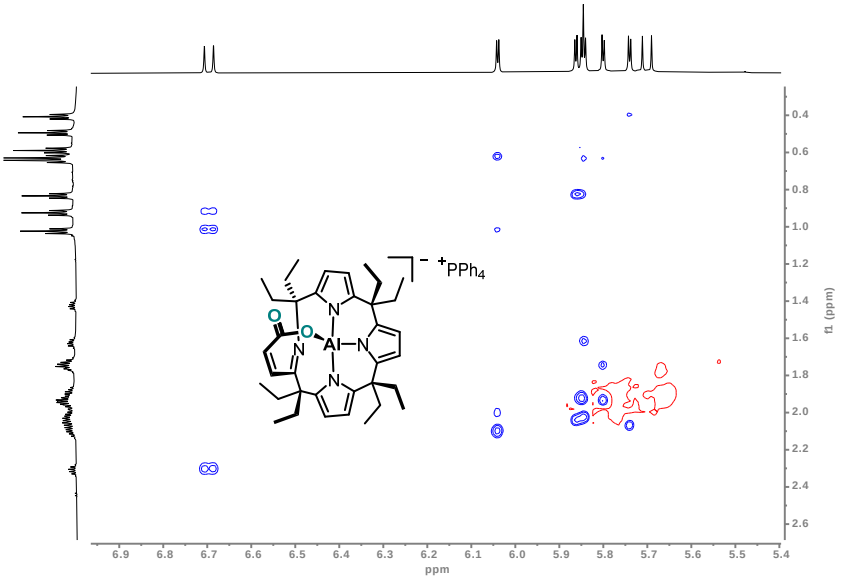

Figure 7.15: **Excerpt of the $^{1}H,^{1}H$ NMR NOESY spectrum (600, CD_2Cl_2, 295 K, t_m = 0.5 s) of [PPh_4][41].** *The full spectrum is shown in Figure 7.14.*[148]

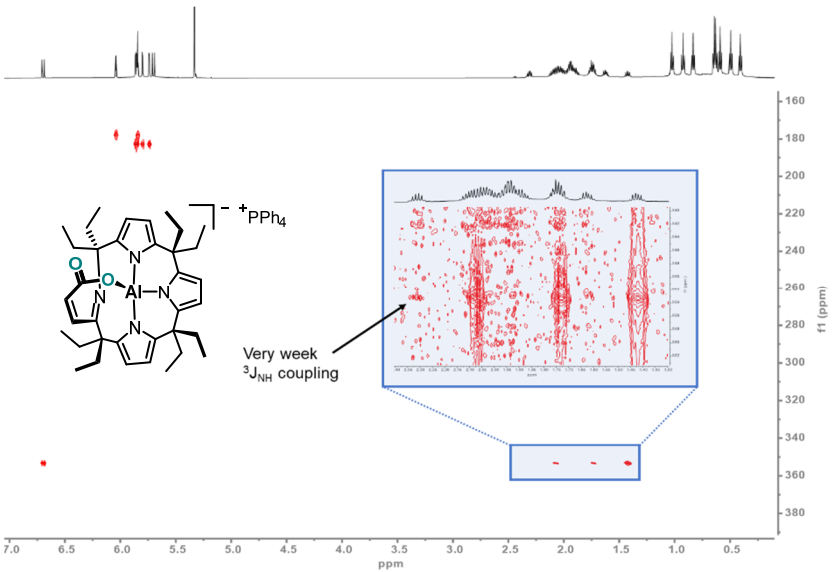

Figure 7.16: $^{1}H,^{15}N$ NMR HMBC spectrum (600, 61 MHz, CD_2Cl_2, 295 K, long-range J_{NH} = 8 Hz) of [PPh_4][41]. *The ^{15}N chemical shifts are plotted with respect to the ammonia reference system. Conversion to the nitromethane reference system (as it is used for the discussion in the main text) was achieved by subtraction with 380.23 ppm.*[148]

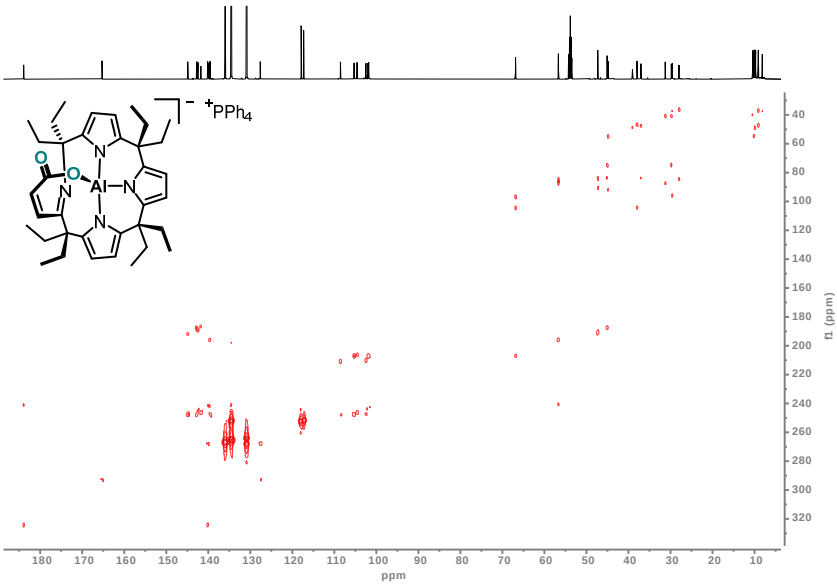

Figure 7.17: $^{13}C,^{13}C$ NMR INADEQUATE spectrum (151, 151 MHz, CD_2Cl_2, 295 K, J_{CC} = 55 Hz) of [PPh_4][41].[148]

7.4 Crystallographic Data

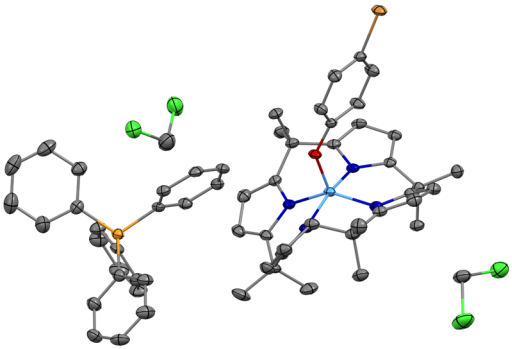

Index name	**[PPh_4][29]**
Database identifier	**YUXVEV, 2013196**
Empirical formula	$C_{60}H_{61}AlBrCl_4N_4OP$
Formula weight	1133.78
Temperature/K	100(2)
Crystal system	monoclinic
Space group	$P2_1/n$
a/Å	9.7658(18)
b/Å	27.696(6)
c/Å	20.719(4)
α/°	90
β/°	102.380(7)
γ/°	90
Volume/Å^3	5473.6(19)
Z	4
ρ_{calc}/gcm^{-3}	1.376
μ/mm^{-1}	1.037
F(000)	2352.0
Crystal size/mm^3	0.258 × 0.246 × 0.132
Radiation	MoK_α (λ = 0.71073)
2Θ range for data collection/°	4.026 to 51
Index ranges	-11 ⩽ h ⩽ 11, -33 ⩽ k ⩽ 33, -25 ⩽ l ⩽ 25
Reflections collected	227575
Independent reflections	10164 [R_{int} = 0.0993, R_{sigma} = 0.0261]
Data/restraints/parameters	10164/0/657
Goodness-of-fit on F^2	1.079
Final R indexes [I⩾2σ (I)]	R_1 = 0.0472, wR_2 = 0.1251
Final R indexes [all data]	R_1 = 0.0553, wR_2 = 0.1338
Largest diff. peak/hole / eÅ^{-3}	0.99/-0.84

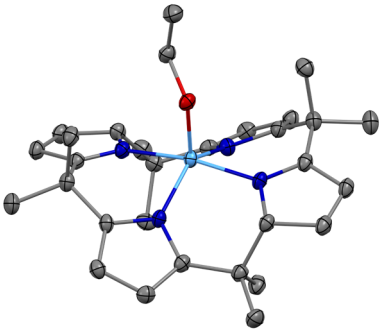

Index name	**31**
Database identifier	**YUXVIZ, 2013197**
Empirical formula	$C_{30}H_{39}AlN_4O$
Formula weight	498.63
Temperature/K	100(2)
Crystal system	orthorhombic
Space group	$Pna2_1$
a/Å	9.7760(9)
b/Å	25.127(2)
c/Å	11.0644(10)
α/°	90
β/°	90
γ/°	90
Volume/Å^3	2717.9(4)
Z	4
ρ_{calc}/gcm^{-3}	1.219
μ/mm^{-1}	0.104
F(000)	1072.0
Crystal size/mm^3	0.454 × 0.173 × 0.17
Radiation	MoK_α (λ = 0.71073)
2Θ range for data collection/°	4.47 to 56.652
Index ranges	-13 ⩽ h ⩽ 13, -33 ⩽ k ⩽ 33, -14 ⩽ l ⩽ 14
Reflections collected	61625
Independent reflections	6756 [R_{int} = 0.0718, R_{sigma} = 0.0365]
Data/restraints/parameters	6756/1/334
Goodness-of-fit on F^2	1.036
Final R indexes [I⩾2σ (I)]	R_1 = 0.0364, wR_2 = 0.0792
Final R indexes [all data]	R_1 = 0.0471, wR_2 = 0.0852
Largest diff. peak/hole / eÅ^{-3}	0.22/-0.24
Flack parameter	-0.02(7)

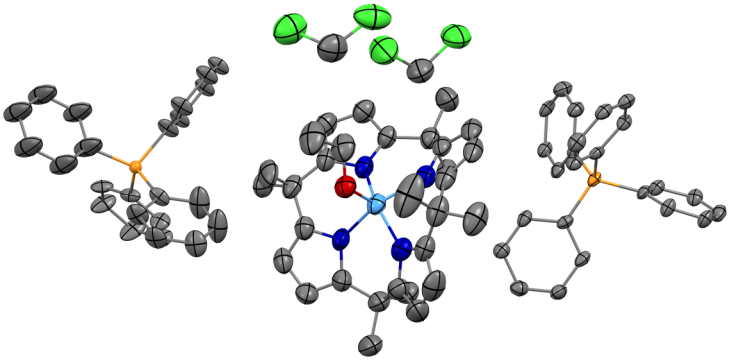

Only atom connectivities were determined due to poor data quality.

Index name	**$[PPh_4]_2$[32]**
Database identifier	**Not deposited**
Empirical formula	$C_{80}H_{81}AlCl_4N_4OP_2$
Formula weight	1345.28
Temperature/K	100(2)
Crystal system	triclinic
Space group	P-1
a/Å	11.9549(12)
b/Å	12.7424(13)
c/Å	25.639(3)
α/°	86.841(3)
β/°	76.942(3)
γ/°	70.049(3)
Volume/Å^3	3575.3(6)
Z	2
ρ_{calc}/gcm^{-3}	0.935
μ/mm^{-1}	0.232
F(000)	1060.0
Crystal size/mm^3	0.214 × 0.133 × 0.07
Radiation	MoK_α (λ = 0.71073)
2Θ range for data collection/°	4.104 to 50.264
Index ranges	$-14 \leqslant h \leqslant 14, -15 \leqslant k \leqslant 15, -30 \leqslant l \leqslant 30$
Reflections collected	66848
Independent reflections	12646 [R_{int} = 0.1210, R_{sigma} = 0.0851]
Data/restraints/parameters	12646/335/786
Goodness-of-fit on F2	1.445
Final R indexes [I⩾2σ (I)]	R_1 = 0.1435, wR_2 = 0.3843
Final R indexes [all data]	R_1 = 0.2086, wR_2 = 0.4313
Largest diff. peak/hole / eÅ^{-3}	1.47/-1.04

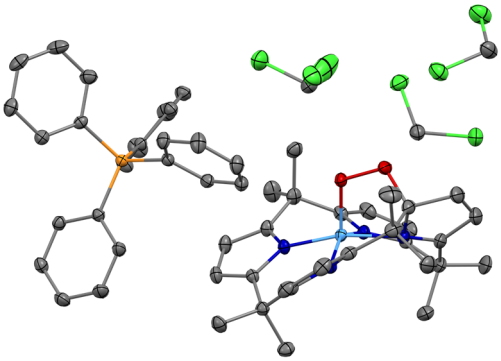

Index name	**[PPh_4][35]**
Database identifier	**OVICAA, 2072557**
Empirical formula	$C_{55}H_{58}AlCl_6N_4O_2P$
Formula weight	1077.70
Temperature/K	100(2)
Crystal system	monoclinic
Space group	$P2_1/c$
a/Å	15.2905(12)
b/Å	17.2541(14)
c/Å	21.0539(14)
α/°	90
β/°	106.068(3)
γ/°	90
Volume/$Å^3$	5337.5(7)
Z	4
ρ_{calc}/gcm^{-3}	1.341
μ/mm^{-1}	0.414
F(000)	2248.0
Crystal size/mm^3	0.136 × 0.104 × 0.045
Radiation	MoK_α (λ = 0.71073)
2Θ range for data collection/°	3.77 to 55.524
Index ranges	$-20 \leqslant h \leqslant 20$, $-22 \leqslant k \leqslant 22$, $-27 \leqslant l \leqslant 27$
Reflections collected	195737
Independent reflections	12566 [R_{int} = 0.0707, R_{sigma} = 0.0268]
Data/restraints/parameters	12566/1/864
Goodness-of-fit on F^2	1.030
Final R indexes [$I \geqslant 2\sigma$ (I)]	R_1 = 0.0361, wR_2 = 0.0896
Final R indexes [all data]	R_1 = 0.0444, wR_2 = 0.0954
Largest diff. peak/hole / $eÅ^{-3}$	0.52/-0.58

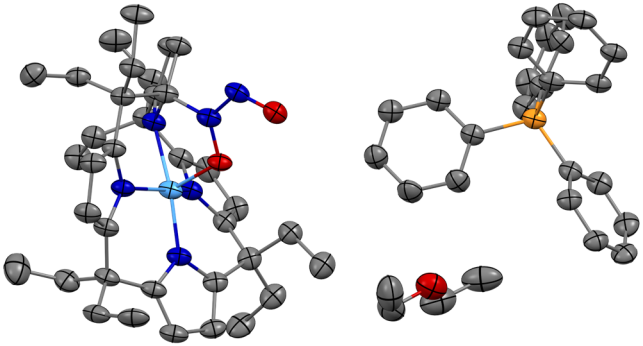

Index name	**[PPh_4][62]**
Database identifier	**Not deposited**
Empirical formula	$C_{64}H_{78}AlN_6O_3P$
Formula weight	1037.27
Temperature/K	100(2)
Crystal system	monoclinic
Space group	$P2_1/n$
a/Å	11.8687(17)
b/Å	27.971(4)
c/Å	21.374(3)
α/°	90
β/°	95.254(5)
γ/°	90
Volume/Å^3	7066.1(18)
Z	4
ρ_{calc}/gcm^{-3}	0.975
μ/mm^{-1}	0.093
F(000)	2224
Crystal size/mm^3	0.35×0.32×0.22
Radiation	MoK_α (λ = 0.71073 Å)
2Θ range for data collection/°	3.74 to 52.97 (0.80 Å)
Index ranges	-14 ⩽ h ⩽ 14, -34 ⩽ k ⩽ 35, -26 ⩽ l ⩽ 26
Reflections collected	198888
Independent reflections	14534 [R_{int} = 0.0923, R_{sigma} = 0.0421]
Data / Restraints / Parameters	14534/900/688
Goodness-of-fit on F^2	1.040
Final R indexes [I⩾2σ(I)]	R_1 = 0.0699, wR_2 = 0.1782
Final R indexes [all data]	R_1 = 0.0953, wR_2 = 0.1949
Largest peak/hole / eÅ^{-3}	0.40/-0.34

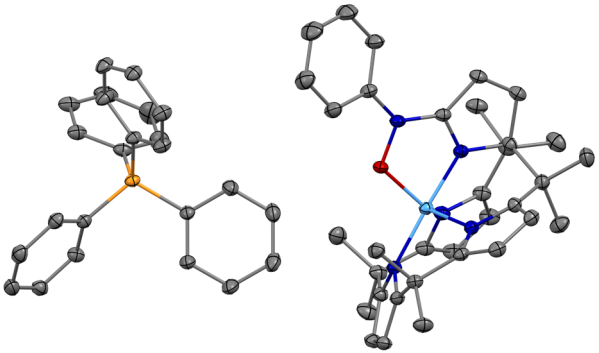

Name	**[PPh_4][64]**
Database identifier	**Not deposited**
Empirical formula	$C_{58}H_{57}AlN_5OP$
Formula weight	898.03
Temperature/K	100(2)
Crystal system	triclinic
Space group	$P\bar{1}$
a/Å	12.7974(8)
b/Å	13.9223(8)
c/Å	17.5632(10)
α/°	72.594(2)
β/°	80.317(2)
γ/°	63.381(2)
Volume/Å^3	2667.3(3)
Z	2
ρ_{calc}/gcm^{-3}	1.118
μ/mm^{-1}	0.110
F(000)	952
Crystal size/mm^3	0.45×0.30×0.11
Radiation	MoK_α (λ = 0.71073 Å)
2θ range/°	4.23 to 67.62 (0.64 Å)
Index ranges	$-19 \leqslant h \leqslant 20, -21 \leqslant k \leqslant 20, -26 \leqslant l \leqslant 27$
Reflections collected	180426
Independent reflections	20863 [R_{int} = 0.0562, R_{sigma} = 0.0364]
Data / Restraints / Parameters	20863/1245/603
Goodness-of-fit on F^2	1.029
Final R indexes [I≥2σ(I)]	R_1 = 0.0424, wR_2 = 0.1122
Final R indexes [all data]	R_1 = 0.0560, wR_2 = 0.1225
Largest peak/hole / eÅ^{-3}	0.47/−0.41

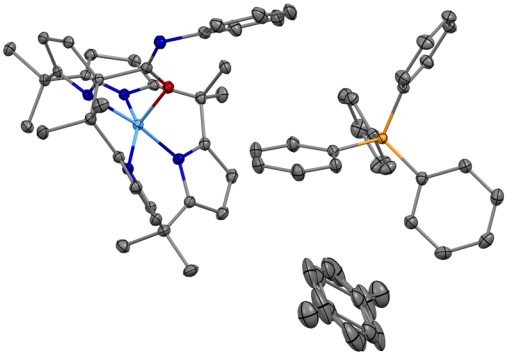

Name	**[PPh_4][61]**
Database identifier	**Not deposited**
Empirical formula	$C_{125}H_{122}Al_2N_{10}O_2P_2$
Formula weight	1912.22
Temperature/K	100(2)
Crystal system	monoclinic
Space group	$P2_1/c$
a/Å	11.9017(7)
b/Å	15.0967(7)
c/Å	28.1951(16)
α/°	90
β/°	93.582(2)
γ/°	90
Volume/Å^3	5056.1(5)
Z	2
ρ_{calc}/gcm^{-3}	1.256
μ/mm^{-1}	0.121
F(000)	2028
Crystal size/mm^3	0.450×0.300×0.210
Radiation	MoK_α (λ = 0.71073 Å)
2Θ range/°	3.96 to 55.88 (0.76 Å)
Index ranges	$-15 \leqslant h \leqslant 15, -19 \leqslant k \leqslant 19, -37 \leqslant l \leqslant 37$
Reflections collected	316682
Independent reflections	12108 [R_{int} = 0.0575, R_{sigma} = 0.0142]
Data / Restraints / Parameters	12108/122/676
Goodness-of-fit on F^2	1.040
Final R indexes [I⩾2σ(I)]	R_1 = 0.0359, wR_2 = 0.0861
Final R indexes [all data]	R_1 = 0.0409, wR_2 = 0.0894
Largest peak/hole / eÅ^{-3}	0.58/-0.36

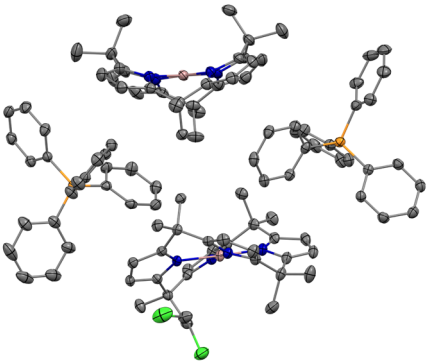

Name	**[PPh$_4$][71]**
Database identifier	**NEMDUI, 2175982**
Empirical formula	$C_{52.5}H_{53}ClGaN_4P$
Formula weight	876.13
Temperature/K	100(2)
Crystal system	monoclinic
Space group	$P2_1/c$
a/Å	25.4110(18)
b/Å	16.6359(13)
c/Å	23.7139(18)
α/°	90
β/°	107.797(3)
γ/°	90
Volume/Å^3	9545.0(12)
Z	8
ρ_{calc}/gcm^{-3}	1.219
μ/mm^{-1}	0.704
F(000)	3672.0
Crystal size/mm^3	0.144 × 0.113 × 0.086
Radiation	MoK$_\alpha$ (λ = 0.71073)
2Θ range for data collection/°	4.108 to 53.998
Index ranges	-32 ⩽ h ⩽ 32, -20 ⩽ k ⩽ 21, -30 ⩽ l ⩽ 30
Reflections collected	141733
Independent reflections	20825 [R_{int} = 0.0912, R_{sigma} = 0.0553]
Data/restraints/parameters	20825/0/1088
Goodness-of-fit on F^2	1.027
Final R indexes [I⩾2σ (I)]	R_1 = 0.0463, wR_2 = 0.1083
Final R indexes [all data]	R_1 = 0.0735, wR_2 = 0.1219
Largest diff. peak/hole / eÅ^{-3}	1.47/-0.81

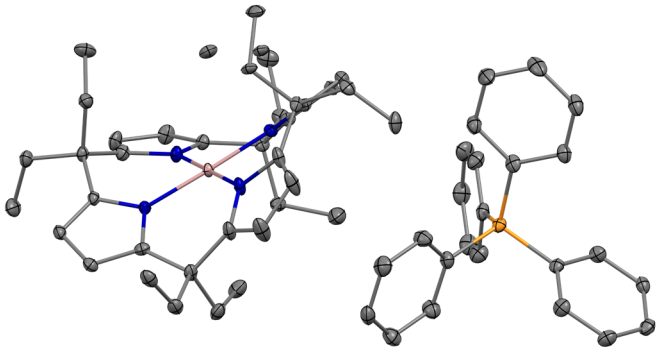

Name	**[PPh_4][72]**
Database identifier	**NEMDOC, 2175981**
Empirical formula	$C_{60}H_{68}GaN_4P$
Formula weight	945.87
Temperature/K	100(2)
Crystal system	monoclinic
Space group	$P2_1/n$
a/Å	11.5827(6)
b/Å	15.4151(5)
c/Å	27.0610(12)
α/°	90
β/°	90.708(2)
γ/°	90
Volume/Å^3	4831.3(4)
Z	4
ρ_{calc}/gcm^{-3}	1.300
μ/mm^{-1}	0.648
F(000)	2008
Crystal size/mm^3	0.231×0.182×0.113
Radiation	MoK_α (λ = 0.71073 Å)
2Θ range for data collection/°	4.40 to 57.61 (0.74 Å)
Index ranges	$-15 \leqslant h \leqslant 15, -20 \leqslant k \leqslant 19, -36 \leqslant l \leqslant 36$
Reflections collected	38808
Independent reflections	12354 [R_{int} = 0.0785, R_{sigma} = 0.0785]
Data / Restraints / Parameters	12354/0/617
Goodness-of-fit on F^2	1.042
Final R indexes [I⩾2σ (I)]	R_1 = 0.0547, wR_2 = 0.1224
Final R indexes [all data]	R_1 = 0.0791, wR_2 = 0.1368
Largest diff. peak/hole / eÅ^{-3}	0.63/-0.56

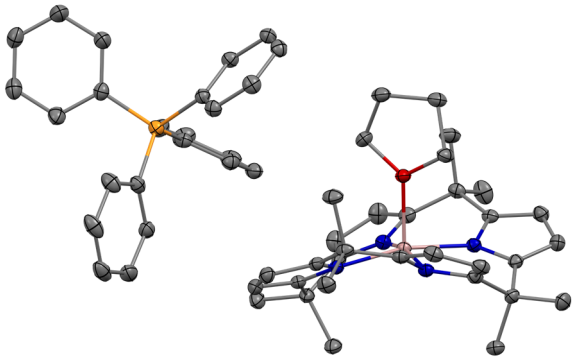

Name	**[PPh$_4$][74]**
Database identifier	**NEMFAQ, 2175983**
Empirical formula	$C_{56}H_{60}GaN_4OP$
Formula weight	905.77
Temperature/K	100(2)
Crystal system	monoclinic
Space group	$P2_1/c$
a/Å	13.0677(6)
b/Å	21.4060(11)
c/Å	17.1423(7)
α/°	90
β/°	108.630(2)
γ/°	90
Volume/Å^3	4543.9(4)
Z	4
ρ_{calc}/gcm^{-3}	1.324
μ/mm^{-1}	0.687
F(000)	1912
Crystal size/mm^3	0.694×0.453×0.342
Radiation	MoK$_\alpha$ (λ = 0.71073 Å)
2Θ range for data collection/°	3.80 to 55.15 (0.77 Å)
Index ranges	$-16 \leqslant h \leqslant 16, -27 \leqslant k \leqslant 27, -22 \leqslant l \leqslant 22$
Reflections collected	302121
Independent reflections	10488 [R_{int} = 0.0585, R_{sigma} = 0.0183]
Data / Restraints / Parameters	10488/0/576
Goodness-of-fit on F^2	1.061
Final R indexes [I⩾2σ (I)]	R_1 = 0.0254, wR_2 = 0.0689
Final R indexes [all data]	R_1 = 0.0272, wR_2 = 0.0700
Largest diff. peak/hole / eÅ^{-3}	0.43/-0.37

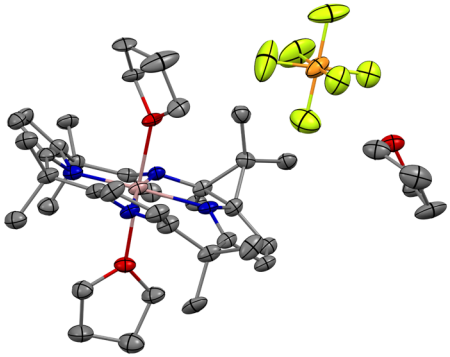

Name	**[83][PF_6]**
Database identifier	**Not deposited**
Empirical formula	$C_{40}H_{56}F_6GaN_4O_3P$
Formula weight	855.57
Temperature/K	100(2)
Crystal system	monoclinic
Space group	$P2_1/c$
a/Å	12.021(4)
b/Å	10.618(3)
c/Å	31.407(10)
α/°	90
β/°	97.781(8)
γ/°	90
Volume/Å^3	3972(2)
Z	4
ρ_{calc}/gcm^{-3}	1.431
μ/mm^{-1}	0.805
F(000)	1792
Crystal size/mm^3	0.39×0.11×0.05
Radiation	MoK_α (λ = 0.71073 Å)
2θ range/°	4.02 to 53.79 (0.79 Å)
Index ranges	$-15 \leqslant h \leqslant 15, -13 \leqslant k \leqslant 13, -39 \leqslant l \leqslant 39$
Reflections collected	71251
Independent reflections	8520 [R_{int} = 0.0889, R_{sigma} = 0.0585]
Data / Restraints / Parameters	8520/0/504
Goodness-of-fit on F^2	1.191
Final R indexes [I⩾2σ(I)]	R_1 = 0.1094, wR_2 = 0.2436
Final R indexes [all data]	R_1 = 0.1339, wR_2 = 0.2549
Largest diff. peak/hole / eÅ^{-3}	1.34/−1.19

7.5 Supplementary Quantum Chemical Data

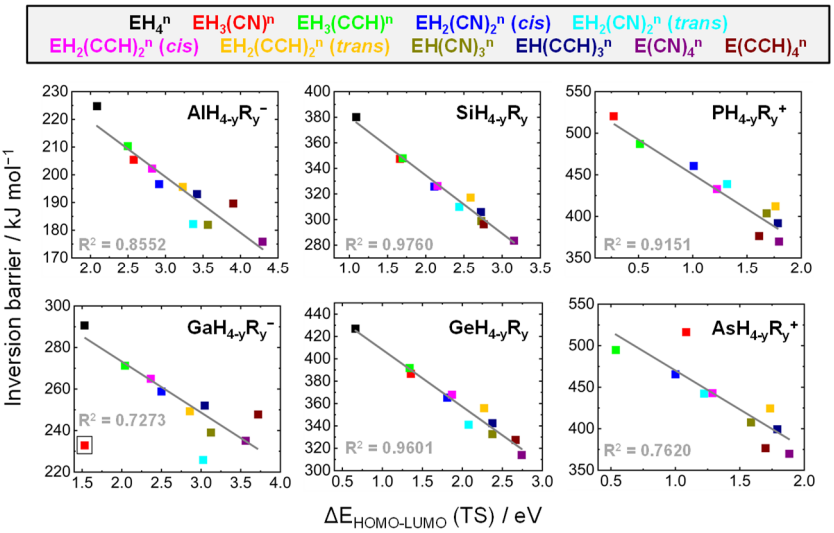

Figure 7.18: The frontier molecular orbital approximation of the second-order Jahn-Teller effect applied to square planar *p*-block atom-based molecules with respect to the degree of substitution. *Correlation plots of the square planar inversion barriers versus the Kohn-Sham HOMO-LUMO gap in the square planar state for $EH_{4-y}R_y^n$, E^n = Al^-, Si, P^+, Ga^-, Ge, As^+ and R = CN, CCH, y = 0, 1, 2, 3, 4. The datapoint for GaH_3CN^- (marked with a box) was not included in the linear regression as the transition structure optimization converged to a dissociative structure. The inversion barriers (deformation energy toward the square planar state) were calculated at the DLPNO-CCSD(T)/cc-pVQZ//B97M-D3(BJ)/cc-pVTZ level of theory and orbital energies were extracted from the B97M calculations.*[7]

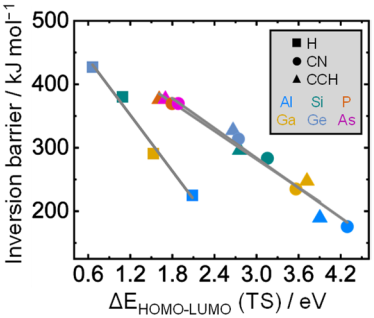

Figure 7.19: The frontier molecular orbital approximation of the second-order Jahn-Teller effect applied to square planar *p*-block atom-based molecules with respect to different substituents. *The inversion barriers (deformation energy toward the square planar state) were calculated at the DLPNO-CCSD(T)/cc-pVQZ//B97M-D3(BJ)/cc-pVTZ level of theory and orbital energies were extracted from the B97M calculations. The HOMO-LUMO gap of the square planar states is plotted for the molecules of constitution ER_4^n ($n = -1$ for E = Al, Ga, $n = 0$ for E = Si, Ge, $n = +1$ for E = P, As).*[7]

Table 7.1: Competition reactions for stereoinversion processes. *Reaction energies and enthalpies of the individual reactions shown in Figure 3.48. All data was obtained at the CCSD(T)/aug-cc-pwCVQZ(-PP)//CCSD(T)/aug-cc-pwCVTZ(-PP) level of theory, and the values are given in kJ mol^{-1}. Green highlights mark the energetically most favorable reaction. Underlined numbers were compared to experimentally determined data which is given in parentheses.*[25]

	BH_4^-	AlH_4^-	GaH_4^-	InH_4^-	TlH_4^-
i)	397.5 | 379.3	364.9 | 351.0	349.4 | 335.0	323.0 | 310.5	298.6 | 285.3
ii)	**320.0 | 307.1 (310)**[333]	323.9 | 315.3 (314)[333]	301.9 | 292.9	299.8 | 292.2	270.6 | 263.4
iii)	--	--	--	--	--
iv)	378.2 | 358.1	**206.5 | 200.0**	**162.4 | 153.7**	**99.2 | 95.0**	**19.4 | 14.5**
v)	376.0 | 358.3	264.7 | 260.8	236.0 | 231.2	181.4 | 180.5	132.9 | 131.9
	CH_4	SiH_4	GeH_4	SnH_4	PbH_4
i)	**469.4 | 436.4 (439.3)**[332]	403.6 | 383.3 (384.7)[332]	373.9 | 354.5 (348.9)[332]	335.9 | 319.6 (346)[332]	298.2 | 281.9
ii)	1342.1 | 1313.1	1113.0 | 1095.0	1071.3 | 1054.2	999.9 | 985.9	947.7 | 934.6
iii)	1780.9 | 1744.2 (1743.1)[552]	1587.9 | 1562.3	1536.0 | 1510.5	1470.0 | 1448.6	1394.3 | 1373.1
iv)	541.3 | 502.1 (503.4)[(a)]	**256.3 | 239.0 (238.6)**[(a)]	**177.7 | 162.0 (163.3)**[553]	**96.7 | 87.2**	**–9.3 | –16.9**
v)	500.4 | 462.9 (465.8)[(a)]	343.4 | 327.3	286.0 | 271.8	212.8 | 204.4	145.0 | 137.6
	NH_4^+	PH_4^+	AsH_4^+	SbH_4^+	BiH_4^+
i)	**558.1 | 519.9**	445.9 | 421.6	403.08 | 381.00	353.23 | 334.92	306.73 | 289.23
ii)	--	--	--	--	--
iii)	886.6 | 852.3 (851.9)[552]	807.8 | 783.8	769.4 | 747.1	758.7 | 739.8	694.0 | 676.5
iv)	801.4 | 752.6	**351.0 | 328.1**	**239.4 | 220.6**	**127.4 | 115.6**	**5.2 | –3.4**
v)	678.5 | 627.8	427.4 | 403.9	341.7 | 322.2	244.9 | 232.2	159.3 | 147.7

(a) Calculated with data from "NIST Computational Chemistry Comparison and Benchmark Database NIST Standard Reference Database Number 101 Release 21, August 2020, Editor: Russell D. Johnson III, http://cccbdb.nist.gov/" (Oct. 06, 2021).

8 ACKNOWLEDGEMENTS

This dissertation bears my name on its cover; and in fact, I have written it. Yet, so many people have made as indispensable as variegated contributions to each and every word within here. The path that I was allowed to embark upon in the past years would have never been possible without them. I would like to close by saying thank you to all of you!

Lutz Greb, thank you that you were my advisor, mentor, huge supporter, fellow campaigner, co-writer, discussion partner, listener, and friend for the past five years. You give everything you can for your coworkers. It was an honor to have been part of your team and knowing that I will soon be a Greb group alumnus makes me sad, though proud at the same time. You gave me the freedom to work on so many different projects, and you supported me during every step I took. I wish you all the best for the future!

I would like to thank all Greb group alumni. When I became part of the lab in the end of 2019, you fantastically included me into the group. Thank you, *Nina Kramer* and *Rezisha Maskey*, for being my lab mates during the first part of my doctorate. I will always remember the good old days of the −1.06 lab more than well. Thank you, *Deborah Hartmann*, for trying to measure even the worst possible "single crystal" for me. Thank you, *Fabian Ebner*, for passing me over your aluminate. I am thankful that I could continue your work.

Heiko Ruppert, *Thaddäus Thorwart*, *Daniel Roth*, the four of us might be considered the second generation of Lutz's doctoral students. I enjoyed every minute of working together with all of you. You are not only fantastic chemists but more importantly also great people. I am grateful to have had you by my side throughout my time as a doctoral student.

Philipp Erdmann, we worked together a lot, and I think we did and do a pretty good job in getting the group's data science "outgrowth" running. Thank you that I could take on this challenge together with you. I will miss your numerous visits to my desk and our vibrant discussions about RDKit, the world, and everything.

I would also like to thank all the Grebfruits – Postdocs, doctoral and master students, and research interns that grew after I joined the lab. You enriched the group in so many different ways. I wish you all the best for the future. Thank you, *Senta Kohl*, for picking up

one of the projects I started. The experiment we literally did together was one of the few which worked exactly as we envisioned. I will stay tuned for any new calix[4]pyrrolato aluminate chemistry; nitroaryls sound fun ...

Simone Ebel, *Senta Kohl*, *Paul Janßen*, *Valentin Hannibal*, *Christoph Bendel*, *Daniel Roth*, *Thaddäus Thorwart*, and *Manuel Schmitt*, thank you very much for proofreading this dissertation.

Thank you also to all the other members of Lutz's research group. It is really great that you joined the group. Thank you, *Ute Eisendick*, *Karin Gissmann*, and *Silke Dussel* for helping me with so much paperwork. It would have been impossible without you. *Manuel Schmitt*, we only overlapped for a short time, though I am already certain that you are the absolute perfect fit. Thank you that I could work together with you for a few months, and maybe one day, there will be a FIA machine learning model that can predict this suspicious antimony compound as accurately as we all wish.

Rouven Maier, *Nick Richert*, *Johannes Zeh*, *Sebastian Pauli*, *Friederike Schneider*, *Lisamaria Wallner*, *Eliane Engels*, *Andreas Albers*, and *Theresa Hähnel*, you were my bachelor students and research interns. Thank you for all the work. Sometimes we were fishing in murky waters, though it was always great fun to work together with all of you. *Andreas*, I am really happy to see you continuing the Greb group's data science branch. Take care that you (don't) get dragged into the lab.

I would like to thank *Hans-Jörg Himmel* and his research group for hosting us during the first time of my doctorate. Thank you, *Lucas Kistner*, that we could work together on one of your projects. My special thank you goes to *Hans-Jörg* for becoming the second referee of this dissertation.

Anya Gryn'ova and *Christopher Ehlert*, thank you for the collaborations. It was a pleasure to work together with you, and I learned a lot from you. I would also like to thank *Florian Schön* for the collaboration on the dehydrocoupling project. I would have never thought that I will end up doing polymer chemistry during my doctoral studies.

At this point, I would also like to explicitly say thank you to all the members of the X-ray team from the Himmel and the Greb group. I had quite some poorly diffracting "crystals", though you always did your best to get as much as possible out of them. I am grateful for your help – thank you!

I would like to thank the cleaning stuff, mechanics, locksmiths, electricians, glass blowers, and all the employees of the chemistry departments in general. Your work and our collaboration are essential. Especially, I would like to thank *Jürgen Graf*, *Markus Enders*, and *Beate Termin*. You helped me a lot with all kinds of NMR spectroscopy-related questions. The research we did together is definitely one of the highlights of my doctorate.

Thank you to all administrators of the JUSTUS 2 cluster. You do a fantastic job in taking care of these computers. You were always very kind and helpful no matter how wrong I submitted a few jobs.

Rob Paton, thank you for hosting me for a couple of months in your group at Colorado State University. I had a wonderful time in Fort Collins. A big thank you also goes to all the Paton and Kim group members. It was fantastic to work together with you in the "theory suite". Thank you, *Shree Sowndarya*; I learned so much from you and you helped me a lot. It was great to finish the FIA regression project together with you.

I would like to thank the German Academic Scholarship Foundation (Studienstiftung des Deutschen Volkes) for my doctoral scholarship. To become part of this organization is something I would never trade in for anything. It enriched my doctorate immensely. In particular, I would like to thank *Katja Patzel-Mattern* for being the best scholar host I could imagine. Also thank you to all the group members. I will miss our Urban Kitchen meetings, the trips, and the long discussions about science, culture, education, and so much more. I would also like to thank the State graduate funding organization (Landesgraduiertenförderung des Landes Baden-Württemberg) for a doctorate completion scholarship.

I would like to say thank you to all my family and friends. Without your support it would have never been possible to get to this point. *Simone*, thank you for going through live with me and for always being there for me. You supported me every day throughout my time as a doctoral student. I am looking forward to our future. *Mum*, *dad*, you are my heroes. You are the true coauthors of this dissertation! Thank you for everything.

„Wahr sind nur die Erinnerungen, die wir mit uns tragen, die Träume, die wir spinnen, und die Sehnsüchte, die uns treiben. Damit wollen wir uns bescheiden." – HEINZ RÜHMANN as Dr. Johannes Pfeiffer in „Die Feuerzangenbowle" (1944) by H. SPOERL and H. WEISS.

GESAMTFAKULTÄT FÜR MATHEMTIK, INGENIEUR- UND NATURWISSENSCHAFTEN

COMBINED FACULTY OF MATHEMATICS, ENGINEERING AND NATURAL SCIENCES

Eidesstattliche Versicherung gemäß § 8 der Promotionsordnung für die Gesamtfakultät für Mathematik, Ingenieur- und Naturwissenschaften der Universität Heidelberg / Sworn Affidavit according to § 8 of the doctoral degree regulations of the Combined Faculty of Mathematics, Engineering and Natural Sciences at Heidelberg University

1. Bei der eingereichten Dissertation zu dem Thema / The thesis I have submitted entitled

   Structural Constraint and Flexibility in the Chemistry of Lewis-Acidic p-Block Atom-Based Molecules

   handelt es sich um meine eigenständig erbrachte Leistung / is my own work.

2. Ich habe nur die angegebenen Quellen und Hilfsmittel benutzt und mich keiner unzulässigen Hilfe Dritter bedient. Insbesondere habe ich wörtlich oder sinngemäß aus anderen Werken übernommeneInhalte als solche kenntlich gemacht. / I have only used the sources indicated and have not made unauthorized use of services of a third party. Where the work of others has been quoted or reproduced, the source is always given.

3. Die Arbeit oder Teile davon habe ich wie folgt/bislang nicht[1)] an einer Hochschule des In- oder Auslands als Bestandteil einer Prüfungs- oder Qualifikationsleistung vorgelegt. / I have not yet/have already[1)] presented this thesis or parts thereof to a university as part of an examination or degree.

   Titel der Arbeit / Title of the thesis: ……
   Hochschule und Jahr / University and year: ……
   Art der Prüfungs- oder Qualifikationsleistung / Type of examination or degree: ……

4. Die Richtigkeit der vorstehenden Erklärungen bestätige ich. / I confirm that the declarations made above are correct.

5. Die Bedeutung der eidesstattlichen Versicherung und die strafrechtlichen Folgen einer unrichtigen oderunvollständigen eidesstattlichen Versicherung sind mir bekannt. / I am aware of the importance of a sworn affidavit and the criminal prosecution in case of a false or incomplete affidavit.

Ich versichere an Eides statt, dass ich nach bestem Wissen die reine Wahrheit erklärt und nichts verschwiegen habe. / I affirm that the above is the absolute truth to the best of my knowledge and that I have not concealed anything.

…… ……

Ort und Datum / Place and date — Unterschrift / Signature

[1)] Nicht Zutreffendes streichen. Bei Bejahung sind anzugeben: der Titel der andernorts vorgelegten Arbeit, die Hochschule, das Jahr der Vorlage und die Art der Prüfungs- oder Qualifikationsleistung. / Please cross out what is not applicable. If applicable, please provide: the title of the thesis that was presented elsewhere, the name of the university, the year of presentation and the type of examination or degree.

The German text is legally binding.